

University of St Andrews



Full metadata for this thesis is available in
St Andrews Research Repository
at:

<http://research-repository.st-andrews.ac.uk/>

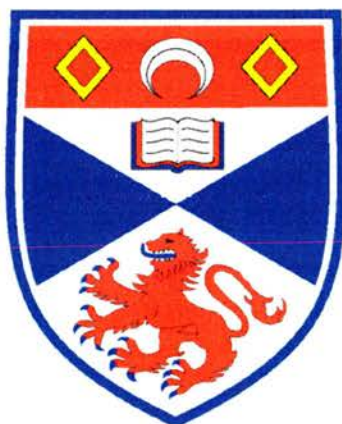
This thesis is protected by original copyright

In Situ Functionalisation & Characterisation of Non-Ionic Block Copolymer Templated Mesoporous Silicas



A thesis presented for the degree of
Doctor of Philosophy
in the faculty of science of the University of St. Andrews
by Robert Peter Hodgkins, BSc (Hons) MRSC

April 2005



University
of
St Andrews

Declarations

- (i) I, Robert P. Hodgkins, hereby certify that this thesis, which is approximately 46,000 words in length, has been written by me, that it is the record of work carried out by me and that it has not been submitted in any previous application for a higher degree.

27/04/05

- (ii) I was admitted as a research student in January, 2002 and as a candidate for the degree of PhD in January, 2003; the higher study for which this is a record was carried out in the University of St Andrews between 2002 and 2005.

27/04/05

- (iii) I hereby certify that the candidate has fulfilled the conditions of the Resolution and Regulations appropriate for the degree of PhD in the University of St Andrews and that the candidate is qualified to submit this thesis in application for that degree.

27/04/05

In submitting this thesis to the University of St Andrews I understand that I am giving permission for it to be made available for use in accordance with the regulations of the University Library for the time being in force, subject to any copyright vested in the work not being affected thereby. I also understand that the title and abstract will be published, and that a copy of the work may be made and supplied to any *bona fide* library or research worker.

27/04/05

Acknowledgements

I would first like to take this opportunity to thank my supervisor Dr. Paul A. Wright for allowing me to undertake a project in physical chemistry. His expert guidance, encouragement and fruitful discussions from start to finish have allowed the work within this thesis to be completed. For allowing my scientific development to broaden a special thanks is also owed.

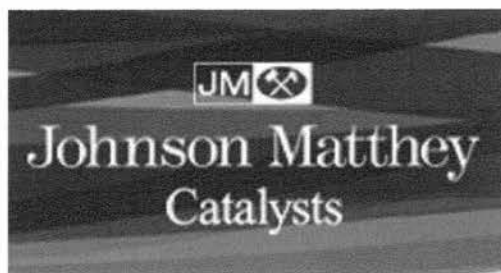
In learning new characterisation techniques I would like to thank: Mrs. Sylvia Williamson (University of St. Andrews) for training on the IGA; Drs. Graham Smith and Hassane El Mkami (Physics department, University of St. Andrews) for high-field ESR measurements and for increasing my knowledge and interpretation of ESR spectra; Dr. Eric McIness (National Multi-frequency ESR facility, University of Manchester) for K-band ESR measurements and discussions; Prof. John Walton (University of St. Andrews) for X-band measurements and for spectrometer usage and to Dr. Alfonso Garcia-Bennett (formerly University of St. Andrews now Stockholm University) for his help in microscopy regardless of his workload. Drs. Tapas Sen (UMIST) and Sonia Fiorilli (Torino, Italy) are thanked for low-angle XRD diffraction data and finally to Prof. M.W. Anderson (UMIST) for STA-11 simulation.

I would like to thank past and present members of the Wright group and also my friends for making my stay at St. Andrews even more enjoyable. So in no particular order, thank you to: Jorge, Mike, Tim, Paul, Aoife, Mark, Ste, Stanton, Alex, Alfonso, Stuart, David & Sandra, Nandini, Jesús, Pierrot and the rest.

Thank you to the EPSRC and Syntex (now Johnson Matthey Catalysts) for their financial support and in particular Drs. Martin Lok and Xavier Baucherel.

The logo for the Engineering and Physical Sciences Research Council (EPSRC), consisting of the letters 'EPSRC' in a bold, sans-serif font, with horizontal lines above and below the text.

Engineering and Physical Sciences
Research Council



Finally I would like to thank my family for their support throughout my studies. Thanks to: Andy, Michelle, Phill, Cassie, Terry, Mark, Billy, Shirley, Anthony, Dad and Sue. I would also like to thank Peter & Mo and Berni & Phil for their support too.

Dedication

This thesis is dedicated to my Mother, *Joan Murphy*, for her endless unconditional support throughout regardless and whom I could never thank enough.

Thank you.

Abstract

Well-ordered functionalised mesoporous solids templated by non-ionic triblock copolymers in acidic media have been prepared and characterised through x-ray diffraction, electron microscopy and N₂ adsorption measurements and investigated as high surface area catalyst supports.

For samples templated by Pluronic P123 (EO₂₀PO₇₀EO₂₀) the internal surfaces were functionalised by co-condensation of various trialkoxysilanes including propylthiol, phenyl, cyanopropyl and propylchloride during the sol-gel syntheses and the resulting solids rendered porous by solvent extraction. The effect of varying the concentration of the organo-siloxane *in situ* at levels of 2, 5, 7 and 10% (based on SiO₂) on the mesophase product symmetry and quality have been studied and the maximum loading possible with simultaneous retention of high order and defined mesoporosity increases in the sequence propylchloride (5%) , phenyl (5%) < propylthiol (7%) < cyanopropyl (10%).

Controlled *in situ* functionalisation of P123 templated silicas with 3-mercaptopropyltriethoxysilane at 7% has resulted in a new large pore cubic Ia $\bar{3}$ d pure phase solid, designated **STA-11**, ($a \cong 22$ nm) with an ordered bicontinuous pore structure. It was found that the hydrolysis temperature played a key role as synthesis below 50 °C (optimum temperature 40 °C) gave the cubic structure while above this hexagonal p6mm SBA-15 was formed. The potential advantage of this new mesoporous solid over SBA-15 and similar cubic MCM-48 derives from the three dimensional connectivity with large pore size (diameter in the region of 8 nm) and should lead to enhanced molecular transport and resistance to pore blocking. It was found that addition of the phenyl-siloxane to the sol-gel at a concentration of 5% also resulted in the cubic structure.

For solids templated by Pluronic F127 (EO₁₀₆PO₇₀EO₁₀₆) the addition of the thiol-siloxane were added at the same concentrations. For the pure siliceous sample the reported FDU-12 (Fm3m) structure based on a cubic close packed system formed whereas introducing thiols directly into the syntheses resulted in structural and

morphological changes. At a 5% loading, stacking faults and twin planes were observed as well as domains of a $P6_3/mmc$ hexagonal phase. The stacking defects result in changes to the morphology with particles displaying well-defined hexagonal prismatic geometry tapering at the basal faces. Thiol loadings of 7% result in morphology changes to hexagonal plates. For all thiol functionalised solids a new route to quantifying the accessible thiol groups within the pores of mesoporous solids, adapted from a reported procedure, using Ellman's reagent lead to quantifications of 54 – 72% for SBA-15/STA-11 samples and 50 – 60% for 'FDU-12' samples.

Propyl-chloride functionalised SBA-15 have been further modified with the azamacrocycles, cyclam (1,4,8,11-tetraazacyclotetradecane) and TACN (1,4,7-triazacyclononane) before transition metal incorporation, for potential use in selective oxidation reactions. Multi-frequency ESR has given information on paramagnetic Cu^{2+} within cyclam. The composite catalysts were found not to be robust or stable to re-use, however.

The use of thiol- and alkylammonium-functionalised mesoporous silicas have been used to incorporate precious metal complexes. Various reduction methods have been investigated to achieve metallic nanoparticles: the most promising was found to be $AuCl_4^-$ anion exchange onto alkylammonium functionalised SBA-15 and subsequent reduction in H_2 , which gave abundant gold particles of 4 – 9 nm located within the mesopores.

Publications

- Synthesis of Large-Pore Ia $\bar{3}$ d Mesoporous Silica and its Tubelike Carbon Replica. Shunai Che, Alfonso E. Garcia-Bennett, Xiaoying Lou, Robert P. Hodgkins, Paul A. Wright, Dongyuan Zhao, Osamu Terasaki, Takashi Tatsumi, *Angew. Chem. Int. Ed.*, 2003, **42**, 3930-3934
- HRTEM Imaging of Mesoporous Phase Transition from Hexagonal p6mm to Cubic Ia $\bar{3}$ d Symmetry. Alfonso E. Garcia-Bennett, Robert P. Hodgkins, Tapas Sen, Michael W. Anderson, Paul A. Wright, *Proceedings: 14th International Zeolite Conference*. ISBN: 0-958-46636-X (CD-ROM)
- Structure and Morphology of Propylthiol-functionalised Mesoporous Silicas Templated by Non-ionic Triblock Copolymers. Robert P. Hodgkins, Alfonso E. Garcia-Bennett, Paul A. Wright, *Micro. Meso. Mater.*, 2005, **79**, 241-252

Abbreviations

	Parallel
⊥	Perpendicular
1D	1-dimensional
2D	2-dimensional
3D	3-dimensional
a	Unit cell parameter
Å	Angstroms (10^{-10} m)
A	Hyperfine coupling constant
ABAB	Hexagonal stacking sequence
ABCABC	Cubic stacking sequence
B	Magnetic field
BET	Brunauer-Emmett-Teller calculation of surface area (m^2g^{-1})
BJH	Barrett-Joyner-Halenda calculation of pore size distribution
c	Unit cell parameter
°C	Degrees celsius
CCD	Charge coupled devices
ccp	Cubic close packed
CHN	Elemental analysis (wt%) for carbon, hydrogen and nitrogen
CLPTES	Chloropropyltriethoxysilane
CMC	Critical micelle concentration
CMK	Carbon mesostructured materials (by KAIST)
CNPTES	Cyanopropyltriethoxysilane
C _n -s-1	Divalent quaternary ammonium surfactant of n carbons within the tail and s carbon atoms between the ammonium groups
CTAB	Cetyltrimethylammonium bromide (16 carbons in the surfactant tail)
d_{hkl}	Interplanar spacing
DNA	Deoxyribonucleic acid
EDX	Energy dispersive x-ray spectroscopy
ENDOR	Electron-nuclear double resonance spectroscopy
EPR	Electron paramagnetic resonance spectroscopy
ESR	Electron spin resonance spectroscopy
eV	Electron volts
F127	Pluronic F127 (triblock polymer PEO-PPO-PEO)
fcc	Face centred cubic
FDU	Fudan University
FFT	Fourier Transform
FSM	Folded sheet mesoporous materials
g	Surfactant packing parameter
g	ESR proportionality constant
g	Gram
G	Gauss
GC	Gas chromatography
h	Hour
hcp	Hexagonal close packed
HMHACO	1,4,7,10,13,16-hexamethyl-1,4,7,10,13,16-hexaazacyclooctadecane
HRTEM	High Resolution Transmission Electron Microscopy

ICP-MS	Inductively coupled plasma – Mass spectrometry
IGA	Intelligent gravimetric analysis
IR	Infra red spectroscopy
K	Kelvin (temperature unit)
LCT	Liquid crystal template mechanism
m	Meter
MAS	Magic angle spinning
MCF	Meso-cellular foam
MCM-	Mobil Composition of Matter –
min	Minute
MPTES	3-Mercaptopropyltriethoxysilane
NLDFT	Non-local density functional theory
nm	Nanometer
NMR	Nuclear magnetic resonance spectroscopy
P123	Pluronic123 (triblock polymer PEO-PPO-PEO)
P	Pressure (bar)
Po	Saturated vapour pressure (bar)
PEO	Polyethylene oxide
PPO	Polypropylene oxide
PTES	Phenyltriethoxysilane
SBA-	Santa Barbara–
SDA	Structure directing agent
SEM	Scanning electron microscopy
SSA	Specific surface area
STA-	St Andrews–
STAC-1	St Andrews Cambridge–1
STP	Standard temperature and pressure (0 °C, 1 atm)
TACN	Tetraazacyclononane
TEOS	Tetraethylorthosilicate, Si(OEt) ₄
TGA	Thermal gravimetric analysis
TMB	Trimethylbenzene
TMPTMAC	N-trimethoxysilylpropyl-N,N,N-trimethylammonium chloride
TMTACN	1,4,7-trimethyl-1,4,7-triazacyclononane
TMTACT	1,4,8,11-tetramethyl-1,4,8,11-tetraazacyclotetradecane
UV-Vis	UV-Visible spectroscopy
V	Volume (dm ³ or ml)
V _m	Monolayer volume
XRD	X-ray Diffraction

Contents

Declarations	i
Acknowledgements	ii
Dedication	iii
Abstract	iv
Publications	vi
Abbreviations	vii
Contents	ix
Preface	xii
Aims	xv

General introduction	Chapter 1
----------------------	-----------

Synopsis	1
1.1 Introduction	2
1.2 Surfactant chemistry	7
1.3 Synthesis	11
1.4 Functionalisation	15
1.4.1 Post-synthetic grafting	16
1.4.2 <i>In situ</i> functionalisation	18
1.5 References	20

Characterisation techniques	Chapter 2
-----------------------------	-----------

Synopsis	24
2.1 X-ray diffraction	25
2.2 Transmission electron microscopy	31
2.3 Nitrogen adsorption	38
2.4 Electron spin resonance spectroscopy	49
2.5 References	61

Functionalisation of SBA-15 ' <i>in situ</i> ': Synthesis & Characterisation	Chapter 3
--	-----------

Synopsis	63
3.1 Introduction	64
3.2 Experimental	68
3.3 Results & Discussion	70
3.3.1 Thiol-functionalised mesoporous silica templated by P123	70
3.3.1.1 Elemental analysis and Ellman's quantification	70
3.3.1.2 X-ray diffraction (XRD)	74
3.3.1.3 SEM	78
3.3.1.4 TEM	81
3.3.1.5 N ₂ Adsorption	87
3.3.1.6 Temperature effect of product mesophase selectivity	92
3.3.1.7 Simulation	94
3.3.1.8 Conclusions	97

3.3.2 Phenyl-functionalised mesoporous silica templated by P123	99
3.3.2.1 XRD	99
3.3.2.2 SEM	101
3.3.2.3 TEM	104
3.3.2.4 N ₂ Adsorption	107
3.3.2.5 Conclusions	112
3.3.3 Cyano-functionalised mesoporous silica templated by P123	113
3.3.3.1 Cyano-analysis	113
3.3.3.2 Characterisation	115
3.3.3.3 Conclusions	121
3.3.4 Chloro-functionalised mesoporous silica templated by P123	122
3.3.4.1 Characterisation	122
3.3.4.2 Conclusions	129
3.4 General Conclusions	130
3.5 References	132

Structure & Morphology changes in Propylthiol Functionalised FDU-12 Chapter 4

Synopsis	135
4.1 Introduction	136
4.2 Experimental	140
4.3 Results & Discussion	141
4.3.1 Elemental analysis and Ellman's quantification	141
4.3.2 XRD characterisation of thiol-functionalised mesoporous silica templated by F127	142
4.3.3 SEM characterisation of thiol-functionalised mesoporous silica templated by F127	144
4.3.4 TEM characterisation of thiol-functionalised mesoporous silica templated by F127	150
4.3.5 N ₂ adsorption characterisation of thiol-functionalised mesoporous silica templated by F127	154
4.3.6 Variation of synthesis of thiol-functionalised mesoporous silica templated by F127	159
4.4 Conclusions	165
4.5 References	166

Metallated Azamacrocycles supported on SBA-15 Chapter 5

Synopsis	168
5.1 Introduction	169
5.2 Experimental	173
5.3 Results & Discussion	177
5.3.1 Multi frequency ESR studies of Cu ²⁺ [cyclam] SBA-15	177
5.3.2 Metallated [TACN] supported SBA-15: Epoxidation of cyclohexene	195
5.4 Conclusions	199
5.5 References	200

Synopsis	203
6.1 Introduction	204
6.2 Experimental	210
6.2.1 Sodium citrate reduction of gold chloride within mesoporous silica	210
6.2.2 'Auto-reduction' of gold chloride within mesoporous silica	211
6.2.3 Metallic gold within mesoporous silica from reduction of reverse gold micelle by sodium borohydride	211
6.2.4 N-trimethoxysilylpropyl-N,N,N-trimethylammonium chloride functionalised mesoporous silica for noble metal complex ion exchange and reduction by hydrogen	213
6.2.5 Allyl palladium chloride dimer reaction with MPTES-functionalised silica	214
6.2.6 Analysis methods	214
6.3 Results & Discussion	215
6.3.1 Chemical analysis	215
6.3.2 Sodium citrate reduction of AuCl ₃ within STA-11	217
6.3.3 'Auto-reduction' of AuCl ₃ within thiol functionalised mesoporous silica	222
6.3.3.1 UV analysis of the uptake of chloraurate complex on pure silica and thiol functionalised SBA-15	222
6.3.3.2 TEM analysis of chloraurate complex 'auto-reduction' on thiol functionalised SBA-15/STA-11	226
6.3.4 Sodium borohydride reduction of reverse Au micelles within thiol functionalised silica	232
6.3.5 Trimethylammonium chloride functionalised SBA-15 for noble metal complex ion-exchange & reduction by H ₂	240
6.3.6 Thiol functionalised silica supports for the allylpalladium chloride complex and reduction under mild conditions	247
6.4 Conclusions	250
6.4.1 Individual methods	250
6.4.1.1 Sodium citrate reduction	250
6.4.1.2 Auto-reduction	250
6.4.1.3 Reverse Au micelles and sodium borohydride reduction	251
6.4.1.4 Alkylammonium chloride functionalised solids and thermal reduction with H ₂	252
6.4.1.5 Allylpalladium chloride incorporated thiol-functionalised silicas	252
6.4.2 Summary	253
6.5 References	254

Synopsis	257
7.1 General conclusions	258
7.2 Further work	260

Preface

Microporous zeolites (pore size $\leq 10 \text{ \AA}$) – the first of the now numerous families of porous solids – occur naturally quite extensively as minerals. The first of these, discovered by the Swedish mineralogist A. F. Cronstedt in 1756 [1], are crystalline aluminosilicates with corner-sharing $[\text{SiO}_4]$ and $[\text{AlO}_4]$ tetrahedra and have a composition:



where M is typically the metal cation of valence n , and both the metal and water are extra-framework species and do not constitute the rigid inorganic framework. The stoichiometric ratio of Si/Al can vary from ∞ down to 1. The aluminium substitutes for silicon and induces a negative charge, which is counterbalanced by a positive cation – normally a proton (H^+) or an alkaline earth metal ion (eg. Na^+). The first successful synthetic zeolite was produced by St. Claire Deville in 1862 [2], opening up an international search for novel nanoporous solids. Such solids have many applications in many branches of the chemical industry due to their properties of large internal surface areas (typically $300 \text{ m}^2\text{g}^{-1}$ [microporous zeolites] – $1000 \text{ m}^2\text{g}^{-1}$ [mesoporous solids]) and narrow pore size distributions enabling them to act as molecular sieves. The size and uniformity of the pore channels and cavities gives rise to shape selectivity and thus determines which molecules pass through or form in the channels and cavities. The ability to functionalise these porous materials uniformly throughout the internal surface area renders them useful in catalysis, ion-exchange and separation (adsorption).

Microporous zeolites are not of use, however, in effecting transformations of molecules which are too large to access the internal channels: larger pore systems were required to open up the field once more, for example for the immobilisation of large biological molecules such as enzymes. The discovery of mesoporous solids ($15 \text{ \AA} \leq \text{pore size} \leq 500 \text{ \AA}$) answered this requirement. C. T. Kresge *et al.* [3] synthesised the first mesoporous solid in 1992 - Mobil Composition of Matter – 41 (MCM-41). The inorganic framework consists of amorphous silica with arrays of ordered

hexagonal mesopores (after template removal) surrounding cylindrical surfactant micelles. The resulting framework forms a honeycomb pattern and is 2-dimensionally connected with a hexagonal array of one dimensional pores. This was one member of the newly discovered mesoporous solids designated M41S, along with MCM-48, a cubic 3-dimensionally connected porous system containing two separately intertwined networks and also a third, lamellar phase, MCM-50. M41S materials and in particular MCM-41 ($\sim 40 \text{ \AA}$ pore size) remain the most widely studied mesoporous molecular sieves although extensive research carried out by Stucky, Zhao and Terasaki amongst others has led to the development of further mesostructures. Research by Stucky (University of California, Santa Barbara) has led to the discovery of the SBA-series and in particular SBA-15 (the main mesoporous solid support researched in this thesis). SBA-15 is a larger pore ($\sim 90 \text{ \AA}$) analogue of MCM-41 synthesised with the aid of non-ionic triblock copolymers as a template rather than the smaller cationic surfactants used for the formation of MCM-41. A large pore analogue of cubic MCM-48 ($\sim 35 \text{ \AA}$) would possess potential advantages over that of MCM-41 and SBA-15 for molecular transportability due to a large cubic pore structure. Recently a large pore analogue was discovered independently by two groups - Wright *et al.* and Zhao *et al.* and is designated STA-11 (St. Andrews) and FDU-5 (Fudan University) respectively with a pore size in the region of 80 \AA [4-6].

The number of publications concerned with mesoporous solids has increased rapidly year by year since their discovery in the early 1990's [7]. As the nanotechnology industry continues to grow, so the interest and research in this area continues (figure 1). The word **nano** is an important one in the fields of both academia and industry, stretching from chemistry/physics to bio-chemistry to the silicon-chip computer industry.

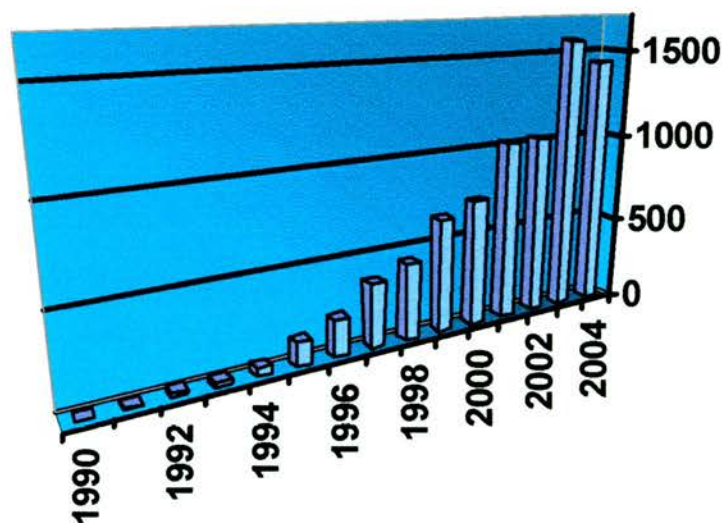


Figure 1. A bar chart to show the rise of mesoporous solid publications per annum [7]

- [1] A.F. Cronstedt, *Kongl. Svenska Vetenskaps Akademiens Handlinger.*, 1756, **17**, 20
- [2] H. de Sainte Claire Deville, *C.R. Hebd. Seances Acad. Sci.*, 1862, **54**, 324
- [3] C.T. Kresge, M.E. Leonowicz, W.J. Roth, J.C. Vartuli, J.S. Beck, *Nature*, 1992, **359**, 710
- [4] A. E. Garcia-Bennett, PhD thesis, University of St. Andrews, September 2002
- [5] X. Liu, B. Tian, C. Yu, F. Gao, S. Xie, B. Tu, R. Che, L.M. Peng, D. Zhao, *Angew. Chem. Int. Ed.*, 2002, **41**, 3876
- [6] R.P. Hodgkins, A.E. Garcia-Bennett, P.A. Wright, *Micro. Meso. Mater.*, 2005, **79**, 241
- [7] The values of the number of publications per year as seen in Figure 1 arise from the number of hits Web of Knowledge finds when searching for the term 'mesoporous.' The values obtained are not the exact figure but are consistent in comparison.

Aims

The aim of this project is to investigate the structural chemistry and possible applications of mesoporous solids templated by non-ionic triblock copolymers and functionalised *in situ* during their synthesis. To achieve this aim we set out the following objectives:

- To synthesis the mesoporous silicate – SBA-15, functionalised *in-situ* by the co-condensation of various trialkoxysilanes;
- To characterise fully the molecular sieves, once rendered porous, using a combination of techniques including diffraction, electron microscopy and porosity measurements;
- To incorporate transition metals with catalytic potential within the pore space via two routes:-
 - (i) to tether or chemisorb azamacrocycles before introducing 1st row transition metals into the ring. ESR spectroscopy is used to determine the environment of the metal cations.
 - (ii) to adsorb noble metal chlorates through the organic functional groups within the pores and to reduce these to their respective metals as colloids/nanoparticles through various routes

Chapter 1

General Introduction

Synopsis

This chapter gives an introduction to mesoporous solids and contains information on their long-awaited discovery by zeolite chemists searching for larger pore analogues to zeolites. They open up the possibility of potential applications further to porous solids. The role of surfactants acting as architectural organic scaffolds is described highlighting the mechanisms in the general synthesis. Finally methods of functionalising silica – post-synthesis modification and co-condensation reactions – are detailed.

1.1 Introduction

Silica can exist both as crystalline or amorphous phases, usually in the form of tetrahedral SiO_4 building units. The most common crystalline phase is quartz, used extensively to manufacture optically pure window glazing and an important part of today's lifestyle. Nature has perfected the nano-scale, 10^{-9} m, art of silica/silicate architecture in the form of zeolites, which possess an open porous framework ideal to host small guest molecules. Synthetically synthesising such analogues – either as micro-, meso- or macroporous solids – is beneficial in a world advancing continually in technological advances.

Zeolites are microporous silicates of crystalline framework consisting of tetrahedral SiO_4 units, possessing pore opening and channels/cavities in the region of ≤ 10 Å with thermally stable inorganic frameworks with high specific surface areas. The commercial applications held by these silicate minerals can be seen in table 1.1.1.

Zeolite Applications	
Ion exchange	Water purification (heavy metal removal) (Clinoptilolite)
	Water softening ($\text{K}^+/\text{Mg}^{2+}$) exchange in washing powders (Zeolite A, P)
Adsorbents	Drying agent: Molecular sieve (Zeolite A, X)
	O_2 air enrichment: using the induced dipole interactions of N_2 vs. O_2 (Zeolite A)
Catalysis	Catalytic converters: doped with Pd/Pt/Rh for NO_x control
	Catalytic cracking of hydrocarbons (H-ZMS-5, H-Zeolite-Y, β)
Table 1.1.1. Commercial applications of zeolites.	

Whereas zeolites have found great utility in their ability to select between small molecules and different cations, mesoporous solids offer possibilities for applications to species up to an order of magnitude larger in dimensions. If a series of larger species are present, say colloidal precious metals or large bio-molecules such as proteins, which due to their bulky nature in comparison cannot diffuse through the

smaller zeolitic network, then a larger pore analogue to the zeolite is required to effectively perform the same molecular sieving action.

To obtain molecular sieves for larger molecules, scientists first had to discover how to synthetically design such materials. Many new synthetic architectures crystallise around structure directing agents or templates, which upon removal render the solid porous. Thinking that bigger templates or aggregations of molecules could act as a mould, the discovery of such materials was finally achieved. The breakthrough of large well-defined porous silicas – mesoporous solids ($\sim 15 \text{ \AA} < \text{pore size} < \sim 500 \text{ \AA}$) – came about by the research of Mobil Corporation, USA, in 1992 [1,2] with the discovery of MCM-41 (**M**obil **C**omposition of **M**atter) templated by amphiphilic surfactant aggregations in a sol-gel synthesis – namely cetyltrimethylammonium bromide, CTAB, $[\text{CH}_3(\text{CH}_2)_{15}\text{N}^+(\text{CH}_3)_3\text{Br}^-]$ (figure 1.1.1).

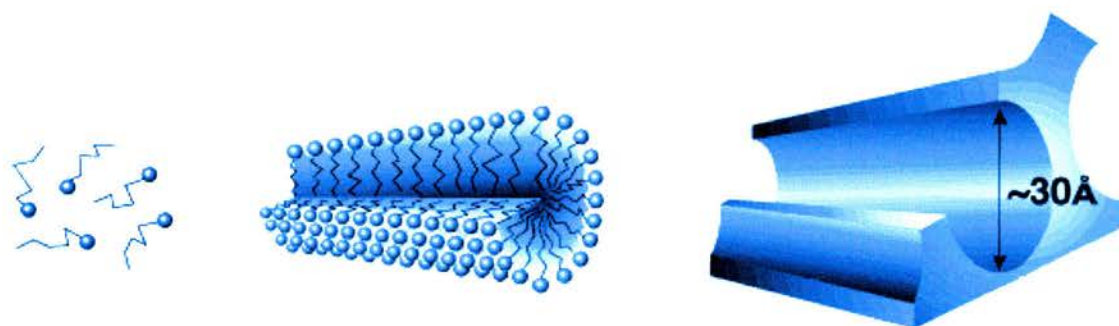


Figure 1.1.1. The novel templating of MCM-41 through silica condensation around aggregations of organic surfactant molecules [3]

This new compound is not crystalline in the conventional way but rather contains amorphous silica walls with a well-defined regular hexagonal array of 1-dimensional pores. The fact that this material has a narrow distribution of pores and also that tuning the synthesis gave various topologies along with the mesoporous family extending to what is now known as the M41S family – MCM-48 (3-dimensional network of cubic symmetry) and MCM-50 (a lamellar phase) – subsequently gave the impetus to scientific groups, such as the group of Stucky from the University of California at Santa Barbara, to extend this new and exciting field.

Although the group of Kresge *et al.* are generally acknowledged in the scientific community as the first to synthesise such an ordered silica on the mesoscale another group led by Kuroda (Waseda University) also synthesised a regularly ordered pore system composed of amorphous walls whose publication date [4] is before the first Mobil patent filing date [5]. There is too another patent filed in 1971 [6] disclosing the synthesis of a material comparable to MCM-41, but those researchers did not foresee the full context of the material produced [7]. The paper by Kuroda is difficult to generalise describing a procedure relying on the intercalation of silicate sheets suggesting a mechanism for folded sheet materials (FSM-n). Mobil described a general pathway that has been extended to other materials [8,9] showing liquid crystal templating where oligomeric inorganic species are organised into mesostructured arrays via the influence of surfactant molecules in solution.

Stucky *et al.* used other surfactants as templates for the condensation of silica with the notion that different systems will form different organic amphiphilic micelles to give rise to individual topologies. Table 1.1.2 observes the silica compounds, designated SBA-n, (Santa Barbra), as the outcome of varying the nature of the surfactant as an organic template source [10-12].

Designated Silica	Year reported	Surfactant	Mesophase
SBA-1	1995	$\text{CH}_3(\text{CH})_n\text{NEt}_3$	Cubic Pm-3n
SBA-2	1995	$\text{C}_n\text{-s-1}^\dagger$	3D Hexagonal P6 ₃ /mmc
SBA-3	1995	$\text{C}_n\text{-s-n}^\dagger$	Hexagonal p6m
SBA-8	1999	Bolaform ⁺	2D Rectangular cmm
SBA-11	1998	$\text{C}_{16}\text{EO}_{10}^*$	Cubic Pm-3n
SBA-12	1998	$\text{C}_{18}\text{EO}_{10}^*$	3D Hexagonal p6 ₃ /mmc
SBA-15	1998	$\text{PEO}_{20}\text{PPO}_{70}\text{PEO}_{20}^*$	Hexagonal p6mm
SBA-16	1998	$\text{PEO}_n\text{PPO}_3\text{PEO}_n^*$	Cubic Im-3m

[†] $\text{C}_n\text{H}_{2n+1}\text{N}^+(\text{CH}_3)_2(\text{CH}_2)_s\text{N}^+(\text{CH}_3)_3 [2\text{Br}^-]$; n = 12,14,16,18,20,22; s = 2,3,6

⁺ $(\text{CH}_3)_3\text{-N}^+-\text{C}_n\text{H}_{2n}-\text{OC}_6\text{H}_4\text{C}_6\text{H}_4\text{OC}_n\text{H}_{2n}\text{N}^+(\text{CH}_3)_3 [2\text{Br}^-]$; n = 2,4,6,8,10,12

*See figure 1.2.2

Table 1.1.2. Mesoporous silica structures by Stucky and co-workers.

The group of Stucky are not the only researchers to successfully develop a series of mesoporous solids. Work by Zhao has led to an FDU-series of solids including: FDU-1 [13]; FDU-2 [14]; FDU-5 [15] and FDU-12 [16]. Furthermore Ryoo *et al.* have also successfully achieved not one series of solids but two: these are (i) mesoporous silicas such as – KIT-1 [17]; KIT-5 [18] and KIT-6 [19] and (ii) a series of porous carbons which are the negative replica of the mesoporous solid templates either as nano-rods or nano-tubes – CMK-1 (MCM-48 template, after silica removal the two carbon networks join) [20]; CMK-2 (SBA-1 template) [21]; CMK-3 (SBA-15 template, nano-rod) [22]; CMK-4 (disordered MCM-48 template, after silica removal the two carbon networks remain) [23]; CMK-5 (SBA-15 template, nano-tubes as only a carbon coating of pores and not complete filling as in CMK-3) [24] and CMK-8,-9 (KIT-6 template and analogous to CMK-3 and CMK-5 with regards to carbon filling respectively) [25].

The main mesoporous silica utilised within this thesis is SBA-15 which is a large pore analogue of MCM-41. SBA-15 has a 2-dimensional well-ordered hexagonal array of 1-dimensional pores with a pore diameter in the region of 10 nm^{*} and so can take up larger guest molecules than MCM-41. A schematic representation of some mesoporous silica pore sizes can be seen in figure 1.1.2.

* As with all mesoporous silica the pore size can be tailored depending on conditions of synthesis.

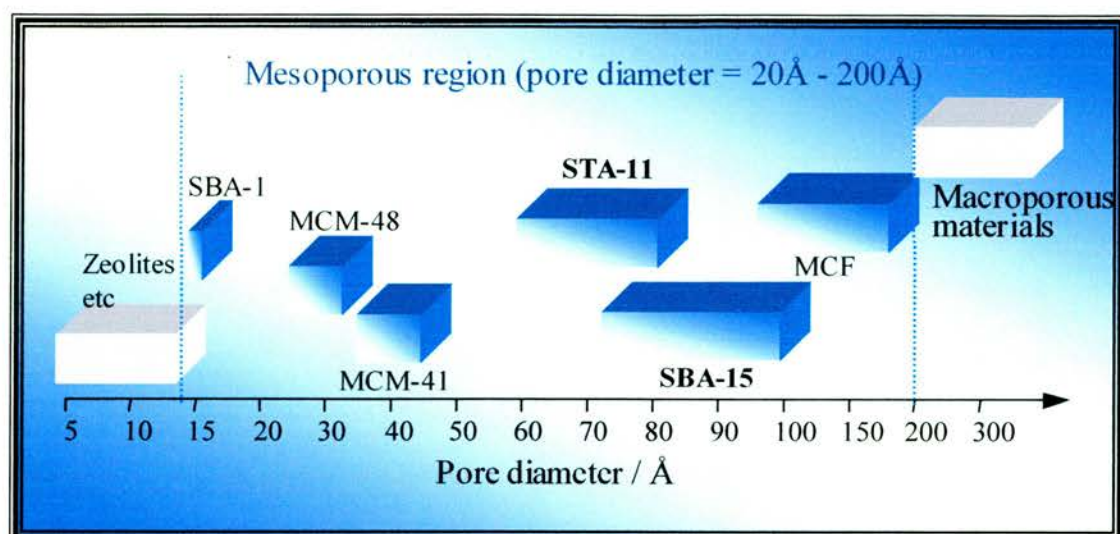


Figure 1.1.2. The range of pore sizes attributed to porous solids with the mesoporous region in blue.

Figure 1.1.2 shows only some of many mesoporous solids. Tailoring of pores – with each having a narrow pore size distribution – can also be achieved, allowing molecular sieving to occur with guest molecules with a wide-range of dimensions. Due to the uniformity of the pore sizes, channels and cavities within the solids whether they are microporous zeolites or well-defined mesoporous silicas can give rise to shape selectivity and it is this which holds the key to determining which molecules diffuse through or form in the channels.

Despite the very considerable amount of research into mesoporous silica the number of commercial applications is disappointing. However Mobil have very recently commercialised and scaled-up the synthesis of MCM-41 for an undisclosed application [26]. The volume of applications that potentially exist for such mesoporous silicas reported over the last decade is huge (table 1.1.3) with increasing emphasis on catalytic properties [27]. The properties of mesoporous materials – the high specific surface areas *ca.* 1000 m²g⁻¹, increased levels of pore volume and modification of the silica walls – makes them ideal for potential catalyst supports.

Potential Applications of Mesoporous Silica

Adsorbents	Remediation of heavy metal ions by thiol functionalisation [28]
Optics	Fiber lasers [29-31]
Catalysis	Silica-alumina-MCM-41 (Propene oligomerisation – gasoline and middle distillates production: C ₉ and C ₁₂ hydrocarbon selectivity) [32]
	Ti-containing silica – selective oxidation [33,34]
	Chiral catalysis [35,36]
	Bimetallic hydrogenation [37,38]
Low dielectric constant insulators	Computer microchip [39-42]
Alternative to silica in above	Mesoporous carbon [20,43]

Table 1.1.3. Potential applications of mesoporous silica

1.2 Surfactant Chemistry

Surfactants play an essential role in the architecture of the mesoporous solids formed within this thesis as the silica is thought to permeate the voids between the surfactant structure and subsequently forms the inorganic framework. Surfactants characterised by a hydrophobic and hydrophilic part – deemed amphiphilic molecules (shown in figure 1.2.1) – can be classified into various types depending on their constituent groups.



Hydrophobic hydrocarbon chain.
Weak interactions with water

Polar or ionic hydrophilic head-group.
Strong interactions with water

Figure 1.2.1. Schematic representation of a surfactant molecule possessing both a hydrophobic hydrocarbon chain and a hydrophilic head group

Surfactants can either be:- **cationic** – whereby the hydrophilic head-groups are amine/quaternary ammonium cations as in CTAB (the surfactant for MCM-41); **anionic** – constituting carboxylate/sulphate/phosphate head-groups; **non-ionic** – (those utilised within this thesis) having polyether/polyhydroxyl polar groups; and **Zwitterionic** – containing two charged head-groups of opposite charge [44]. The hydrophobic section of surfactants tend to be long alkyl chains [45]. However the non-ionic surfactants used within this thesis – Pluronic P123 (template for SBA-15 and STA-11) and Pluronic F127 (template for FDU-12) – are triblock copolymers of ethylene oxide/ propylene oxide / ethylene oxide of various quantities and ratios as shown in figure 1.2.2.

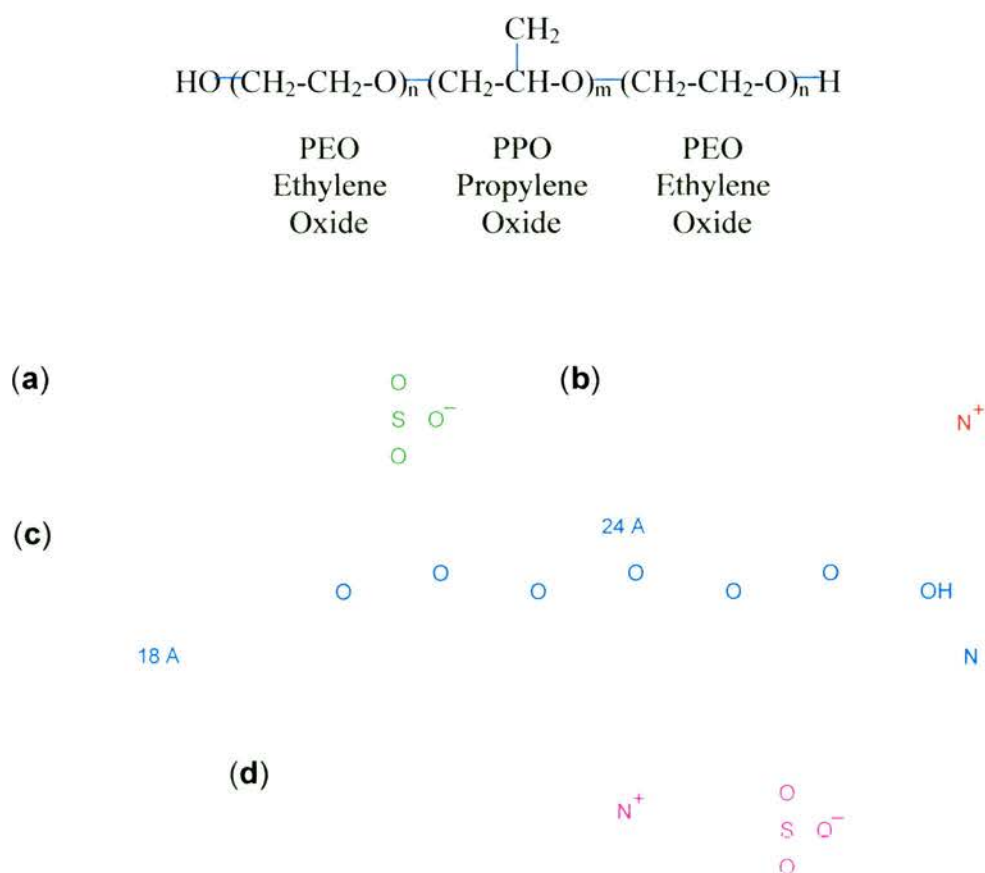


Figure 1.2.2: Classes of surfactant types – (above) non-ionic triblock copolymers and (below) a) anionic; b) cationic; c) non-ionic and d) zwitterionic.

At low concentrations surfactants exist as discrete entities and only above a certain concentration, the so-called **critical micelle concentration (cmc)**, the surfactant

molecules aggregate as a result of forces on them to micelles [46]. The insoluble hydrophobic constituents pack to reduce their contact with water and the aggregation is limited by the electrostatic repulsion between the hydrophilic (polar) head-groups. The balance between these forces acting on the agglomeration of surfactants gives rise to various forms of micellular packing shapes. Other factors other than the nature of the surfactant in producing other micellar geometries are the concentration and temperature.

An increase in the surfactant concentration can indeed lead to changes in the geometric formation which results in the differences of the mean packing shapes of the micelles. The shape of the micelle can be roughly predicted by calculating the packing parameter, g , which describes the balance between the hydrophobic and hydrophilic sections during the self-assembly. Equation 1.2.1 describes the packing parameter and is given by:

$$g = \frac{v}{a_0 l} \quad \text{Equation 1.2.1}$$

where v relates to the total volume of the hydrocarbon chain; a_0 the head group area at the micelle surface and l the length of the hydrocarbon chain.

Values of g indicating the final phase of the micellar solution can be seen in table 1.2.1 which shows upon an increase in g the surface curvature decreases from spherical micelles to lamellar packing. $g < \frac{1}{3}$ leads to the formation of spherical micelles, whereas $\frac{1}{3} < g < \frac{1}{2}$ favours cylindrical micelles and $g > \frac{1}{2}$ forms parallel stacks of bilayers (lamellar).

g	Critical packing shape	Structures formed
$< \frac{1}{3}$	Cone	Spherical micelles
$\frac{1}{3} - \frac{1}{2}$	Truncated cone	Cylindrical micelles
$\frac{1}{2} - 1$	Truncated cone	Flexible bilayers

~1

Cylinder

Planar bilayers

 Table 1.2.1. The expected mean packing shapes of surfactants and the structures they form as a function of g .

The assembly of the surfactants give rise to several possible geometries including lamellar (parallel stacks of bilayers), hexagonal (spherical or cylindrical aggregates hexagonally close packed) and cubic all of which mainly depends on the a_0 value as shown in figure 1.2.3 [47]. A high a_0 value tends to adopt the cubic formation with smaller a_0 values arranging in the spherical/cylindrical hexagonal whilst lamellar phases form with surfactants having the smallest headgroup.

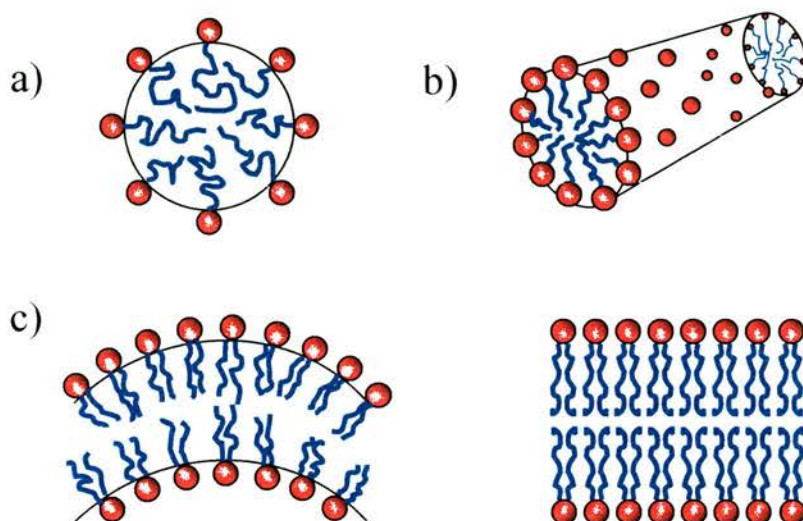


Figure 1.2.3. The mesophase sequence with decreasing curvature from a) spherical b) cylindrical c) flexible bilayers and d) planar bilayers (lamellar) [47].

The surfactant monomers can constantly join and leave the aggregate due to their dynamic nature and the differences in energy between surfactant packing (i.e. their geometric arrangement of micelles) is small. Thus changes in the types of surfactant aggregation is found fairly easily simply by small changes in the synthesis – variation of temperature, pH or electrolyte concentration. A phase diagram (figure 1.2.4) of the single chained cationic surfactant, cetyltrimethylammonium bromide $[\text{CH}_3(\text{CH}_2)_{15}\text{N}^+(\text{CH}_3)_3\text{Br}^-]$ – the template for MCM-41, shows changes in the surfactant geometry from hexagonal to cubic through to lamellar phases upon discrete

changes in temperature and surfactant concentration [48]. Since micelles usually have well-defined shapes and a narrow size distribution, they are ideal templates for the formation of inorganic templates in sol-gel syntheses.

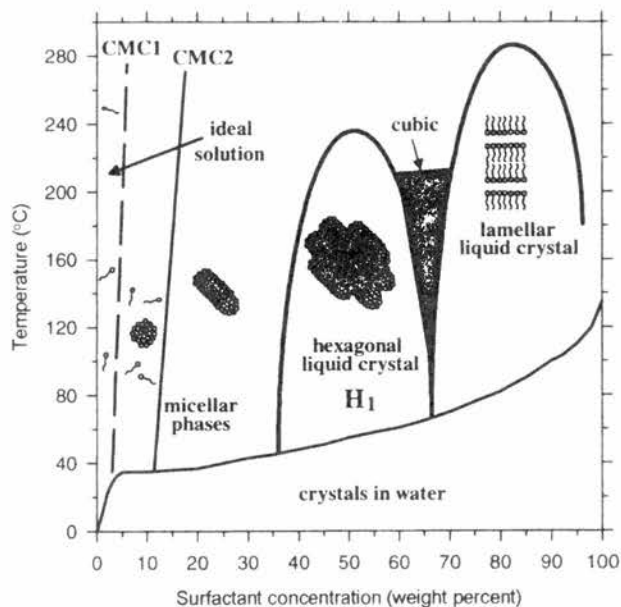


Figure 1.2.4. Phase diagram for the micellar packing of the surfactant cetyltrimethylammonium bromide changing with respect to temperature and surfactant concentration [48].

1.3 Synthesis

The emergence of mesoporous silica with well defined structures came about using micelles as organic scaffolds, around which inorganic species present within the interstitial sites between the micelles could polymerise. Mobil researchers began the debate on the mechanism of formation and along with further studies the **liquid crystal templating** (LCT) mechanism was eventually proposed. Solution based formation of ordered mesoporous silica was first proposed by Beck *et al.* [2] where the LCT mechanism is based on the interaction between the ordered organic micellar phase and the inorganic precursor (figure 1.3.1).

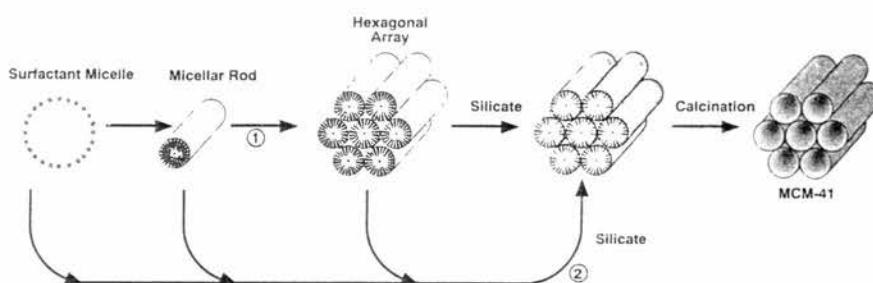


Figure 1.3.1. The LCT proposed mechanism for the synthesis of MCM-41 by Beck *et al.* [2]

Initially the group suggested that there may be two ways in which the final silica structure is created. In the first pathway the silica condenses around the agglomerated micelles which have self-assembled into supermolecular arrays before the onset of the silica organisation and in doing so counter balances the charges formed at the exterior micelle surfaces. In the second proposed possible pathway the mesophase order arises due to the interactions of the silica source with the surfactant. The second mechanism is favoured and is supported by the work of Davis and co-workers [49] who refute the concept of ordered hexagonal arrays of micelles before the onset of silica condensation, mainly through ^{14}N MAS NMR studies. Their results show that route 1 (figure 1.3.1) is absent in the formation of the molecular sieve throughout the sol-gel procedure. The data suggested that the silicate species interact with the randomly ordered rod-like micelles to yield approximately 2 – 3 monolayers of silica encapsulation around the external micelle surface which only then organise to the long-range honeycomb ordering. In addition, Stucky *et al.* proposed a co-operative formation mechanism [8,50] whereby multicharged inorganic species in an aqueous medium interact with the surfactant species and co-operatively form a liquid crystalline arrangement minimising the overall charge effects before silica condensation occurs. The work of Anderson [51] also looks at how silica structures interact with micelles in an acidic solution and how the silica surface wraps around the micelles. Simulations find that the final inorganic meso-product (based on 3-dimensional packing of globular micelles, in the case of SBA-1) after template removal retains the micellar structure, including oblate distortions of globular micelles. Here the micelles, surrounded by a water layer and then the silica wall,

generate a window of size governed by the contact angle between the micelles as the water layer excludes the silica wall from a region between the micelles.

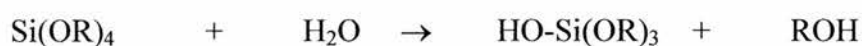
Final silica structures depend on the solution conditions of charge balancing between the organic and inorganic species. If there are variations in the charged species then various mechanisms of self-assembly can be envisaged (table 1.3.1).

Mechanism of formation	
S^+I^-	S^+ denotes the cationic surfactant and I^- the condensed silica
S^+XI^-	X^- , a counter-ion of appropriate charge balancing the charges of the cationic surfactant and ionic species when working in acidic media below the isoelectric point of silica ($pH < 2$) where the silica species is protonated
$N^0H^+XI^-$	Non-ionic surfactants (such as PEO-PPO-PEO) protonated under acidic conditions with N^0 denoting the neutral surfactant

Table 1.3.1. Mechanism of self-assembly via variation in charged species.

The route to obtaining the final mesoporous silica within this thesis is by a sol-gel route. A gel is a state of matter intermediate between a solid and liquid while a sol is a colloidal suspension. This particular method involves two processes, a *hydrolysis* step followed by a *condensation* step. The silica source is a silicon alkoxide – where the central silicon atom is surrounded by hydrolysable ligands (-OR) in the presence of an acid or base.

The hydrolysis step (figure 1.3.2):



under acidic conditions (figure 1.3.2 (a)) protonates the alkoxy group causing the withdrawal of electron density from the silicon which in turn gives rise to nucleophilic attack by the oxygen in water forming a pentacoordinated transition state. Removal of the alkoxide group as an alcohol by deprotonation leaves the silicon tetrahedron with the presence of a silanol group (SiOH). Under basic conditions the hydroxyl (OH⁻) ion acts as a nucleophile towards the silicon (figure 1.3.2 (b)) [52].

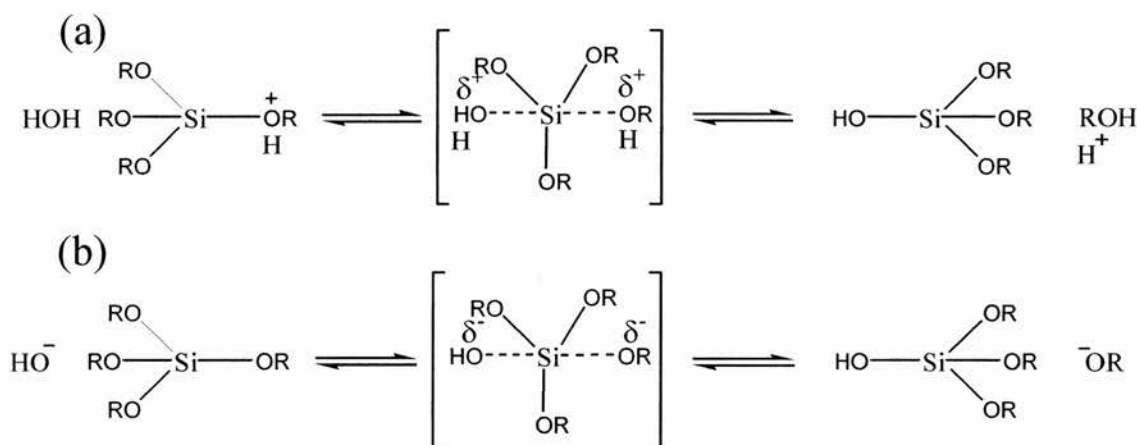
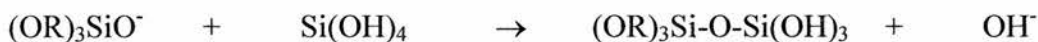


Figure 1.3.2. The hydrolysis step of a tetraalkoxysilane undertaken in either (a) acidic or (b) basic conditions

The condensation step involves the attack of negatively charged deprotonated silanol on neutral silica (figure 1.3.3) [53]:



Under acidic conditions protonation initially occurs creating a silicon that is more electrophilic and thus susceptible to nucleophilic attack (figure 1.3.3 (a)). Under basic conditions the silanol groups are deprotonated forming negatively charged silica species (figure 1.3.3 (b)).

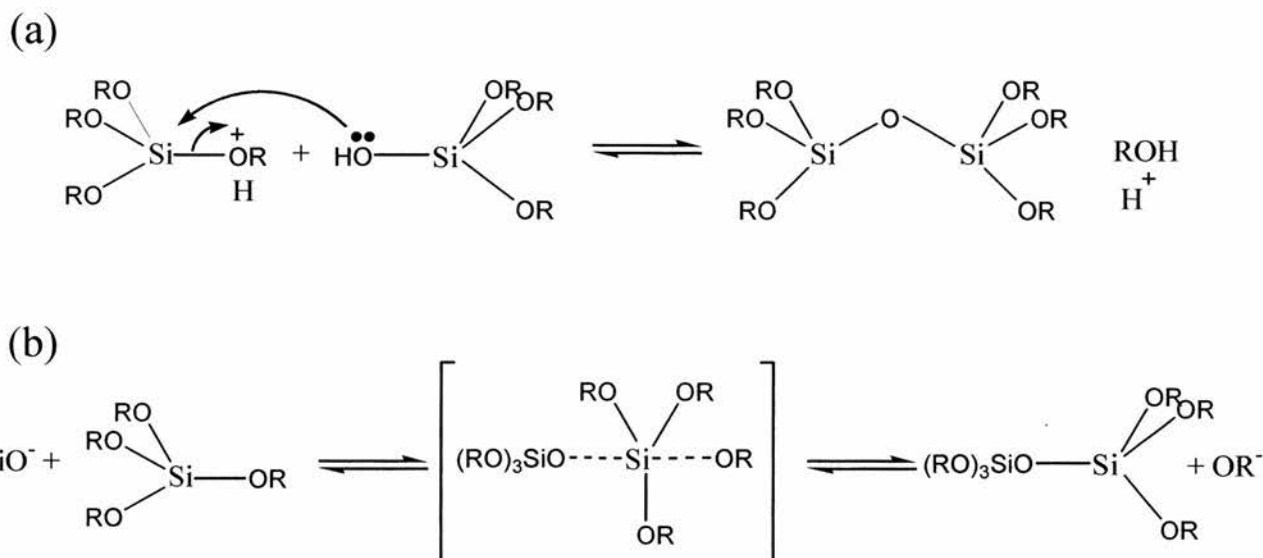


Figure 1.3.3. Condensation of the silanol group to form the Si-O-Si bond under acidic conditions (a) and basic conditions (b).

The as-made sample retains the surfactant and the materials are not porous until the surfactant is removed. This can be achieved by (i) calcination at temperatures in the region of (400 – 550 °C), (ii) template removal by microwave heating or (iii) extraction with an appropriate solvent under reflux conditions.

1.4 Functionalisation

Uses as catalysts, sensors and host materials for large guest molecules were envisaged when well-defined mesoporous silicas were first discovered. Applications in traditional zeolite hydrocarbon cracking reactions were unsuccessful due to the lower hydrothermal stability and reactivity of mesoporous solids when compared to their zeolite counterparts. Through considerable research over the last decade on mesoporous silicas some of these limitations have been reduced. For example the hydrothermal stability can be improved by the addition of salts to the synthesis [54] or producing materials with thicker walls [10,55,56] but reservations remain. Further research led to routes to organic modification of the internal surface of mesoporous silicas which has greatly increased the potential applications of these materials.

Modification can take place during the synthesis of the mesoporous solid by adding an organic functional group, eg. functionalised-trialkoxysilane, as a co-condenser to the silica source or by post-synthetic grafting to a pre-fabricated support after the removal of the template.

1.4.1 Post-synthetic grafting

When functionalising the material after the material has formed it is normally the case that the template is removed via calcination (typically 4 hrs under N_2 at 550 °C followed by 4 hrs under O_2 at 550 °C) since complete removal of the surfactant results. Since no organic moieties (in the form of required functionalities) are present at this stage it is best to burn out the organic surfactant rather than to remove the template via solvent extraction where residual template remains. In doing so calcination further condense the inorganic silica framework and any remaining silanol groups present are likely to form Si-O-Si bonds.

Post synthesis modification can however only occur where there are silanol groups as these act as an anchor for the organic functionality thus Q^3 silicon (or below) must be present as Q^4 silicon have fully condensed to form the rigid framework (figure 1.4.1.1). Since calcination condenses the framework there is a decreased volume of silanol groups available for organic modification by silylation and so the silanol groups have to be replenished if a high surface coverage of functional groups is required. This is achieved by rehydrating the surface by refluxing the calcined material in water. Figure 1.4.1.2 [57] shows some examples of post-synthesis functionalisation through organic-trialkoxysilanes to give functionalities protruding

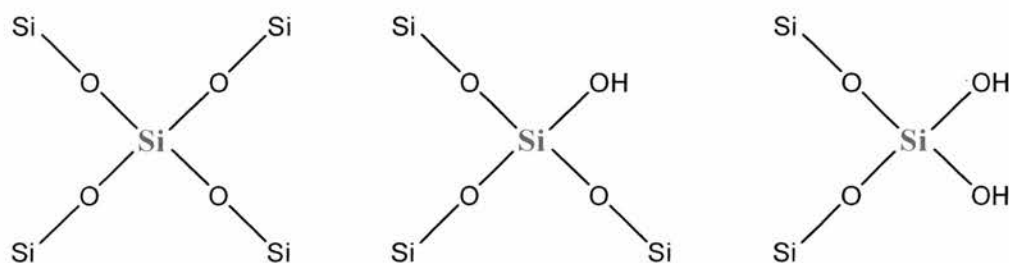


Figure 1.4.1.1. Functionalisation post-synthetically on the central silicon atom only achieved if silanol groups are present. Q^4 silicon (left), Q^3 silicon (middle) and Q^2 silicon (right).

from the surface of the silica walls. Some constituent groups are reactive, allowing further functionalisation. The cyano group (CN) can be hydrolysed to form carboxylic acids [58,59] while the thiol group (SH) can be oxidised to form sulphonic acids [60].

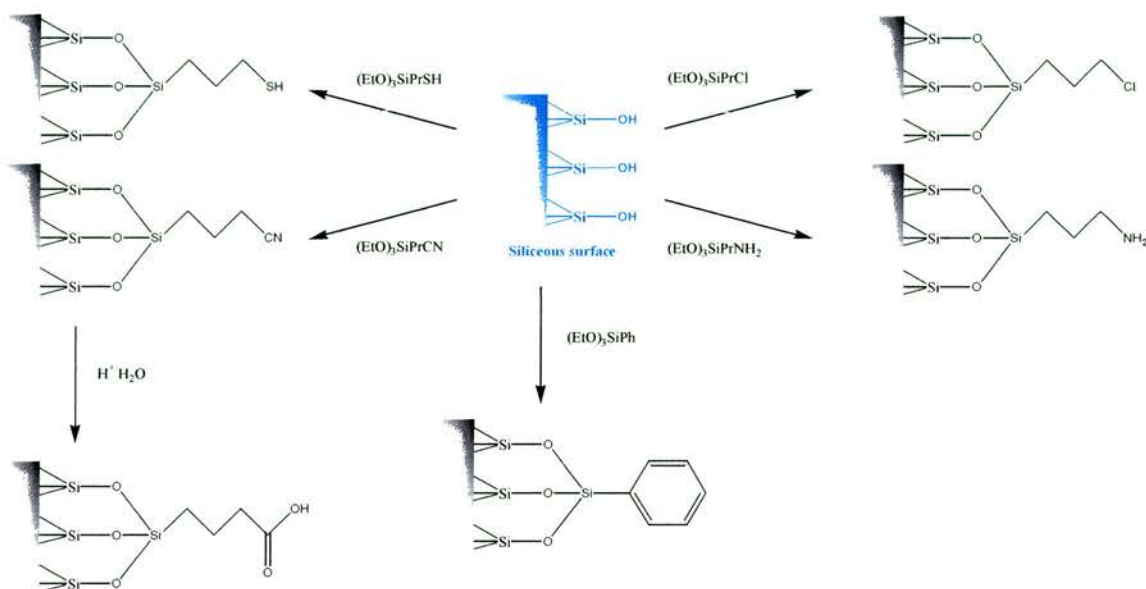


Figure 1.4.1.2. Post synthesis functionalisation with organic-trialkoxysilanes via silanol anchoring groups. Organic functionalities can be either passive or reactive which can be further functionalised for specific applications ([57] adapted).

The advantage of the grafting method is that good preservation of the mesostructure is retained after organic-modification. The disadvantage is that covalently attaching organic-groups, which protrude from the silica walls reduces the pore size/volume and can be undesired in applications. In addition the degree of functionality that can be achieved using the post-synthetic modification route is limited to the amount of reactive surface silanols present. Furthermore this process is time consuming in the fact that it takes two steps: preparation of the parent mesostructure followed by treatment with the required organosilane taking care that complete drying of both the mesostructure and solvent is sustained before grafting commences. Finally control over the loading and the homogeneity of the functional group is difficult to achieve.

1.4.2 *In situ* functionalisation

Functionalisation can also be achieved via a “one-pot” synthesis where both tetraalkoxysilane and an organoalkoxysilane co-condense together as an alternative method to post-synthetic grafting to form inorganic-organic hybrid solids.* Avoiding phase separation of the precursors should lead to a uniform distribution of the functionality across the final porous network. The prevention of Si-C bond cleavage during this *in situ* sol-gel method and during template removal by solvent extraction has to be considered. Template removal from materials created by the co-condensation method is usually via solvent extraction. Although the efficiency of the extraction is below that of calcination the organic functionalities remain. Calcination would burn out both the organic template and the organic-functional group introduced in the synthesis. The extraction process which curtails the loss of silanol groups is normally performed with alcohols if the surfactant within the pores is neutral and with acid/alcohol mixtures if a cationic surfactant was employed in the synthesis [61]. Table 1.4.2.1 highlights some of the co-condensation reactions.

Functionalised mesoporous solids via co-condensation			
Functional group	Surfactant	Mesophase	Ref
3-aminopropyl	CTAB	MCM-41	[62]
2-cyanoethyl	n-dodecylamine	HMS	[63]
Vinyl	CTAB	MCM-41	[62,64]
COOH	P123	SBA-15	[58]
3-mercaptopropyl	P123	STA-11	[65]
		FDU-5	[15]

Table 1.4.2.1. *In situ* functionalisation of mesoporous silica solids via the co-condensation of tetraalkoxysilane and organoalkoxysilanes.

* Note the framework here is not a hybrid and is only inorganic silica with the organic constituent tethering from the inorganic framework. True hybrid solids possess both inorganic and organic species constituting the framework.

The advantage of applying the co-condensation method is that it is only a one-step process instead of the two stages that are required in the post-grafting modification and thus is not as time consuming. Control over the surface property of the material and a more uniform distribution of surface-coverage functionality results [15,66]. In addition adopting such an approach one can observe the effect that a specific organic-functionality can have on the mesophase outcome which would be denied when grafting. The disadvantage however is the extent of functionalisation when adopting an *in situ* approach is limited, to an extent that depends on the organic alkoxide introduced to the synthesis. Increasing the loading of organoalkoxysilane allows an increased level of the functional group taking part in a desired application per gram of solid. However, the long-range order of the material is compromised upon an increased loading of functionality as fully-linked Q₄ silica groups are required to form stable wall structures. Local disruptions to the silicate framework can occur if cross-linking occurs between the surface silanols and the organic functional group, e.g., amino groups protonating in acidic media used to synthesis such materials as SBA-15 (cross-linking can also occur in the grafting approach and also render the functionality ineffective, but the long-range order of the mesostructure still remains intact). It has also been reported that elevated levels of thiol-groups as co-condensers can perturb the formation and self-assembly of surfactant aggregations resulting in a poorly ordered mesostructure [67].

This project adopts the *in situ* method to functionalise such materials as it offers the greatest chance that the functional siloxanes become fully linked into the growing framework. This may be less likely for the post-synthesis grafting modification approach where the framework is rigidly set and therefore the mobility of the silanol groups are limited. This direct approach allows one to observe the organic-functional group's effect on the resultant solid that forms, which is a significant aim of the work carried out within this thesis.

1.5 References

- [1] C.T. Kresge, M.E. Leonowicz, W.J. Roth, J.C. Vartuli, J.S. Beck, *Nature*, 1992, **359**, 710
- [2] J.S. Beck, J.C. Vartuli, W.J. Roth, M.E. Leonowicz, C.T. Kresge, K.D. Schmitt, C.T.-W. Chu, D.H. Olson, E.W. Sheppard, S.B. McCullen, J.B. Higgins, J.L. Schlenker, *J. Am. Chem. Soc.*, 1992, **114**, 10834
- [3] <http://ohtaki.cube.kyushu-u.ac.jp/lab/research/nano/quantum.html>
- [4] T. Yanagisawa, T. Shimizu, K. Kuroda, C. Kato, *Bull. Chem. Soc. Jpn.*, 1990, **63**, 988
- [5] J.S. Beck, N.Y. Princeton, US Patent No. 5 057 296, 1991
- [6] V. Chiola, J.E. Ritsko, C.D. Vanderpool, US Patent No. 3556725, 1971
- [7] F. DiRenzo, H. Cambon, R. Dutartre, *Micropor. Mesopor. Mater.*, 1997, **10**, 283
- [8] A. Monnier, F. Schüth, Q. Huo, D. Kumar, D. Margolese, R.S. Maxwell, G. Stucky, M. Krishnamurty, P. Petroff, A. Firouzi, M. Janicke, B. Chmelka, *Science*, 1993, **261**, 1299
- [9] Q. Huo, D. Margolese, U. Ciesla, P. Feng, T. Gier, P. Sieger, R. Leon, P.M. Petroff, F. Schüth, G. Stucky, *Nature*, 1994, **368**, 317
- [10] Q. Huo, R. Leon, P.M. Petroff, G.D. Stucky, *Science*, 1995, **268**, 1324
- [11] D. Zhao, Q. Huo, J. Feng, B.F. Chmelka, G.D. Stucky, *J. Am. Chem. Soc.*, 1998, **120**, 6024
- [12] D. Zhao, Q. Huo, J. Feng, J. Kim, Y. Han, G.D. Stucky, *Chem. Mater.*, 1999, **11**, 2668
- [13] C. Yu, Y. Yu, D. Zhao, *Chem. Commun.*, 2000, **7**, 575
- [14] S. Shen, Y. Li, Z. Zhang, J. Fan, B. Tu, W. Zhou, *Chem. Commun.*, 2002, **19**, 2212
- [15] X. Liu, B. Tian, C. Yu, F. Gao, S. Xie, B. Tu, R. Che, L. Peng, D. Zhao, *Angew. Chem. Int. Ed.*, 2002, **41**, 3876
- [16] J. Fan, C. Yu, F. Gao, J. Lei, B. Tian, C. Wang, Q. Luo, B. Tu, W. Zhou, D. Zhao, *Angew. Chem. Int. Ed.*, 2003, **115**, 3254
- [17] R. Ryoo, J.M. Kim, C.H. Ko, C.H. Shin, *J. Phys. Chem.*, 1996, **100**, 17718
- [18] F. Kleitz, D. Liu, G.M. Anilkumar, I.N. Park, L.A. Solovyov, R. Ryoo, *J. Phys. Chem. B*, 2003, **107**, 14296

- [19] F. Kleitz, S. H. Choi, R. Ryoo, *Chem. Commun.*, 2003, **17**, 2136
- [20] R. Ryoo, S.H. Joo, S. Jun, *J. Phys. Chem. B*, 1999, **103**, 7743
- [21] R. Ryoo, S.H. Joo, S. Jun, T. Tsubakiyama, O. Terasaki, *Stud. Surf. Sci. Catal.*, 2001, **135**, 150 – see also *Adv Mater.*, 2001, **13**, 677
- [22] S. Jun, S.H. Joo, R. Ryoo, M. Kruk, M. Jaroniec, Z. Liu, T. Ohsuna, O. Terasaki, *J. Am. Chem. Soc.*, 2000, **122**, 10712
- [23] S.H. Joo, R. Ryoo, *J. Phys. Chem. B*, 2002, **106**, 1256
- [24] S.H. Joo, S.J. Choi, I. Oh, J. Kwak, Z. Liu, O. Terasaki, R. Ryoo, *Nature*, 2001, **412**, 169
- [25] F. Kleitz, S.H. Choi, R. Ryoo, *Chem. Commun.*, 2003, **17**, 2136
- [26] C.T. Kresge, J.C. Vartuli, W.J. Roth, M.E. Leonovich, *Stud. Surf. Sci. Catal.*, 2004, **148**, 53
- [27] A. Corma, *Chem. Rev.*, 1997, **97**, 2373
- [28] X. Feng, G.E. Fryxell, L.Q. Wang, A.Y. Kim, J. Lui, K.M. Kemmer, *Science*, 1997, **276**, 923
- [29] Q. Huo, D. Zhao, J. Feng, K. Weston, S.K. Buratto, G.D. Stucky, S. Schacht, F. Schüth, *Adv. Mater.*, 1997, **9**, 974
- [30] F. Marlow, M.D. McGehee, D. Zhao, B.F. Chmelka, G.D. Stucky, *Adv. Mater.*, 1999, **11**, 632
- [31] J. Loerke, F. Marlow, *Adv. Mater.*, 2002, **14**, 1745
- [32] G. Bellussi, C. Perego, A. Carati, S. Peratello, E.P. Massara, G. Perego, *Stud. Surf. Sci. Catal.*, 1994, **84**, 85
- [33] J.M. Thomas, *Nature*, 1994, **368**, 289
- [34] T. Maschmeyer, R. Rey, G. Sankar, J.M. Thomas, *Nature*, 1995, **378**, 159
- [35] J.M. Thomas, *Angew. Chem. Int. Ed. Engl.*, 1999, **38**, 3588
- [36] M.D. Jones, R. Raja, J.M. Thomas, B.F.G. Johnson, D.W. Lewis, J. Rouzard, K.D.M. Harris, *Angew. Chem. Int. Ed. Engl.*, 2003, **42**, 4326
- [37] D.S. Shephard, T. Maschmeyer, J.M. Thomas, B.F.G. Johnson, G. Sankar, D. Ozkaya, W. Zhou, R.D. Oldroyd, R.G. Bell, *Angew. Chem. Int. Ed. Engl.*, 1997, **36**, 2242
- [38] J.M. Thomas, R. Raja, B.F.G. Johnson, T.J. O'Connell, G. Sankar, T. Khimyak, *J. Chem. Soc. Chem. Commun.*, 2003, **10**, 1126. See also *Science*, 2003, **300**, 867
- [39] M.A. Carreon, V.V. Guliyants, *Eur. J. Inorg. Chem.*, 2005, **1**, 27

- [40] D.A. Doshi, A. Gibaud, V. Goletto, M. Lu, H. Gerung, B. Ocko, S.M. Han, C.J. Brinker, *J. Am. Chem. Soc.*, 2003, **125**, 11646
- [41] H. Fan, H.R. Bentley, K.R. Kathan, P. Clem, Y. Lu, C.J. Brinker, *J. Non-Cryst. Solids*, 2001, **285**, 79
- [42] R.D. Miller, *Science*, 1999, **286**, 421
- [43] S. Che, A.E. Garcia-Bennett, X. Liu, R.P. Hodgkins, P.A. Wright, D. Zhao, O. Terasaki, T. Tatsumi, *Angew. Chem. Int. Ed.*, 2003, **42**, 3930
- [44] B. Johnson, B. Lindman, K. Holmberg, B. Kronberg, *Surfactants and polymers in aqueous solution*, John Wiley and sons, 1998.
- [45] Clint J.H., *Surfactant aggregation*, Blackie and son, 1992
- [46] Q. Huo, D.I. Margolese, G.D. Stucky, *Chem. Mater.*, 1996, **8**, 1147
- [47] J.N. Israelachvili, *Intermolecular and surface forces*, 2nd ed., 1991, Academic press, New York
- [48] N.K. Raman, M.T. Anderson, C.J. Brinker, *Chem. Mater.*, 1996, **8**, 1682
- [49] C. Y. Chen, S.L. Burkett, H.L. Li, M.E. Davis, *Microporous Mater.*, 1993, **2**, 27
- [50] Q. Huo, D. Margolese, U. Ciesla, D. Demuth, P. Feng, T. Gier, P. Sieger, A. Firouzi, B. Chmelka, F. Schüth, G.D. Stucky, *Chem. Mater.*, 1994, **6**, 1176
- [51] M.W. Anderson, C.C. Egger, G.J.T. Tiddy, J.L. Casci, *Stud. Surf. Sci. Catal.*, 2002, **142**, 1149
- [52] C.J. Brinker, G.W. Scherer, *Sol-Gel Science*, Academic Press, San Diego, 1990
- [53] R.K. Iler, *The chemistry of silica – Solubility, polymerisation, colloid and surface properties and biochemistry*, John Wiley and sons, 1979
- [54] R. Ryoo, S. Jun, *J. Phys. Chem. B.*, 1997, **101**, 317
- [55] P.T. Tanev, T.J. Pinnavaia, *Science*, 1995, **267**, 8650
- [56] P.T. Tanev, T.J. Pinnavaia, *Chem. Mater.*, 1996, **8**, 2068
- [57] H.H.P. Yiu, P.A. Wright, N.P. Botting, *J. Mol. Catal. B Enzym.*, 2001, **15**, 81
- [58] C.M. Yang, B. Zibrowius, F. Schüth, *Chem. Commun.*, 2003, **14**, 1772
- [59] C.M. Yang, Y. Wang, B. Zibrowius, F. Schüth, *Phys. Chem. Chem. Phys.*, 2004, **6**, 2461
- [60] I. Diaz, C. Marquez-Alvarez, F. Mohino, J. Perez-Pariente, E. Sastre, *J. Catal.*, 2000, **193**, 283
- [61] M.H. Lim, C.F. Blanford, A. Stein, *J. Am. Chem. Soc.*, 1997, **119**, 4090
- [62] C.E. Fowler, S.L. Burkett, S. Mann, *Chem. Commun.*, 1997, **18**, 1769
- [63] D.J. Macquarrie, *Chem. Commun.*, 1996, **16**, 1961

- [64] M.H. Lim, A. Stein, *Chem. Mater.*, 1999, **11**, 3285
- [65] A.E. Garcia-Bennett, University of St. Andrews, September 2002
- [66] A. Stein, B.J. Melde, R.C. Schroden, *Adv. Mater.*, 2000, **12**, 1403
- [67] W. D. Bossaert, D.E. De Vos, W.M. Van Rhijn, J. Bullen, P.J. Grobet, P.A. Jacobs, *J. Catal.*, 1999, **182**, 156

Chapter 2

Characterisation Techniques

Synopsis

The characterisation of mesoporous solids play an important role in determining not only the type of materials produced but also their 'quality'. Characterisation of mesoporous silicas is mainly through diffraction using electron microscopy and XRD which give details of the mesophase structure type and quality including any defects. N₂ adsorption measurements give indications of how well defined the porous system is including details of surface areas and pore size distributions. Functionalised silicas including tethered organic groups have been characterised by elemental analysis and UV and the incorporation of precious metals and transition metal complexes have been monitored by HRTEM/EDX and ESR respectively.

2.1 X-ray Diffraction

X-rays are a form of electromagnetic radiation having wavelengths characteristically in the region of 1 \AA ($1 \cdot 10^{-10} \text{ m}$) [1]. X-ray diffraction (XRD) is a technique utilised within this thesis to enable the long-range order of the synthesised mesoporous solids. XRD (a diffractometer shown in figure 2.1.1) is a powerful technique to determine geometric arrangements of particular atoms, which makes use of the property of diffraction of waves by objects with similar dimensions to the wavelength of the x-ray waves. Diffraction is the interference of the wave caused by regular objects in the path of the wave and the diffraction pattern is the pattern of varying intensity that results.



Figure 2.1.1. An X-ray diffractometer typically used to produce diffraction patterns of crystalline materials.

X-rays are the name given to the highly penetrating rays which emanate when high-energy electrons strike a metal target, usually heavy elements like tungsten or copper. These high frequency electromagnetic rays are produced when electrons emitted from a cathode accelerate through an x-ray tube under vacuum due to an applied voltage to the metal anode and suddenly decelerate upon impact of the metal and are called Bremsstrahlung which have a continuous range of wavelengths. X-rays are also produced when electrons make transitions between lower atomic energy levels in heavy elements and have quantised energies. These are characteristic x-rays since they have specific energies determined by the atomic energy levels. Collisions with

incoming electrons eject electrons from the inner shells of the tungsten or copper. X-ray photons are produced as electrons from a higher energy level drop into the vacant hole as depicted in figure 2.1.2 [2].

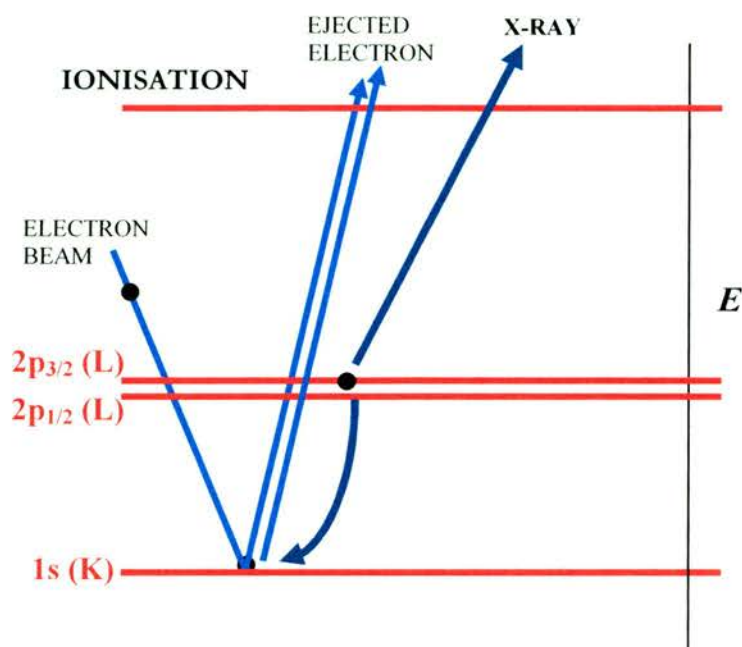


Figure 2.1.2. An electron bombardment onto the metal target area produces $K\alpha$ characteristic x-rays when a $L \rightarrow K$ transition occurs.

Electrons emitted from a heated filament are typically used to ionise K-shell ($1s$) electrons of the metal to which the higher energy L-shell electrons drop to lower energies and give rise to $K\alpha$ lines. An electronic transition from the M-shell to the K-shell gives rise to $K\beta$ lines. $K\alpha$ lines are generally of higher intensity than the corresponding $K\beta$ lines. Both are produced. Since an x-ray diffractometer only requires a single wavelength of radiation then a monochromator is introduced, usually to select the $K\alpha$ lines.

Max von Laue in 1912 [3] suggested that x-rays may be diffracted upon passing through a crystal as their wavelengths are in the same range as the crystal lattice spacing. XRD has subsequently become a powerful technique. W. H. Bragg and his son W. L. Bragg produced a law of diffraction and designed a spectrometer to look at

crystals in this way. W.L. Bragg showed diffraction could be mathematically described as ‘reflection’ by atomic planes [4].

This equation is now known as Bragg’s law [4] and is depicted in figure 2.1.3., The extra distance travelled depends on the interplanar spacing of the crystal, d_{hkl} , and the angle, θ , at which the incident beam entered the crystal lattice. This wave must travel a whole number of wavelengths inside the crystal for there to be no incongruity between the phases of the wave reflecting at the surface and itself and for intensity maxima to occur.

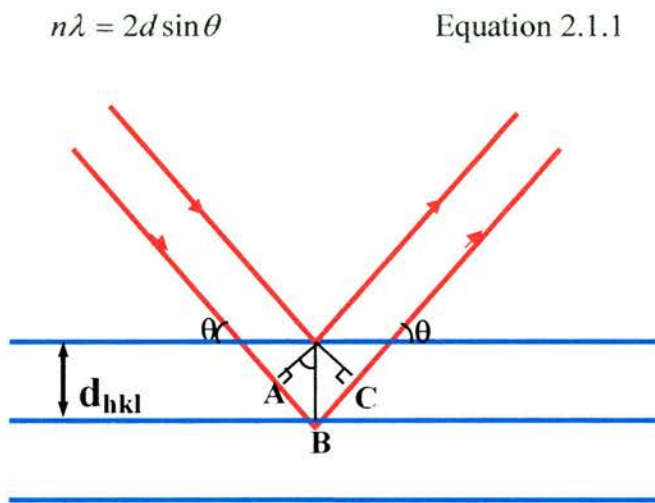


Figure 2.1.3. Bragg diffraction by a crystal.

where;

λ = wavelength of the x-rays

θ = angle between the incident rays and the surface of the crystal

d = interplanar spacing between atomic layers

Powder x-ray diffraction patterns displayed as intensity maxima versus the 2θ diffraction angle are collected from the sum of all possible orientations and as such all possible hkl planes satisfy the Bragg equation. Miller indices (hkl) can be used to index the lattice planes present. The 2θ angle representative of the peak position designates the interplanar spacing, d , which is characteristic of the lattice parameters and symmetry of the material. From the appropriate equations, unit cell dimensions can be determined from the interplanar spacings, d .

The unit cell of a hexagonal symmetry where $a = b \neq c$ and $\alpha = \beta = 90^\circ$, $\gamma = 120^\circ$ can be determined from equation 2.1.2.

$$\frac{1}{d^2} = \frac{4}{3a^2}(h^2 + k^2 + hk) + \frac{l^2}{c^2} \quad \text{Equation 2.1.2}$$

For SBA-15 exhibiting the space group $p6mm$ there is no repeat unit in the c -axis and determining the unit cell from the $[1,0]$ reflection (the main peak in SBA-15) then the k and l term are void, therefore equation 2.1.2. becomes equation 2.1.3.

$$\frac{1}{d^2} = \frac{4}{3a^2} \quad \text{Equation 2.1.3}$$

The unit cell from a material possessing cubic symmetry, such as STA-11, can be determined from equation 2.1.4.

$$\frac{1}{d^2} = \frac{h^2 + k^2 + l^2}{a^2} \quad \text{Equation 2.1.4}$$

Systematic absences arise if a set of planes occupy a position such that they reflect x-rays completely out of phase with another set of lattice planes and therefore no reflections are observed although the Bragg condition is satisfied. The destructive interference omits the reflection. Systematic absences indicate the presence of centring and specific elements in the lattice providing information on the space group. The systematic absences in cubic crystals gives rise to h,k,l reflection conditions whereby a body centred cubic lattice has the condition: $h+k+l = 2n$ – the total giving an even number, e.g., the $[1,1,1]$ reflection would not be observed for MCM-48 ($Ia\bar{3}d$) (figure 2.1.4).

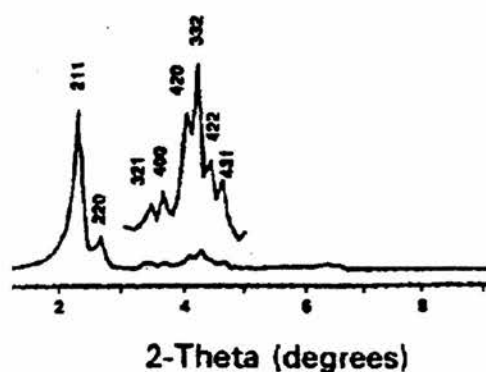


Figure 2.1.4. Typical XRD pattern of MCM-48 (Ia3d) where for all peaks $h + k + l = 2n$ [5]

Face centred cubic materials such as FDU-12/KIT-5 have h,k,l reflection conditions where either all are even or odd ($h + k, k + l, h + l = 2n$) so that the $[2,1,0]$ reflection, for example, would be absent (figure 2.1.5).

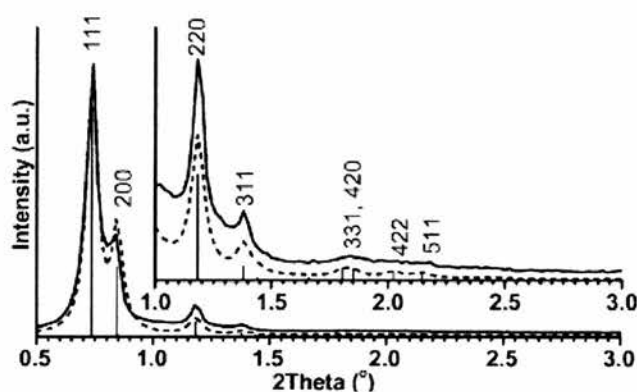


Figure 2.1.5. Simulated XRD pattern of KIT-5 where h,k,l values are either all odd or all even for each reflection [6]

X-ray diffractograms can reveal the crystalline properties of the materials investigated. Mesoporous materials have diffractograms with few peaks present at low 2θ angles – typically below $8^\circ 2\theta$ – reflecting their large unit cells in comparison to microporous solids due to their amorphous silica framework (figure 2.1.6) [7 – 11]. Long-range order (with respect to the pores) of mesoporous silica is defined but determining the atomic coordinates is not possible. There is a difficulty in using XRD on mesoporous solids in theory due to few peaks present and in addition it may also be difficult to determine the phase purity because of the broad first (major) peak and lack of definition in the secondary region. Practically problems arise too due to the

peak positions at low-angles. Here positioning of the detector at such low angles is critical because exposure to a direct beam can damage the detector.

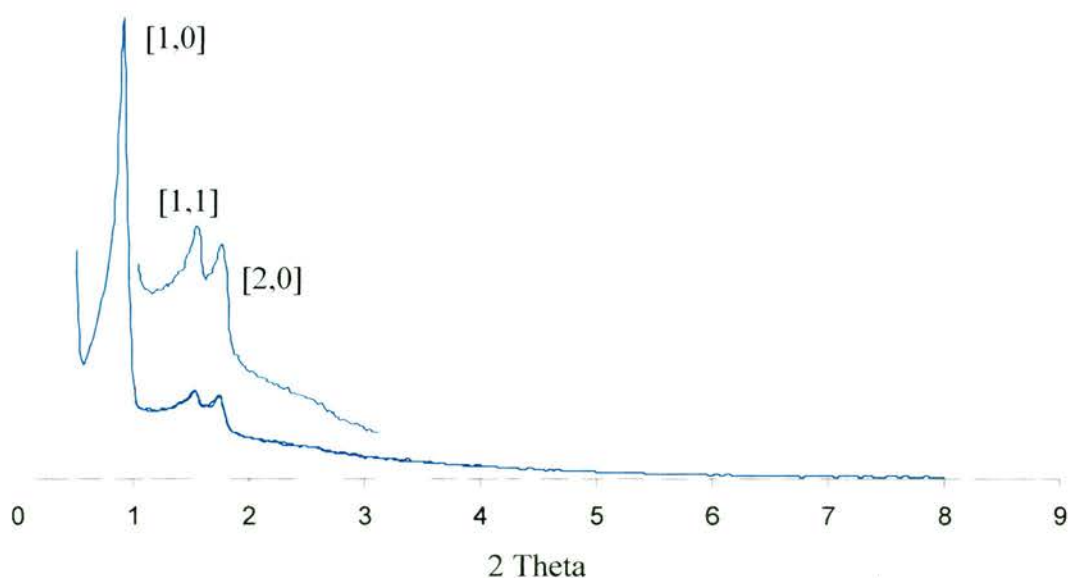


Figure 2.1.6. Typical XRD pattern of SBA-15 showing low angle reflections with the [1,0] reflection below $1^\circ 2\theta$ due to large unit cells. Few reflections present as mesoporous solids are not crystalline solids

XRD within this thesis is only used to determine if long-range order is present after the synthesis of mesoporous materials and to confirm whether hexagonal or cubic systems are present by comparing the diffractogram with known literature diffractograms.

In this thesis powder X-ray diffraction patterns of samples either with residual template remaining as in the extracted form or with no organic surfactant as in the calcined form were recorded using $\text{Cu K}\alpha$ radiation ($\lambda = 1.5418 \text{ \AA}$) on a Philips X'Pert diffractometer in the region of $0.5 - 8.0^\circ 2\theta$.

2.2 Transmission Electron Microscopy

TEM (figure 2.2.1) is used in material science to give direct space information of the local structure. In particular, mesoporous silicas are amenable to structure characterisation by high resolution imaging. However, it is indeed important to investigate the material's structure together with XRD because the local and bulk structures complement each other.



Figure 2.2.1. High resolution transmission electron microscope equipped with EDX operating at 200 keV at St. Andrews University.

In 1932 the first electron microscope was built by Knoll and Ruska and for surpassing the resolution of the light microscope Ruska received the Nobel price in 1986 [12]. The work of Hirsch *et al.* (1977) [13] is credited for the theory of TEM for material scientists and in the last 25 years this technique has been applied to elucidate many

structural details of materials, including defects (figure 2.2.2) – such as twin planes, stacking faults etc., as found in Chapter 4 of this thesis.



Figure 2.2.2. HRTEM micrograph of a mesoporous solid of cubic symmetry containing structural defects. A single stacking fault is represented by the off-set of the blue lines

Within the electron microscope electrons are emitted under a high vacuum, usually from a heated source of a lanthanum hexaboride (LaB_6) crystal or a tungsten filament. The momentum of the electron is increased due to an applied potential drop of 100-1000 keV generating a high energy beam of kinetic energy (equation 2.2.1):

$$eV = \frac{m_0 v^2}{2} \quad \text{Equation 2.2.1}$$

This leads to the relationship between the electron wavelength, λ and the accelerating voltage of the electron microscope, V (equation 2.2.2):

$$\lambda = \frac{h}{(2m_0 eV)^{1/2}} \quad \text{Equation 2.2.2}$$

where m_0 and e are the mass and charge of the electron respectively and h is Planck's constant.

Increasing the accelerating voltage decreases the wavelength of the electrons and hence increases the theoretical resolution to give images in more detail and exceeds the limited resolution in light microscopes due to the wavelength of visible light. As the electron's wavelength is much smaller the increased resolution allows details at higher magnification at the atomic level to be seen. The smallest distance that can be resolved, according to the Rayleigh equation is (equation 3.2.3):

$$\delta = \frac{0.61\lambda}{\mu \sin \beta} \quad \text{Equation 3.2.3}$$

with λ equalling the wavelength of radiation, μ the refractive index of the viewing medium and β the semi-angle of collection of the magnifying lens. μ and β are approximately unity so the resolution is equal to about half the wavelength of light. Therefore visible light, for example green light with a wavelength of 550 nm has a resolution of about 300 nm which corresponds to 1000 atom diameters. Therefore characteristic features of materials below this resolution cannot be observed. The wavelength of the electrons is related to their energy, E . De Broglie's equation approximates (equation 3.2.4):

$$\lambda = \frac{1.22}{E^{1/2}} \quad \text{Equation 3.2.4}$$

with E in electron volts (eV) and λ in nm. So for a 100 keV electron microscope the theoretical wavelength is about 4 pm (0.004 nm), much smaller than the diameter of the atom, although electron microscopes do not achieve such theoretical resolutions due to imperfections in the magnetic lenses. A series of lenses are required in order to focus and magnify the beam through the microscope. Since an electron has a charge the path of the beam can be altered by magnetic fields. A schematic representation of an electron microscope from the electron source to the image is shown in figure 2.2.3 [14].

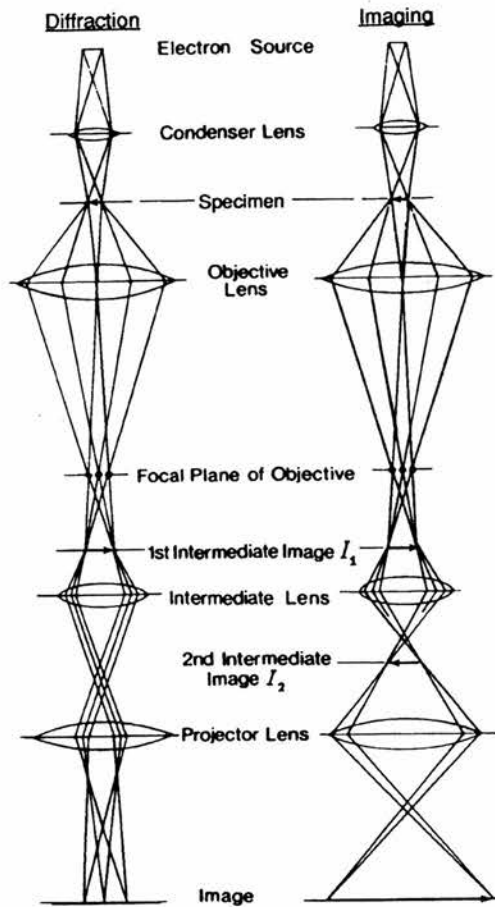


Figure 2.2.3. A diagrammatic view of the electron pathway within the evacuated column showing both the diffraction and imaging modes [14].

The lenses in a TEM are the magnetic equivalent of the convex glass lens in an optical microscope and are used to either (I) take all the rays emanating from a focal point in an object and recreate a point in an image or (II) focus parallel rays to a point in the focal plane of the lens. As the lens cannot collect all the rays from the object the collection angle is limited with an aperture which controls the beam current and the convergence of the beam hitting the specimen. The strength of the lens is important in TEM as if the lens is too weak and the image forms below the desired image plane, the image will be out of focus and the lens is said to be underfocused. At the same time, if the lens is too strong and the image forms above the image plane, then the lens is overfocused. However the conditions required to take images using TEM are that the lens must be underfocusing. If the beam is underfocused it is focused beneath the plane of the specimen which means it is a more parallel beam than if it were focused above (or at) the plane of the specimen since then the electrons would be diverging strongly [15]. Figure 2.2.4 addresses this issue. A parallel beam is needed since it is

more coherent than a con- or divergent beam and this enhances phase contrast and makes interpretation of such images more straight forward.

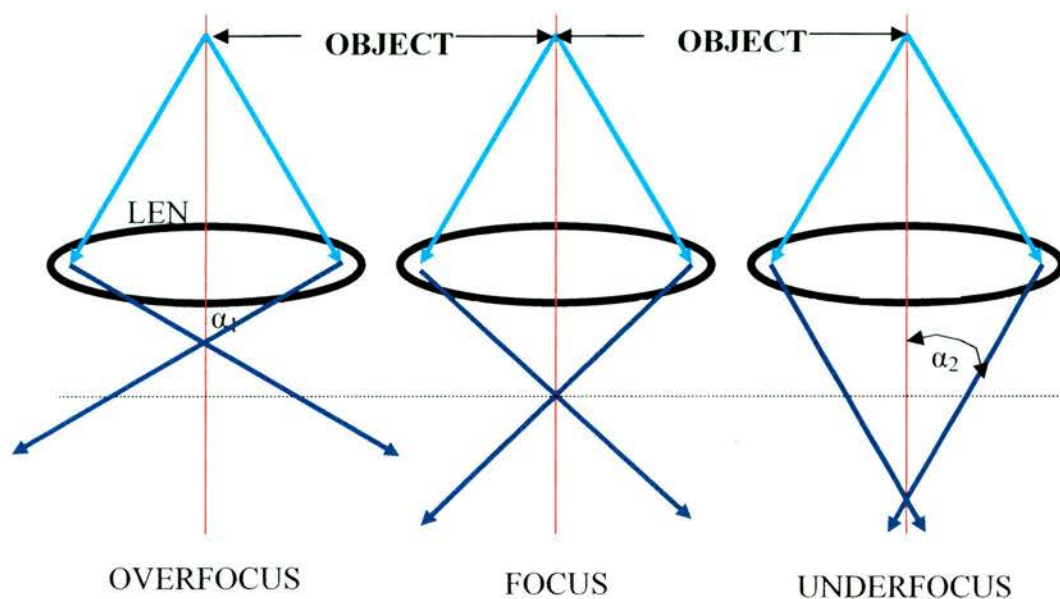
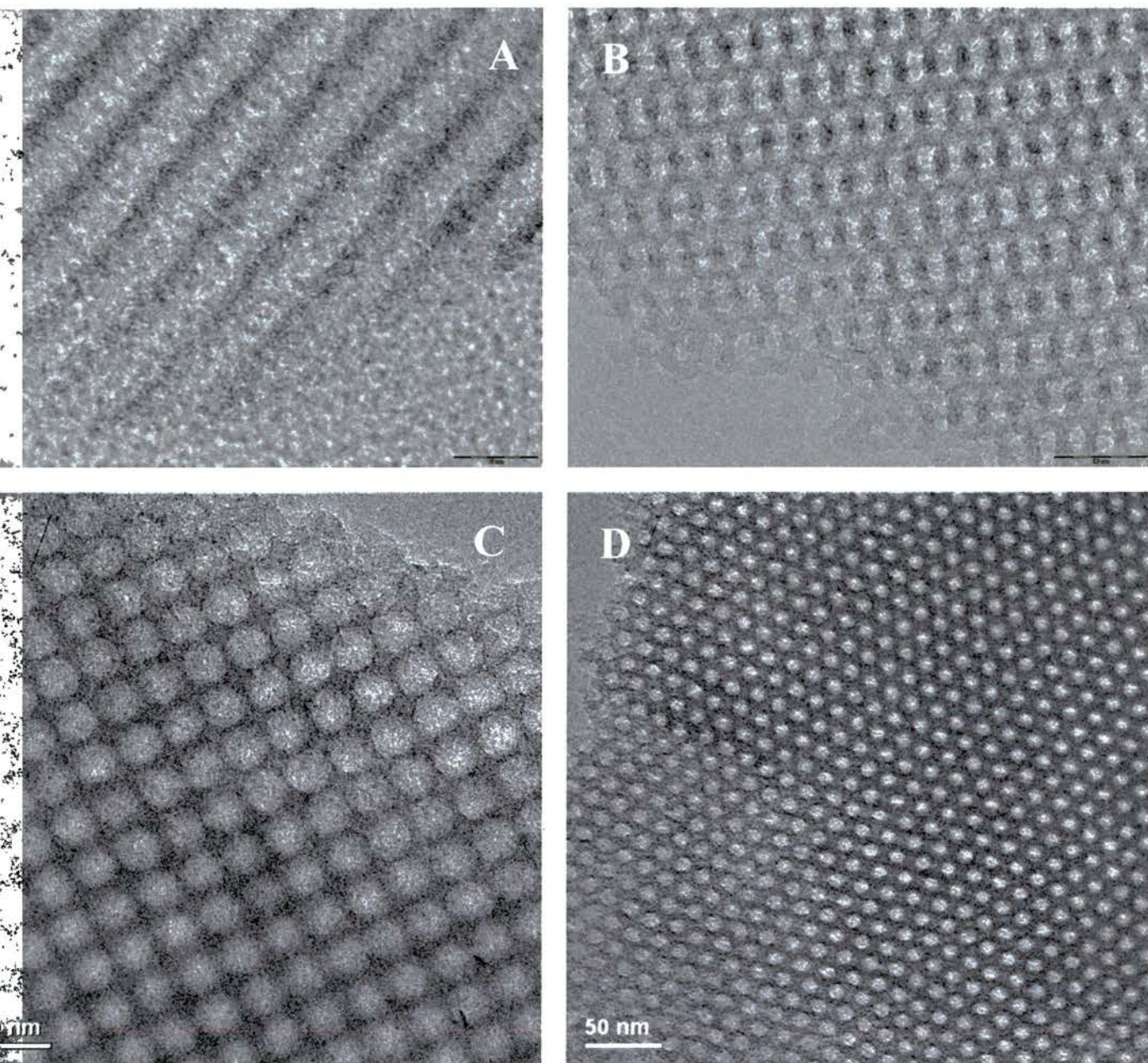


Figure 2.2.4. Underfocusing gives a more parallel beam and thus enhances phase contrast of the image

There are limitations with TEM due to imperfections in the lenses used, which limit the resolution of the microscope but give rise to better depth of focus/field from the microscope. These lens imperfections are better known as lens defects and the most important defect affecting the quality of the high-resolution images are spherical aberration (rays refracted too strongly), chromatic aberration (rays less strongly refracted) and astigmatism (inhomogeneous magnetic field).

Transmission electron microscopy is used to understand the local structure of a sample and in mesoporous solids high resolution TEM is used to elucidate the structure, together with XRD. In addition the mesoporous solids can be imaged at relatively low magnifications without any loss of information due to their large unit cells. There has therefore been extensive research on mesoporous solids using HRTEM to help solve their structures [16,17]. Many structures can be easily observed that represent varying mesophases and topologies along with local structural defects (figure 2.2.5). Figure 2.2.5 are HRTEM micrographs of (a) hexagonal SBA-15; (b) cubic STA-11; (c) cubic FDU-12; (d) thiol-functionalised FDU-12 containing structural defects and (e,f) SBA-15 *in situ* functionalised with a mercapto-siloxane with varying addition of decane to the synthesis mixture (synthesised by L. Ritchie,

University of St. Andrews). In the latter example distortion due to decane acting as a swelling agent – from large particles to that of a branched network of smaller particles – are observed (e) and also nanoparticles with an ‘onion-ring’ type structure (f).



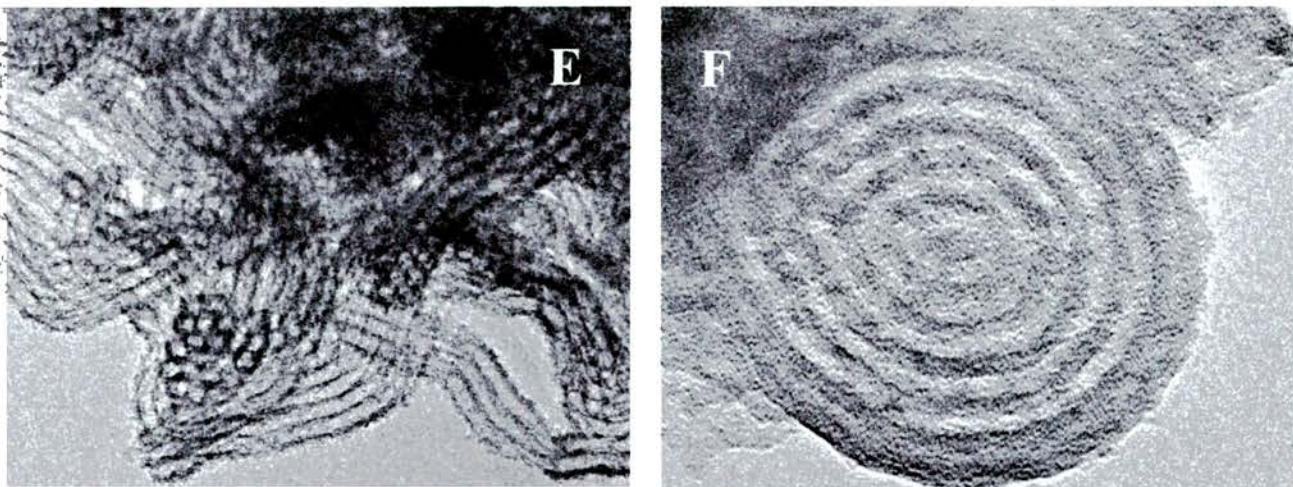


Figure 2.2.5. HRTEM images of varying mesoporous silica. (A) Hexagonal $p6mm$ SBA-15 viewing the $[1,1]$ zone axis; (B) cubic STA-11(7%SH) viewing the $[3,1,1]$ zone axis; (C) cubic $Fm3m$ FDU-12 viewing the $[0,0,1]$ zone axis; (D) *in situ* thiol-functionalised FDU-12 with structural defects present; (E,F) *in situ* thiol-functionalised SBA-15 with the addition of decane as a swelling agent causing nanobranch formation (E) and ‘onion-ring’ type nanoparticles (F).

The importance of TEM in structural characterisation of mesoporous solids becomes apparent when observing changes to the mesophase by both TEM and XRD. Structural defects and differences in particle morphology can only be observed by TEM.

The HRTEM micrographs in this thesis were taken using a JEOL-JEM 2011 electron microscope equipped with a CCD Gatan digital camera operating at 200 keV. Samples were ground before being dispersed in acetone then deposited onto a holey carbon film, supported on a Cu grid. The objective lens parameters, $C_s = 0.50$ nm and $C_c = 1.10$ nm gave a point resolution of ca. 1.94 \AA . Imaging the micrographs were at magnifications in the region of $20000\times$ and $120000\times$. For enhanced stability only extracted or calcined samples were imaged as as-made samples containing template decompose rapidly in the beam.

2.3 Nitrogen Adsorption

In general the uptake by adsorption of a gas onto a solid surface is measured at equilibrium as a function of the pressure, p , of the gas at constant temperature. The adsorption isotherms, measured here gravimetrically (figure 2.3.1) can in general be classified into one of five types as shown in the Brunauer classification of isotherms (figure 2.3.2).



Figure 2.3.1. A Hiden IGA (Intelligent Gravimetric Analyser) used to measure N_2 isotherms at 77K.

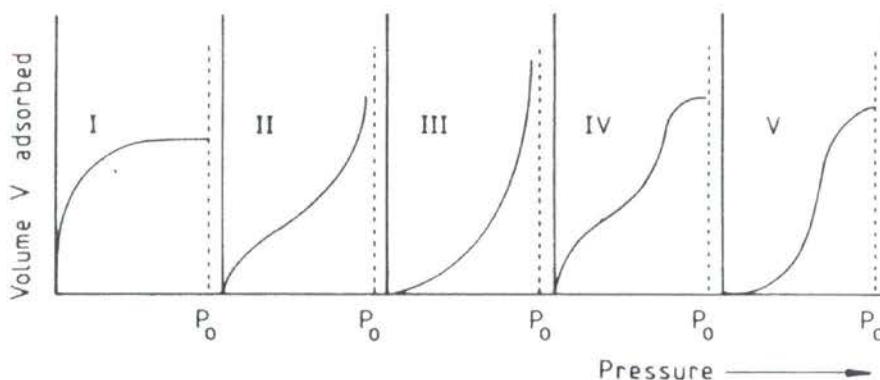


Figure 2.3.2. The Brunauer classification of the five types of adsorption isotherms. P_0 is the saturation vapour pressure [18]

Type I and II are the most common. Type I isotherms, typical of microporous solids are characterised by a rapid rise in the volume adsorbed at low pressures corresponding to pore filling followed by a plateau governed by total pore volume. Any gradual increase in adsorption at high partial pressures, therefore, is attributable to multilayer coverage of the external surfaces.

Mesoporous solids adsorb according to type IV, where the initial monolayer coverage is built upon by multilayer adsorption at higher adsorbate pressures, in an exactly similar way to that observed in type II. At higher relative pressures a steeper upward slope forms as a direct result of capillary condensation characteristic of the type IV isotherm. As the internal surface and volume decrease upon multilayer adsorption a critical pressure is reached at which capillary condensation occurs to fill the remaining volume preferentially over any larger diameter pores. There is a significant increase in uptake over a narrow pressure region and the type IV isotherm – now distinguished from type II isotherm – upon pore filling reaches a plateau with the upper limit of adsorption governed by the total pore volume.

Adsorption in mesoporous solids is a combination of physical adsorption on the mesoporous walls with physical condensation of adsorbate in the pores. Generally isotherms measured on large mesoporous solids display hysteresis loops in the mesoporous region, thought to occur as a result of adsorption of a metastable multilayer, which remains on the pore wall before the onset of capillary condensation. The pressure differences that create the loop are said to occur as a result of the adsorbed fluid forming a meniscus in the pores of the material. This observation is often correlated to the curved geometric pore shapes and connectivity of the mesoporous solid. In this case the curves representing adsorption onto the surface and desorption from the surface are no longer identical and the isotherm shows a hysteresis loop as shown in figure 2.3.3. There are two types of hysteresis loops displayed by large pore mesoporous solids depending on the type of porous network. Cylindrical porous systems like that of SBA-15 display H1 hysteresis loops whilst large-pore meso-caged silicas like FDU-12 exhibit larger H2 hysteresis loops. Note also that some mesoporous solids exhibit significant adsorption at low partial pressures ($< 0.02 P/P_0$) due to micropore filling.

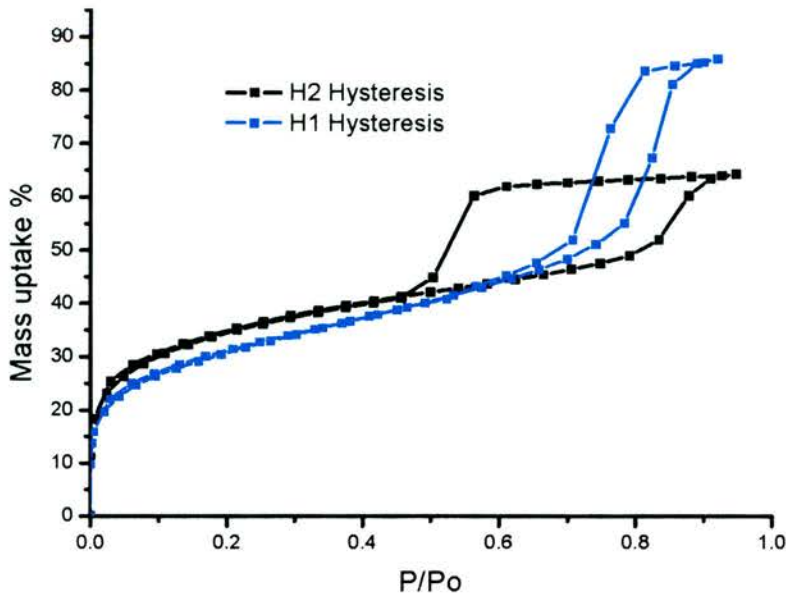


Figure 2.3.3. Hysteresis loop where condensation of the gas forms at pressures lower than the normal saturated vapour pressure of the gas. Either H1 or H2 type hysteresis forms depending on pore system.

In large-pore meso-caged materials whereby cavities are connected by smaller windows the majority of the N_2 uptake occurs within the larger cavity which can be traced through the adsorption branch of the isotherm. However de-gassing the adsorbate from the solid is governed through the size of the smaller entrance connecting windows which can be traced through the desorption branch [19] and so the smaller the entrance size the lower the relative pressure has to be for the adsorbate to leave the host (figure 2.3.4).

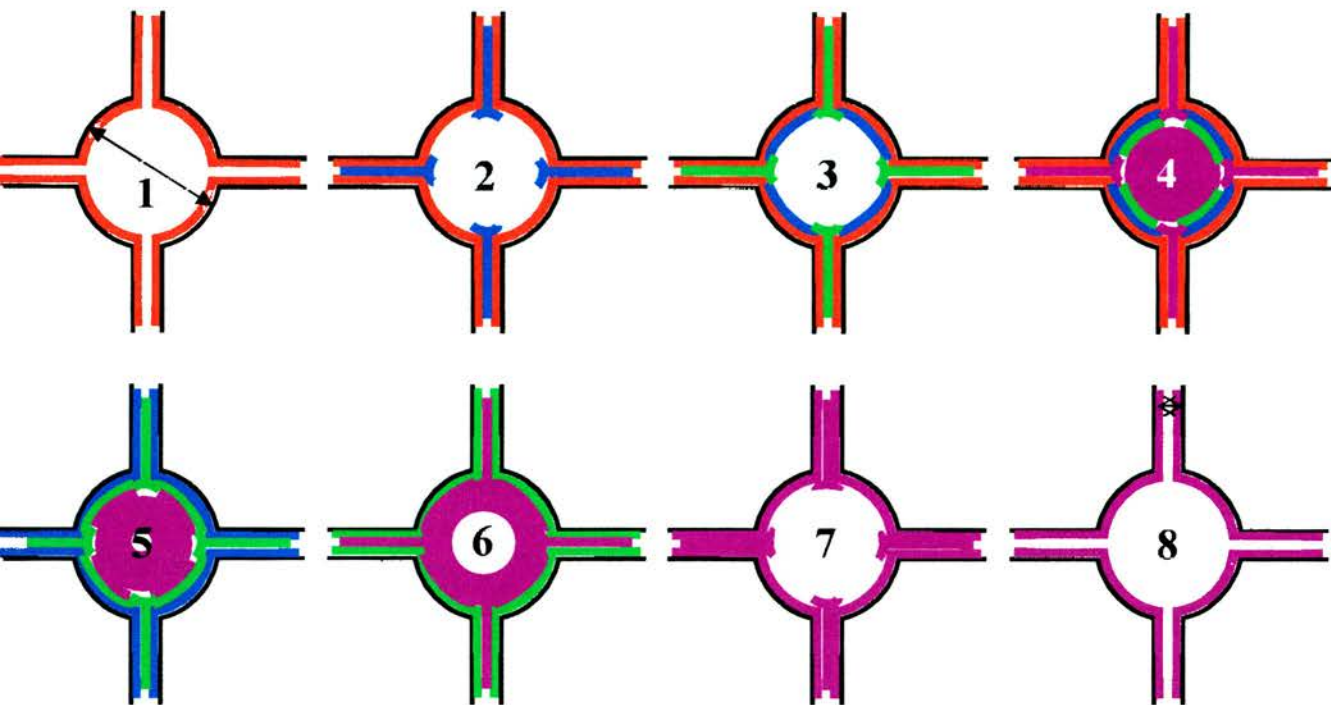


Figure 2.3.4. Adsorption and desorption process of large pore meso-caged silicas where the smaller entrance channel govern the pressures at which the adsorbate leaves and thus contributes greatly to a more dominant hysteresis loop

Adsorption (1 – 4). (1) Initial monolayer of adsorption; (2 – 3) multilayer - smaller entrance pore filled but mobile adsorbate diffuses to larger cavity (2) with continuous progression of process (3); (4) capillary condensation in cavity governed by diameter (1), as seen through adsorption branch.

Desorption (5 – 8). (5 – 7) Desorption through smaller entrance window with adsorbate from cavity continually exiting through entrance window. Entrance window effectively filled throughout this process. (8) Finally all adsorbate desorbed at low relative pressures governed by diameter (8). Hence the smaller the window size the larger the hysteresis.

Further analysis of the adsorption data of mesoporous solids displaying type IV isotherms can lead to measurements of specific surface areas and pore size distributions. The Brunauer, Emmett and Teller (BET) equation is applicable to multilayer adsorption reflected in type II isotherms and also the lower pressure regions of type IV isotherms displayed by mesoporous solids.

The BET model is relevant to the isotherms throughout this thesis as large pore mesoporous solids possess type IV isotherms. The BET theory - an extension of the Langmuir theory - allows for the formation of multilayers to form on top of the initial monolayer. There are however assumptions made in order to derive such a theory: (i) the heat of adsorption for the monolayer is independent of surface coverage, and (ii) the heat of formation of the second, third etc (multilayers) all of which are assumed to be the same but different to that of the monolayer. The multilayers comprise of gas molecule to gas molecule type interactions and the heat of formation of these layers are similar to the condensation of these molecules. The monolayer involves interactions of gas molecule - surface site which will be different from gas-gas interactions and probably significantly larger. If so, then the BET equation can be expressed as (equation 2.3.1) [20]:

$$\frac{P}{V(P_0 - P)} = \frac{c-1}{V_m c} * \frac{P}{P_0} + \frac{1}{V_m c} \quad \text{Equation 2.3.1}$$

Where V is the volume of gas adsorbed (corrected to STP) at a specific value of P an equilibrium pressure with the constant c (equation 2.3.2);

$$c \sim \exp \frac{\Delta H_{liquid} - \Delta H_{monolayer}}{RT} \quad \text{Equation 2.3.2}$$

In practice the assumptions on which the derivation of the BET equation is derived are such that the above equation is only applicable up to P/P₀ values of about 0.03 → 0.4.

In order to obtain a straight line from the above equation - which in turn shows the data from the experiment obeying the BET model - a plot of P/P₀ as x and P/[V(P₀-P)] as y is plotted, with gradient and intercept (equations 2.3.3 and 2.3.4 respectively);

$$\text{gradient} = \frac{c-1}{V_m c} \quad \text{Equation 2.3.3}$$

$$\text{intercept} = \frac{1}{V_m c} \quad \text{Equation 2.3.4}$$

In many cases the gradient is much larger than the intercept (equivalent to $c \gg 1$) and thus the equation for the volume of the monolayer simplifies to (equation 2.3.5);

$$V_m = \frac{1}{\text{gradient}} \quad \text{Equation 2.3.5}$$

Below is a calculation of the specific surface area of an extracted SBA-15 functionalised with 5% cyano-propyl. In order to determine that the sample obeys the BET model values of P/P_0^* and V^+ (calculated from the primary data of the isotherm) are required in order to plot the graph in question. The nitrogen adsorption isotherm (figure 2.3.5) shows the total weight of the sample as a function against pressure. Here individual weights can be read off at specific pressure points.

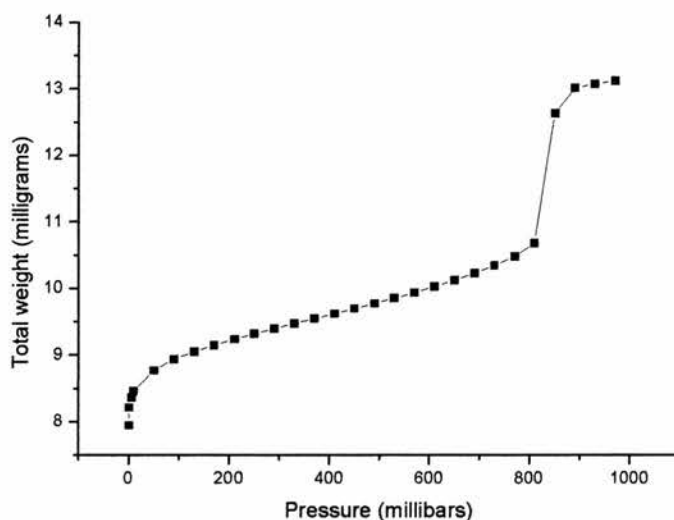


Figure 2.3.5. An N_2 isotherm measured at 77 K showing the total real weight of the sample as a function of pressure.

* P_0 of N_2 at a specific temperature can be obtained by interpolation of a plot of $1/T$ (x-axis) vs. $\ln P$ (y-axis) (taken from CRC Handbook of Chemistry and Physics, 80th edition)

+ Volume of gas adsorbed obtained through the total weight of sample at individual pressure points

Once the saturation vapour pressure along with individual pressures are established together with the corresponding weights for the pressure points then a table can be drawn to give the necessary values of P/P_0 and $10^3 P/P_0[V(1-P/P_0)]$ (table 2.3.1).

P/bars	P/P_0	V/cc	$P/P_0[V(1-P/P_0)]*10^3$
0.610313	0.526123	1.628679	681.7131
0.569559	0.490999	1.554252	620.6414
0.530425	0.457263	1.487500	566.3952
0.489627	0.422131	1.426264	512.1747
0.450538	0.388395	1.364947	465.2500
0.409785	0.353263	1.303711	418.9758
0.370651	0.319527	1.241356	378.2682
0.329891	0.284394	1.180040	336.7827
0.290763	0.250658	1.125356	297.2419
0.250010	0.215526	1.064122	258.1839
0.210876	0.181790	0.996251	223.0157
0.170213	0.146658	0.922943	186.2116
0.129369	0.111525	0.843080	148.8875
0.090235	0.077789	0.757701	111.3240

Table 2.3.1. List of variable parameters for further calculation into specific surface area

Only the data highlighted in blue can be used to determine the specific surface area as this is the region applicable to the derivation of the BET model (P/P_0 values between 0.03 \rightarrow 0.4). The plot of the data P/P_0 vs. $10^3 P/P_0/[V(1-P/P_0)]$ (figure 2.3.6) can now determine the specific surface area of the sample.

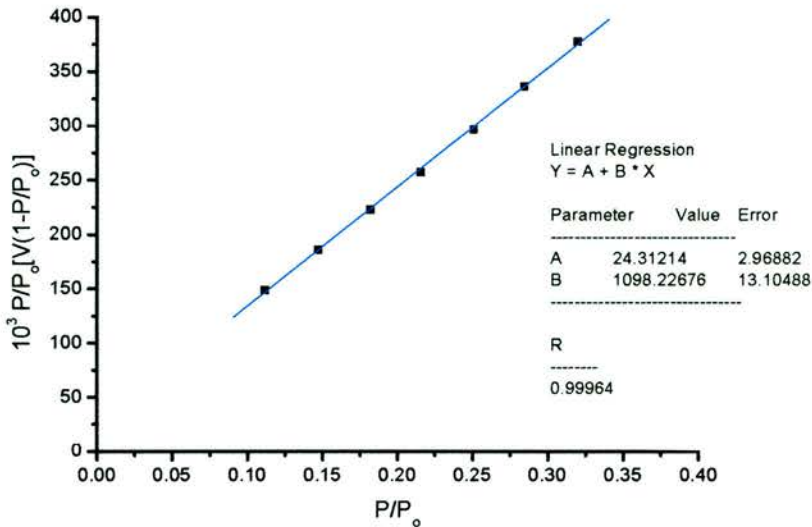


Figure 2.3.6. Plot of the variables from the BET equation ($y = mx + c$) to obtain the gradient of slope and hence the volume of the monolayer to determine the specific surface area.

Linear regression shows that:

$$\text{gradient} = 1098.2 \times 10^{-3} \text{ cm}^{-3}$$

$$V_m = 0.91 \text{ cm}^3$$

The units of V_m need to be converted to the molar volume (dm^3), $V_m = 9.1 \times 10^{-4} \text{ dm}^3$ and the monolayer converted to moles, then molecules then surface area (m^2) by multiplying by the area occupied by the adsorbate molecule as shown:

$$\text{surface area}^\dagger = \frac{V_m}{22.4} \times 6.0221 \times 10^{23} \times 16.2 \times 10^{-20}$$

The specific surface area ($\text{m}^2 \text{g}^{-1}$) of the solid is:

$$S.S.A. = \frac{3.97}{7.99 \times 10^{-3}} = 497 \text{ m}^2 \text{ g}^{-1}$$

[†] Mass of sample = $7.99 \times 10^{-3} \text{ g}$ – non-specific surface area = $3.97 \text{ m}^2 \text{ g}^{-1}$

and is comparable with that calculated through the IGA software ($490 \text{ m}^2\text{g}^{-1}$) (figure 2.3.7).

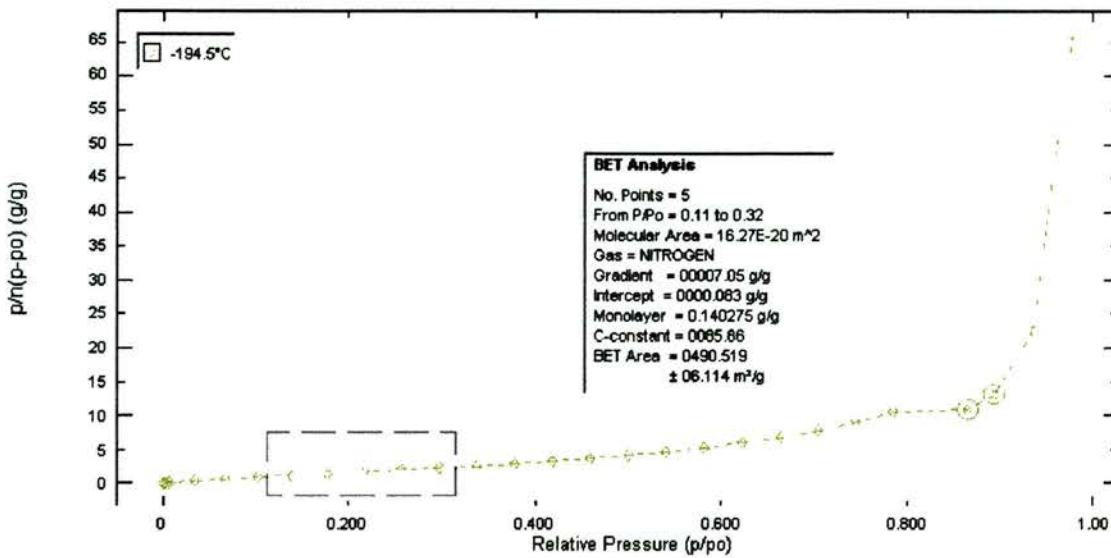


Figure 2.3.7. Specific surface area calculated automatically from the IGA-II software.

In the region of a sharp mass uptake over a narrow P/P_0 range, (i.e. the capillary condensation step), the pore size distribution can be derived traditionally using the Barrett-Jayner and Halenda (BJH) [21] and the De Boer modification [22], which are based on the Kelvin equation (equation 2.3.6) and expressions for the multi layer adsorbate film thickness as a function of adsorbate pressure, P .

$$RT \ln\left(\frac{P}{P_0}\right) = \frac{2\gamma V_m}{r} \quad \text{Equation 2.3.6}$$

where γ = surface tension; V_m = molar volume and r = radius of curvature of condensed gas assuming 0° contact angle of liquid nitrogen with pores.

Within cylindrical pores, the spherical meniscus radius is complicated by a multilayered adsorbed film, of thickness t , lining the pore walls. In the Kelvin equation, the radius must account for the observed meniscus whose radius is larger than that of the reduced cylindrical pore (r^*) (figure 2.3.8) related to the meniscus radius (r) through the contact angle, θ (equation 2.3.7).

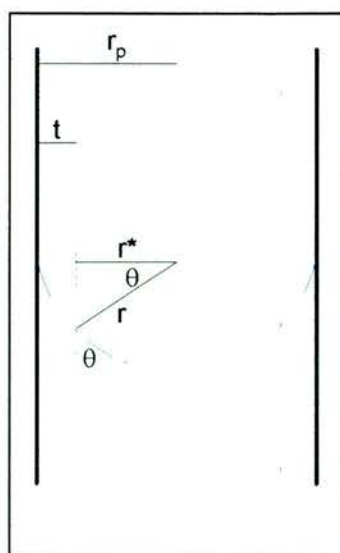


Figure 2.3.8. Vertical cross-section of a cylindrical pore showing the relationship of the meniscus radius for the Kelvin equation (r) and the radius of the core (r^*). Θ is the contact angle, t the multilayer adsorbed thickness and r_p the pore radius ($r_p = r^* + t$).

$$r^* = r \cos \theta \quad \text{Equation 2.3.7}$$

In practice, however, $\cos \theta = 1$, i.e., the contact angle is assumed to be zero. The BJH model thus underestimates the pore size [23,24] and therefore the De Boer model is used within this thesis. Note, the models for calculating pore sizes are for comparative purposes only and are not the actual pore size of the solid. The De Boer model tries to take into account the thickness of the adsorbed film at specific pressures to give a more accurate pore diameter. The latest development for the analyses of pore size distributions is the non-local density functional theory (NLDFT) [24,25] although not widely available. As with all models assumptions are made that the porous system is uniform throughout and it is the non-uniform pores and pore shapes that limits the accuracy of the models.

Figure 2.3.9 is a typical type IV isotherm of a large pore mesoporous solid of cyanopropyl-functionalised SBA-15. Measurements of specific area are based on the Brunauer-Emmett-Teller (BET) method which, may be applied to Type IV isotherms at pressures below those at which capillary condensation occurs, and more importantly below P/P_0 values of ~ 0.4 and are calculated approximately within the box. Along with this is the pore size distribution curve calculated on the adsorption branch of the isotherm in the high relative pressure region using the De Boer model.

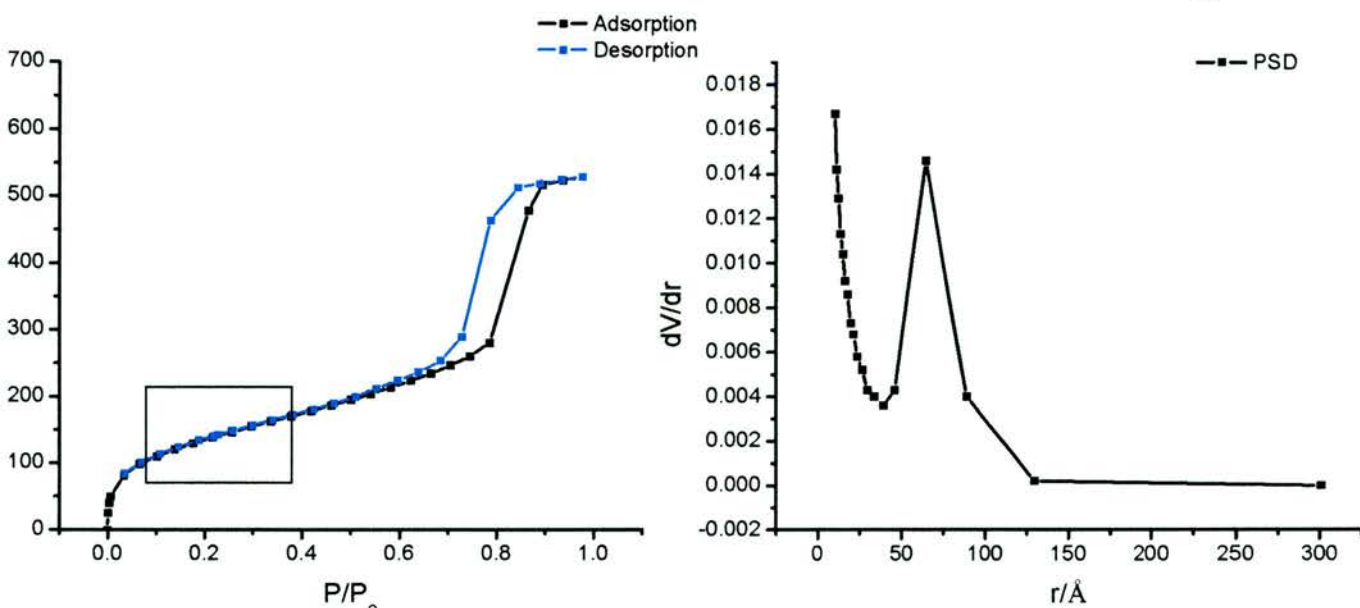


Figure 2.3.8. N_2 adsorption type IV isotherm of a cyano-functionalised SBA-15 mesoporous solid with boxed region indicating the region where the derivation of the BET equation is applicable. Pore size distribution calculated by the De Boer model on the adsorption branch of the isotherm.

Porosity measurements were obtained gravimetrically using an IGA-II series automated gravimetric analyser. Typically between 10 – 25 mg of sample are used in each isotherm run. Samples were degassed at 393 K with a ramp rate of 276 K minute^{-1} for 2 hrs once final temperature has been reached. The sample is then cooled down to typically 308 K before the dry mass is set. The sample is emerged in a liquid nitrogen dewar and data collection started at typically 273 K*. The isotherm run followed a program consisting of an adsorption branch followed by a desorption branch.

The equilibrium adsorption values were those calculated by mathematical analysis of the asymptotic increase or decrease of weight within a 1 h time period. BET analysis estimates specific surface areas obtained on the physisorbed multilayer region of the type IV isotherms where the derivation of the BET equation is applicable. Pore size distributions are obtained via the De Boer model on the adsorption branch of each isotherm.

* Data collection should ideally be started at 77 K, however, with the sample being under vacuum attaining such a temperature would take a very long time for convection reasons. In any case there is also a 10 min delay from injection of N_2 to each recorded point even if equilibrium is found and in this time a rapid decrease of temperature results.

2.4 Electron Spin Resonance Spectroscopy

ESR has been used to investigate metal complexes with unpaired electrons (used in Chapter 5). First observed by the Russian Zavoisky in 1945 [26] the form of spectroscopy known as electron spin resonance (ESR) initially was exploited by physicists who were concerned with transition metals. Chemists became involved with this technique – also known as electron paramagnetic resonance (EPR) – once free radicals demonstrated their properties to ESR. Developments in instrumentation (figure 2.4.1) have resulted in application in chemical studies of organic free radicals, transition metal complexes, photochemistry, biological and medicinal studies and catalysis and surface science.



Figure 2.4.1. An Electron Spin Resonance Spectrometer operating at X-Band – 9.5 GHz with a variable temperature controller.

ESR detects molecules or ions which are paramagnetic and possess one or more unpaired electrons where no complete electron spin pairing is possible. (Where there is virtually no net spin of magnetism exhibited the material is said to be diamagnetic and ESR gives no signal). Unpaired electrons oriented within a magnetic field, \mathbf{B} , usually align themselves parallel to the applied field, \mathbf{B}_z , which lifts the degeneracy of the $m_s \pm \frac{1}{2}$ states of the unpaired electron (figure 2.4.2) [27].

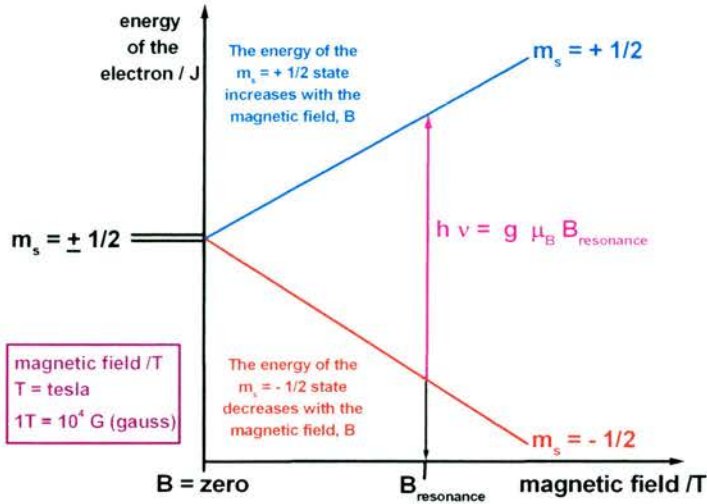


Figure 2.4.2. The basics of electron spin resonance. Splitting of the $\{s=1/2, m_s=+1/2\}$ and $\{s=1/2, m_s=-1/2\}$ states when a magnetic field, B , is applied [27].

When electromagnetic radiation in the form of microwaves is applied at a frequency which corresponds to the energy of separation of the $m_s \pm 1/2$ levels then resonance occurs.

An electron has a spin leading to a magnetic moment, μ_s . If the electron is subjected to a steady magnetic field, $B_0 \parallel z$, it experiences a tendency to align the magnetic moment with the field, the correlation of which is (equation 2.4.1):

$$\mu_s = -\frac{g\mu_B}{\hbar} S \quad \text{Equation 2.4.1}$$

where where μ_B is the Bohr magneton* and g the Landé factor[†]. The energy of the system depends upon the vector that the magnetic moment experiences when aligning with the field along B_0 . Only two quantum values for an electron exist. $S_z = \pm \hbar/2$ and hence the magnetic moment can only assume two projections onto the applied field. Consequently (equation 2.4.2),

* $\mu_B = \frac{e\hbar}{2m} = 9.2741010 \cdot 10^{-24} \text{ Joule} \cdot \text{Tesla}^{-1}$

[†] $g = 2.0023$ for a free electron

$$\mu_z = \pm \frac{1}{2} g \mu_B \quad \text{Equation 2.4.2}$$

and all energy levels therefore reduce to (equation 2.4.3) the two values (figure 2.4.3);

$$E = \pm \frac{1}{2} g \mu_B B_0 \quad \text{Equation 2.4.3}$$

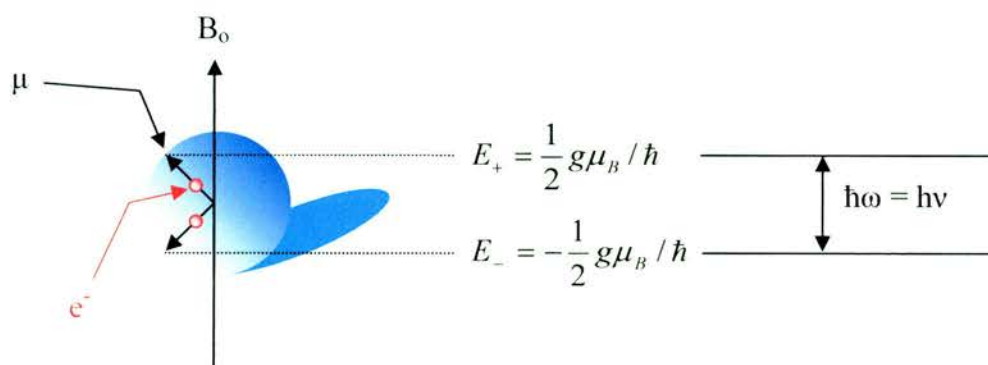


Figure 2.4.3. A schematic representation of a single electron spin associated with an applied magnetic field, B_0 , together with the quantised energy-levels.

A measured sample is in fact a macroscopic ensemble of magnetic moments and therefore consideration of the relative populations within the ground state – N_+ , and excited state – N_- , should be made given by the Boltzmann distribution (equation 2.4.4):

$$\frac{N_+}{N_-} = \exp\left(-\frac{\Delta E}{k_B T}\right) \quad \text{Equation 2.4.4}$$

where $\Delta E = E_+ - E_-$, k_B Boltzmann constant and T the absolute temperature. As with NMR, in ESR the energy difference between the excited and ground state is small enough that the electrons occupy ground and excited states with similar populations and there is little overall net absorption. Since the absorption observed is due to a greater population of electrons in the ground state the difference in population of the two levels should be maximised. This can be achieved by lowering the absolute temperature to maximise the ESR signal.

The proportionality constant, g (equation 2.4.5):

$$h\nu = g\mu_B B \quad \text{Equation 2.4.5}$$

where ν is the fixed microwave frequency and B , the magnitude of the static field at resonance measures the rate of divergence of the $m_s = \pm \frac{1}{2}$ levels in a magnetic field (figure 2.4.4). Magnetism due to the electron spin only adopts a g_e value of 2.0023. Independent of any electron-nuclear hyperfine interactions the g -value is unique to the molecule as a whole and small deviations from g_e , which can be measured, serve to help characterise one species from the next [28].

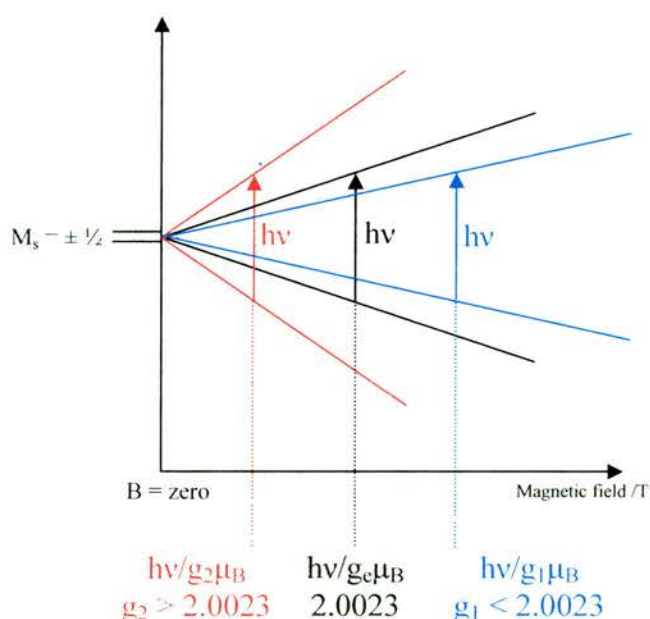


Figure 2.4.4. m_s levels degenerate at zero field split at a rate of divergence measured by g upon an applied magnetic field.

Deviations from the free spin (2.0023) arise due to another source of magnetism that is present in the system, namely orbital magnetism that can add to, or subtract from, the spin magnetism induced by the presence of an applied magnetic field. For organic radicals the mixing of the spin magnetism can be treated as a small perturbation on the spin magnetism and so deviations from g_e are small. The extent of the mixing of magnetisms depends on the magnitude of the spin orbit coupling constant, ζ . As ζ increases with increasing atomic number the deviation from g_e – i.e. Δg – can be significant for systems with high spin density in p or d orbitals and so for heavy

transition metal complexes the metal ion is usually the source of the deviation away from g_e .

The hyperfine coupling is a term to describe the interaction between the magnetic moment of an electron with the magnetic moment of nearby nuclei and resembles spin-spin coupling in NMR spectroscopy. Nuclei have a magnetic moment, I , with $(2I + 1)$ orientations in the applied field, where n is the number of equivalent spin I nuclei. The magnetic field associated with the nuclear moment can either add to, or subtract from, the applied field experienced by the electron spin giving rise to a split of the original Zeeman splitting into $(2I + 1)$ components described by (equation 2.4.6):

$$H_{hfs} = A I \cdot S \quad \text{Equation 2.4.6}$$

with A the coupling constant.

The hyperfine coupling constant is a measure concerning the electronic and nuclear spins interaction the strength of which varies with varying nuclear species. Figure 5 is an illustration of the hyperfine splitting with respect to a Mn^{2+} ion with a nuclear spin, $I = 5/2$ interacting with the 3d electrons which split the resonance line into six sub-levels (figure 2.4.5).

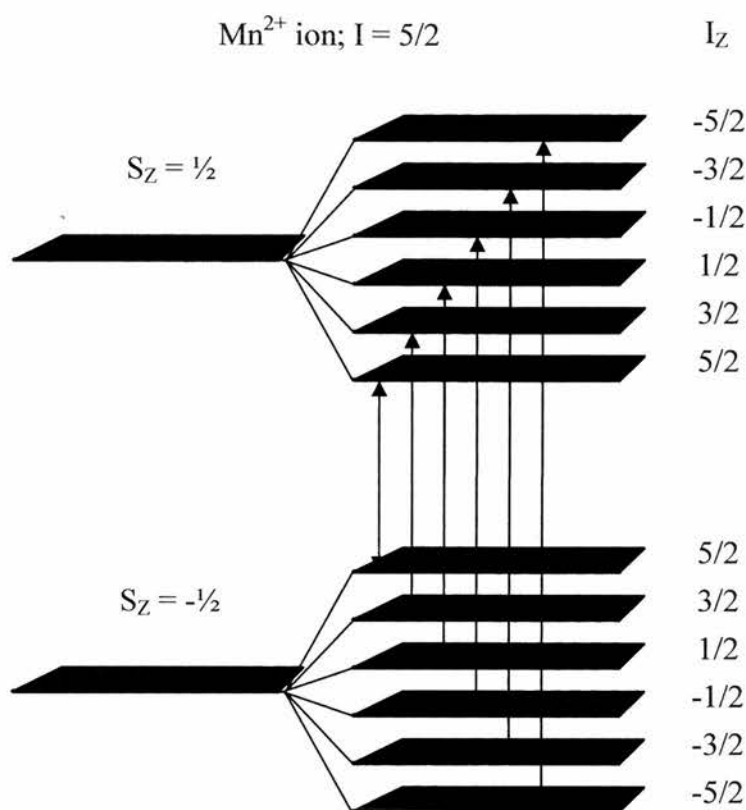


Figure 2.4.5. The six sub-levels of the Mn^{2+} ion. Splitting of the initial Zeeman ESR line by the hyperfine interaction.

Modern instruments now use a phase sensitive method of detection, and hence produce a first derivative of the absorption spectrum. This is based on Zeeman modulation since the peak position is then the base-line crossover, and the width is conveniently measured between the maximum slope.

Most common instruments are calibrated to display spectra in Gauss (G), though a recommendation to use SI units of Tesla (T) as the fundamental unit is suggested. Fortunately conversion only involves factors of 10^{-4} [$G = 10^{-4}$ T], or mT which is only ten times smaller than G as shown in table 2.4.1 [29].

Conversions

$$\begin{aligned}
 1 \text{ G} &= 10^{-4} \text{ T} \\
 &= 10^{-1} \text{ mT} \\
 &= (g_{\text{exp}}/0.7145) \text{ MHz} \\
 &= (g_{\text{exp}}/2.142 \cdot 10^4) \text{ cm}^{-1}
 \end{aligned}$$

Table 2.4.1. Conversion of spectrometer units,
Gauss, to the standard unit of Tesla.

The samples under ESR investigation may be in various physical properties and mediums and hence can be liquids and solids in the form of glasses, fine powders or crystals. In this sensitive technique samples are positioned within a cavity and too big a sample can lower the sensitivity especially for liquids so the use of flat cells or capillary tubes helps to diminish the problem. Note it is important to remove any O₂ that is present as dioxygen is a paramagnetic molecule which can attribute to line broadening.

A standing wave, as in an ESR cavity, has the electric and magnetic vectors mutually orthogonal to each other (figure 2.4.6 (top)), with the magnetic component concentrated along the central axis of the cavity where the electronic component is zero (figure 2.4.6 (bottom)). For narrow samples positioned in the centre of the cavity it is possible to absorb only the magnetic radiation whilst simultaneously rejecting the electronic component. This scenario is important because if the electronic vector is not rejected then the sample heats up causing difficult and often impossible tuning of the spectrometer [30].

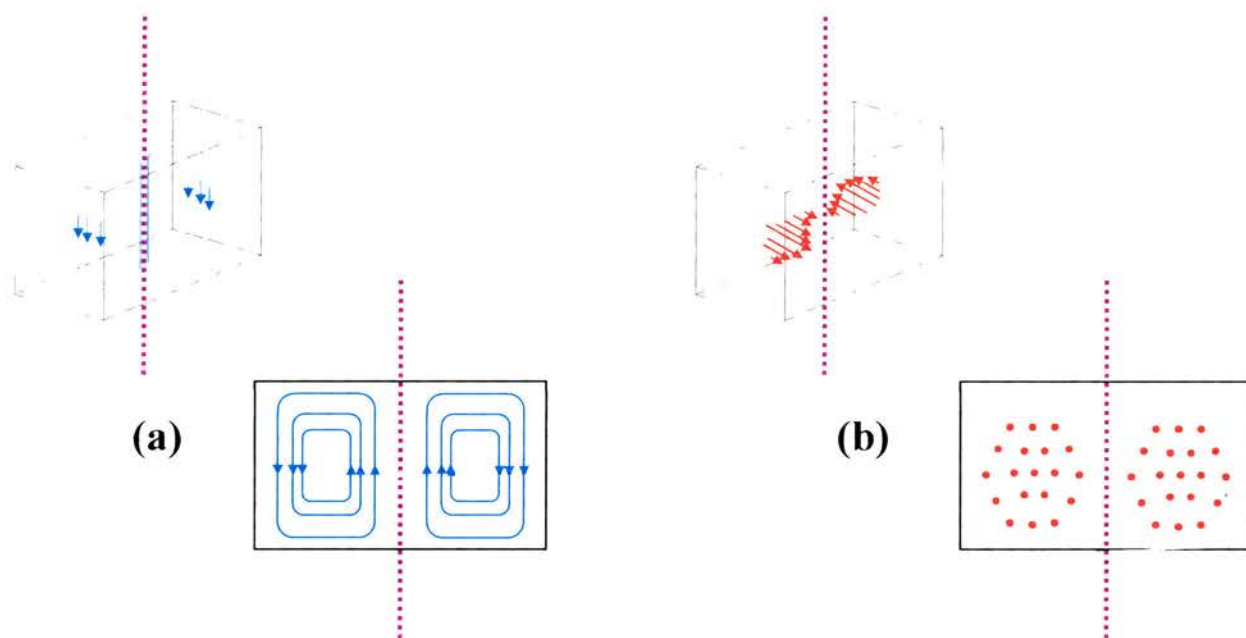
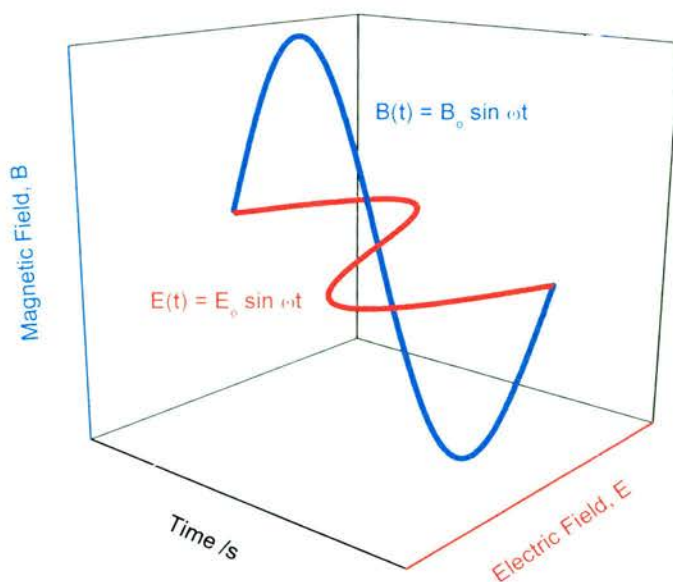


Figure 2.4.6. The electric and magnetic vectors mutually orthogonal with respect to each other (top) and contour lines of constant microwave magnetic field (a) and electric field (b) vectors (bottom) [27].

The set up of the ESR spectrometer produces a dc current, which is proportional to the amount of microwave radiation being absorbed by the sample. Due to a low difference in populations between the upper and lower spin states the intensity of the signal is low. Consequently this small signal would be hidden by the electronic noise of the spectrometer. Zeeman modulation is required to remove the noise before the resulting signal is amplified. In the ESR spectrometer a pair of Helmholtz coils

(Zeeman modulation coils) – as shown in figure 2.4.7 – are fixed to opposite sides of the cavity which can add a low amplitude oscillating magnetic field to the static field by the electromagnet.

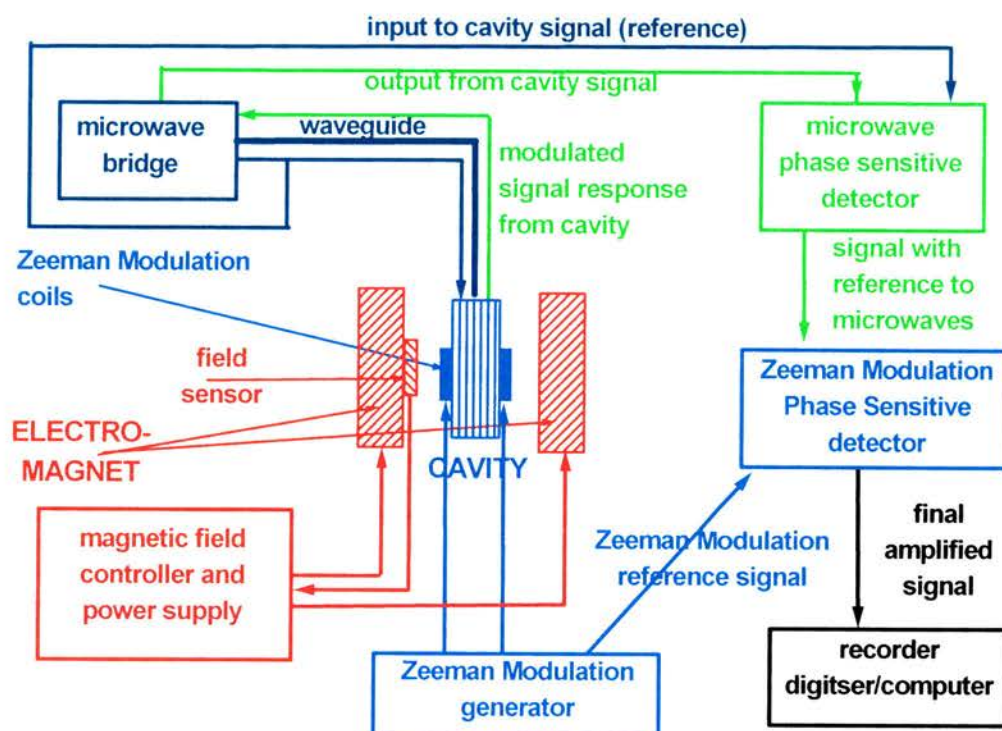


Figure 2.4.7. A block diagram of the main components within an X-band electron spin resonance spectrometer [28].

For example, if the static field is set at 3500 G and the modulation of the Helmholtz coils set at 2 G, then the magnetic field seen by the sample will vary sinusoidally from from $3500 - 1$ G, to $3500 + 1$ G at the Zeeman modulation frequency (figure 2.4.8).

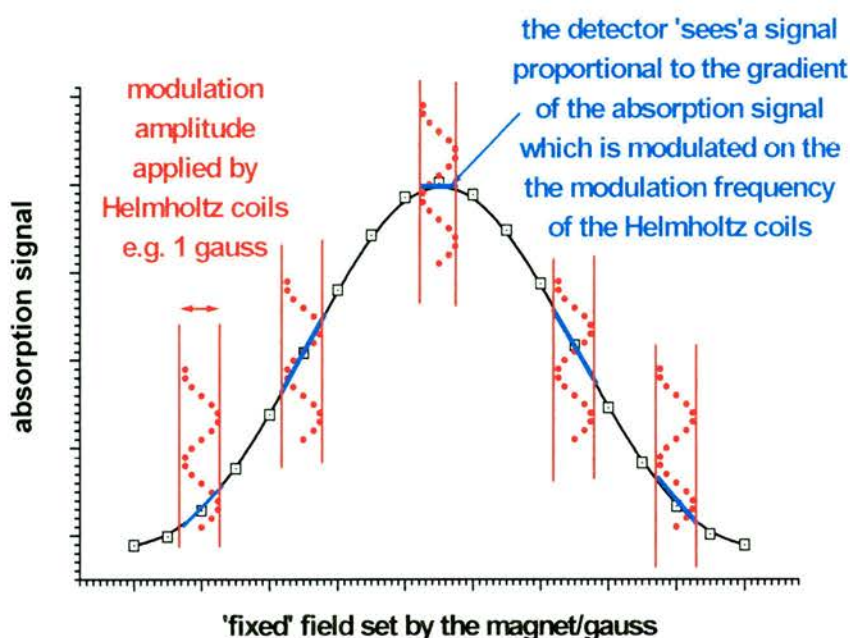


Figure 2.4.8. Magnetic field modulation of the output from the microwave detector. In addition to the static applied field by the electro-magnet an oscillating magnetic field of relatively low amplitude is applied via a set of Helmholtz coils [27].

The result is that the dc output is modulated onto an ac carrier of the same frequency as the oscillating magnetic field. A second effect is that the amplitude of the signal is proportional to the gradient of the absorption curve. Thus the output is the derivative of the absorption signal with the centre of the spectrum being where the curve intersects the baseline (figure 2.4.9) [31].

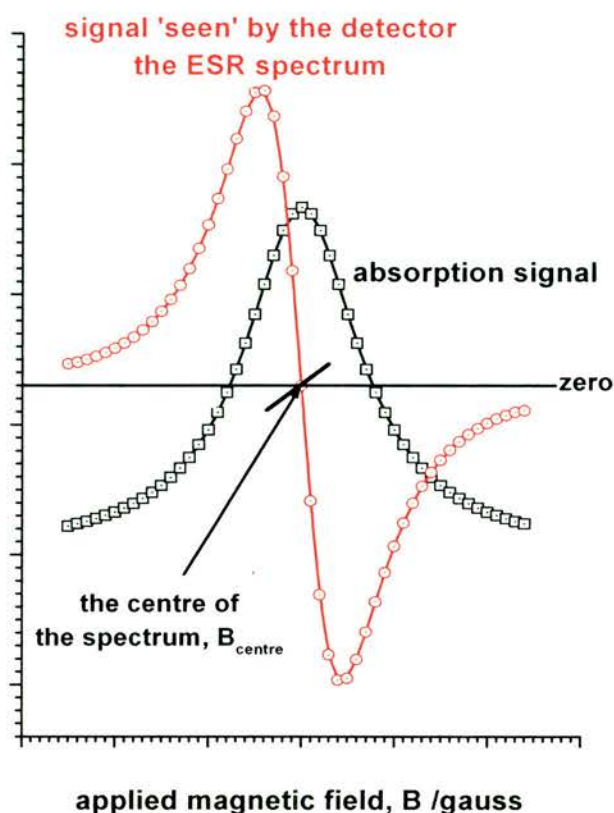


Figure 2.4.9. The effect of Zeeman magnetic field modulation is that the spectrum is presented as the derivative of the absorption curve rather than the absorption curve itself [27].

X-Band

ESR spectra were obtained using a Bruker EMX 10/12 spectrometer operating at 9.5 GHz with 100 kHz modulation. Powder samples were inserted into a quartz ESR tube (4 mm diameter) within a standard super high-Q cavity. Spectra were recorded at ambient temperature down to liquid nitrogen temperature. g factors were not measured with reference to known standards so g values are not given to four decimal places. The spectrometer parameters when running spectra are as follows:

Microwave frequency	9.50 – 9.53 GHz
Microwave power	16 – 20 dB attenuation
Amplitude modulation	4 – 5 Gpp
Receiver gain	$5 \cdot 10^2$ – $5 \cdot 10^3$ at a frequency of 100 kHz
Magnetic field sweep width	2000 – 6000 Gauss
Field centre	3300 Gauss

Conversion time	5.12 ms
Time constant	5 ms
Temperature	Room temperature – 105 K

K-Band

Samples measured at K-Band were obtained at the EPSRC National ESR multi-frequency facility at the University of Manchester using a Bruker ESP 300E spectrometer with an ER5106QT cavity. Magnetic fields were calibrated with a Bruker ER035M gaussmeter and microwave frequency measured with an EIP588C microwave counter. The spectrometer parameters when running spectra are as follows:

Microwave frequency	24.15 – 24.16 GHz
Microwave power	16 – 20 dB attenuation
Amplitude modulation	5 Gpp
Receiver gain	5×10^3 at a frequency of 100 kHz
Magnetic field sweep width	4000 Gauss
Field centre	8300 Gauss
Conversion time	164 ms
Time constant	1.28 ms
Temperature	293 K

W-Band

High-field measurements were obtained at the EPSRC national ESR high-field facility at St. Andrews University. The spectrometer is an in-house built one and is not a commercially available [32] using a non-resonating sample holder operating in induction mode.

Microwave frequency	94 GHz
---------------------	--------

2.5 References

- [1] A.R West, Basic Solid State Chemistry, 1988, John Wiley and Sons, Chichester, UK
- [2] J.M. Thomas, W.J. Thomas, Principles and Practice of Heterogeneous Catalysis, 1997, VCH, Weinheim, Germany
- [3] <http://66.102.9.104/search?q=cache:gowcIXbq87gJ:www.answers.com/topic/x-ray-crystallography+max+von+laue+and+1912+and+x-ray&hl=en>
- [4] <http://www.eserc.stonybrook.edu/ProjectJava/Bragg/>
- [5] A. Firouzi, D. Kumar, L.M. Bull, T. Besier, P. Sieger, Q. Huo, S.A. Walker, J.A. Zasadzinski, C. Glinka, J Nicol, D. Margolese, G.D. Stucky, B.F. Chmelka, *Science*, 1995, **267**, 1138
- [6] F. Kleitz, D. Liu, G.M. Anilkumar, I.S. Park, L.A. Solovyov, A.N. Shmakov, R. Ryoo, *J. Phys. Chem. B*, 2003, **107**, 14296
- [7] M. Kaneda, T. Tsubakiyama, A. Carlsson, Y. Sakamoto, T. Ohsuna, O. Terasaki, *J. Phys. Chem. B*, 2002, **106**, 1256
- [8] C. Yu, J. Fan, B. Tian, G.D. Stucky, D. Zhao, *J. Phys. Chem. B*, 2003, **107**, 13368
- [9] M. Kruk, M. Jaroniec, C.H. Ko, R. Ryoo, *Chem. Mater.*, 2000, **12**, 1961
- [10] D. Zhao, J. Feng, Q. Huo, N. Melosh, G.H. Fredrickson, B.F. Chmalka, G.D. Stucky, *Science*, 1998, **279**, 548
- [11] S. Che, A.E. Garcia-Bennett, T. Yokoi, K. Sakamoto, H. Kunieda, O. Terasaki, T. Tatsumi, *Nat. Mater.*, 2003, **2**, 801
- [12] <http://nobelprize.org/physics/laureates/index.html>
- [13] P.B. Hirsch, Electron Microscopy of Thin Materials, 1977, Krieger Publishing Company
- [14] D.B. Williams, C.B. Carter, Transmission Electron Microscopy, 1996, Plenum Press, New York
- [15] Personal communication, Prof. D.B. Williams, Lehigh University, USA
- [16] W. Zhou, H.M.A. Hunter, P.A. Wright, Q. Ge, J.M. Thomas, *J. Phys. Chem. B.*, 1998, **102**, 6933
- [17] Y. Sakamoto, I. Díaz, O. Terasaki, D. Zhao, J. Pérez-Pariente, J.M. Kim, G.D. Stucky, *J. Phys. Chem. B.*, 2002, **106**, 3118
- [18] S. Brunauer, Physical Adsorption of Gases and Vapours, OUP, 1944

- [19] J. Fan, C. Yu, F. Gao, J. Lei, B. Tian, L. Wang, Q. Luo, B. Tu, W. Zhou, D. Zhao, *Angew. Chem. Int. Ed.*, 2003, **42**, 3146
- [20] S. Brunauer, P.H. Emmett, E. Teller, *J. Am. Chem. Soc.*, 1938, **60**, 309
- [21] E.P. Barret, L.G. oyneser, P.H. Halendar, *J. Am. Chem. Soc.*, 1951, **73**, 373
- [22] B.C. Lippens, B.G. Linsen, J.H. De Boer, *J. Catal.*, 1965, **4**, 319
- [23] P. Ravikovitch, G. Haller, A. Neimark, *Adv. Colloid Interface Sci.*, 1998, **76-77**, 203
- [24] P. Ravikovitch, A. Neimark, *Langmuir*, 2002, **18**, 1550
- [25] P.I. Ravikovitch, D. Wei, W.T. Chueh, G.L. Haller, A.V. Neimark, *J. Phys. Chem. B*, 1997, **101**, 3671
- [26] <http://www.thch.uni-bonn.de/pc/bargon/ESR/esr-allgemeines.html>
- [27] Robert P. Hodgkins, Final year project, Liverpool John Moores University, 2001
- [28] F.E.Mabbs, D.Collison, *Studies in inorganic chemistry 16, Electron Paramagnetic Resonance of d-Transition Metal Compounds*, Elsevier, Amsterdam, 1992
- [29] M. Symons, *Chemical and Biological Aspects of Electron Spin Resonance Spectroscopy*, Van Nostrand Reinhold Company, 1978
- [30] Personal communication, Dr. H. Morris, Liverpool John Moores University
- [31] Personal communication, Prof. C.J. Rhodes
- [32] G.M. Smith, J.C.G. Lesurf, R.H. Mitchell, P.C. Reidi, *Rev. Sci. Instrum.*, 1998, **69**, 3924

Chapter 3

Functionalisation of SBA-15 'in situ': Synthesis & Characterisation

Synopsis

This chapter details the synthesis of SBA-15 templated by the non-ionic triblock copolymer Pluronic P123. The synthesis also incorporates functional groups by co-condensation of trialkoxysilanes with the silica source. The effects of adding the functionalised siloxane on the mesophase product are monitored by electron microscopy, diffraction and porosimetry. A new solid, designated STA-11, a large-pore $Ia\bar{3}d$ cubic bicontinuous phase is formed by specifically controlling the synthesis of functionalised SBA-15.

3.1 Introduction

The ground-breaking work that led to the introduction of the MCM-type mesoporous materials [1 – 3] opened up the field of porous solids to applications in fields of adsorption [4] and catalysis [5] that allowed the inclusion of guest molecules with dimensions an order of magnitude larger than before. A second breakthrough came about when Stucky *et al.* showed that by using non-ionic triblock copolymers as templates in acidic media the formation of an extra large pore analogue of MCM-41, designated SBA-15 (p6mm) [6,7] could be formed. This further expanded the potential range of applications for mesoporous solids to include the inclusion of nanoparticles from 4 – 8 nm [8] and large biomolecules [9].

Recent advancements through using block copolymers in similar acidic media has permitted the preparation of other mesoporous silicas such as SBA-12 (P6₃/mmc), a slightly larger pore analogue of SBA-2 and SBA-16 [10]. Although SBA-12 and SBA-16 (Im3m) are three-dimensionally connected, they consist of large cages connected through smaller windows (HRTEM investigations of SBA-16 indicate that the window size is 2 nm) [10,11]. Therefore a large pore analogue of the bicontinuous cubic phase MCM-48 would be desirable for enhanced molecular transport and an increased pore size has advantages in applications where larger molecules are to be separated, for instance biological molecules, such as proteins [12,13].

The study of amphiphilic block copolymer-templated mesostructure materials is an emerging research area offering great scientific and technological promise. Block copolymers are becoming increasingly widely used as templates for mesoporous materials due to their diverse structural characteristics and low cost amongst others. Manipulation of synthesis variables such as temperature, pH and reaction time can produce materials with well-defined order on the meso-scale using non-ionic block copolymers with different physical properties. However, the work carried out within this chapter does not concentrate on such effects of variable manipulation (with the exception of temperature in section 3.3.1.6) but instead details the effects of co-

condensation of organo-siloxanes introduced during the synthesis on the product properties.

Either ordered or disordered mesoporous solids can be prepared using block copolymers as templates. Disordered mesoporous silica materials templated by non-ionic copolymers have also been reported. The group of Pinnavaia synthesised a family of silica molecular sieves with 'wormhole-like' frameworks, MSU-X materials, with uniform pore diameters in the range of 2 – 6 nm [14] using poly(ethylene oxide) surfactants. Su and co-workers have prepared structures analogous to these MSU-X type materials using $C_{18}EO_{10}$ and $C_{16}EO_{10}$ type surfactants [15].

Typical ordered mesostructured silica materials synthesised using amphiphilic block copolymers are classified into their mesoscale topologies in table 3.1.1. Attard *et al.* reported the synthesis of ordered silica [16] using the non-ionic surfactants octaethylene glycol monododecyl ether ($C_{12}EO_8$ [$C_{12}H_{25}(CH_2CH_2O)_8OH$]) and octaethylene glycol monohexadecyl ($C_{16}EO_8$) in acidic media. Silica mesostructures were prepared from ordered liquid-crystalline mesophases, (mainly small pore (~ 3 nm) hexagonal $p6mm$ phase). Blin *et al.* again using the non-ionic copolymers utilised by Attard under mild acidic conditions with varying surfactant concentration have produced similar structures to Attard with spherical or rod-like particle shapes [15]. The successful synthesis of a new family of mesoporous structures (such as SBA-15) employing non-ionic triblock copolymers in acidic aqueous media have produced [6,7] a well-ordered family of mesoporous silicas. El-Safty *et al.* using Brij 56 ($C_{16}EO_{10}$) as the surfactant and alkanes of variable chain lengths as additives have produced a series of nanostructured silica monoliths (HOM-n) [17,18] with 2-D and 3-D structures with controllable pore size in the region of 3 – 8 nm, and Feng *et al.* [19] report the synthesis of large pore (up to 11 nm) mesoporous silica monoliths templated by non-ionic surfactants Pluronic – F127 and – P123.

Space group	Researcher/Material	Block Copolymer	Remark	Ref.
$\bar{Fm}3m$	FDU-1	EO ₃₉ PO ₄₇ EO ₃₉	Large cage	[20]
	FDU-12	EO ₁₀₆ PO ₇₀ EO ₁₀₆	Ultra large cage	[21]
	HOM-10	C ₁₆ EO ₁₀	Additive alkanes	[18]
$\bar{Im}3m$	HOM-1	C ₁₆ EO ₁₀	Low [surfactant]	[17,18]
	SBA-16	EO ₁₀₆ PO ₇₀ EO ₁₀₆	TMOS over TEOS	[7]
$\bar{Pm}3m$	ST-SBA-16	C ₁₈ EO ₁₀	Small pore, thin wall	[22]
	SBA-11	C ₁₆ EO ₁₀		[7]
$\bar{Pn}3m$	HOM-4	C ₁₆ EO ₁₀	Additive alkanes	[23]
	HOM-7	C ₁₆ EO ₁₀	High [surfactant] or additive alkanes	[17,18,23]
$\bar{Pm}3n$	HOM-9	C ₁₆ EO ₁₀	Additive alkanes	[18]
	SBA-12	C ₁₈ EO ₁₀	Mixed hcp & ccp phases	[7]
$P6_3/mmc$	HOM-3	C ₁₆ EO ₁₀	Medium [surfactant]	[17,18]
	Hodgkins <i>et al.</i>	EO ₁₀₆ PO ₇₀ EO ₁₀₆	Large pore mixed hcp & ccp phases, additive MPTES	[24]
$p6mm$	Attard	C ₁₂ EO ₈ , C ₁₆ EO ₈	Small pore	[14]
	SBA-15	EO ₂₀ PO ₇₀ EO ₂₀	Large pore highly ordered	[6,7]
	Feng	EO ₁₀₆ PO ₇₀ EO ₁₀₆	Organic additives	[19,25]
	CMI-1	C ₁₆ EO ₁₀		[15]
	HOM-2	C ₁₆ EO ₁₀	Medium [surfactant]	[17,18,23]
	MSU-H	EO ₂₀ PO ₇₀ EO ₂₀	Neutral pH	[26,27]
$\bar{Ia}3d$	FDU-5	EO ₂₀ PO ₇₀ EO ₂₀	MPTMS, ethanol evaporation	[28]
	FDU-5	EO ₂₀ PO ₇₀ EO ₂₀	Post-solvothermal synthesis	[29]
	Hodgkins <i>et al.</i>	EO ₂₀ PO ₇₀ EO ₂₀	Additive MPTES	[24]
	Chan	EO ₁₇ MA ₂₃		[30]
	Flodstrom	EO ₂₀ PO ₇₀ EO ₂₀	Inorganic salts	[31]
	Wright	EO ₂₀ PO ₇₀ EO ₂₀	MPTES	[32]
	KIT-6	EO ₂₀ PO ₇₀ EO ₂₀	Additive butanol	[33]
	Schüth	EO ₂₀ PO ₇₀ EO ₂₀	Vinyl, inorganic salts	[34]
	Che <i>et al.</i>	EO ₂₀ PO ₇₀ EO ₂₀	MPTES	[35]
	HOM-5	C ₁₆ EO ₁₀	Medium [surfactant]	[17,18,23]
L	HOM-6	C ₁₆ EO ₁₀	Higher [surfactant]	[23]
	Wiesner	PI-b-PEO	Organically modified aluminosilicate	[36]

Table 3.1.1. Ordered mesoporous silicas templated by non-ionic block copolymers

In this chapter we describe the synthesis of a large-pore bicontinuous cubic material analogous to that of MCM-48. This new mesoporous silica was independently discovered by two groups; Wright and co-workers and Zhao co-workers and is designated STA-11 (St. Andrews) [32] and FDU-5 (Fudan) [28] respectively with a pore size in the region of 80 Å. Since the discovery of the large-pore $Ia\bar{3}d$ cubic material various groups have now also synthesised this material with the majority using the common template of Pluronic P123 – a non-ionic poly(alkylene oxide) copolymer surfactant consisting of poly(ethylene oxide) (PEO) and poly(propylene oxide) (PPO) moieties in the ratio $EO_{20}PO_{70}EO_{20}$ – in the synthesis. The ability to functionalise SBA-15 *in situ* with organo-siloxanes or the addition of organic/inorganic additives to the controlled synthesis in the sol-gel phase allows a change of the product from hexagonal SBA-15 to the cubic $Ia\bar{3}d$ structure (figure 3.1.1). So far, no evidence for the occurrence of a phase transformation is observed, unlike that for the phase transformation of hexagonal MCM-41 to cubic MCM-48 [37]. Within this chapter the effect of the functional group on the micellar packing geometry is detailed – the precise mechanism of the modification of the surfactant/silica geometry remains an open question.

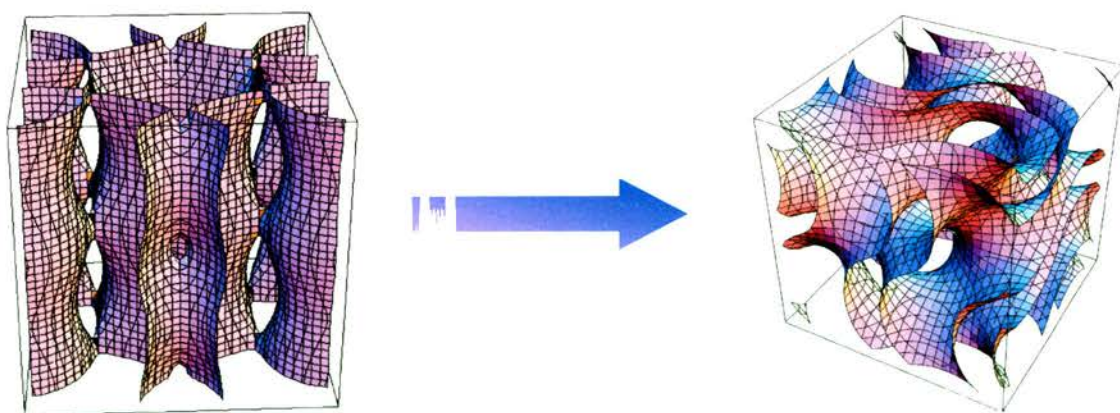


Figure 3.1.1. Phase from (left) SBA-15 – hexagonal $p6mm$ to (right) large pore cubic $Ia\bar{3}d$ upon organo-siloxane and/or additives to the direct synthesis. Solid region showing silica wall.

Also described within this chapter are the characterisation of Pluronic P123 templated functionalised-mesoporous materials by diffraction, microscopy and adsorption

properties together with other chemical analyses. A new method developed for the quantification of accessible thiol groups is described. In addition simulation of STA-11 complementing the experimental data is given.*

3.2 Experimental

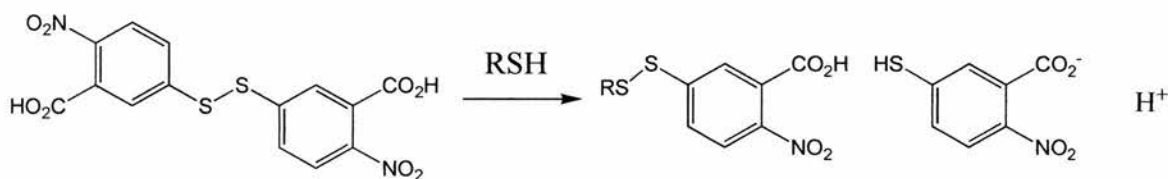
Synthesis of organo-functionalised silicas using Pluronic P123

Organically-modified molecular sieves were prepared by the co-condensation of both tetraethylorthosilicate and trialkoxysilanes. The general procedure adopted was similar to that reported for SBA-15 [7]. The non-ionic triblock copolymer Pluronic P123 (EO₂₀-PO₇₀-EO₂₀, MW_{av.} 5750; BASF) was used as the surfactant template and tetraethylorthosilicate (TEOS, 98% Aldrich) was the source of the majority of the silica. The organo-siloxanes in the form (EtO)₃Si(CH₂)₃-X, where X denotes the groups -SH (3-mercaptopropyltriethoxysilane, 95%, Avacado), -CN (3-cyanopropyltriethoxysilane, 95%, Aldrich) and -Cl (3-chloropropyltriethoxysilane, 95%, Aldrich) and (EtO)₃Si-Ph (Phenyltriethoxysilane, 98%, Aldrich) are introduced to the sol-gel at concentrations of 0 - 10 mole % (based on silica). Molar compositions of the sol-gels were (1-x) Si(OEt)₄ : x (EtO)₃Si(CH₂)₃X/(EtO)₃SiPh : 0.017 P123 : 2.9 HCl : 200 H₂O, 0 ≤ x ≤ 0.10. The surfactant was dissolved in the acidic media and stirred at 313 K. TEOS and the organo-siloxanes were added simultaneously and the mixture stirred for 24 h to allow the onset of hydrolysis and the mesostructure formation to take place. Finally the mixture was transferred to a Teflon bottle and hydrothermal treatment applied at 373 K for 48 h enabling further condensation of the silica framework. The resulting solids were washed with H₂O, filtered, air dried and rendered porous by either calcination (N₂ 823 K, 4 h; O₂ 823 K, 4h) or solvent extraction (3 washings: refluxing with EtOH 50 ml/g, 8 h).

* The author would like to point out that the details of calculation of simulation are not given here. Simulation was in collaboration with Prof. M.W. Anderson (UMIST).

Quantifying the accessibility of thiols within mesoporous silica with Ellman's Reagent

To determine the accessibility of the -SH groups included during the synthesis, extracted propyl-thiol functionalised mesoporous silicas were analysed using Ellman's reagent [38]. The method has been adapted from Badyal *et al.* [39]: it can be used quantitatively because the disulphide within 5,5'-dithiobis(2-nitrobenzoic acid) (Ellman's reagent; 99% Aldrich) reacts with the propyl-thiol groups bound to the silica framework to form an anion which exhibits a strong yellow colour absorbing at 412 nm [Scheme 3.2.1].



Scheme 3.2.1. The disulphide within Ellman's reagent (left) reacts with the thiol group to give an intense yellow anion that absorbs at 412 nm

In a typical analysis, Ellman's reagent, 0.1 g, in excess (250 μ mol) is dissolved in 25 ml MeOH. A known amount of mesoporous solid (based on the expected moles of SH present) was added to a 100 ml volumetric flask with *ca.* 20 ml MeOH. Ellman's solution was added together with 500 μ l of N,N-diisopropylethylamine (DIPEA; 99% Aldrich) and the flask was shaken for 30 mins. The solid was then filtered off and the filtrate transferred to a 250 ml volumetric flask. The solid was washed with MeOH and the filtrate added to the 250 ml volumetric flask before bringing the volume to 250 ml with MeOH. A 10 ml aliquot was taken and 90 ml MeOH added to reduce further the concentration for UV analysis. The values are compared against those from the reaction of known amounts of cysteine in methanol. Typically between 50 μ mol and 200 μ mol of SH are quantified in this way.

3.3 Results & Discussion

The results within this chapter have been divided into sections depending on the organic functionality used in the synthesis. Each division is sub-divided into the characterisation techniques employed to characterise such syntheses. Details of the experimental parameters for the technique are given in chapter 2.

3.3.1 Thiol-functionalised mesoporous silica templated by P123.

3.3.1.1 Elemental analysis and Ellman's quantification

Extracted silicas templated by P123 surfactant and functionalised by co-condensation using different amounts of 3-Mercaptopropyltriethoxysilane (MPTES) have been analysed (table 3.3.1.1.1). The trialkoxysilane groups are incorporated into the final silica product in ratios close to those in the sol-gel synthesis.

Non-ionic surfactant	SH loading (based on SiO ₂)	C content	H content	S content	S _{expected}
P123	2%	11.58%	2.65%	0.81%	0.76%
P123	5%	14.05%	3.04%	1.84%	1.91%
P123	7%*	11.21%	2.47%	2.49% ⁺ 2.51% ⁺	2.58% 2.58%
P123	7%#	14.44%	3.26%	2.57%	2.65%

*313 K hydrolysis step; #323 K hydrolysis step; ⁺repeat values

Table 3.3.1.1.1. Elemental analysis of extracted propyl-thiol functionalised mesoporous silica templated by P123

The accessible thiol content in extracted materials prepared with 2 – 7% MPTES has been determined using Ellman's reagent. Since the method of functionalisation is by direct co-condensation of the trialkoxysilane it may be that not all of the organics are orientated within the channels, extending from the pore walls. A fraction may be included within the silica walls and therefore will not be accessible to reagents diffusing through the porous network. By comparison, post-synthetic modification (covalent bonding to the accessible silanols by hydrolysis and condensation) would be expected to give a very high percentage of accessible groups. Knowing the accessible fraction of the functional group rather than the total incorporated in the sol-gel synthesis is important when using such functional groups within materials to further functionalise the material or in assessing the specific activity of functional sites in adsorption or catalytic applications.

The analyses indicate (table 3.3.1.1.2) that at least 54 – 76 % of the total incorporated thiol groups are accessible to Ellman's reagent, suggesting that at least this fraction is attached to the internal surface of the materials. Considering that a large fraction of the MPTES are accessible these solids would be suitable for applications requiring such functional groups, say for heavy metal extraction or through further reaction, as sulphonic acids for acid catalysis.

Sample*	% SH accessibility
2% MPTES	54
5% MPTES	76
#7% MPTES	72

*All samples extracted; #hydrolysis temperature – 313 K.

Table 3.3.1.1.2. Quantification of thiol groups via Ellman's reagent for extracted MPTES-functionalised materials templated by P123

In the analysis, a known amount of solid is treated according to the expected maximum content of thiols and compared to a standard (cysteine) where a known amount of the thiol group is measured. The mesostructure is retained after Ellman's

analysis with no degradation to the solid (figure 3.3.1.1.1). The isotherm for a previously treated calcined 7% MPTES material is clearly type IV with a well-defined capillary condensation step with a high uptake of N_2 and a narrow pore size distribution. The UV analyses are shown for the Ellman's treated solids in figure 3.3.1.1.2. The molecule responsible for the UV absorbance is due to the disulphide group within the Ellman's reagent reacting with accessible thiol groups to form an anion which has as intense yellow colour which absorbs at 412 nm [38,39].

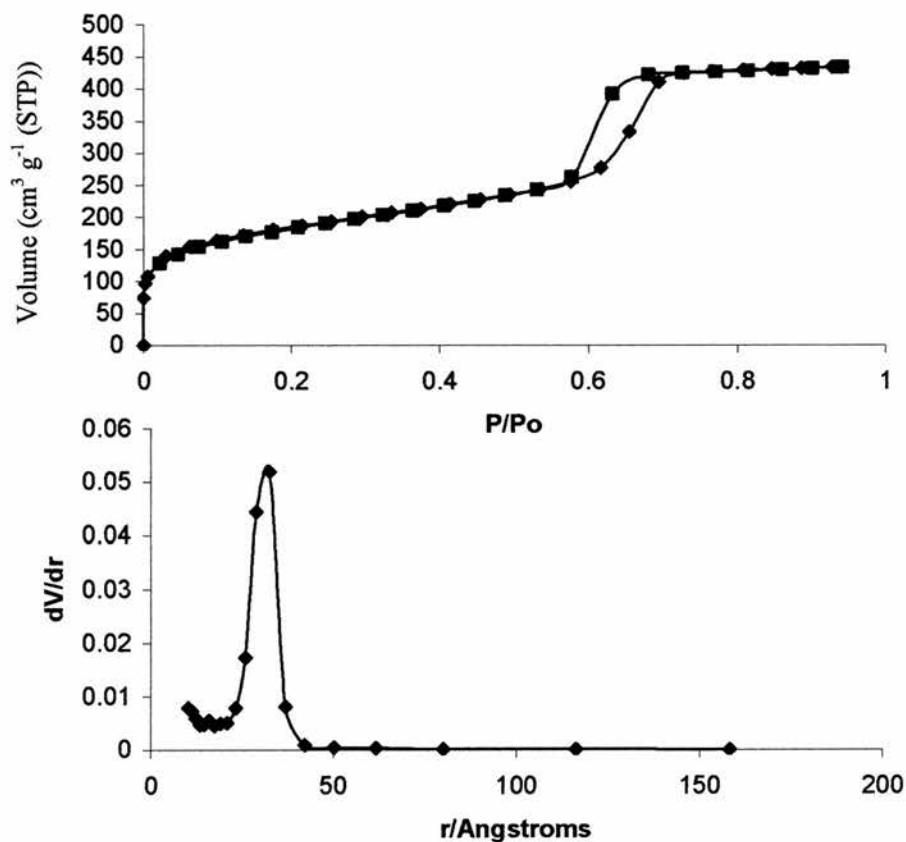


Figure 3.3.1.1.1. N_2 isotherm of a previously Ellman's treated calcined mesoporous silica (top) together with the pore size distribution curve (bottom) showing that the mesostructure is obtained after Ellman's analysis

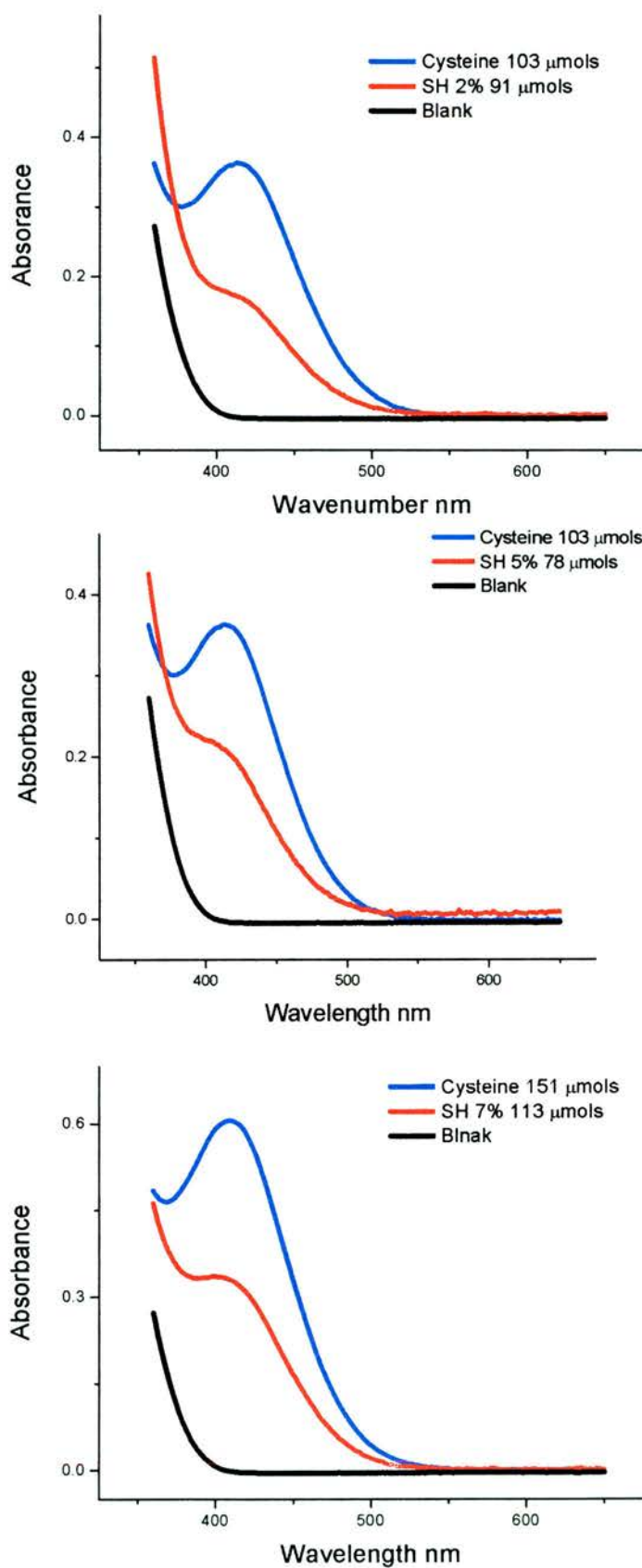


Figure 3.3.1.1.2. Examples of raw data used for the quantification of MPTES solids treated with Ellman's reagent through comparison with cysteine as a standard. From top to bottom: 2% MPTES; 5% MPTES and 7% MPTES.

It can be seen in figure 3.3.1.1.3 that as the loading of MPTES increases from 2% - 7% that the total MPTES groups accessible to the Ellman's reagent increases as expected considering that more thiol groups are added in the initial synthesis. However, the percentage of the accessible MPTES groups compared to the total amount incorporated for individual solids varies. The 2% MPTES solid has just over half of the functional groups accessible whereas the 5% and 7% have around $\frac{3}{4}$ accessible to the Ellman's reactant. Repeat results show similar accessibilities with an error margin of $\pm 7\%$.

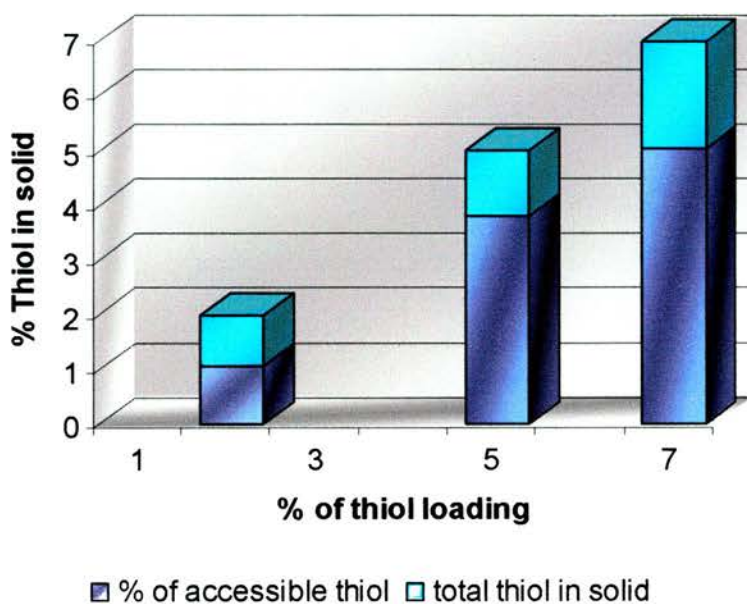


Figure 3.3.1.1.3. Quantification of MPTES groups as a percentage of total MPTES groups within extracted samples.

3.3.1.2 X-ray diffraction (XRD)

As described in chapter 2, well ordered mesoporous solids possess an array of pores and walls therefore XRD identifies the long-range order by reflections corresponding to interplanar spacings dictated by the unit cell. As a consequence of the large unit cell (and interplanar spacings) of mesoporous SBA-15 the angles at which diffraction maxima occur are low (i.e. below $4^\circ 2\theta$) (figure 3.3.1.2.1). SBA-15 has its main characteristic (1,0) peak at $\sim 0.95^\circ 2\theta$ with two smaller peaks at $\sim 1.55^\circ$ (1,1) and 1.76° (2,0) 2θ , the exact position depending on the unit cell a dimension.

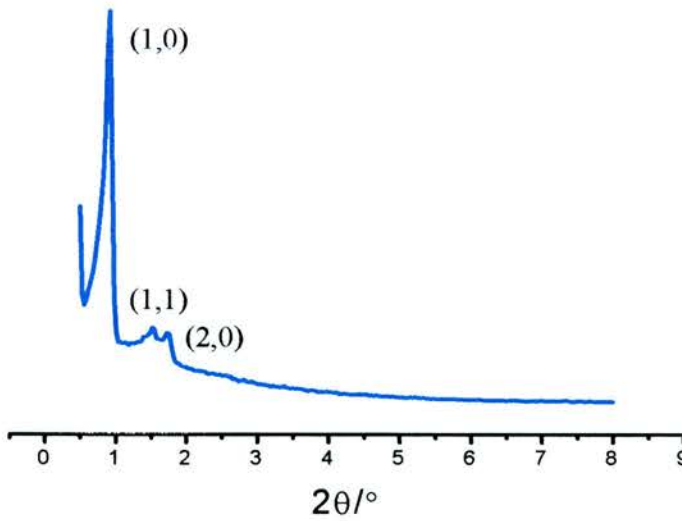


Figure 3.3.1.2.1. XRD diffraction pattern of SBA-15 showing peaks at low angle with no intensity maxima after $2^\circ 2\theta/^\circ$

Functionalising SBA-15 directly with 0 – 10% MPTES results in a series of mesoporous silicas with the amorphous silica network possessing both ordered and disordered mesopores depending on the organic loading. In addition the symmetry of the ordered mesophase silica varies from the expected hexagonal $p6mm$ to cubic $Ia\bar{3}d$. The low-angle XRD patterns (figure 3.3.1.2.2) reveal typical SBA-15 type diffractograms for pure siliceous solids and for silica prepared with 2% MPTES added to the synthesis. A lower degree of long-range order can be attributed to the silica solid prepared with 5% MPTES, and the hexagonal lattice parameter is determined using only the (1,0) reflection, with no observable secondary peaks. SBA-15 functionalised *in situ* with 7% MPTES gives an X-ray pattern which no longer corresponds to the hexagonal $p6mm$ symmetry but instead is characteristic of silica with cubic $Ia\bar{3}d$ symmetry. There is a shoulder on the first major peak and in addition further diffracted intensity at *ca.* $2^\circ 2\theta$. This new solid was designated **STA-11** and further characterisation is presented later in this section. The 10% MPTES solid is again poorly ordered and no secondary peaks are observed. HRTEM micrographs later (section 3.3.1.4) reveal there to be a cubic phase present.

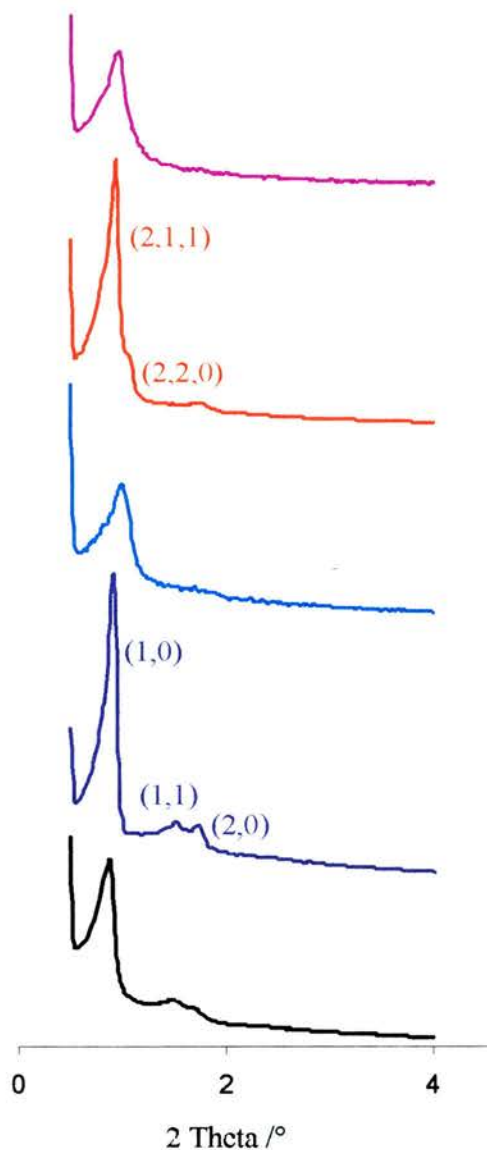


Figure 3.3.1.2.2. X-ray diffraction patterns of propyl-thiol functionalised mesoporous silica templated by Pluronic P123. Bottom to top: SBA-15-pure silica; 2% added MPTES; 5% added MPTES; 7% added MPTES (STA-11) and 10% added MPTES.

The solid prepared with 2% MPTES gives a diffractogram which indicates better long-range order than for the corresponding pure silica. Although a slight decrease in order might be expected upon direct functionalisation, the MPTES groups must readily co-condense with TEOS without disruption of the silica network. If the hydrophobic interaction of the silicate network with the core PPO portion of the surfactant micelles is enhanced with MPTES addition then it could give rise to the

long-range order being increased for the MPTES-containing solids over that of the pure siliceous solid [40].

Using the positions of the major reflections – (10) for p6mm symmetry (pure siliceous; 2% and 5% MPTES solids) and (211) for Ia $\bar{3}$ d symmetry (7% and 10% MPTES solids) – gives a_{hex} and a_{cub} unit cell parameters of 101 – 117 Å and 223 – 230 Å, respectively (table 3.3.1.2.1). The general trend is for the unit cell size to decrease as the level of co-condensing organo-siloxane increases. This may indicate that hydrophobic interactions between the organic-functionality/silica and P123 copolymer surfactant is strong enough to ‘pull-in’ the silica framework towards the surfactant micelle core.

Sample	$^{\circ} / 2\theta$	XRD interplanar d spacing / Å	Unit cell / Å
Pure siliceous	0.87	102 ^a	117 ^c
2% MPTES	0.92	96 ^a	111 ^c
5% MPTES	1.01	88 ^a	101 ^c
7% MPTES	0.94	94 ^b	230 ^d
10% MPTES	0.97	91 ^b	223 ^d

Interplanar spacing – ^a d_{100} , ^b d_{211} ; ^chexagonal lattice parameter, ^dcubic lattice parameter

Table 3.3.1.2.1. Measured interplanar spacings and derived unit cell parameters of pure siliceous and propyl-thiol functionalised mesoporous silica templated by P123 by XRD

The order of STA-11 (7% SH) is indeed high by XRD. No decrease in the long-range order is observed upon calcination and the mesostructure is retained, albeit unit cell contraction – due to further condensation of the silica at high temperatures – is noticed as expected (figure 3.3.1.2.3).

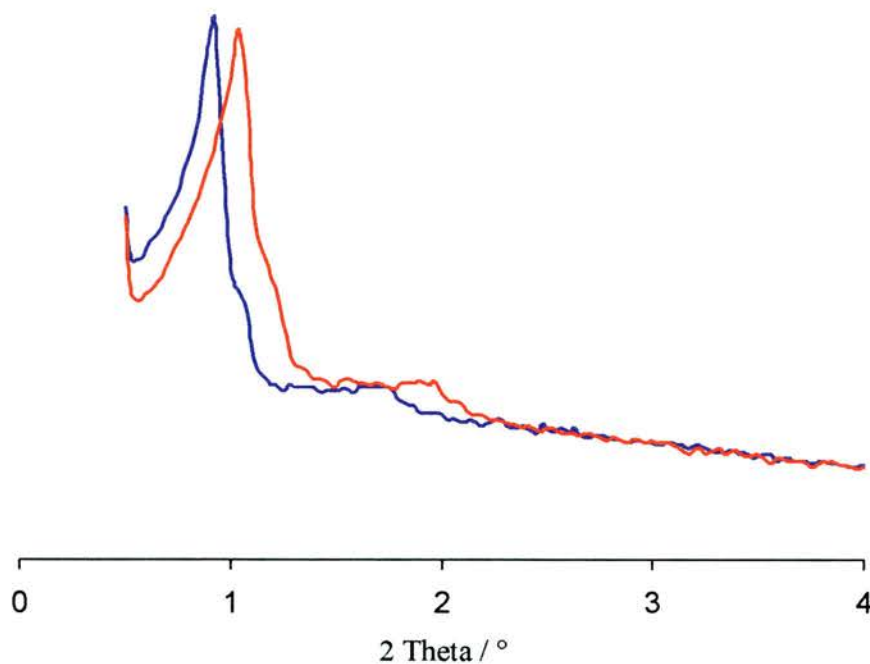
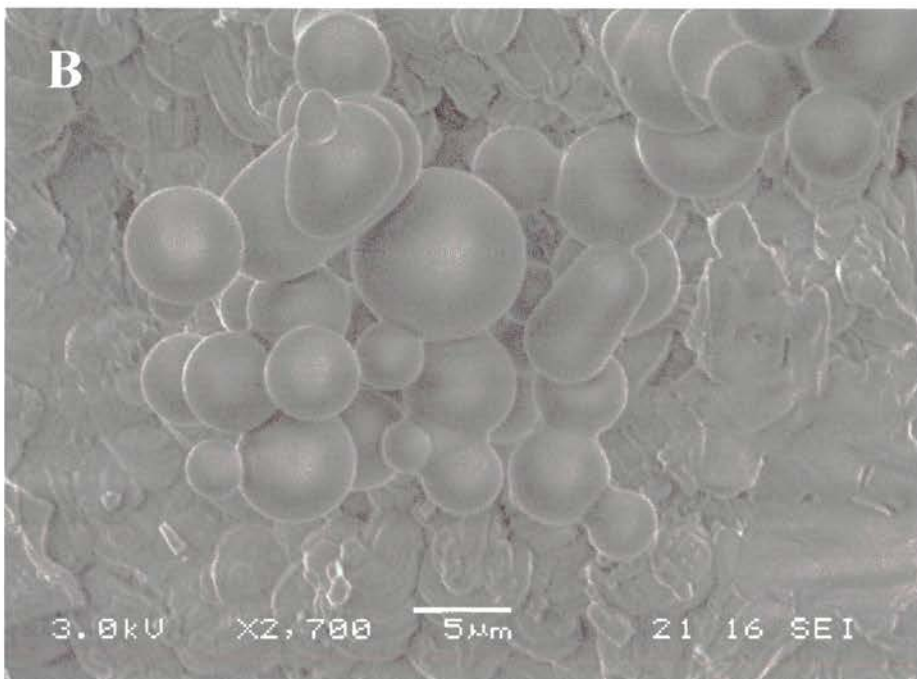
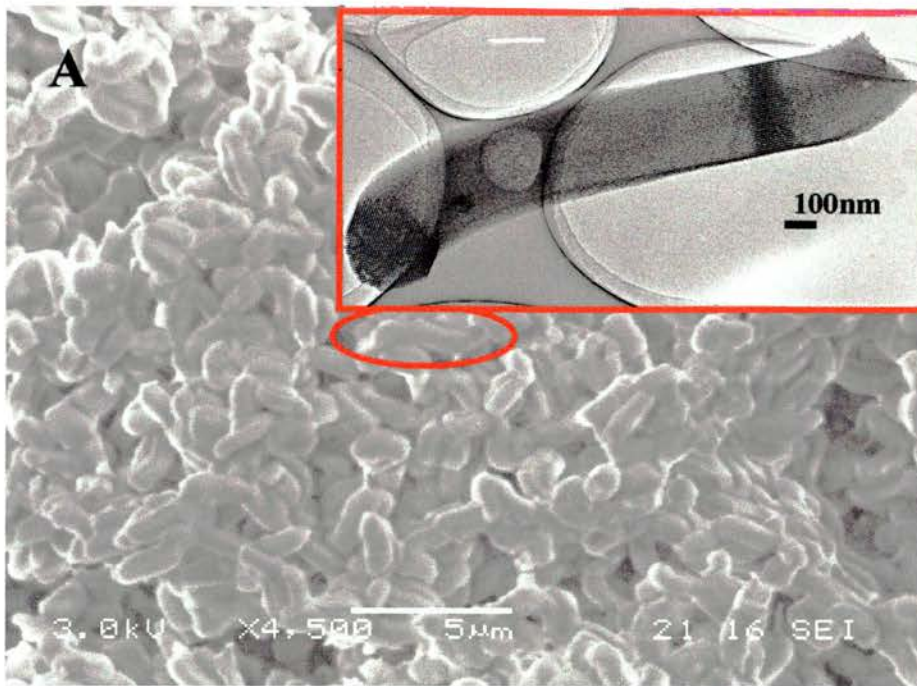


Figure 3.3.1.2.3. XRD diffractograms of **extracted** STA-11 and **calcined** STA-11.

3.3.1.3 SEM

Scanning electron microscopy reveals that a change in morphology is observed as the product changes from hexagonal SBA-15 to cubic STA-11 as a result of introducing MPTES to the syntheses (figure 3.3.1.3.1). SBA-15 is reported to have an elongated prismatic morphology [41] and this can be seen for the pure siliceous material and for the sample containing 2% MPTES (figure 3.3.1.3.1a). Solids with higher thiol contents have a spherical morphology with particles in the region of 1 – 10 μm (figure 3.3.1.3.1b – d). The change in morphology occurs under the same conditions of co-condensing MPTES that give rise to a change in the mesophase product. The cubic MCM-48 is also reported to possess a spherical morphology [42].



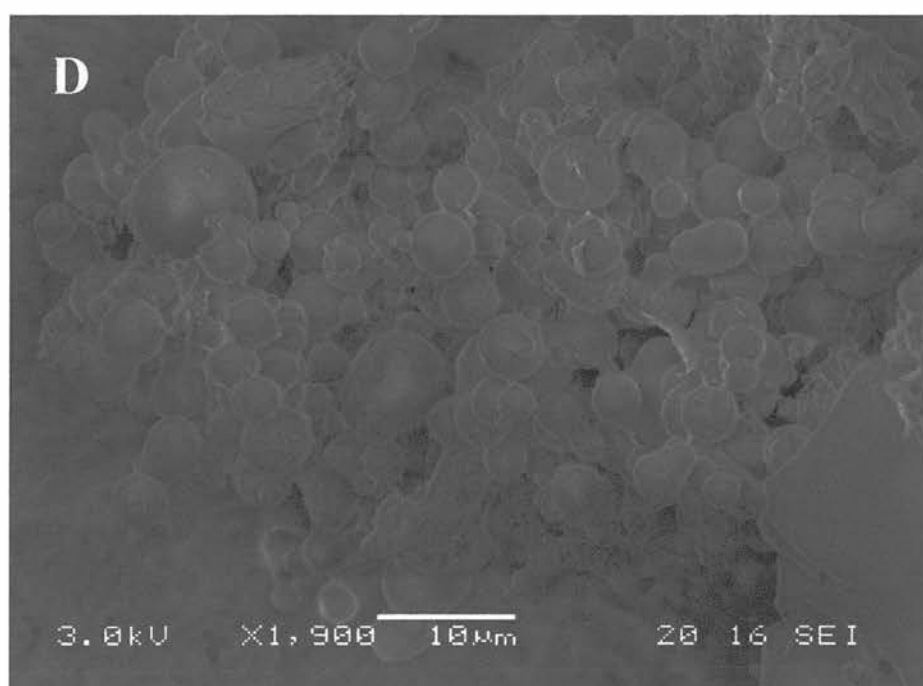
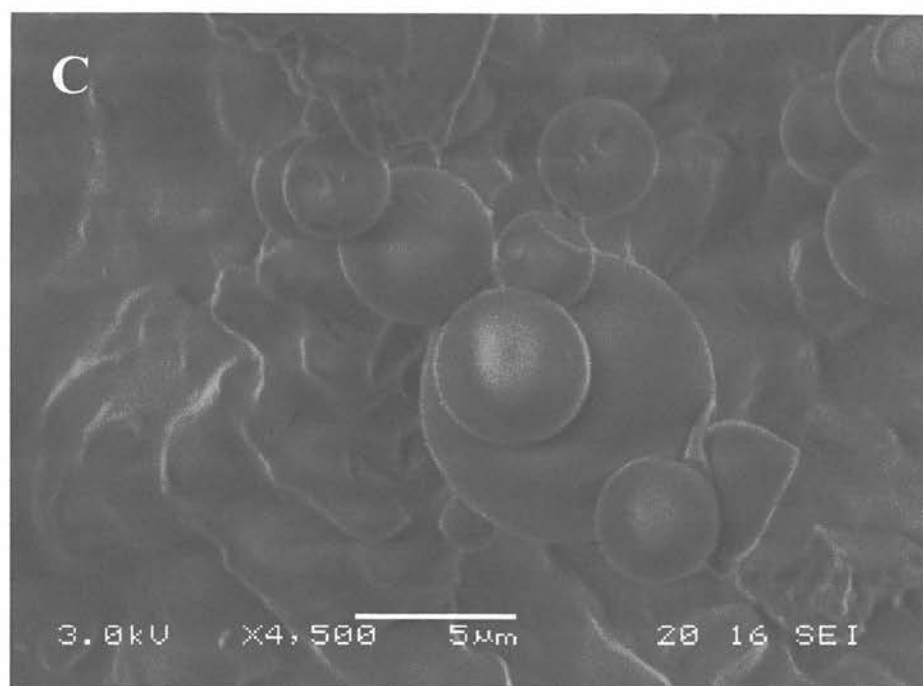


Figure 3.3.1.3.1. SEM micrographs of propyl-thiol functionalised P123 templated materials. (A) 2% SH (bottom a TEM micrograph with which the highlighted morphological shape can be attributed to); (B) 5% SH, (C) 7% SH and (D) 10% SH

3.3.1.4 TEM

High resolution transmission electron microscopy confirms the product mesophase outcome when varying the levels of MPTES during the sol-gel synthesis. The pure siliceous SBA-15 and the 2% MPTES solid gives the expected typical micrographs associated with hexagonal $p6mm$ symmetry, and so are consistent with the XRD patterns. Both the pure siliceous and 2% thiol-containing samples show a degree of order that reflects the quality of the long-range order found by XRD (figure 3.3.1.4.1a – f). Upon increasing the loading of MPTES to 5% the structure (as observed by TEM) is best described as poorly ordered, as expected from the XRD. However both hexagonal and cubic domains can be observed by TEM, although no particles were found containing both phases even after extensive examination. From TEM the unit cell parameters of both phases can be measured directly (figure 3.3.1.4.1h – i). Materials containing 7% MPTES in the synthesis where the hydrolysis temperature was maintained at 313 K show well-defined cubic $Ia\bar{3}d$ symmetry consistent with the XRD pattern. The micrographs of the 7% MPTES containing solids (figure 3.3.1.4.1j – l) are representative of the bulk material and the effect of the thiol-loading is found to be reproducible: samples with SH contents of 2.49, 2.51 and 2.57% all show the cubic geometry by TEM. This is evidence of a new mesoporous silica templated by non-ionic triblock copolymers that is a large pore analogue to that of MCM-48. Materials possessing a 10% SH loading have a much more poorly ordered structure by TEM observation, with no predominance of a clear hexagonal or cubic phase predominance. TEM does show that cubic domains are present in the sample (figure 3.3.1.4.1M – N) and so the indexing of the lattice parameters by TEM (table 3.3.1.4.1) are given for the cubic symmetry.

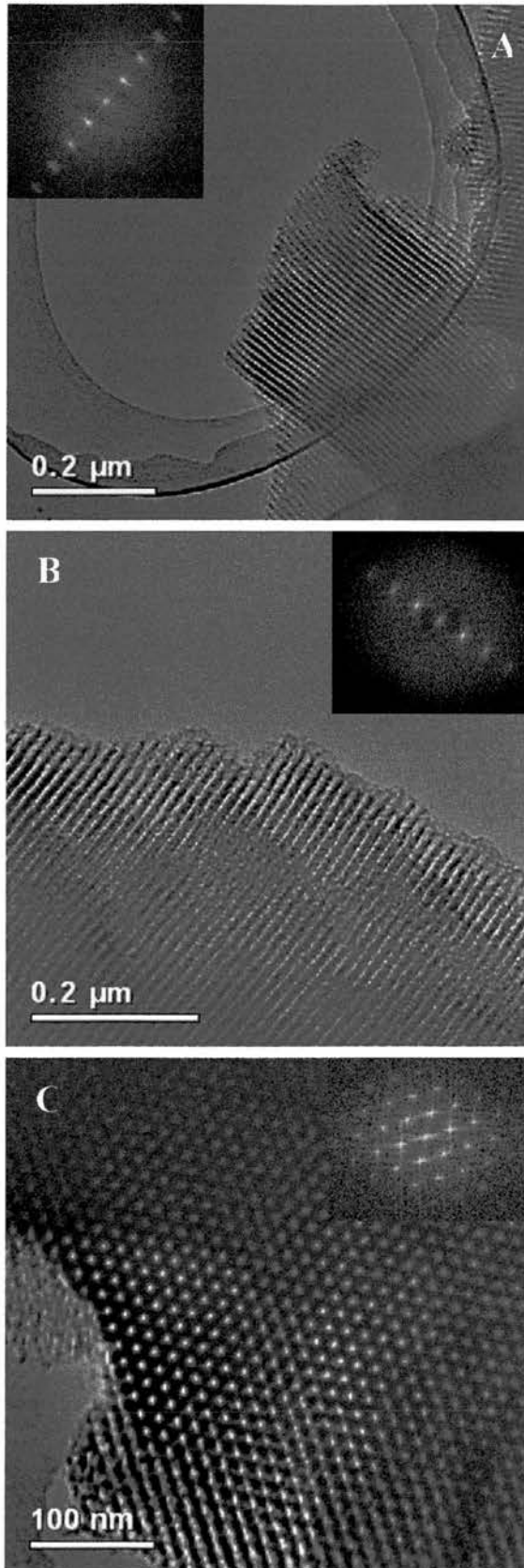


Figure 3.3.1.4.1. HRTEM micrographs of pure siliceous SBA-15 templated by P123 with pores running perpendicular (A,B) and parallel (C) to the incident beam observing high quality material

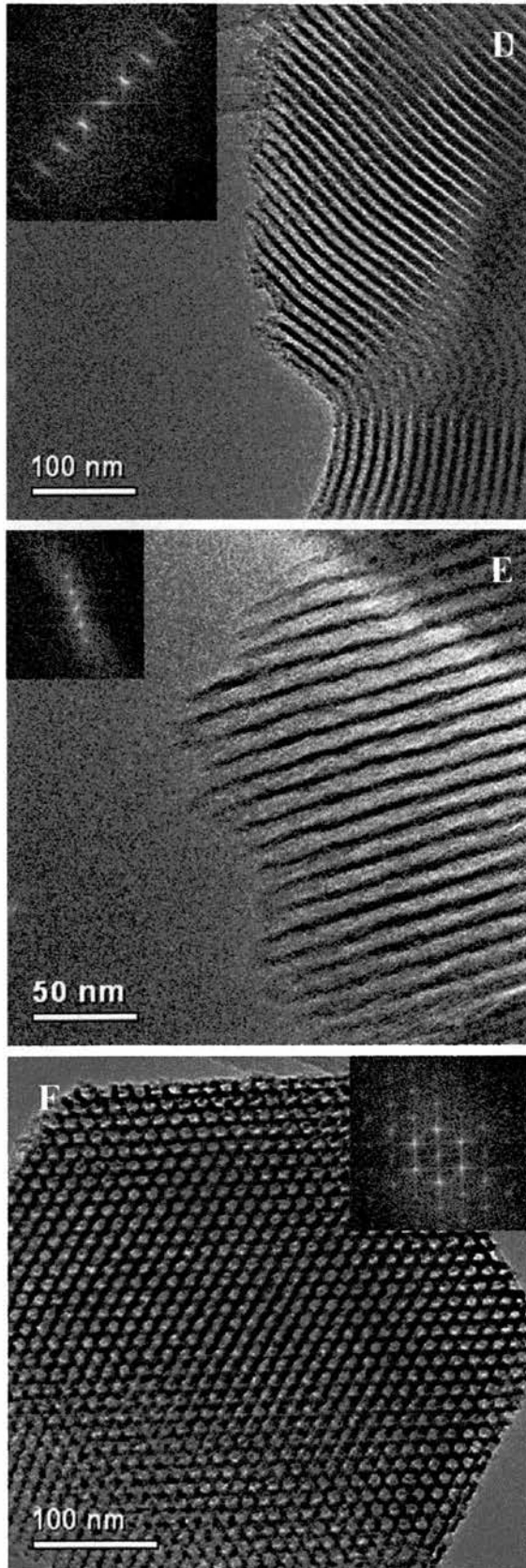


Figure 3.3.1.4.1. HRTEM micrographs of P123 templated SBA-15 with 2% MPTES loading. (D,E) Viewing the pores perpendicular to the incident electron beam and (F) pores parallel to the beam again retaining meso-structural quality

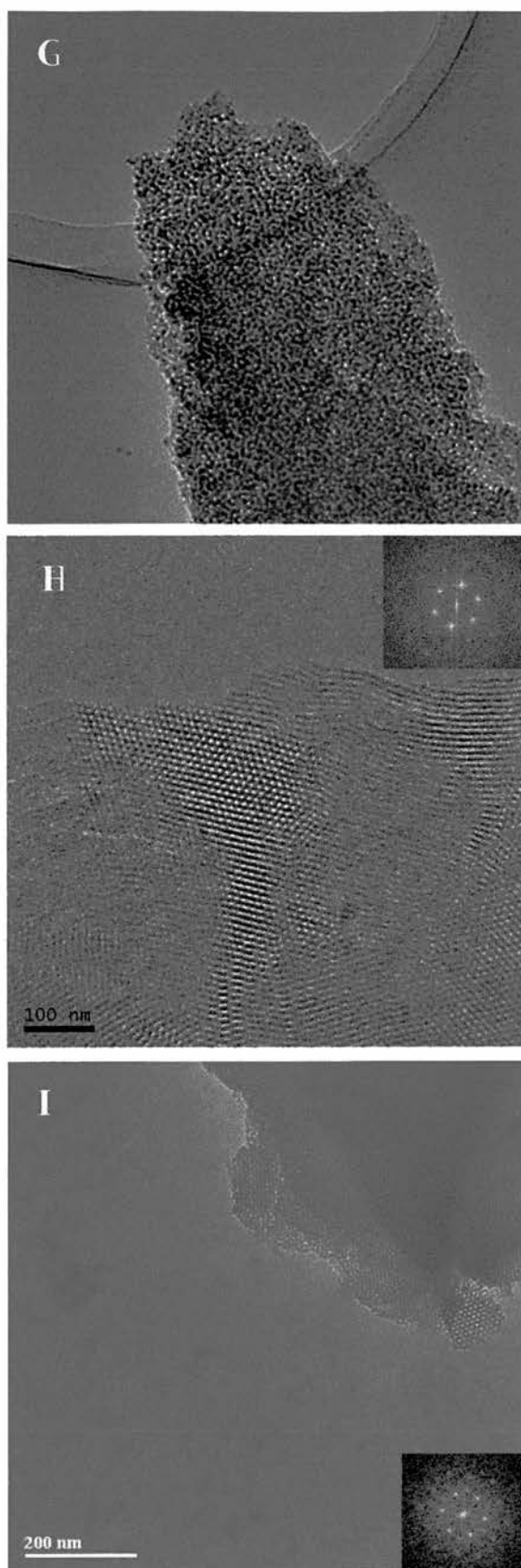


Figure 3.3.1.4.1. HRTEM micrographs of P123 templated solids loaded with 5% MP TES showing (G) amorphous disorder (scale bar as H); (H) the hexagonal phase viewing both pores parallel $[0,0,1]$ and perpendicular $[1,1,0]$ to the incident beam and (I) the cubic phase viewing the $[1,1,1]$ zone axis.

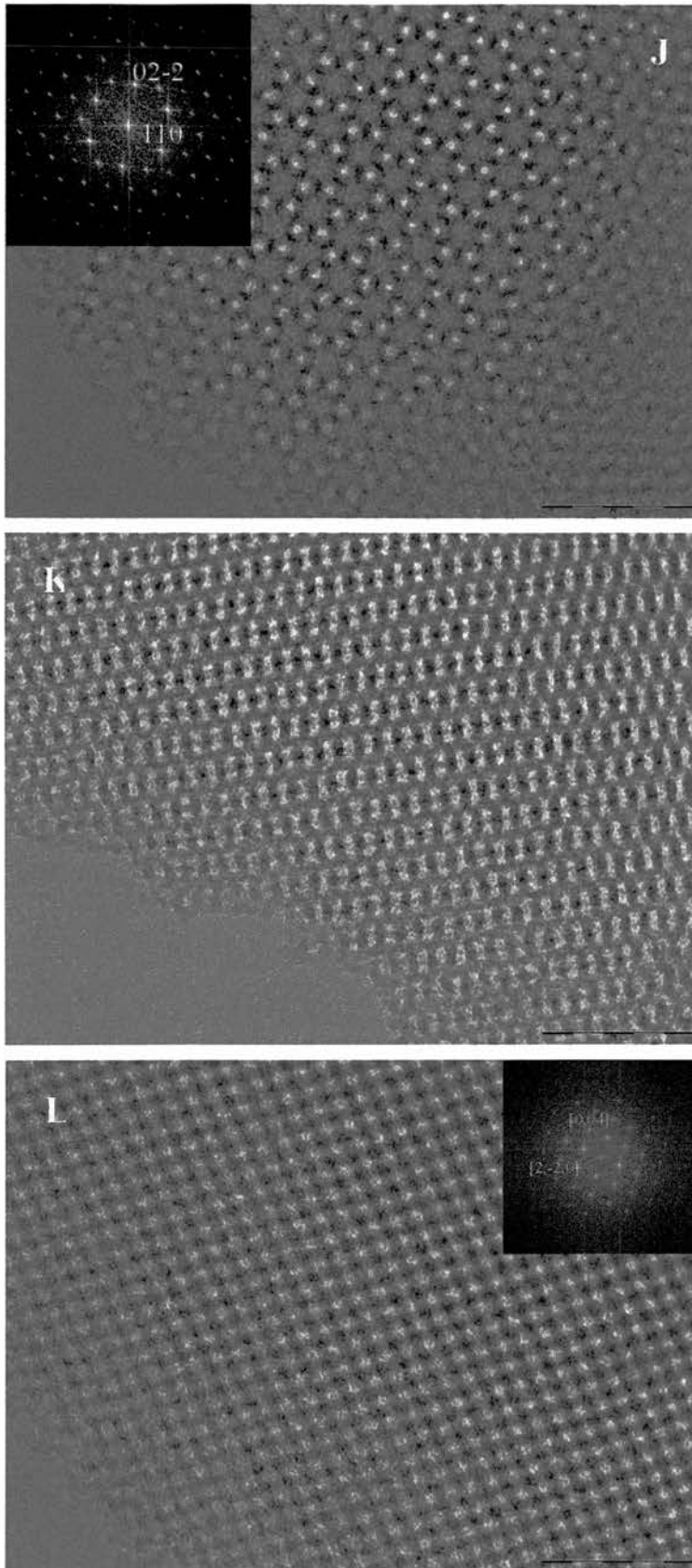


Figure 3.3.1.4.1. HRTEM micrographs of STA-11 (7% MP TES) observing high quality cubic materials viewing the zone axes (J) $[1,1,1]$; (K) $[3,1,1]$ and (L) $[1,1,0]$ parallel to the incident electron beam

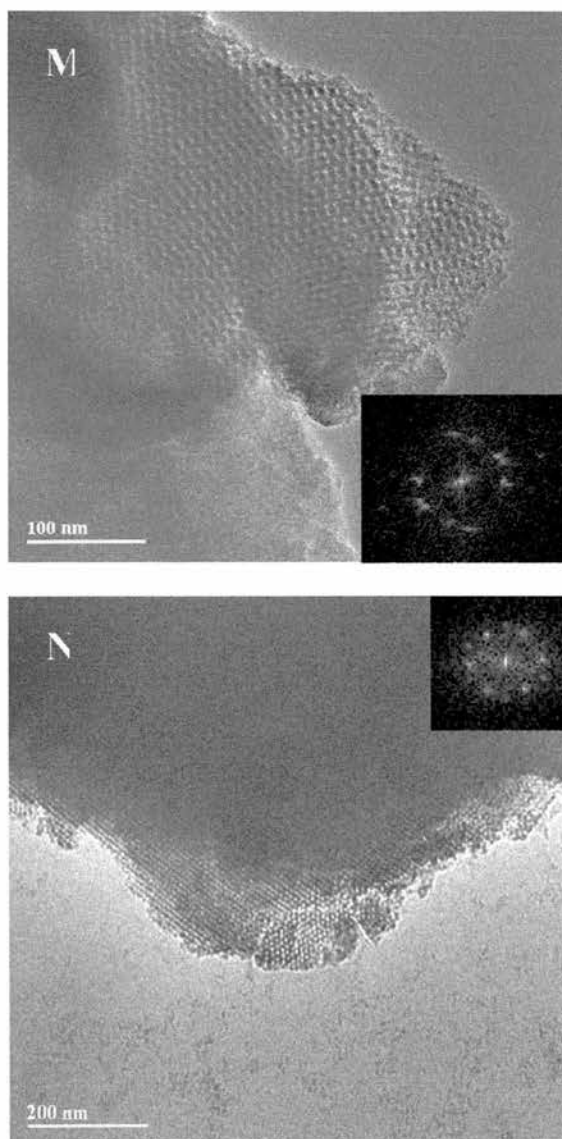


Figure 3.3.1.4.1. HRTEM micrographs of P123 templated silicas with 10% MP TES viewing the [311] zone axis (M) and the [111] zone axis (N) parallel to the beam

Sample	Unit cell / Å TEM	Unit cell / Å XRD
Pure siliceous	119 ^a	117 ^a
2% MPTES	119 ^a	111 ^a
5% MPTES	102 ^a	101 ^a
	227 ^b	
7% MPTES	230 ^b	230 ^b
10% MPTES	205 ^b	223 ^b

Unit cell calculated using ^ahexagonal and ^bcubic lattice parameters.

Table 3.3.1.4.1. Unit cell parameters of pure siliceous and propylthiol functionalised mesoporous silica templated by P123 by HRTEM and for comparison by XRD

3.3.1.5 N_2 Adsorption

Nitrogen adsorption isotherms for both extracted and calcined samples prepared either as the pure siliceous analogue or by MPTES addition to the synthesis typically display type IV isotherms with well defined hysteresis. Further analysis of the isotherms are given in table 3.3.1.5.1 and include specific surface areas calculated from the BET model (at regions where the BET equation is applicable) and also pore size distributions measured on the adsorption branch using the De Boer model. Considering the extracted samples the isotherms (figure 3.3.1.5.1) of both the pure siliceous sample and the 2% MPTES material show a well-defined adsorption with a similar high uptake of N_2 and a sharp capillary condensation step at P/P_0 of ca. around 0.85. The sharp uptake over a short P/P_0 range gives an indication to the high degree of order of the material. The pore size distribution taken from the mode (or the maximum) of the pore size distribution curve (figure 3.3.1.5.2) shows that the 2% MPTES containing material has a slightly larger pore size than that of the pure siliceous analogue indicating that the 2% MPTES containing sample has thinner walls considering similar unit cells. The 5% MPTES functionalised material has a much lower uptake of N_2 by comparison and together with the broad pore size distribution

underline the evidence of XRD and HRTEM pointing to the reduction in ‘quality’. The isotherm shows a poorly-defined capillary condensation step over a broad P/P_0 range due to the broad distribution of pore sizes of the two-phases together with amorphous regions. The pore size is smaller than that for the ordered hexagonal pure siliceous and 2% MPTES materials. The broad pore size distribution is thought to include both smaller pores from the cubic structure and larger pores from the hexagonal phase. Upon 7% MPTES loading the isotherm is again a well-defined type IV isotherm with a high N_2 uptake. However, the region of sharp capillary condensation is in a region lower than for typical SBA-15, at P/P_0 around 0.75 for the cubic $Ia\bar{3}d$ structure. In addition, the capillary condensation is obtained at higher values than that reported for similar MCM-48 [42-45] where the condensation step occurs at P/P_0 around 0.3. Nitrogen isotherms therefore shows STA-11 to have greater pore sizes than the corresponding MCM-48. Materials with 10% MPTES loading results in a reduced adsorption capacity. The hysteresis loop is less well-defined and smaller than that for materials with lower thiol-contents. The loss of mesoporosity must result from a disruption to the surfactant aggregates forming poorly ordered micelles with less in volume for this high level of organic functionality. Similar systems have shown equivalent effects when including MPTMS to the synthesis [46].

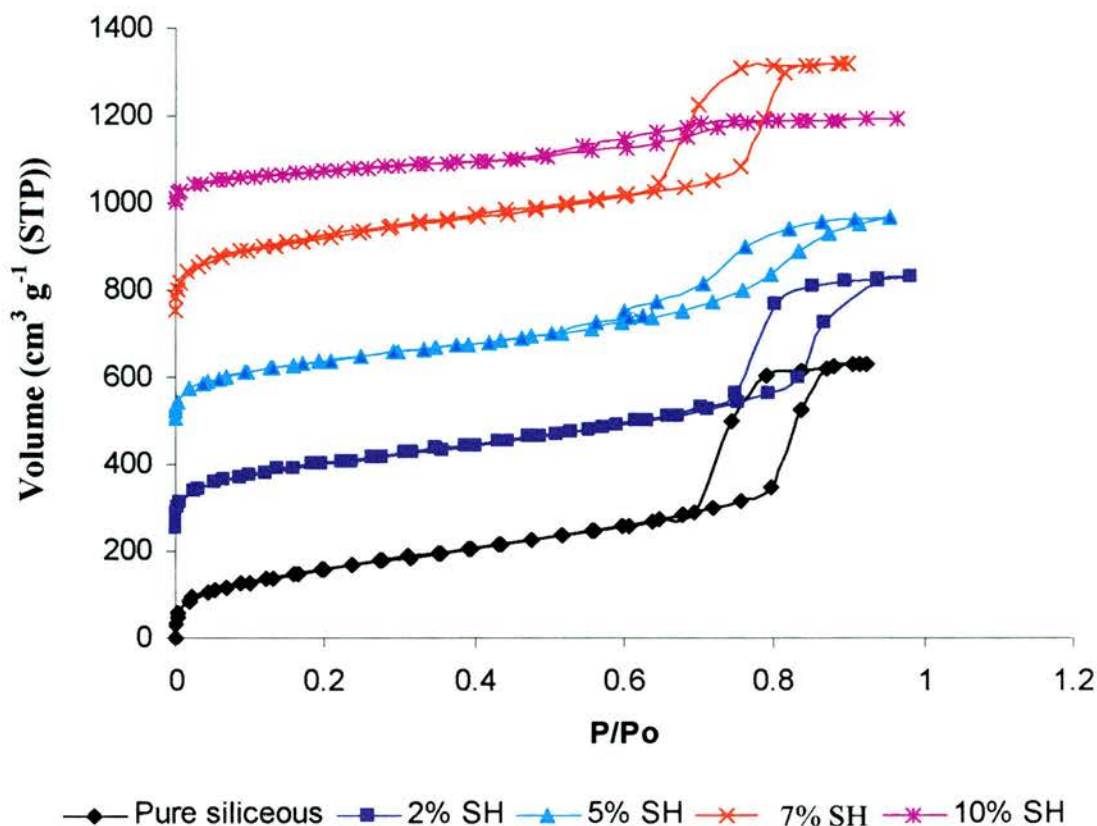


Figure 3.3.1.5.1. N_2 adsorption isotherms of extracted P123 templated mesoporous silicas. Isotherms are off-set by $250 \text{ cm}^3(\text{STP})/\text{g}$ for clarity.

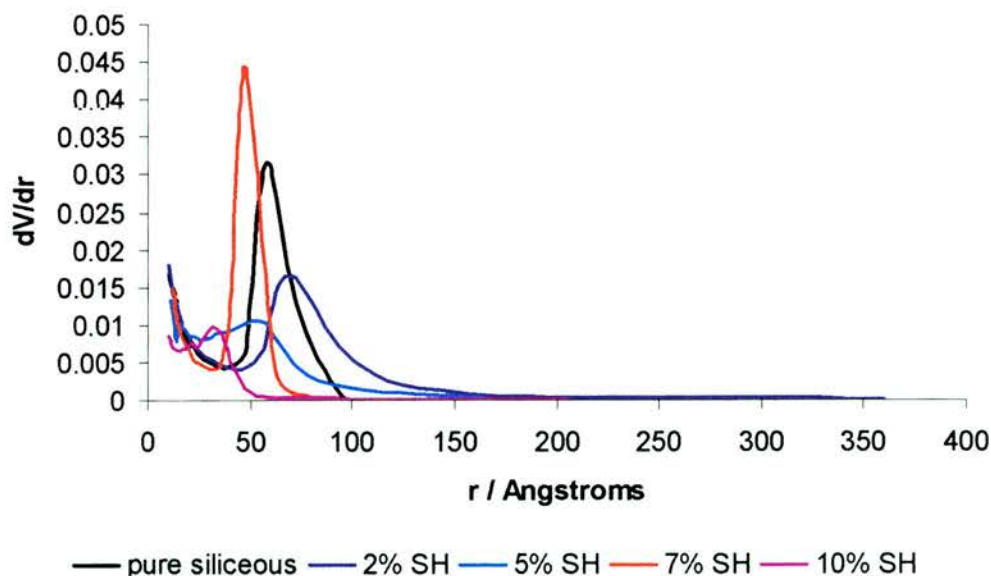


Figure 3.3.1.5.2. Pore size distributions of extracted P123 templated materials. Modelled according to the De Boer approximation on the adsorption branch of the isotherm.

Material	*Specific surface area BET m ² /g	+Pore size mode Å	Total N ₂ uptake cm ³ (STP) g ⁻¹
SiO ₂ pure siliceous - extracted	587	116	632 (79 wt%)
SiO ₂ 2% SH - extracted	534	143	576 (72 wt%)
SiO ₂ 5% SH - extracted	490	114	472 (59 wt%)
SiO ₂ 7% SH - extracted	602	92	571 (71 wt%)
SiO ₂ 10% SH - extracted	264	63	192 (24 wt%)

*BET surface area calculated within 0.05 – 0.4 P/P₀.

+Pore size distribution calculated on the adsorption branch of the isotherm using the de Boer model. Taken as the maximum in the pore size distribution curve

Table 3.3.1.5.1. Porosity measurements of extracted thiol-functionalised mesoporous silica templated by P123

For N₂ adsorption measured on the calcined samples (figure 3.3.1.5.3 – isotherms; figure 3.3.1.5.4 – pore size distribution and table 3.3.1.5.2 – porosity measurements) the trends are similar to those of the extracted analogues. For both the pure siliceous and 2% MPTES containing samples the isotherms for each show that there is well-defined porosity with high N₂ uptakes and well-defined hysteresis. The 5% MPTES solid again shows a reduced capacity for N₂ with a broad region of condensation indicating low structure regularity due to both the two different phases present and amorphous silica. Calcined STA-11 (7% added thiol) shows a well-defined type IV isotherm with a high degree of N₂ uptake whilst the 10% MPTES isotherm shows is similar to the 5%-loaded MPTES material in the isotherm shape and capillary condensation step but with a much reduced N₂ uptake value. There is an increase in adsorption capacity for all samples upon calcination, as residual surfactant remains after extraction. Most of the increase in capacity is in the micropore region indicating that much of the residual surfactant after extraction is in the micropores in the structure.

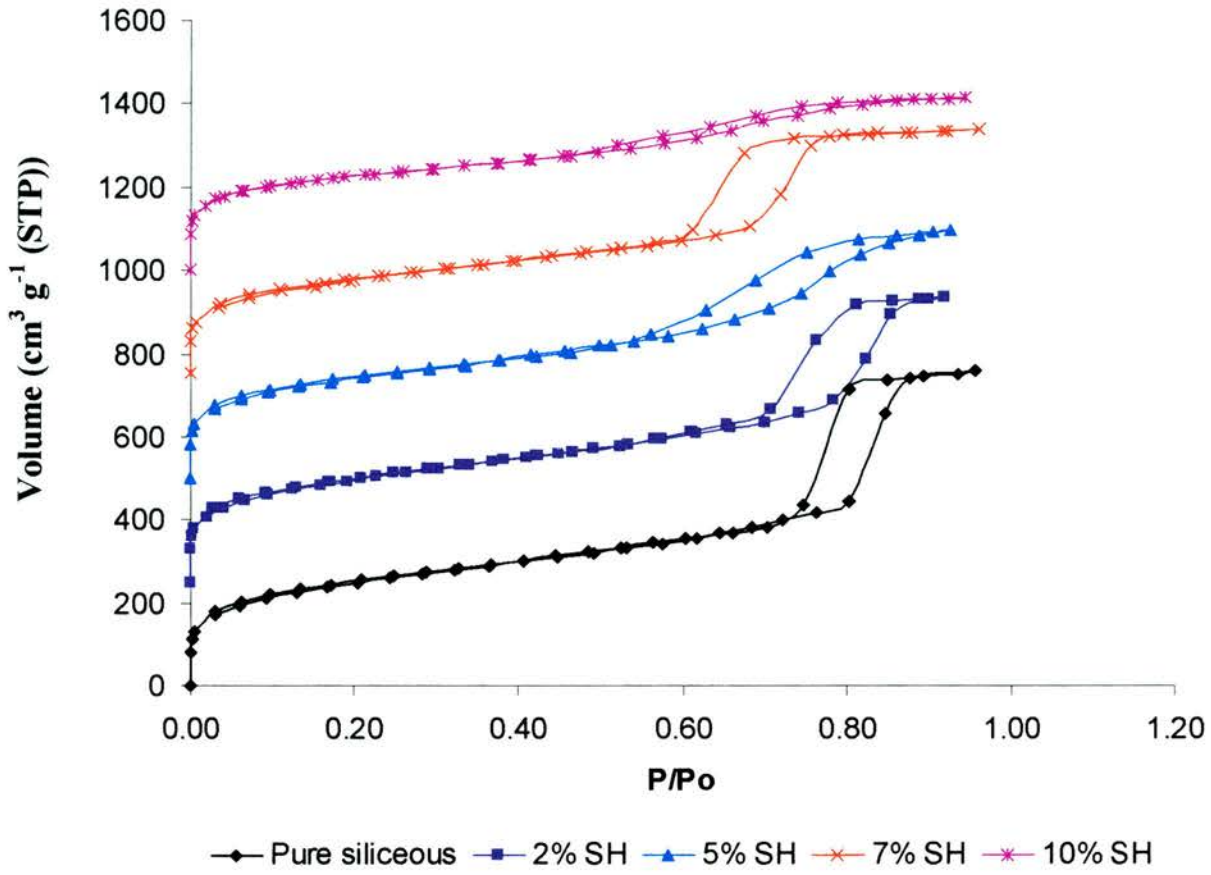


Figure 3.3.1.5.3. N_2 adsorption isotherms of calcined P123 templated mesoporous silicas. Isotherms are off-set by $250 \text{ cm}^3 \text{(STP)}/\text{g}$ for clarity.

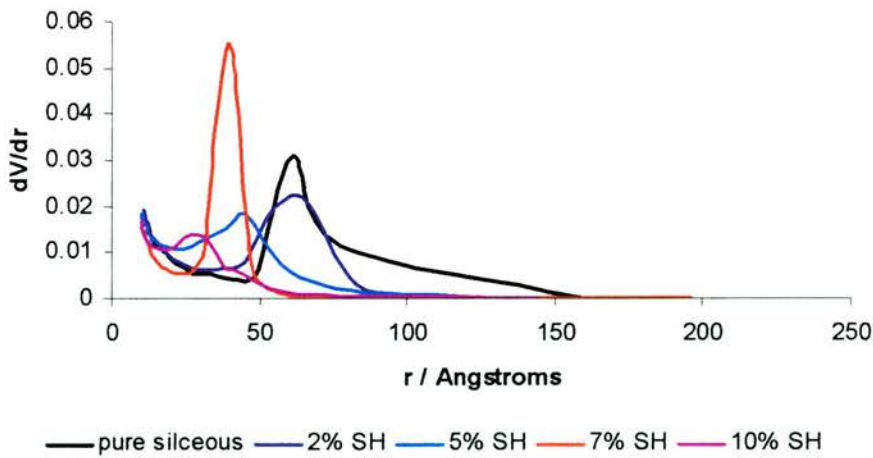


Figure 3.3.1.5.4. Pore size distributions of calcined P123 templated materials. Modelled on the De Boer on the adsorption branch of the isotherm.

Material	*Specific surface area BET m ² /g	+Pore size mode Å	Total N ₂ uptake cm ³ (STP) g ⁻¹
SiO ₂ pure siliceous - calcined	793	122	760 (95 wt%)
SiO ₂ 2% SH - calcined	812	120	687 (86 wt%)
SiO ₂ 5% SH - calcined	791	90	598 (75 wt%)
SiO ₂ 7% SH - calcined	815	82	593 (74 wt%)
SiO ₂ 10% SH - calcined	710	58	419 (52 wt%)

*BET surface area calculated within 0.05 – 0.4 P/P₀.

+Pore size distribution calculated on the adsorption branch of the isotherm using the de Boer model. Taken as the maximum in the pore size distribution curve

Table 3.3.1.5.2. Porosity measurements of calcined thiol-functionalised mesoporous silica templated by P123

3.3.1.6 Temperature effect of product mesophase selectivity

Within this thesis manipulation of synthetic variables, although important, has not been a primary concern, rather the aim was to look at the effect of organo-siloxanes as co-condensers on the product selectivity and quality. Just as the formation of the highly ordered cubic Ia3d STA-11 is only defined at specific concentrations of the organo-siloxane in the synthesis mixture, it was found that the effect of the temperature of the hydrolysis step is also critical in obtaining the cubic STA-11 or hexagonal phases. Through XRD (figure 3.3.1.6.1) and HRTEM (figure 3.3.1.6.2) it is observed that upon increasing the hydrolysis temperature from 313 K to 333 K the effect is that the hexagonal SBA-15 structure is formed at the higher temperature but with reduced order whereas at 313 K and 323 K the cubic phase is observed: 313 K being the optimum temperature. The change in temperature must affect the relative stabilities of the silica-coated micelles that give rise to the hexagonal and cubic phases.

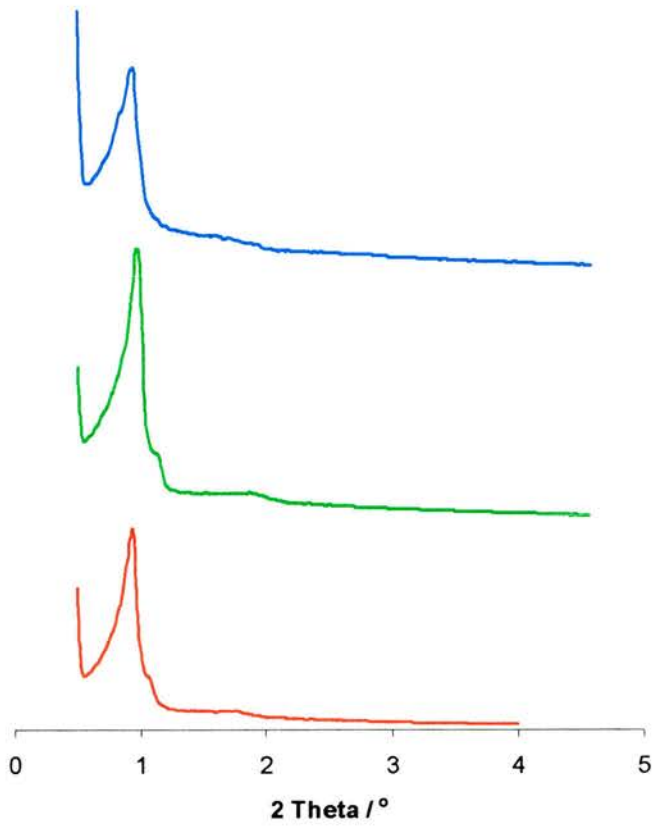
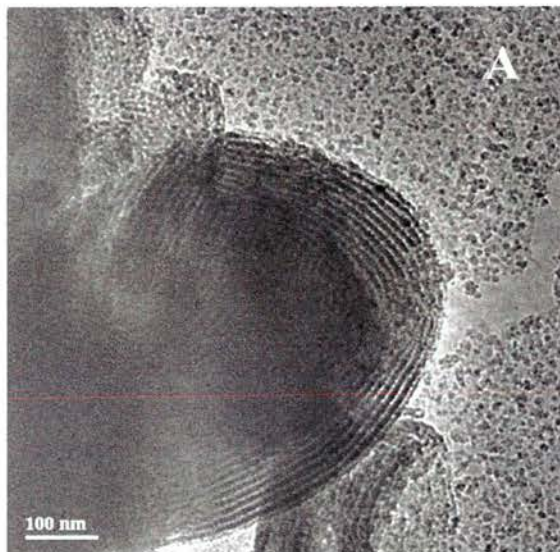


Figure 3.3.1.6.1. XRD of extracted 7% MPTES containing mesoporous silica templated by P123 showing mesophase product as a function of hydrolysis temperature. From bottom to top: 313 K; 323 K and 333K.



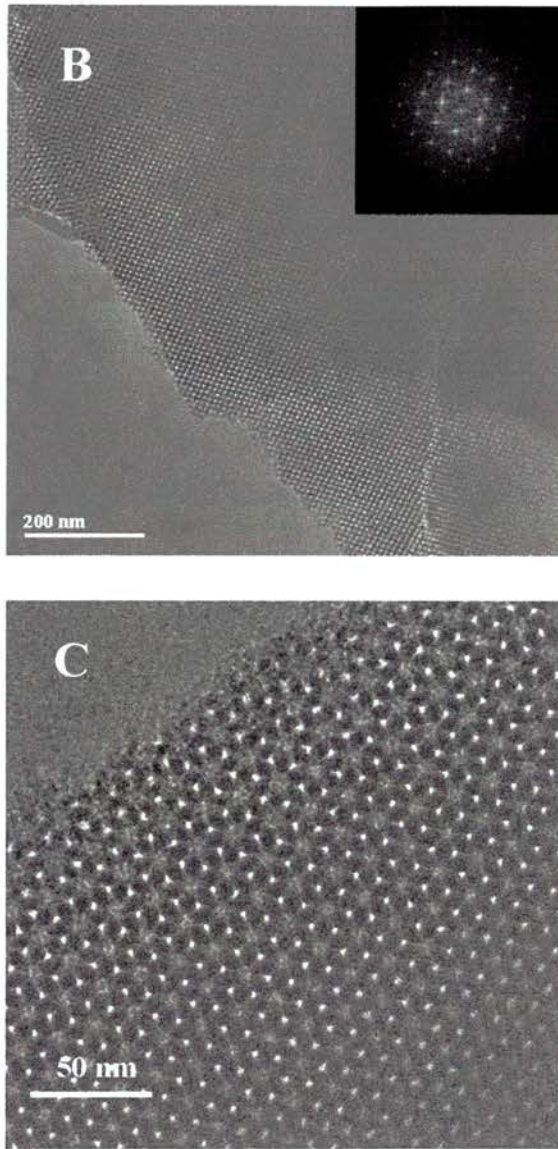
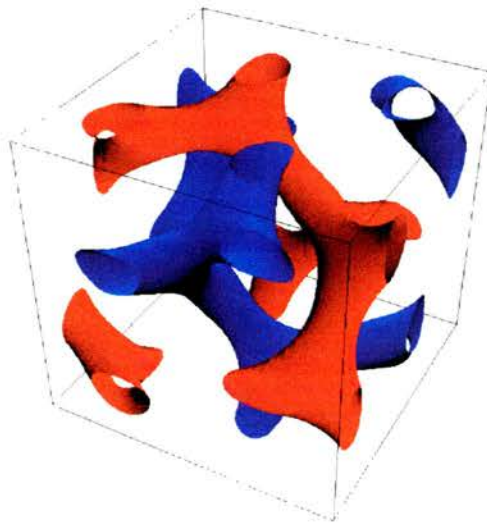
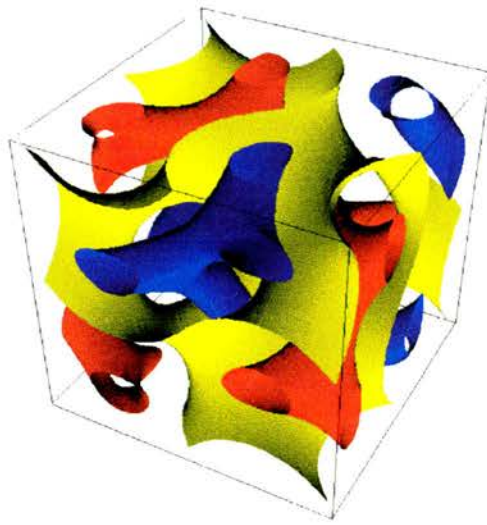


Figure 3.3.1.6.2. HRTEM micrographs of P123 templated silica containing 7% MPTES loading varying the hydrolysis temperature (A) – 333 K (pores perpendicular to the incident beam with hexagonal $p6mm$ symmetry); (B) – 323 K (viewing the $[110]$ zone axis of cubic $Ia\bar{3}d$ symmetry) and (C) – 313 K (viewing the $[111]$ zone axis of STA-11).

3.3.1.7 Simulation

The gyroid surface of STA-11 has been simulated that is consistent with XRD, TEM and adsorption measurements (figure 3.3.1.7.1). The gyroid surface separates the surfactant in two interpenetrating pore systems similar to that of cubic MCM-48. Highly ordered SBA-15 materials are high in quality of structural regularity and

possess thick inorganic silica walls [6,7] which gives rise to excellent thermal and hydrothermal stability. The wall thickness in STA-11 from comparing simulated XRD to the experimental XRD pattern (figure 3.3.1.7.2) is found to be around 33 Å corresponding to ~ 39% of the unit cell compared to a 26% wall thickness for SBA-15 ($a \cong 12$ nm) [7]. Therefore the potential stability of STA-11 may equal or exceed that over SBA-15 along with the potential advantage of molecular transportability and pore blocking.



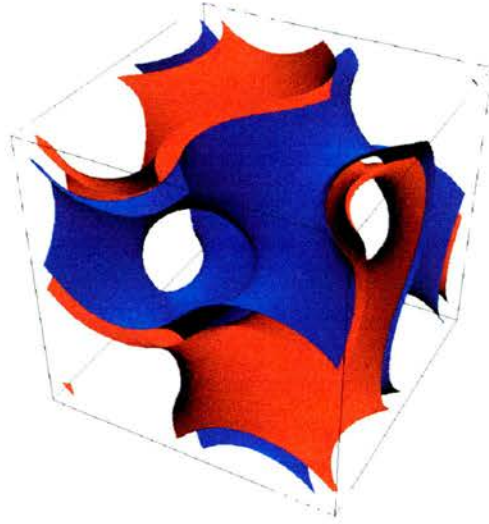


Figure 3.3.1.7.1. Simulated STA-11 with bicontinuous cubic $Ia\bar{3}d$ symmetry large pore analogue to MCM-48. separating the surfactant by two separate pore networks (top); surfactant (middle) and pore wall (bottom).

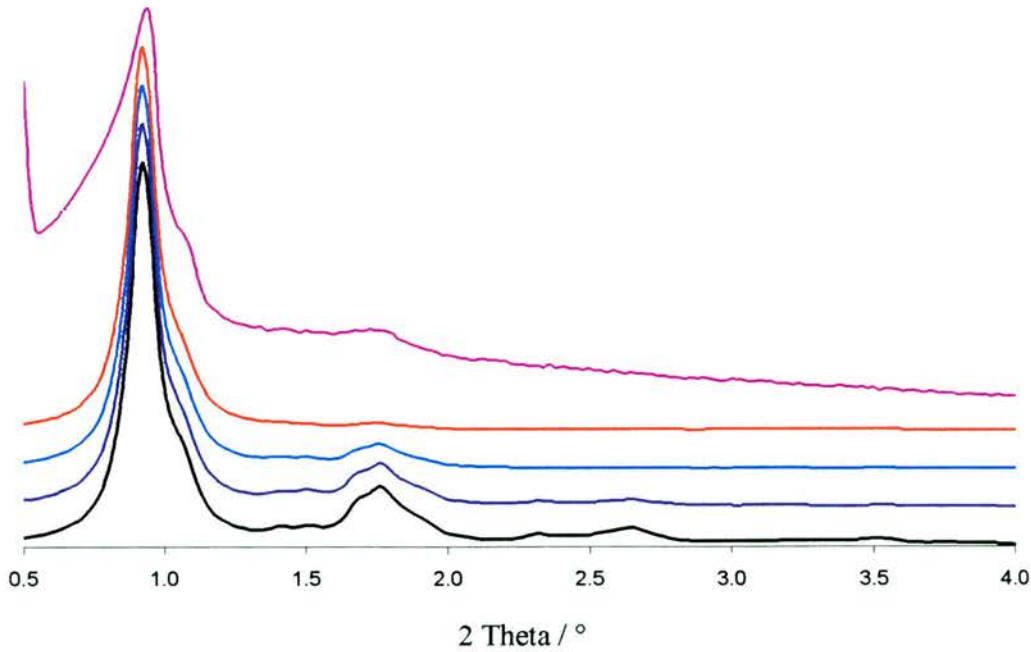


Figure 3.3.1.7.2. Simulated XRD patterns for $Ia\bar{3}d$ silica, $a = 235 \text{ \AA}$ using a model for the bicontinuous cubic phase with different wall thicknesses compared with the experimental diffraction pattern (top). The simulated wall thicknesses are, reading upwards, 11, 22, 33, and 44 \AA .

3.3.1.8 Conclusions

SBA-15 can be prepared with 3-Mercaptopropyltriethoxysilane as a co-condenser with loading of 2% using the non-ionic triblock copolymer Pluronic P123 as a surfactant template under mild acidic conditions. Here the long-range order is apparent through the diffraction pattern and further complemented from the HRTEM micrographs. The capacity for N₂ adsorption is high and the isotherm too is typical type IV. The synthesis of a well-defined large pore mesoporous solid containing a bicontinuous cubic Ia $\bar{3}$ d structure analogous to MCM-48 has been prepared by the *in situ* addition of MPTES to the sol-gel mixture. The synthetic conditions are narrow in achieving such a highly-ordered material as only a definite concentration (7% MPTES, based on total silica) and a narrow temperature range (under 333 K) give this new material designated STA-11. Structural characterisation confirms the new material as given by XRD and HRTEM. Adsorption measurements show that the scale of the mesoporosity (P/P_0 for capillary condensation ~ 0.75) is larger than that of similar MCM-48 ($P/P_0 \sim 0.3$) and that high surface areas (815 m²/g) and narrow pore size distributions are observed. The relative stability of STA-11 is potentially further enhanced over that of SBA-15, which shows excellent stability, as STA-11 has thick inorganic silica walls corresponding to around 40% of the unit cell ($a \cong 235 \text{ \AA}$) through simulation.

A decrease in the hexagonal unit cell parameter can be noted from an increase of MPTES concentration and a decrease in pore size. A considerable decrease in pore size is also observed from the 2% to 7% MPTES concentration. This may suggest a decrease in the micellar volume on addition of MPTES and as such the propyl-thiol group presumably renders the micelle more hydrophobic (or an increase in the interaction of the thiols with the hydrophobic PPO), previously suggested by the group of Zhao [28]. The change in product symmetry is accompanied by an increase in the surfactant packing parameter, g , with the high-curvature hexagonal p6mm changing to low-curvature bicontinuous cubic Ia $\bar{3}$ d. A suggestion for the reasons is outlined in figure 3.3.1.8.1. As reported previously [28,34] organic groups if hydrophobic enough can interact with the hydrophobic inner portion (PPO) of the

surfactant template. This interaction may bring the PPO portion closer to the surface of the micelle and in doing so may – remembering that the PPO and PEO portions stack in a way to minimise their interactions – separate the PEO portions further apart hence reducing the curvature of the micelle.

In addition, the quantification of the accessible thiol groups within the pores has been assessed by Ellman's reagent suggesting that the fraction of accessible thiol groups to the reagent is in the region of 54 – 76%. The reason for the relative accessibilities is unclear. Why does the disordered 5% MPTES solid have the highest percentage of accessible thiol groups to Ellman's reagent considering that molecular diffusion may be suppressed whereas the 2 and 7% MPTES solids have a much lower accessibility? Considering the direct role of the thiol groups on the mesophase product selectivity from SBA-15 to STA-11 (also unclear) a direct comparison of accessible values may not be the answer as changes in the micelle-silica-thiol interface upon increased MPTES loadings is likely to effect the relative orientations of the thiol groups. If increasing the thiol loading had no effect on the mesophase outcome it would be easier to compare directly the results. However, since the 2% MPTES loading gives one mesophase – the hexagonal, the 5% MPTES loading the boundary between the two phases – hexagonal and cubic and the 7% MPTES loading the pure cubic mesophase structure then a direct comparison of the percentage of thiol groups within the three solids is challenging!

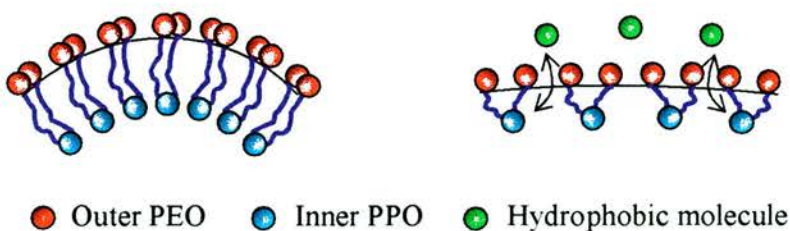


Figure 3.3.1.8.1. Schematic diagram: left: Normal stacking sequence of high-curvature hexagonal SBA-15 with outer PEO and inner PPO portions of the surfactant minimising electrostatic interactions; right: in the presence of hydrophobic molecules interacting with hydrophobic PPO and drawing PPO portion nearer to the surface of the micelle causing the PEO to withdraw away to minimise conflicting interactions resulting in a decrease in micellar curvature

3.3.2 Phenyl-functionalised mesoporous silica templated by P123.

To observe the effects of functionalising the surface with hydrophobic groups, different levels of phenyltriethoxysilane (PTES) were co-condensed with TEOS during synthesis. This was found to result in similar effects to the addition of MPES, and so the results are discussed at this point.

3.3.2.1 XRD

It can be seen that upon a 2% loading of PTES to the synthesis mixture that the XRD diffraction pattern (figure 3.3.2.1.1) indicates the $p6mm$ symmetry associated with the SBA-15 structure. The diffractogram suggests that the long-range order is of a high quality with the secondary (11) and (20) reflections shown and therefore that the effect of the organo-siloxane on the micellar geometry remains unchanged at this specific functional loading.

A transition in the product phase from hexagonal $p6mm$ to a cubic $Ia\bar{3}d$ symmetry is observed upon a 5% PTES loading. The XRD pattern shows the (220) shoulder at $0.92^\circ 2\theta$, ($a = 272 \text{ \AA}$) (HRTEM reveals both hexagonal and cubic phases present). The 7% PTES loaded sample is disordered on the long-range scale to XRD and would suggest that the level of loading of the bulky phenyl constituent does indeed affect the aggregation of micelles involved at the silica-surfactant interface. HRTEM reveals there to be particles of the cubic phases present and so the unit cell calculated by XRD (table 3.3.2.1.1) is estimated based on the cubic structure. At an increased loading of PTES to (10%) the XRD pattern shows long-range order is present but with $p6mm$ hexagonal symmetry.

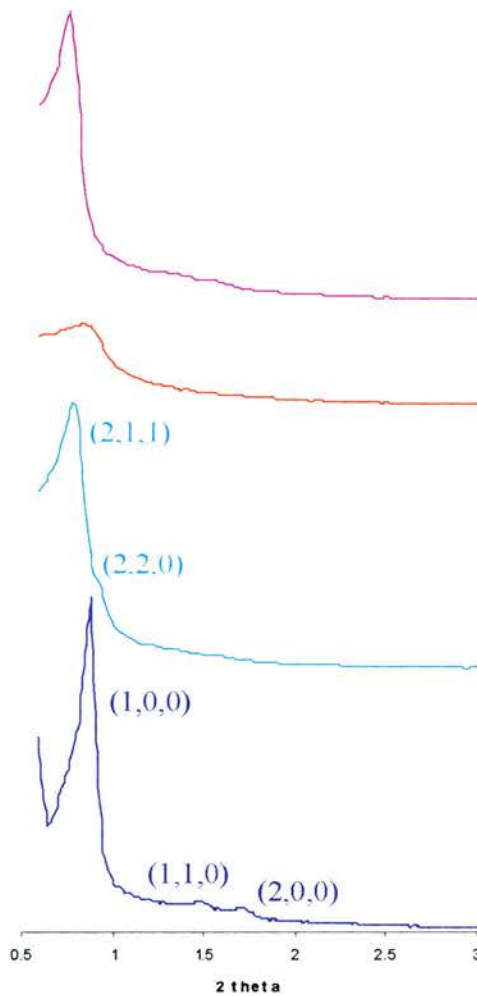


Figure 3.3.2.1.1. X-ray diffraction patterns of phenyl-functionalised mesoporous silica templated by Pluronic P123. Bottom to top: 2% added PTES; 5% added PTES; 7% added PTES and 10% added PTES.

It would seem that inclusion of the phenyl siloxane has a similar effect on the product selectivity to that of addition of the thiol groups but with a greater influence at the lower concentration of 5%, when the transition to the cubic symmetry is observed with nearly the pure phase formed. Although the phase formed with 7% added PTES is poorly ordered, as might be expected for bulky phenyl groups assembling in a cubic structure, it is remarkable that at a loading of 10%, a $p6mm$ structure again results, along with disordered regions. Some degree of phase separation cannot be ruled out in this case.

Sample	$^{\circ} / 2\theta$	XRD interplanar d spacing / Å	Unit cell / Å
2% PTES	0.88	100 ^a	116 ^c
5% PTES	0.78	113 ^b	277 ^d
7% PTES	0.85	104 ^b	254 ^d
10% PTES	0.76	116 ^a	134 ^c

Interplanar spacing – ^ad₁₀₀, ^bd₂₁₁; ^chexagonal lattice parameter, ^dcubic lattice parameter

Table 3.3.2.1.1. Interplanar spacing and unit cell parameters phenyl functionalised mesoporous silica templated by P123 by XRD

3.3.2.2 SEM

Scanning electron microscopy reveals there to be both the elongated morphology typical of SBA-15 and spherical particles in the range of 4 – 10 μm consistent with the cubic MCM-48/STA-11 type materials for the 2% PTES loading material (figure 3.3.2.2.1). This would appear to correlate with the more marked effect of the phenyl siloxane in bringing about the change in product.

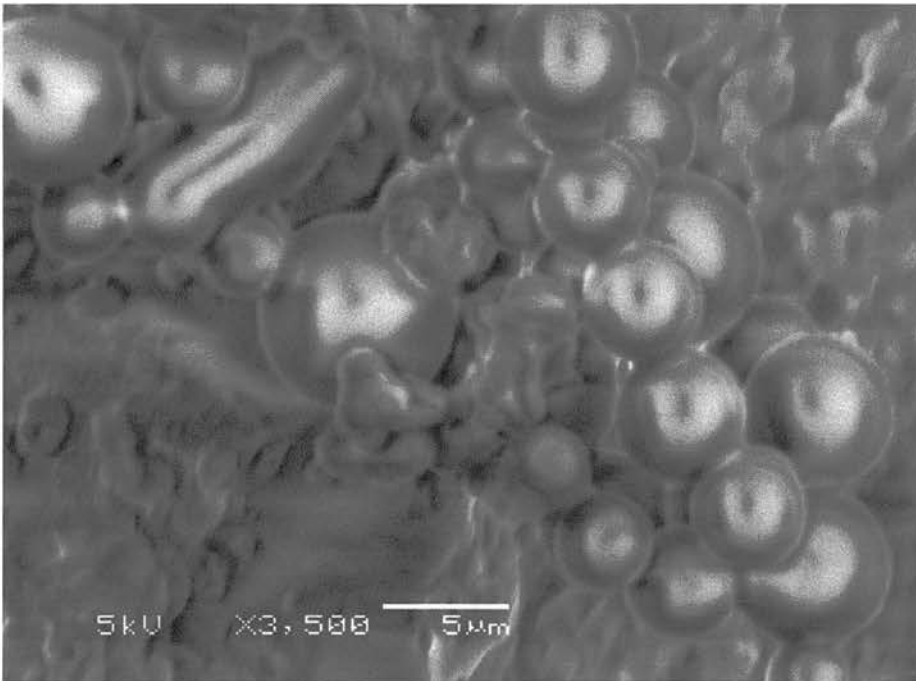
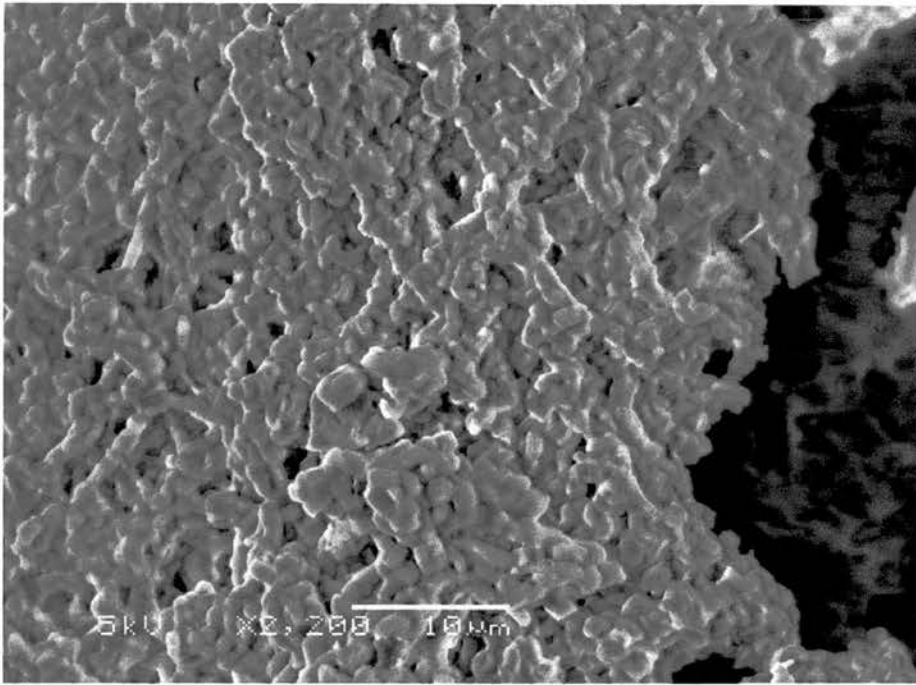


Figure 3.3.2.2.1. Scanning electron micrographs of 2% PTES-functionalised mesoporous silica templated by P123 showing (above) typical SBA-15 'worm-like' morphology and (below) spherical particles corresponding to the cubic structure.

The 5%-PTES containing solid (cubic symmetry) shows complementary morphology with spherical particles, varying in size up to 10 μm . The 7% PTES sample also has spherical morphology as the majority with no sign of the typical ‘worm-like’ morphology. The 10% PTES material shows spherical morphology but with the spheres merging into single particles (figure 3.3.2.2.2). Whether this distinct morphology is due to the silica material being on the phase boundary between the ‘worm-like’ hexagonal phase and spherical cubic phase is an open question. It is worth noting that this morphology where the spheres appear to be merging is also observed for the 5% MPTES containing solid where the mesophase is at the boundary between the two phases and could represent an intermediate morphology characteristic of the phase transition from hexagonal to cubic.

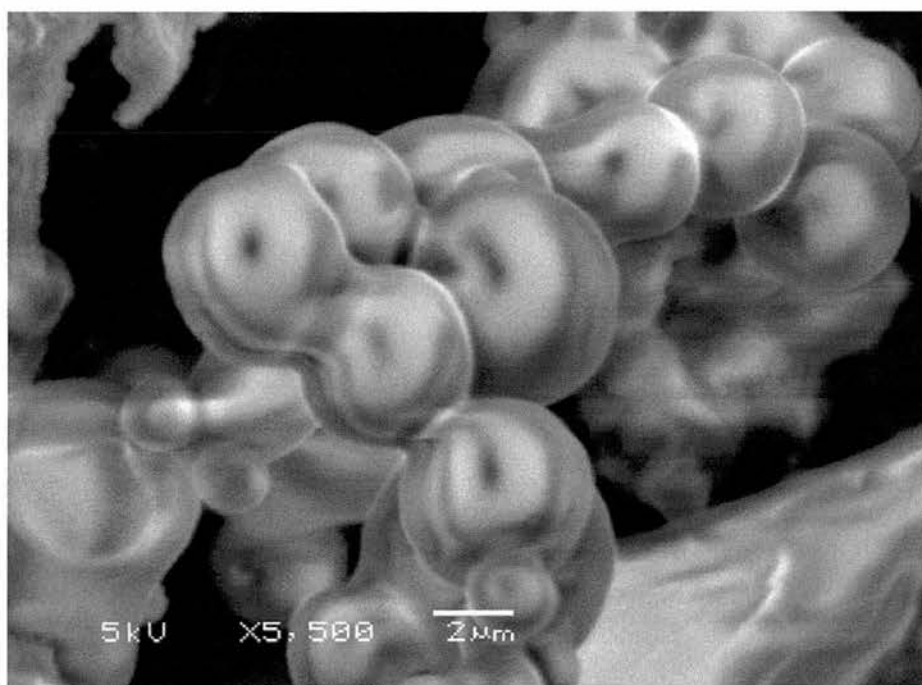


Figure 3.3.2.2.2. SEM micrograph of the morphology of 10% PTES mesoporous silica templated by P123 showing a possible intermediate morphology.

3.3.2.3 TEM

Transmission electron microscopy for the 2% PTES material complements the corresponding XRD pattern as the micrographs show that SBA-15 is the meso-product from the direct functionalisation synthesis. Figure 3.3.2.3.1 shows SBA-15 with the pores perpendicular to the incident electrons over a low- and high-magnification. It can be observed that the high order of the channels is maintained over the μm range.

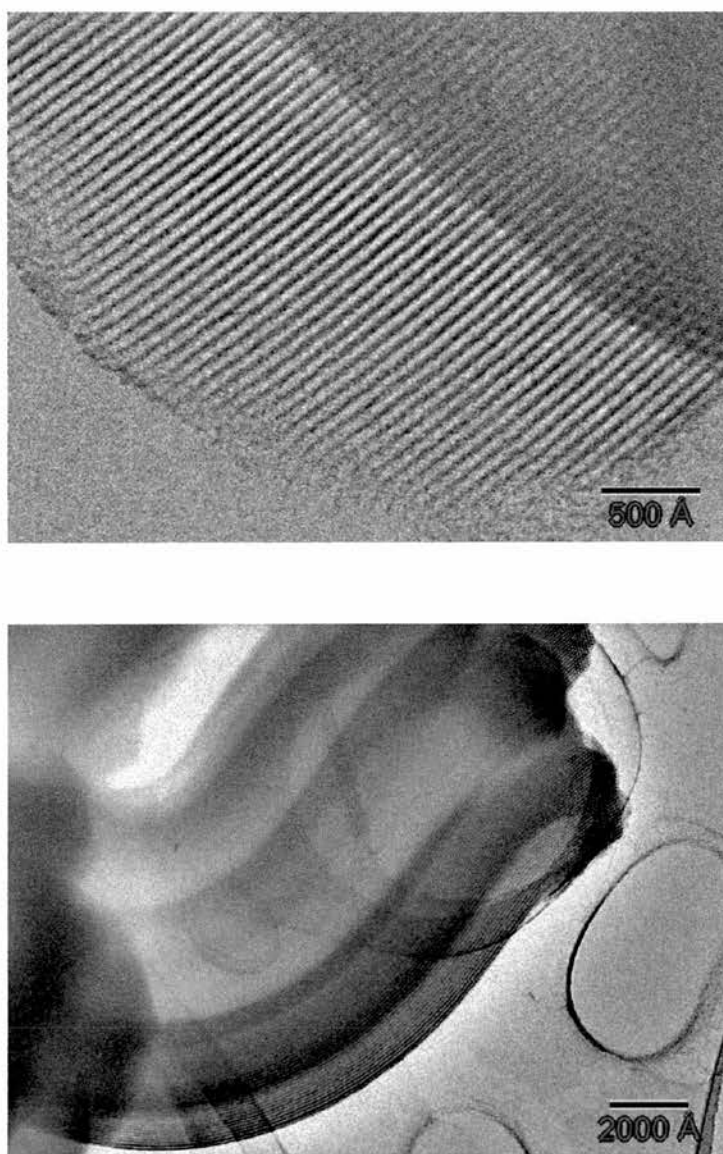


Figure 3.3.2.3.1. HRTEM micrograph of SBA-15 functionalised with 2% PTES with the pores running perpendicular to the electron beam over (bottom) low- and (top) high-magnification

The 5% PTES sample appears cubic to XRD. However although the major mesophase is indeed the cubic $Ia\bar{3}d$ symmetry (figure 3.3.2.3.2) there is a minority hexagonal phase also present.

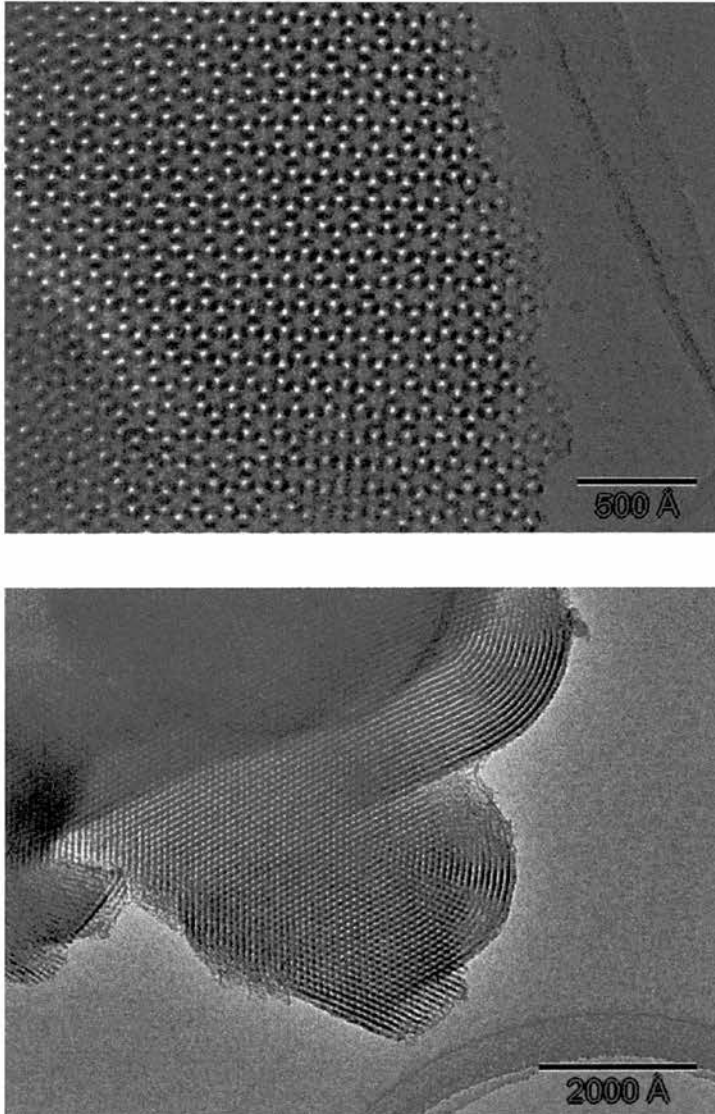


Figure 3.3.2.3.2. HRTEM micrographs of mesoporous silica templated by P123 with 5% PTES functionality showing (top) the cubic $Ia\bar{3}d$ symmetry as the predominant phase, viewing the $[111]$ zone axis and (bottom) the minor hexagonal SBA-15 with pores running both parallel and perpendicular to the incident electrons

Functionalising with 7% PTES leads to a poorly ordered product that is shown by TEM to contain domains with the cubic $Ia\bar{3}d$ symmetry (figure 3.3.2.3.3).

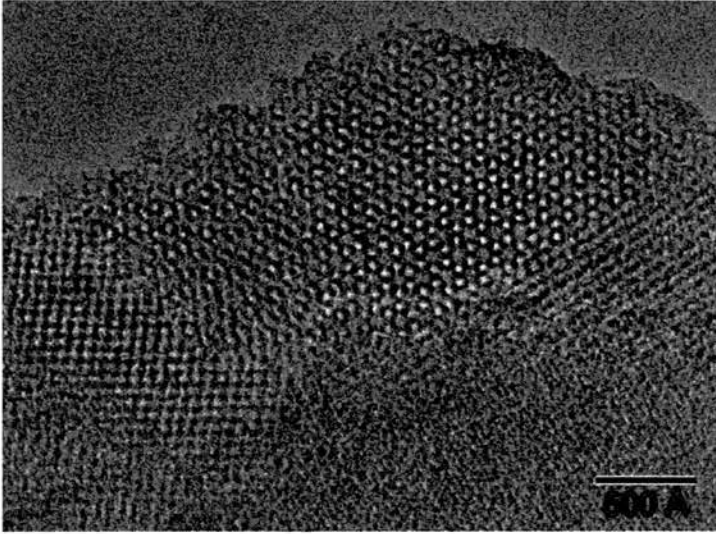
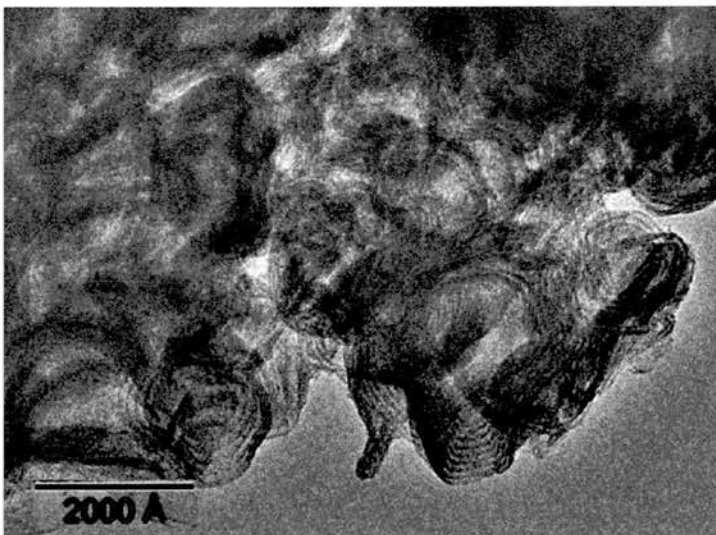


Figure 3.3.2.3.3. HRTEM micrograph of 7% PTES loading mesoporous silica viewing the cubic $Ia\bar{3}d$ symmetry along the $[111]$ zone axis.

As previously described the 10% PTES sample displayed the XRD pattern indicating hexagonal $p6mm$ symmetry. HRTEM micrographs show SBA-15 character amongst a disordered sample (figure 3.3.2.3.4).



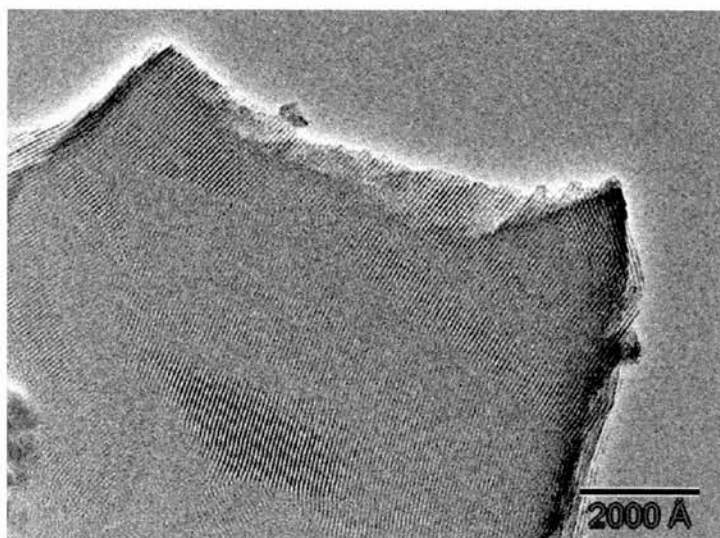


Figure 3.3.2.3.4. HRTEM micrographs of sample with 10% PTES loading showing (above) amorphous disorder and (below) characteristic SBA-15 with channels orthogonal to the incident electrons.

3.3.2.4 N_2 Adsorption

The nitrogen adsorption isotherms of extracted phenyl-containing mesoporous solids are shown in figure 3.3.2.4.1. These all show Type IV isotherms, but with a clear trend of reduced mesoporosity as the amount of included phenyl is increased. This is most clearly seen in the reduction of the size of the hysteresis loop on going from 2 – 10% added PTES. The absolute values of the pore diameters (figure 3.3.2.4.2) calculated here using the De Boer method* on the adsorption branch, appear all to be too large (greater in some cases than the unit cell parameter calculated from X-ray diffraction) but they clearly show a decrease as the amount of added phenyl is increased. Table 3.3.2.4.1 summarises the adsorption measurements.

* This is the only available method available to assess the pore size (apart from the BJH method which is known to underestimate the pore size [47]) and so the pore sizes given should be a relative series of comparisons only. The Non-Local Density Functional Theory (NLDF) [47] unavailable to many is the most promising model for calculating pore size distributions.

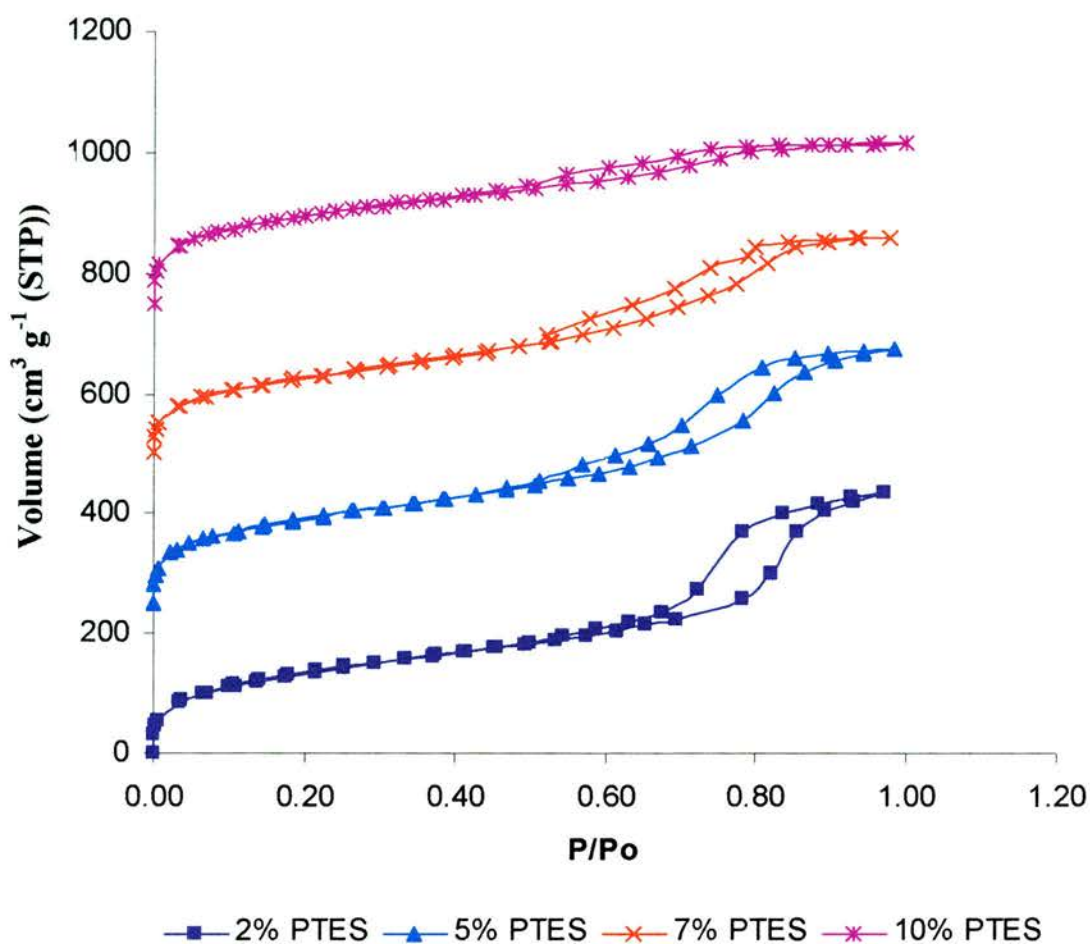


Figure 3.3.2.4.1. N₂ isotherms of extracted PTES functionalised silicas templated by P123. Isotherms are off-set by 250 cm³ (STP) / g for clarity.

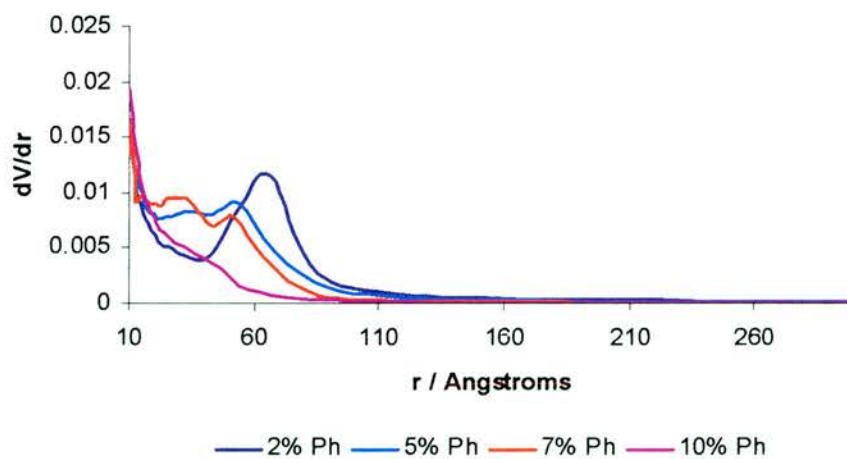


Figure 3.3.2.4.2. Pore size distribution curves calculated on the De Boer model for extracted PTES functionalised mesoporous silicas templated by P123

Material	*Specific surface area BET m ² /g	+Pore size mode Å	Total N ₂ uptake cm ³ (STP) g ⁻¹
SiO ₂ 2% Ph - extracted	464	122	431 (54 wt%)
SiO ₂ 5% Ph - extracted	492	70 [^] 109 [^]	423 (53 wt%)
SiO ₂ 7% Ph - extracted	447	64 [^] 104 [^]	360 (45 wt%)
SiO ₂ 10% Ph - extracted	503	-	272 (34 wt%)

*BET surface area calculated within 0.05 – 0.4 P/P₀.

+Pore size distribution calculated on the adsorption branch of the isotherm using the de Boer model. Taken as the maximum in the pore size distribution curve

[^]Poorly defined.

Table 3.3.2.4.1 Porosity measurements of extracted phenyl-functionalised mesoporous silica templated by P123

Similar effects are seen for the calcined samples (figure 3.3.2.4.3 – isotherms; figure 3.3.2.4.4 – pore size distribution), which demonstrate much higher micropore volumes. This effect results from thermal removal of unextracted surfactant and included phenyl groups, and is similar to that observed for the thiol-loaded samples. No evidence of ordering of the pore structure is observed in these materials. The information from these measurements is summarised in table 3.3.2.4.2.

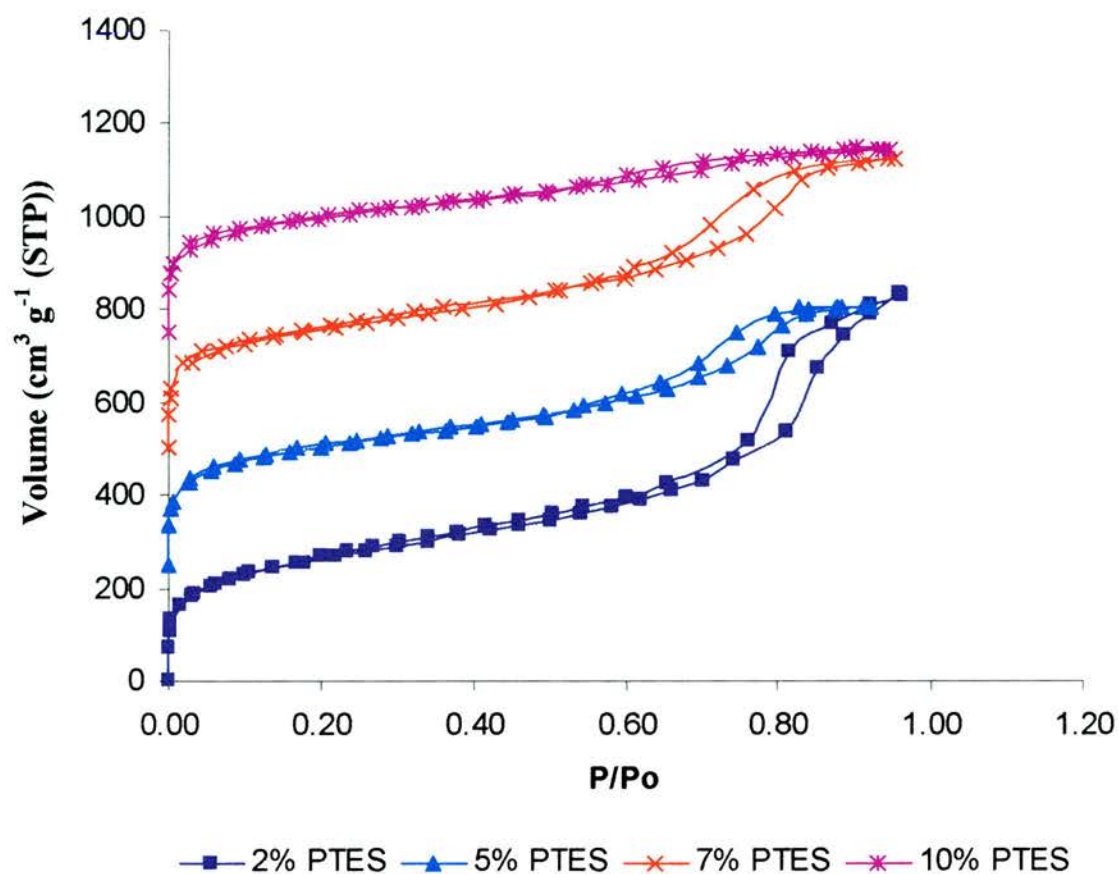


Figure 3.3.2.4.3. N_2 isotherms of calcined PTES functionalised silicas templated by P123. Isotherms are off-set by $250 \text{ cm}^3 \text{ (STP) / g}$ for clarity.

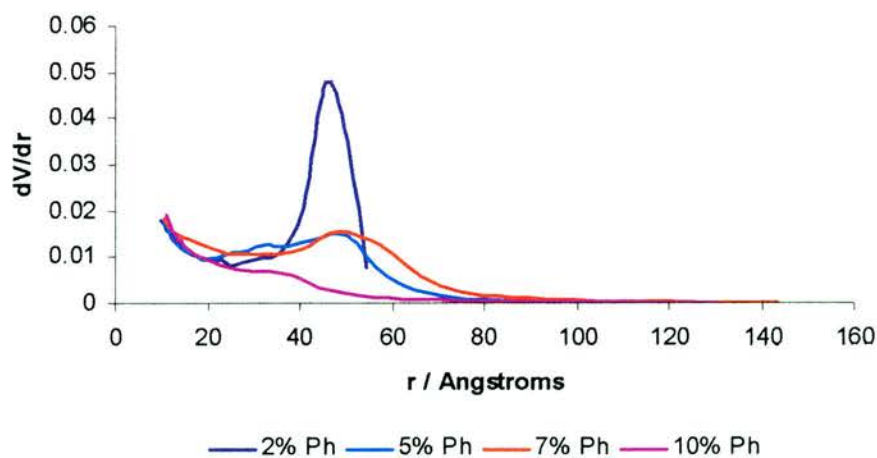


Figure 3.3.2.4.4. Pore size distribution curves calculated on the De Boer model for calcined PTES functionalised mesoporous silicas templated by P123

Material	*Specific surface area BET m ² /g	+Pore size mode Å	Total N ₂ uptake cm ³ (STP) g ⁻¹
SiO ₂ 2% Ph - calcined	845	92	848 (105 wt%)
SiO ₂ 5% Ph - calcined	812	65 [^] 101 [^]	560 (70 wt%)
SiO ₂ 7% Ph - calcined	857	96 [^]	624 (78 wt%)
SiO ₂ 10% Ph - calcined	772	-	400 (50 wt%)

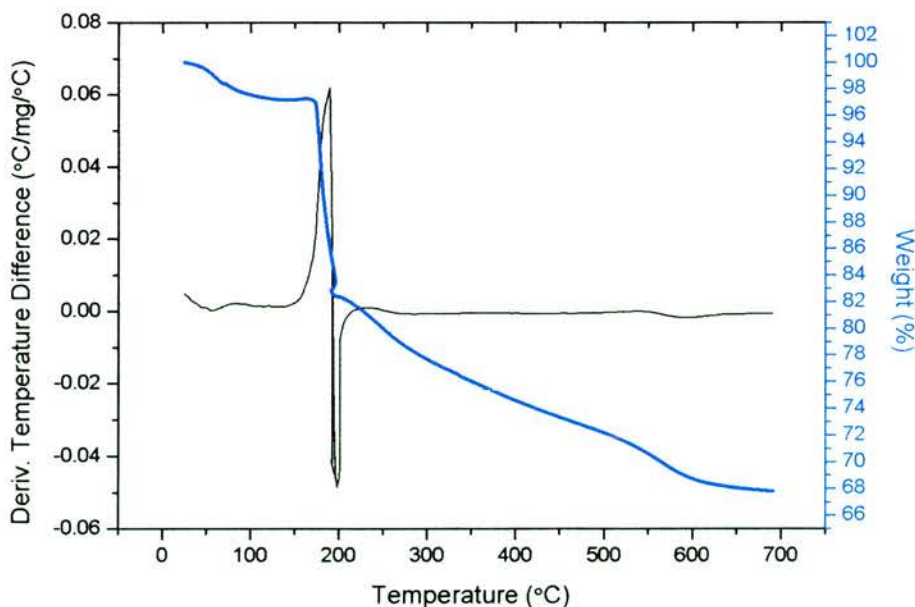
*BET surface area calculated within 0.05 – 0.4 P/P₀.

+Pore size distribution calculated on the adsorption branch of the isotherm using the de Boer model. Taken as the maximum in the pore size distribution curve

[^] Poorly defined.

Table 3.3.2.4.2 Porosity measurements of calcined phenyl-functionalised mesoporous silica templated by P123

Thermogravimetric analysis (figure 3.3.2.4.5) shows that after the initial weight loss, presumably due to solvent, the residual surfactant is removed above *ca.* 165 °C. The main weight loss is from removal of the surfactant but a more marked weight loss for the 7%-loaded sample at *ca.* 550 °C may be attributable to loss of the phenyl groups.



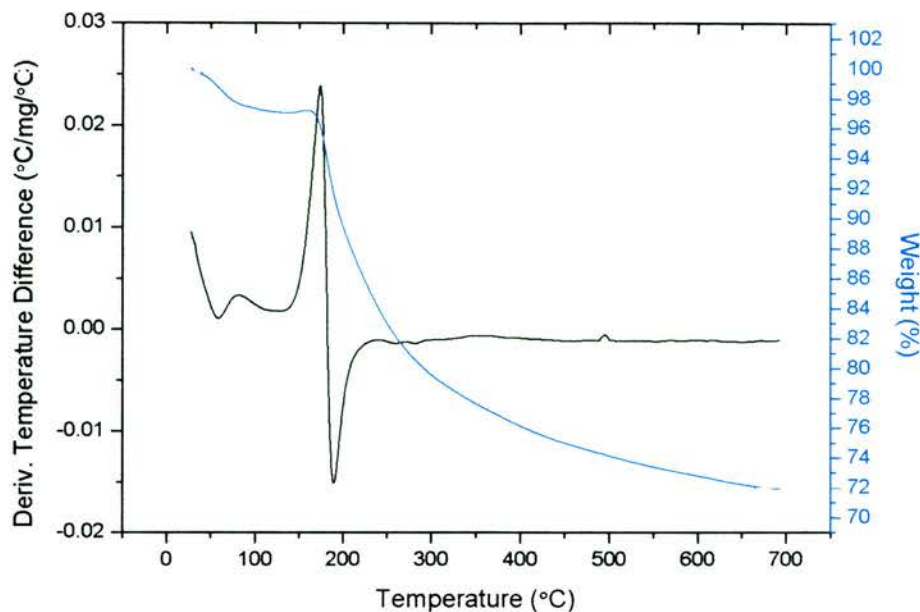


Figure 3.3.2.4.5. Thermo-gravimetric analysis of extracted (top) 7% and (bottom) 2% PTES solid. The initial loss of weight of solvent precedes the weight loss of the organics including the residual surfactant.

3.3.2.5 Conclusions

Incorporating PTES directly into the synthesis causes a change in the product phase from hexagonal SBA-15 to cubic STA-11 in a similar way that MPTES addition does: by 5% added PTES the cubic Ia3d phase has already formed. However the order of the cubic structure from the 5% PTES sample is lower than that of the corresponding 7% MPTES solid although the cubic phase is in a high yield. This is clear from XRD, TEM and N₂ adsorption. The pore size is reduced upon addition of the phenyl groups, and the capillary condensation loop is strongly reduced as addition of the bulky phenyl siloxane groups disrupts the micellar structure.

3.3.3 Cyano-functionalised mesoporous silica templated by P123.

3.3.3.1 Cyano analysis

Whereas propylthiol- and phenyl-functionalised siloxanes are expected to be relatively hydrophobic, the addition of cyanopropyl-functionalised (CNPTES) silica is expected to increase the hydrophilicity of the surface, particularly because it is known that the cyano groups are partially hydrolysed to carboxylic acids under acidic conditions of the synthesis [48]. This was also observed to be the case for our materials, where IR spectroscopy of solids loaded between 5-10% of the cyanosiloxane clearly shows resonance due to both cyano and carboxy groups (figures 3.3.3.1.1 and 3.3.3.1.2 are courtesy of Sonia Fiorilli – Torino (Italy)).

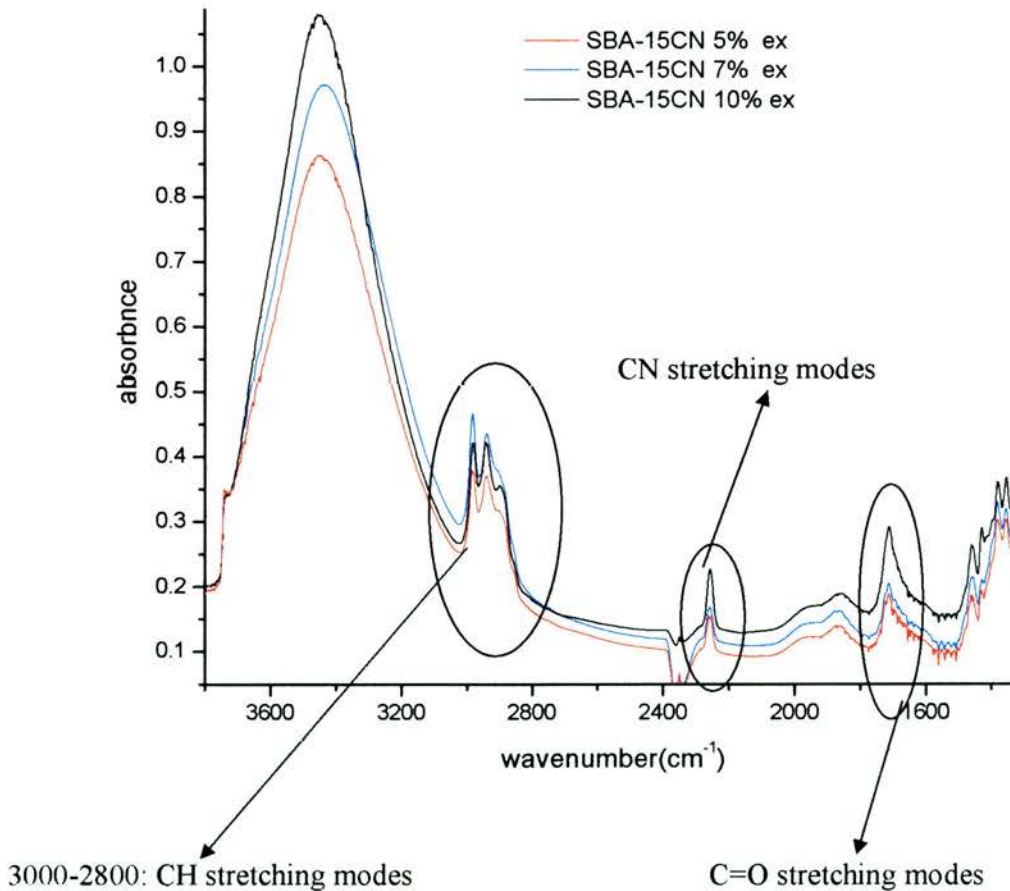


Figure 3.3.3.1.1. IR spectroscopy spectra of CNPTES samples varying in organic loading showing peaks for both cyano and carboxyl groups

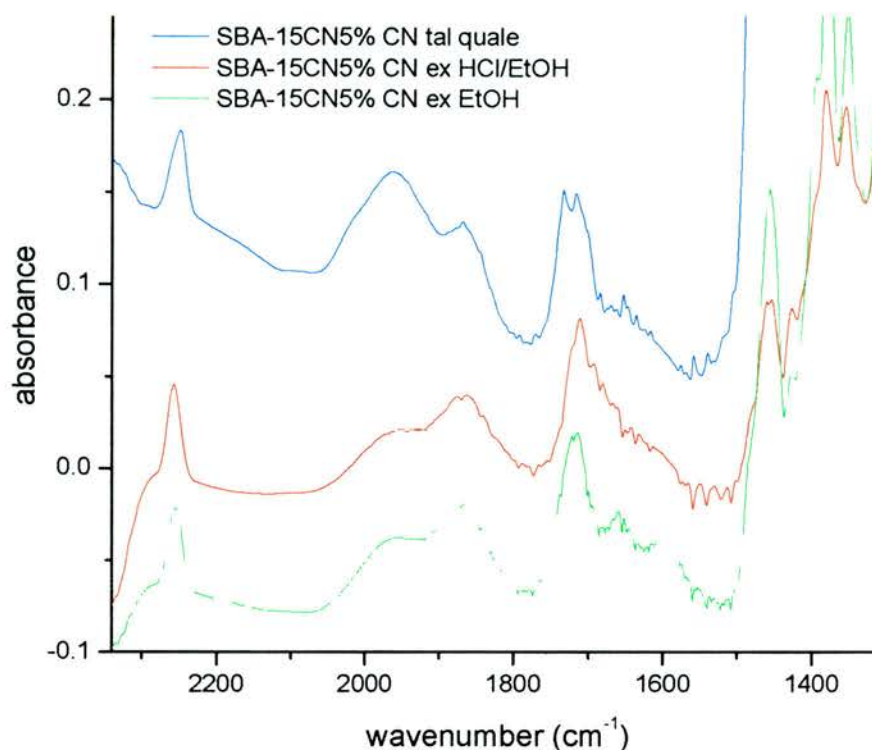


Figure 3.3.3.1.2. IR spectra for as-made and extracted SBA-15 solids functionalised *in situ* with CNPTES

The band at 2256 cm^{-1} is due to the stretching frequency of the CN groups observed for both the as-made and extracted forms. This suggests that not all of the CN groups have been hydrolysed to carboxylic acid groups. No further hydrolysis of CN to the carboxylic acid occurs after extraction and therefore some CN groups must be protected through orientation within the silica walls and also that hydrolysis occurs during formation of the mesoporous product. The presence of CN groups remaining on obtaining the final mesoporous product suggests that during hydrolysis of the mesoporous product formation some of the CNPTES is included and orientated within the silica walls before the CN hydrolysis can occur and gives an indication of the relative rates of hydrolysis. The region between $1800 - 1600\text{ cm}^{-1}$ are signals assigned to C=O stretching frequencies.

3.3.3.2 Characterisation

X-ray diffraction indicates that very well defined SBA-15 is prepared up to loading levels of 7% CNPTES, as shown by the presence of the (1,1) and (2,0) reflection maxima (figure 3.3.3.2.1). The 10% loading of the functional siloxane is a well ordered sample although a reduction in (1,1) and (2,0) reflection maxima occurs. No significant change in the unit cell (table 3.3.3.2.1) parameter is observed suggesting that the hydrophilic cyano/carboxylic groups do not interact with the micellar ordering.

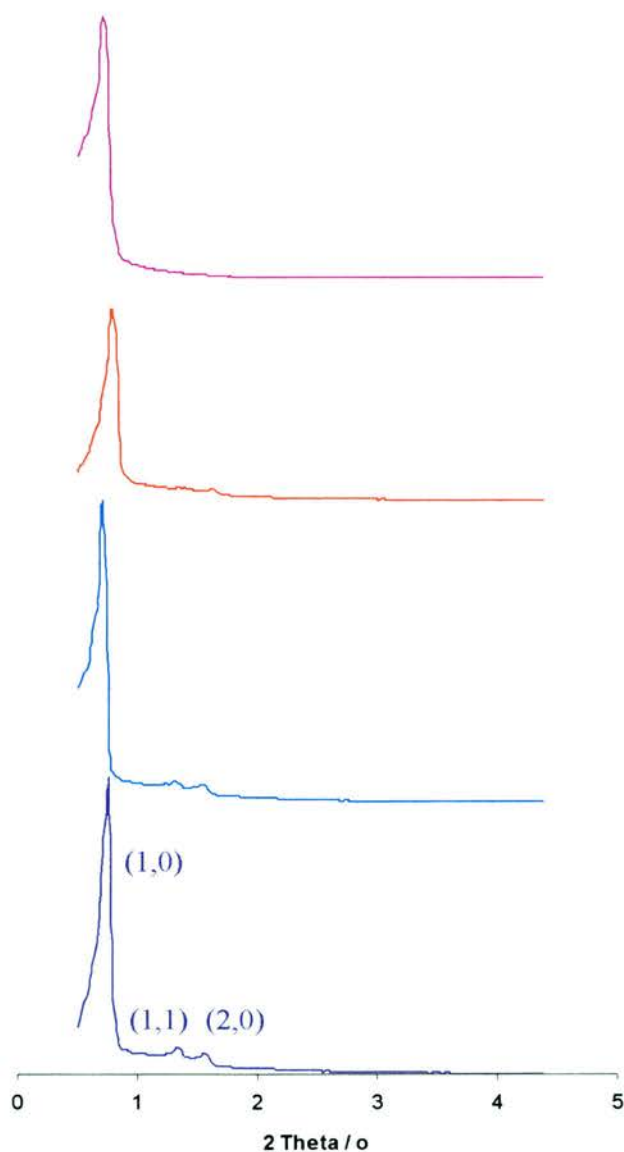


Figure 3.3.3.2.1. XRD diffraction patterns of SBA-15 functionalised with 2% CNPTES, 5% CNPTES, 7% CNPTES and 10% CNPTES showing diffractograms expected of p6mm symmetry

Sample	XRD interplanar d spacing / Å	Unit cell / Å
2% CNPTES	100 ^a	116 ^b
5% CNPTES	108 ^a	124 ^b
7% CNPTES	98 ^a	113 ^b
10% CNPTES	108 ^a	124 ^b

Interplanar spacing – ^ad₁₀₀; ^bhexagonal lattice parameter,

Table 3.3.3.2.1. Interplanar spacing and unit cell parameters of cyano-functionalised mesoporous silica templated by P123 by XRD

Scanning electron microscopy reveals the retention of typical ‘worm-like’ SBA-15 morphology at all CNPTES loadings (figure 3.3.3.2.2) and HRTEM all show mesostructure typical of SBA-15, even at 10% loading (figure 3.3.3.2.3).

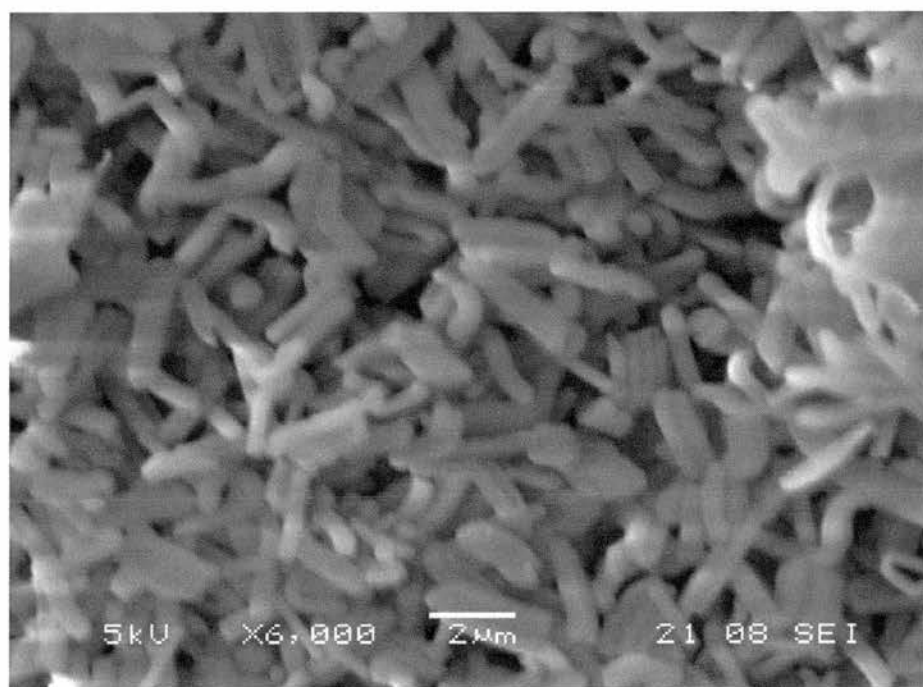


Figure 3.3.3.2.2. Scanning electron micrograph of mesoporous silica templated by P123 showing ‘worm-like’ morphology typical of *in situ* functionalisation with all CNPTES loadings

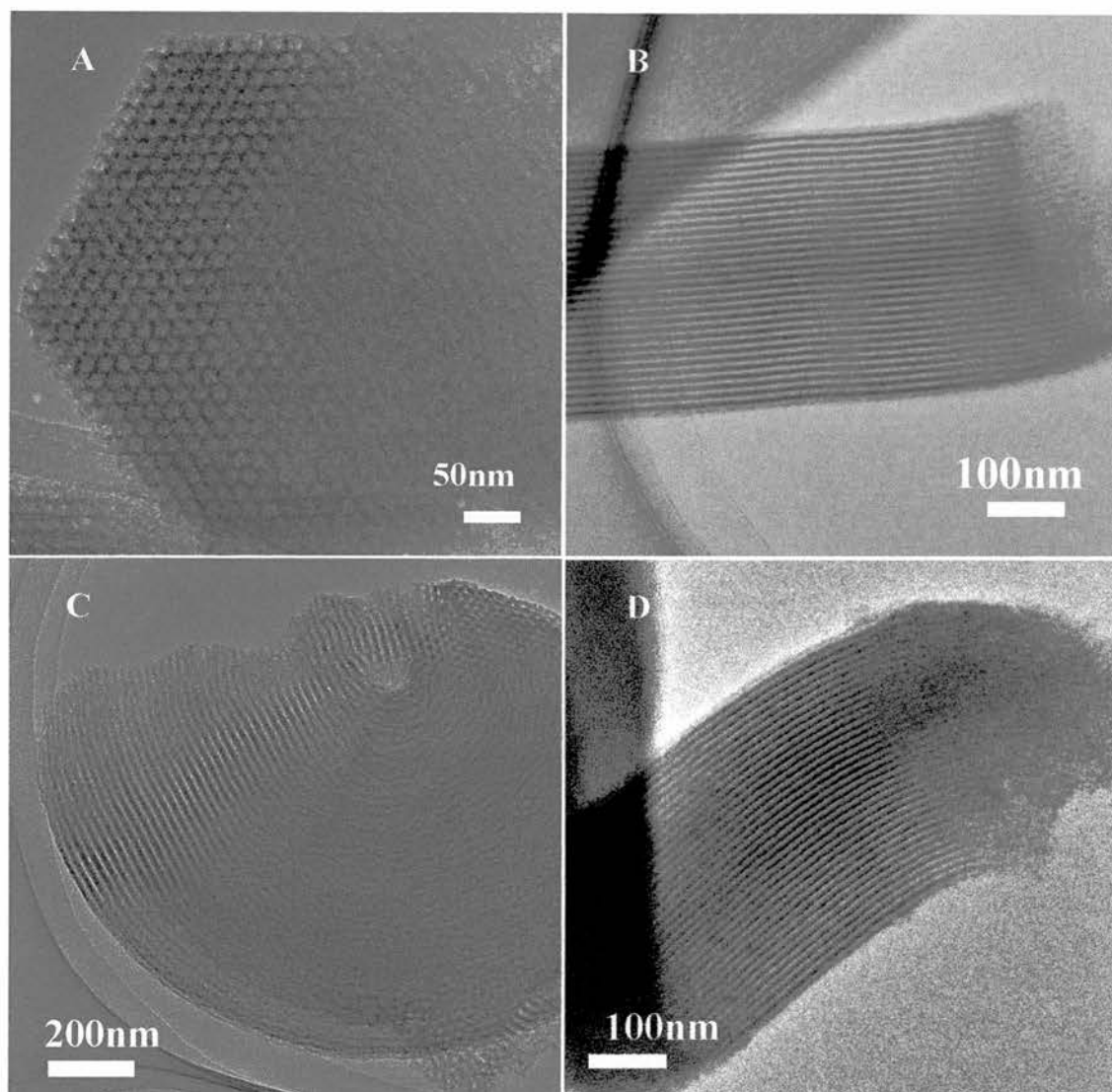


Figure 3.3.3.2.3. HRTEM micrographs of CNPTES functionalised mesoporous silicas templated by P123 surfactant showing SBA-15 in all cases. (A) 2% CNPTES with pores running parallel to the incident electrons; (B) 5% CNPTES with pores perpendicular to the electron beam; (C) 7% CNPTES showing pores orientated perpendicular (E) to the incident beam and (D) 10% CNPTES with SBA-15 channels perpendicular to the beam

The nitrogen adsorption isotherms further illustrate that the addition of this functionalised siloxane has relatively little effect on the pore structure, with all samples displaying well defined type IV isotherms and defined H_1 hysteresis loops with high N_2 adsorption capacity (figure 3.3.3.2.4).

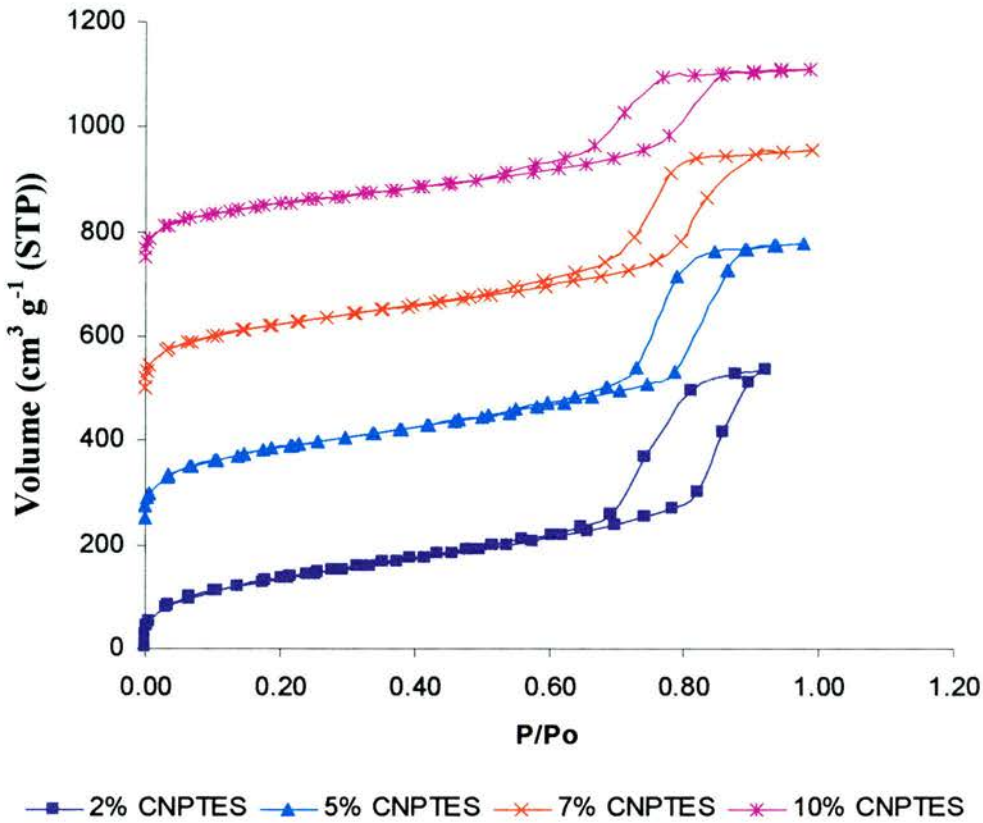


Figure 3.3.3.2.4. Nitrogen adsorption/desorption isotherms of extracted CNPTES functionalised silicas templated by P123. Isotherms are off-set by $250 \text{ cm}^3 \text{ (STP) / g}$ for clarity.

The pore size (figure 3.3.3.2.5) of these samples decrease slightly upon increase of the organo-siloxane indicating that the groups are protruding within the pores and further show a non-broad distribution of pores as indicated from the narrow capillary condensation at high relative pressures. Porosity data can be seen in table 3.3.3.2.1.

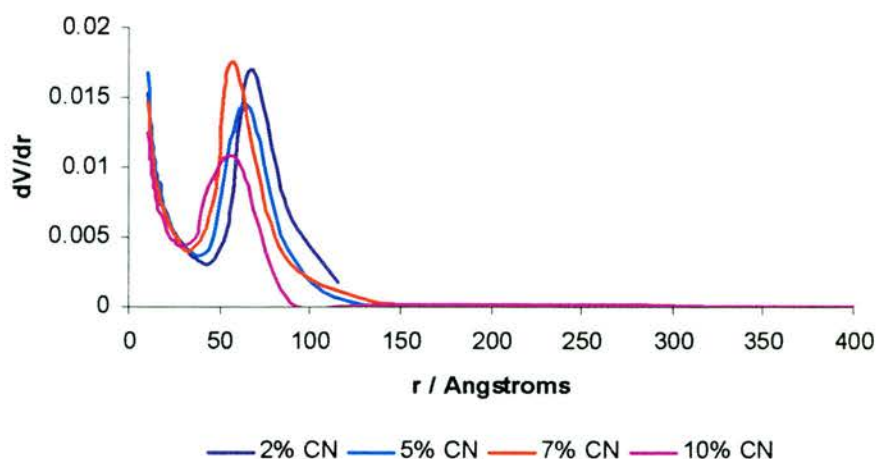


Figure 3.3.3.2.5. Pore size distribution curves calculated on the De Boer model for extracted CNPTES functionalised mesoporous silicas templated by P123

Material	*Specific surface area BET m^2/g	+Pore size mode \AA	Total N_2 uptake cm^3 (STP) g^{-1}
SiO_2 2% CN - extracted	472	134	536 (67 wt%)
SiO_2 5% CN - extracted	500	128	528 (66 wt%)
SiO_2 7% CN - extracted	442	116	456 (57 wt%)
SiO_2 10% CN - extracted	370	112	360 (45 wt%)

*BET surface area calculated within 0.05 – 0.4 P/P_0 .

+Pore size distribution calculated on the adsorption branch of the isotherm using the de Boer model. Taken as the maximum in the pore size distribution curve

Table 3.3.3.2.1. Porosity measurements of extracted cyano-functionalised mesoporous silica templated by P123

The isotherms of the calcined samples (figure 3.3.3.2.6) show the same trend with increased specific surface areas and adsorption capacity due to the removal of both organic functionality and organic template along with a reduction in pore size (figure 3.3.3.2.7) through unit cell contraction as further condensation of the framework at high temperatures arise.

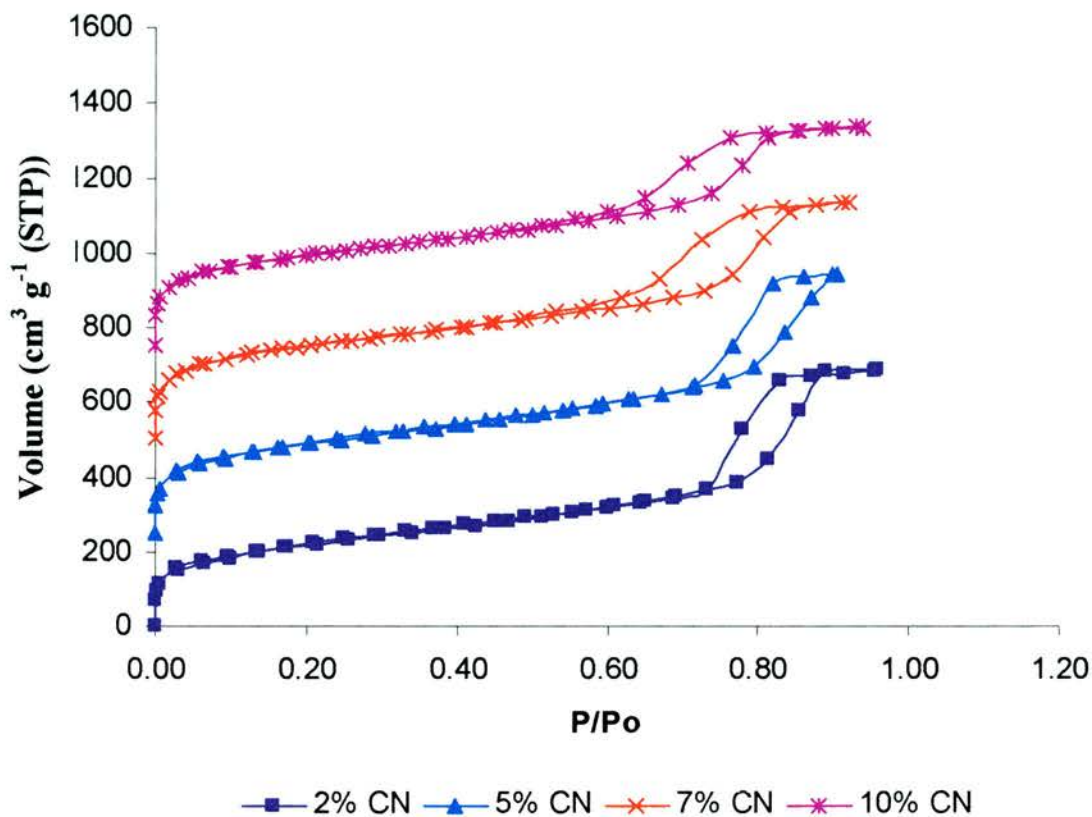


Figure 3.3.3.2.6. Nitrogen adsorption/desorption isotherms of calcined CNPTES functionalised silicas templated by P123. Isotherms are off-set by $250 \text{ cm}^3 \text{ (STP) / g}$ for clarity.

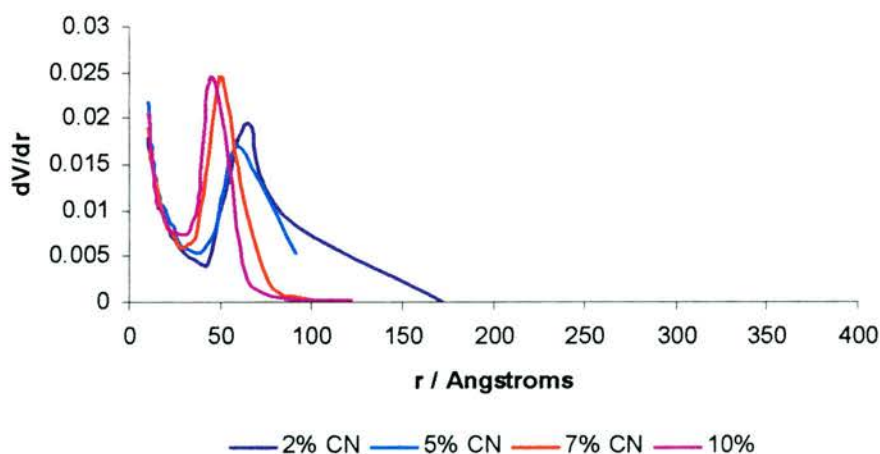


Figure 3.3.3.2.7. Pore size distribution curves calculated on the De Boer model for calcined CNPTES functionalised mesoporous silicas templated by P123

Material	*Specific surface area BET m ² /g	+Pore size mode Å	Total N ₂ uptake cm ³ (STP) g ⁻¹
SiO ₂ 2% CN - calcined	732	130	688 (86 wt%)
SiO ₂ 5% CN - calcined	797	116	696 (87 wt%)
SiO ₂ 7% CN - calcined	829	102	632 (79 wt%)
SiO ₂ 10% CN - calcined	792	88	592 (74 wt%)

*BET surface area calculated within 0.05 – 0.4 P/P₀.

+Pore size distribution calculated on the adsorption branch of the isotherm using the de Boer model. Taken as the maximum in the pore size distribution curve

Table 3.3.3.2.2. Porosity measurements of calcined cyano-functionalised mesoporous silica templated by P123

3.3.3.3 Conclusions

Inclusion of CNPTES in the synthesis at all loadings leads to the formation of hexagonal SBA-15. The degree of the structural regularity is generally of a high quality. By the 10% loading the long-range order (to XRD) is diminishing but according to HRTEM and N₂ adsorption there is good local structural order remaining. The morphology throughout shows elongated ‘worm-like’ particles and the HRTEM micrographs show the characteristic structure. Overall, it is possible to incorporate higher loadings of CNPTES compared to the other organo-siloxanes whilst still retaining order on the mesoscale and the mesoporosity is still very well defined, even at the 10% loading as seen by the corresponding isotherms. Parallel studies using the similar additive CNPTES indicate that by careful manipulation of the preparative conditions, up to 20% of the functional group can be added *in situ* without appreciable loss of pore structure [49].

3.3.4 Chloro-functionalised mesoporous silica templated by P123.

The inclusion of chloropropyl groups onto the internal surface of mesoporous silicas offers a convenient route to further functionalisation of the solid, via reactions such as the reaction of amines with the chloride group (scheme 3.3.4.1). Previous work had shown that the propylchloride groups incorporated at 5% could be clearly recognised by analysis of solid state ^{13}C MAS NMR [50].



Scheme 3.3.4.1. Nucleophilic substitution, $\text{S}_{\text{N}}2$, of a secondary amine onto a halogenoalkane

This route is investigated further in Chapter 5. In order to confirm that the chloropropyl group can be included at acceptable levels without disruption of the structure, a series of chloropropyl-containing silicas were prepared using the P123 block copolymer and characterised by XRD, TEM and N_2 adsorption in the usual way.

3.3.4.1 Characterisation

XRD shows that a maximum loading of 5% chloropropyltriethoxysilane (CLPTES) can be obtained by co-condensation with retention of reasonable long-range order (figure 3.3.4.1.1). Increasing the organic-group in the sol-gel mixture above this results in poorly ordered materials. The 2% CLPTES sample gives a typical XRD diffractogram of $p6mm$ symmetry with the main (10) peak and the secondary (11) and (20) reflections as well. By 5% these secondary reflections are not observed although some poorly defined maxima are still observed. At 7% and 10% the order is very strongly reduced. Structural parameters based on XRD results are given in table 3.3.4.1.1.

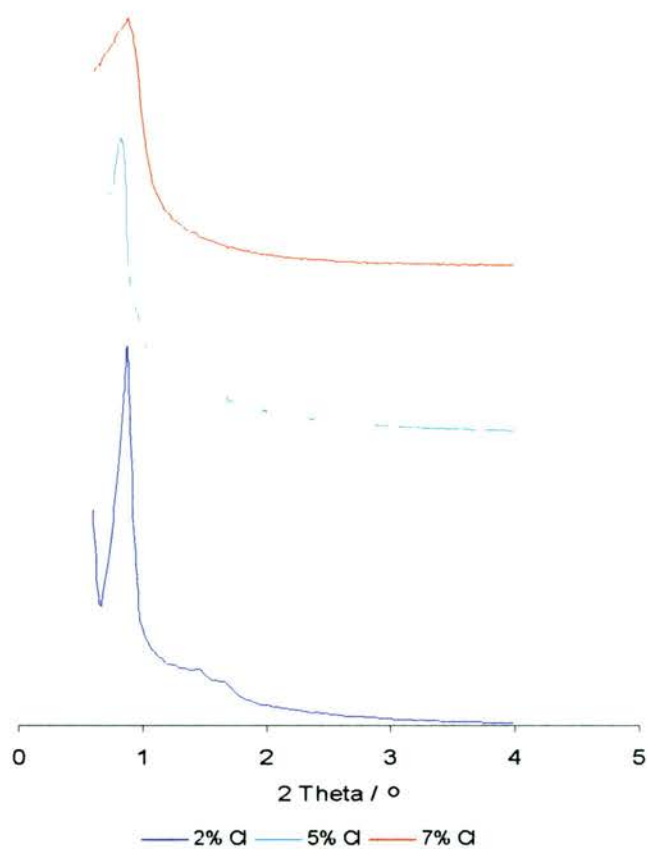


Figure 3.3.4.1.1. X-ray diffraction patterns of chloropropyl functionalised SBA-15 containing templated by Pluronic P123. Bottom to top: 2% CIPTES; 5% CIPTES and 7% CIPTES

Sample	XRD interplanar d spacing / Å	Unit cell / Å
2% CIPTES	100 ^a	116 ^b
5% CIPTES	108 ^a	124 ^b
7% CIPTES	100 ^a	116 ^b

Interplanar spacing – ^ad₁₀₀; ^bhexagonal lattice parameter

Table 3.3.4.1.1. Interplanar spacing and unit cell parameters of chloro-functionalised mesoporous silica templated by P123 by XRD

SEM (figure 3.3.4.1.2) reveals there to be both the ‘worm-like’ and spherical morphology present in all levels of loading although no cubic phase is observed. Unlike the change in morphology that is accompanied with a phase change in the case of SBA-15/STA-11 with thiol addition, a change in morphology showing no difference in structure can be explained by variations in the surface free energy, F , as reported by Zhao [51].

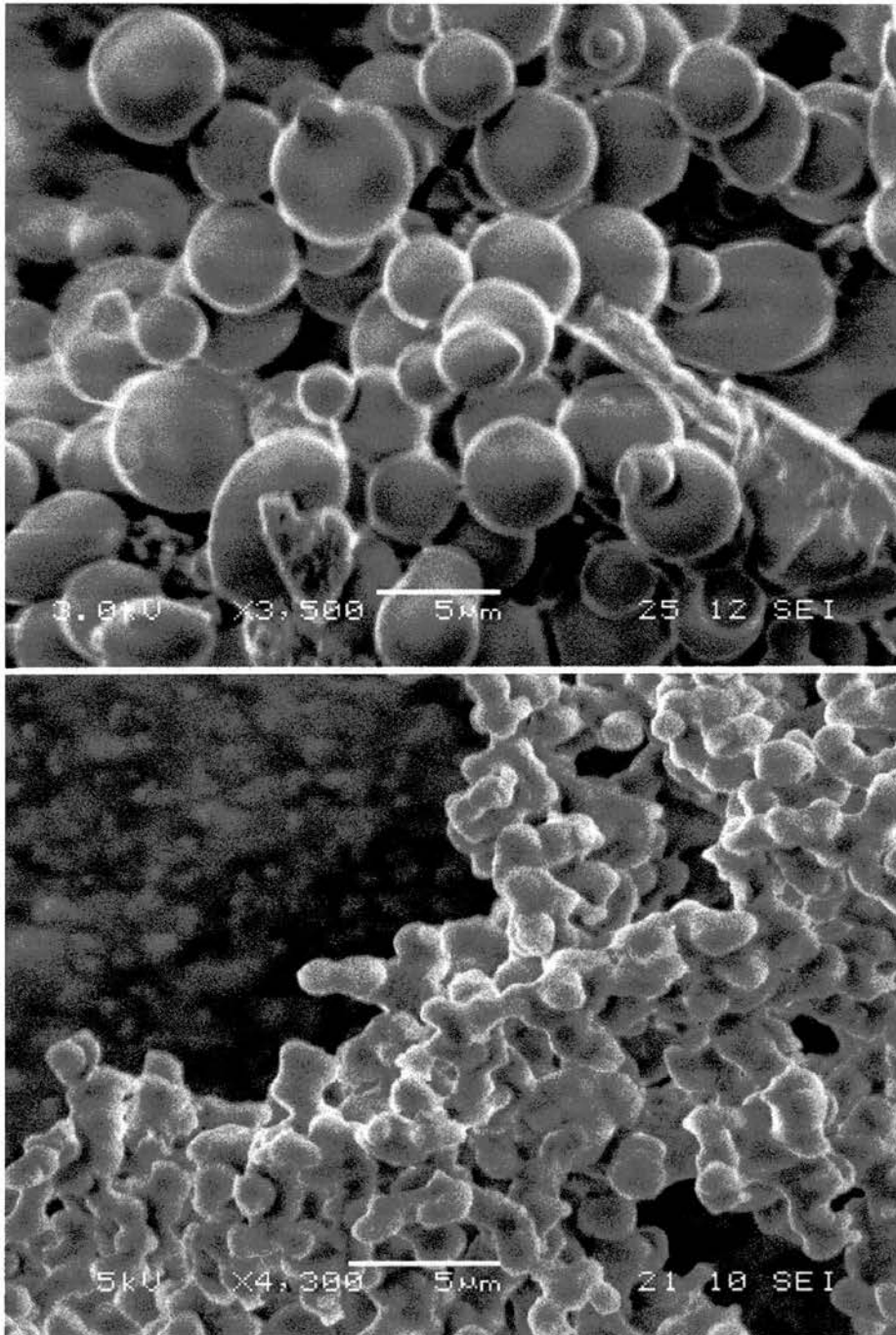
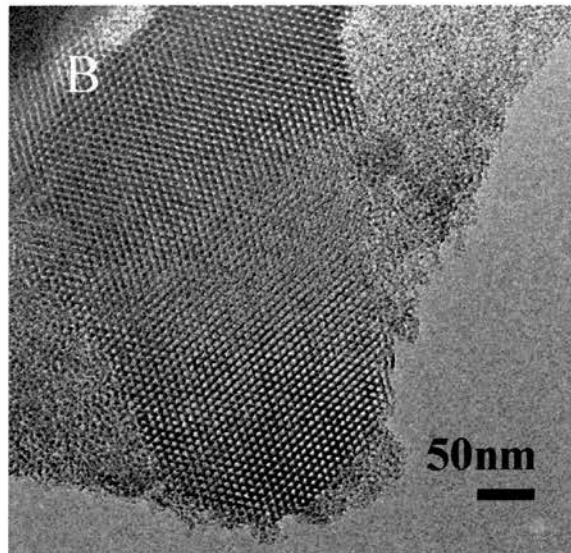
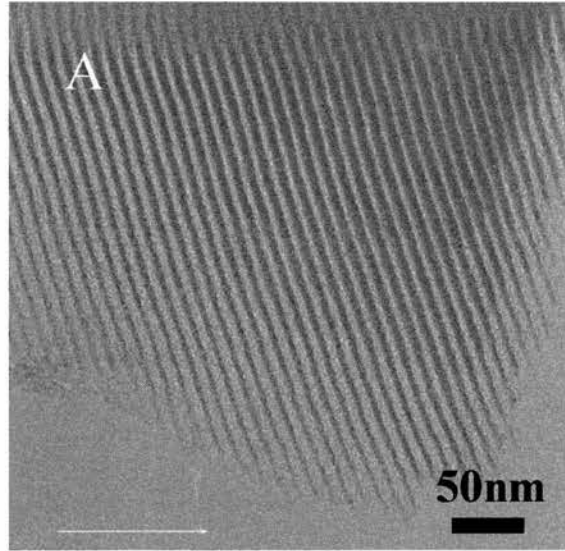


Figure 3.3.4.1.2. SEM micrographs of CIPTES containing solids displaying spherical (above) and a mix of spherical/‘worm-like’ morphologies.

Transmission electron microscopy reveals the SBA-15 hexagonal structure for both the 2% and 5% CIPTES solids which both possess good local structural regularity (figure 3.3.4.1.3). The loadings of 2% and 5% correspond to the hexagonal symmetry with no observations of the cubic $Ia\bar{3}d$ symmetry whilst for the 7% and 10% CIPTES loadings just amorphous silica is the ensemble of the silica framework (not shown).



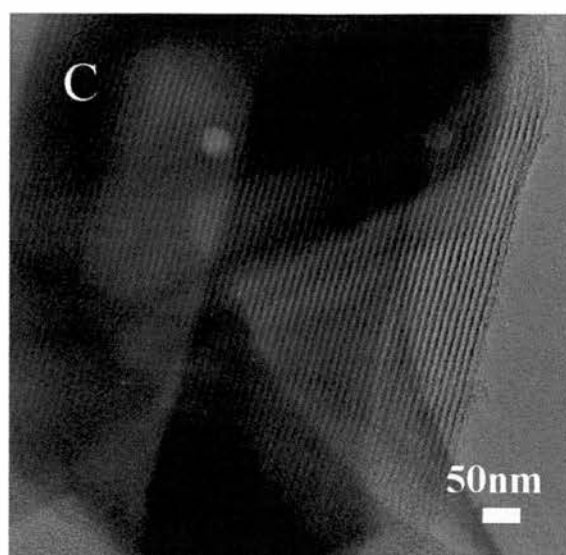


Figure 3.3.4.1.3. HRTEM micrographs of mesoporous silica templated by P123 functionalised with CIPTES showing hexagonal SBA-15 geometry with (A) displaying the channels running perpendicular to the incident electrons for the 2% loading; the 5% solid with (B) the pores parallel and (C) perpendicular to the electron beam

The rapid loss of structural order as the loading level of CIPTES is increased is reflected in the N_2 adsorption isotherms. Loadings above 5% result in isotherms without defined capillary adsorptions and also a lowered capacity for N_2 . The extracted isotherms (figure 3.3.4.1.4) reveal that a high uptake of N_2 is observed for the 2% and 5% CIPTES samples and that capillary condensation occurs around P/P_0 of 0.8. The 7% CIPTES containing sample shows a similar uptake of N_2 compared to the 5% solid but does not possess a well-defined hysteresis and by 10% there is a much lower uptake and further reduced hysteresis loop. The pore size distribution of such solids (figure 3.3.4.1.5) indicates that large pore materials are formed in line where the capillary condensation for the 2% and 5% solids occurs. A reduction of pore size is observed in the 5% CIPTES solid but the high loading materials do not show a defined distribution due to the broad region of the higher pressure end of the isotherms. Adsorption parameters are shown in table 3.3.4.1.2.

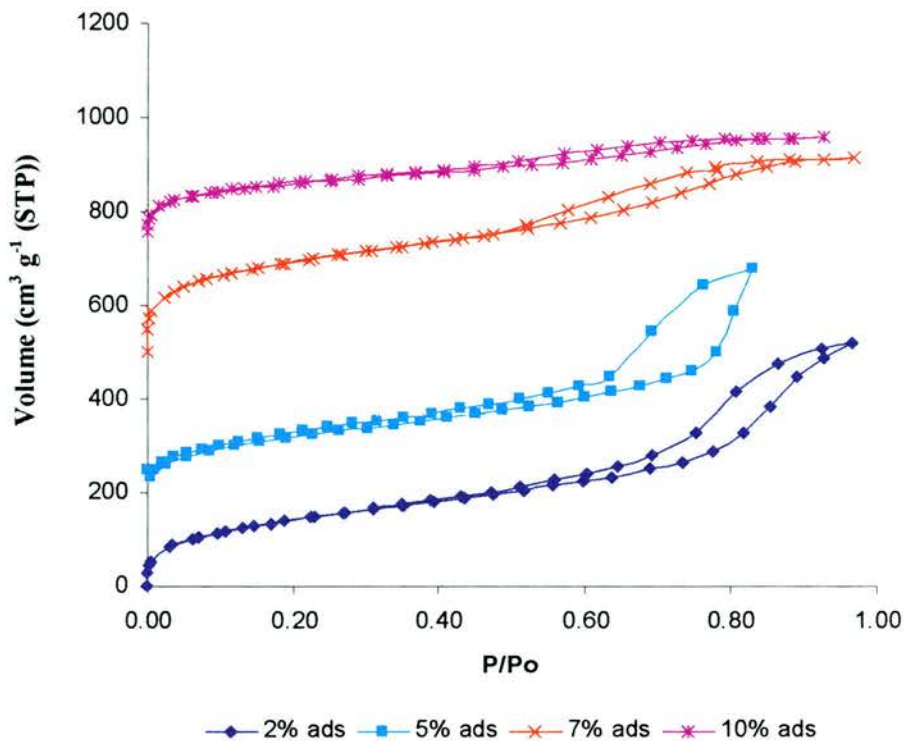


Figure 3.3.4.1.4. N_2 adsorption/desorption isotherms of extracted CIPTES containing samples templated by P123. Isotherms are off-set by $250 \text{ cm}^3 \text{ (STP) / g}$ for clarity

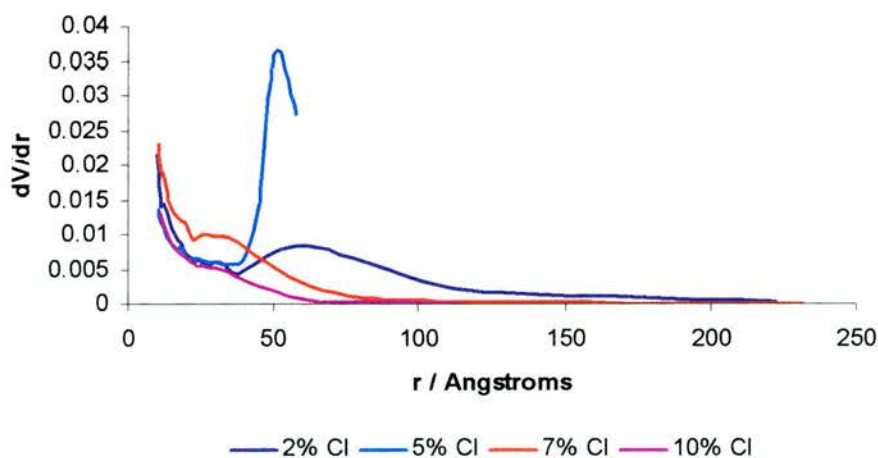


Figure 3.3.4.1.5. Pore size distribution curves calculated on the De Boer model for extracted CIPTES functionalised mesoporous silicas templated by P123

Material	*Specific surface area BET m ² /g	+Pore size mode Å	Total N ₂ uptake cm ³ (STP) g ⁻¹
SiO ₂ 2% Cl - extracted	509	130	520 (65 wt%)
SiO ₂ 5% Cl - extracted	347	102	432 (54 wt%)
SiO ₂ 7% Cl - extracted	642	-	416 (52 wt%)
SiO ₂ 10% Cl - extracted	368	-	208 (26 wt%)

*BET surface area calculated within 0.05 – 0.4 P/P₀.

+Pore size distribution calculated on the adsorption branch of the isotherm using the de Boer model. Taken as the maximum in the pore size distribution curve

Table 3.3.4.1.2. Porosity measurements of extracted chloro-functionalised mesoporous silica templated by P123

Similar trends are also observed for the calcined analogues with the increase in adsorption capacity as residual surfactant is no longer observed to be present. Again the isotherms (figure 3.3.4.1.6) are only defined for the 2% and 5% CIPTES containing samples. The relative pore size distributions are given in figure 3.3.4.1.7 and further analysis in table 3.3.4.1.3.

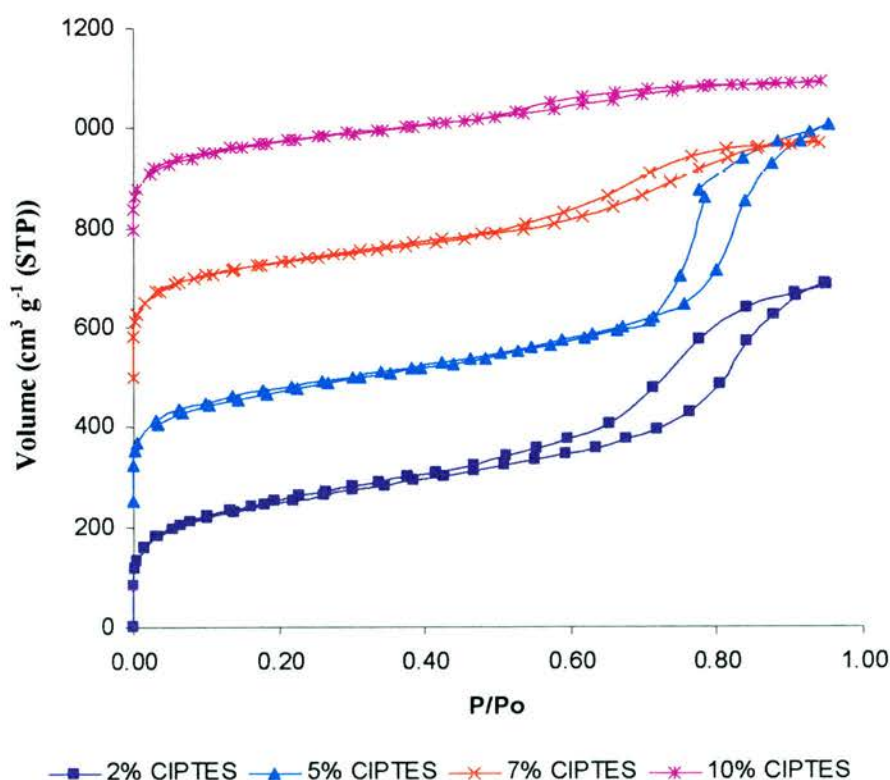


Figure 3.3.4.1.6. N₂ adsorption/desorption isotherms of CIPTES containing samples templated by P123 then calcined. Isotherms are off-set by 250 cm³ (STP) / g for clarity

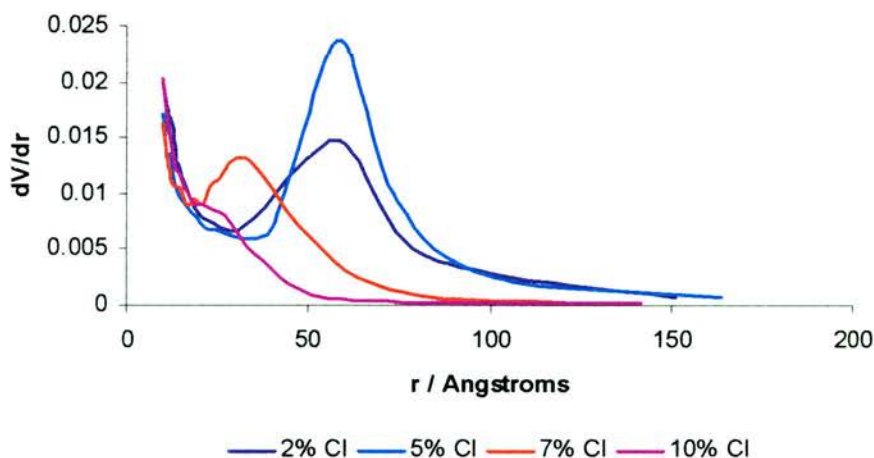


Figure 3.3.4.1.7. Pore size distribution curves calculated on the De Boer model for calcined CIPTES functionalised mesoporous silicas templated by P123

Material	*Specific surface area BET m ² /g	+Pore size mode Å	Total N ₂ uptake cm ³ (STP) g ⁻¹
SiO ₂ 2% Cl - calcined	797	120	688 (86 wt%)
SiO ₂ 5% Cl - calcined	738	118	750 (95 wt%)
SiO ₂ 7% Cl - calcined	722	-	472 (59 wt%)
SiO ₂ 10% Cl - calcined	695	-	336 (42 wt%)

*BET surface area calculated within 0.05 – 0.4 P/P₀.

+Pore size distribution calculated on the adsorption branch of the isotherm using the de Boer model. Taken as the maximum in the pore size distribution curve

Table 3.3.4.1.3. Porosity measurements of calcined chloro-functionalised mesoporous silica templated by P123

3.3.4.2 Conclusions

Propylchloride containing samples with 2% loadings give well-ordered hexagonal SBA-15 symmetry, but a 5% loading is the maximum level of incorporation at which the SBA-15 pore structure is retained. The morphology of the CIPTES materials is a mixture of typical ‘worm-like’, spherical and what may be an intermediate morphology. This spherical morphology seems to evolve from the ‘worm-like’ counterpart with either the middle section of the ‘worm-like’ particles tapering inwards at the centre or the ends of the particles curling tighter.

3.4 General Conclusions

The effects of the inclusion of various organo-siloxanes as co-condensing silica species has been investigated in Pluronic P123-templated syntheses of mesoporous silicas in acidic media. Characterisation via diffraction, microscopy and adsorption measurements of the products has established the degree of order and mesoporosity achieved in these preparations. The maximum loading of the co-condensing siloxane that can be included while retaining a high degree of order and well defined mesoporosity, increasing in the sequence propylchloride (5%) , phenyl (5%) < propylthiol (7%) < cyanopropyl (10%), where the maximum molar loading as a percentage of the total siloxane in the preparation is given in brackets.

Under specific levels of loading, both the phenyl- and propylthiol-functionalised samples can condense as cubic silicas with the $Ia\bar{3}d$ symmetry (similar to MCM-48): the solid of this sort with the highest degree of long range order is the material prepared with 7% thiol, designated STA-11. The observed change in product mesophase is attributed to an increase in the surface packing parameter, g , and hence a lower surface curvature of the micellar arrangements from 2D hexagonal $p6mm$ to 3D cubic $Ia\bar{3}d$. It is thought that if the functional groups are hydrophobic enough to interact with the inner PPO portion of the micelle then a change in mesophase can occur also observed for the phenyl-siloxane. The STA-11, $Ia\bar{3}d$ bicontinuous structure possesses potential advantages in catalytic and sorption applications over the SBA-15, $p6mm$ phase in terms of enhanced molecular transport and resistance to pore blocking. In addition the stability of STA-11 is potentially greater than that of SBA-15 as thicker inorganic silica walls forming roughly 40% of the large unit cell of 230 Å make up the solid.

Quantification of the accessible thiol groups in silicas functionalised using 3-Mercaptopropyltriethoxysilane has been achieved via the use of Ellman's reagent in a modified procedure. Typically 50 – 70% accessibility of included thiol groups was measured. Knowing the fraction of accessible groups rather than the total

incorporated into the solid is important if using the thiol groups to further stoichiometrically functionalise the solid or use the organic group in catalysis.

Incorporation of the phenyl-siloxane directly into the sol-gel mixture can form SBA-15 at a 2% loading whereas a 5% loading forms the cubic $Ia\bar{3}d$ product. However, although the cubic symmetry is prominent there are small hexagonal domains indicating that the product is not phase pure.

Functionalisation with the cyano-siloxane allows inclusion at high loadings without loss of order: the phase is always SBA-15 ($p6mm$). Increased levels of loading up to 20% can be included if phase separation of the functional-siloxane occurs before TEOS addition. The hydrophilic cyano groups are partially hydrolysed during synthesis in acidic media and convert to carboxylic groups.

SBA-15 can be prepared directly including chloropropyl groups but the degree of loading is limited before compromising the quality of the final mesoporous product. There is a 5% upper limit when synthesising in this way and so a higher loading could only be achieved via a post-synthetic modification procedure.

Overall, *in situ* functionalisation of SBA-15 and the characterisation of the mesoporous products have been widely investigated as a function of specific loadings of organic-groups to give information on the conditions necessary to form well-defined solids and in doing so has brought about a potentially interesting mesoporous solid, STA-11 with its mentioned advantages. In this way the feasibility of preparing mesoporous solids functionalised in this way as possible catalyst supports has been established.

3.5 References

- [1] J.S. Beck, N.Y. Princeton, US Patent No. 5 057 296, 1991
- [2] C.T. Kresge, M.E. Leonowicz, W.J. Roth, J.C. Vartuli, J.S. Beck, *Nature*, 1992, **359**, 710
- [3] J.S. Beck, J.C. Vartuli, W.J. Roth, M.E. Leonowicz, C.T. Kresge, K.D. Schmitt, C.T.-W. Chu, D.H. Olson, E.W. Sheppard, S.B. McCullen, J.B. Higgins, J.L. Schlenker, *J. Am. Chem. Soc.*, 1992, **114**, 10834
- [4] Y.F. He, N.A. Seaton, *Langmuir*, 2003, **19**, 10132
- [5] M.D. Jones, R. Raja, J.M. Thomas, B.F.G. Johnson, *Top. Catal.* 2003, **25**, 71
- [6] D. Zhao, J. Feng, Q. Huo, N. Melosh, G.H. Fredrickson, B.F. Chmelka, G.D. Stucky, *Science*, 1998, **279**, 548
- [7] D. Zhao, Q. Huo, J. Feng, B.F. Chmelka, G.D. Stucky, *J. Am. Chem. Soc.*, 1998, **120**, 6024
- [8] L.Y. Bronstein, *Top. Curr. Chem.*, 2003 **266**, 55
- [9] H.H.P. Yiu, P.A. Wright, N.P. Botting, *J. Mol. Catal. B Enzyme*, 2001, **15**, 275
- [10] Y. Sakamoto, I. Diaz, O. Terasaki, D.Y. Zhao, J. Pérez-Pariente, J.M. Kim, G.D. Stucky, *J. Phys. Chem. B.*, 2002, **106**, 3118
- [11] Y. Sakamoto, M. Kaneda, O. Terasaki, D.Y. Zhao, J.M. Kim, G.D. Stucky, H.J. Shim, R. Ryoo, *Nature*, 2000, **408**, 449
- [12] H.J. Han, G.D. Stucky, A. Butler, *J. Am. Chem. Soc.*, 1999, **121**, 9897
- [13] H.H.P. Yiu, C.H. Botting, N.P. Botting, P.A. Wright, *Phys. Chem. Chem. Phys.*, 2001, **3**, 2983
- [14] E. Prouzet, F. Cot, G. Nabias, A. Larbot, P. Kooyman, T.J. Pinnavaia, *Chem. Mater.*, 1999, **11**, 1498
- [15] J.L. Blin, A. Léonard, B.L. Su, *Chem. Mater.*, 2001, **13**, 3542
- [16] G.S. Attard, J.C. Glyde, C.G. Göltner, *Nature*, 1995, **378**, 366
- [17] S.A. El-Safty, T. Hanaoka, *Chem. Mater.*, 2003, **15**, 2892
- [18] S.A. El-Safty, T. Hanaoka, *Chem. Mater.*, 2004, **16**, 384
- [19] P. Feng, X. Bu, G.D. Stucky, D.J. Pine, *J. Am. Chem. Soc.*, 2000, **122**, 994
- [20] C.Z. Yu, Y.H. Yu, D.Y. Zhao, *Chem. Commun.*, 2000, **7**, 575
- [21] J. Fan, C.Z. Yu, T. Gao, J. Lei, B.Z. Tian, L.M. Wang, Q. Luo, B. Tu, W.Z. Whou, D.Y. Zhao, *Angew. Chem. Int. Ed.*, 2003, **42**, 3146

- [22] L.M. Wang, H. Fan, B.Z. Tian, H.F. Yang, C.Z. Yu, B. Tu, D.Y. Zhao, *Micro. Meso. Mater.*, 2004, **67**, 135
- [23] S.A. El-Safty, T. Hanaoka, Nanotechnology in mesostructured materials, **146**, 2003, 173
- [24] R.P. Hodgkins, A.E. Garcia-Bennett, P.A. Wright, *Micro. Meso. Mater.*, 2005, **79**, 241
- [25] P.Y. Feng, X.H. Bu, D.J. Pine, *Langmuir*, 2000, **16**, 5304
- [26] S.S. Kim, A. Karkamkar, T.J. Pinnavaia, M. Kruk, M. Jaroniec, *J. Phys. Chem. B.*, 2001, **105**, 7663
- [27] S.S. Kim, T.R. Pauly, T.J. Pinnavaia, *Chem. Commun.*, 2000, **17**, 1661
- [28] X. Liu, B. Tian, C. Yu, F. Gao, S. Xie, B. Tu, R. Che, L.M. Peng, D. Zhao, *Angew. Chem. Int. Ed.*, 2002, **41**, 3876
- [29] B.Z. Tian, X.Y. Liu, L.A. Solovyov, Z. Liu, H.F. Yang, Z.D. Zhang, S.H. Xie, F.Q. Zhang, B. Tu, C.Z. Yu, O. Terasaki, D.Y. Zhao, *J. Am. Chem. Soc.*, 2004, **126**, 865
- [30] Y.T. Chan, H.P. Lin, C.Y. Mou, S.T. Liu, *Chem. Commun.*, 2002, **23**, 2878
- [31] K. Flodstrom, V. Alfredsson, N. Kallrot, *J. Am. Chem. Soc.*, 2003, **125**, 4402
- [32] A.E. Garcia-Bennett, PhD thesis, University of St. Andrews, September 2002
- [33] F. Kleitz, S.H. Choi, R. Ryoo, *Chem. Commun.*, 2003, **17**, 2136
- [34] Y.Q. Wang, C.M. Yang, B. Zibrowius, B. Spliethoff, M. Lindén, F. Schüth, *Chem. Mater.*, 2003, **15**, 5029
- [35] S. Che, A.E. Garcia-Bennett, X. Liu, R.P. Hodgkins, P.A. Wright, D. Zhao, O. Terasaki, T. Tatsumi, *Angew. Chem. Int. Ed.*, 2003, **42**, 3930
- [36] M. Templin, A. Franck, A. DuChesne, H. Leist, Y.M. Zhang, R. Ulrich, V. Schadler, U. Wiesner, *Science*, 1997, **278**, 1795
- [37] K.W. Gallis, C.C. Landry, *Chem. Mater.*, 1997, **9**, 2035
- [38] G.L. Ellman, K.D. Courtney, R.B. Merrifield, *J. Am. Chem. Soc.*, 1972, **94**, 3102
- [39] J.P. Badyal, A.M. Cameron, N.R. Cameron, D.M. Coe, R. Cox, B.G. Davis, L.J. Oates, G. Oyc, P.G. Steel, *Tetrahedron Lett.*, 2001, **42**, 8531
- [40] A.S.M. Chong, X.S. Zhao, A.T. Kustedjo, S.Z. Qiao, *Micro. Meso. Mater.*, 2004, **72**, 33
- [41] S. Che, K. Lund, T. Tatsumi, S. Iijima, S.H. Joo, R. Ryoo, O. Terasaki, *Angew. Chem. Int. Ed.*, 2003, **42**, 2182

- [42] K. Schumacher, P.I. Ravikovitch, A. Du Chesne, A. V. Neimark, K.K. Unger, *Langmuir*, 2000, **16**, 4648
- [43] P.I. Ravikovitch, A.V. Neimark, *Langmuir*, 2000, **16**, 2419
- [44] M. Kruk, M. Jaroniec, R. Ryoo, J.M. Kim, *Chem. Mater.*, 1999, **11**, 2568
- [45] M. Kaneda, T. Tsubakiyama, A. Carlsson, Y. Sakamoto, T. Ohsuna, O. Terasaki, S.H. Joo, R. Ryoo, *J. Phys. Chem. B.*, 2002, **106**, 1256
- [46] W.D. Bossaert, D.E. De Vos, W.M. Van Rhijn, J. Bullen, P.J. Grobet, P.A. Jacobs, *J. Catal.*, 1999, **182**, 156
- [47] P. Ravikovitch, A. Neimark, *Langmuir*, 2002, **18**, 1550
- [48] C.M. Yang, Y. Wang, B. Zibrowius, F. Schüth, *Phys. Chem. Chem. Phys.*, 2004, **6**, 2461
- [49] C.M. Yang, B. Zibrowius, F. Schüth, *Chem. Commun.*, 2003, **14**, 1772
- [50] H.H.P. Yiu, P.A. Wright, N.P. Botting, *J. Mol. Catal. B Enzym.*, 2001, **15**, 81
- [51] C.Z. Yu, J. Fan, B.Z. Tian, D.Y. Zhao, *Chem. Mater.*, 2004, **16**, 889

Chapter 4

Structure & Morphology changes in Propylthiol Functionalised FDU-12

Synopsis

This chapter details the effect of the co-condensation of mercaptopropyltriethoxysilane on the structure and morphology of the large pore mesoporous solid FDU-12. In the absence of the organo-siloxane the mesophase (symmetry $Fm\bar{3}m$) is formed: introducing the thiol functionality results in particles with well defined hexagonal prismatic geometry. Electron microscopic investigation reveals that a structure based on hexagonal close packing (symmetry $P6_3/mmc$) is present in nanodomains along with regions of the cubic close packed structure that include frequent twin planes and stacking faults.

4.1 Introduction

Mesoporous solids [1 – 9] since their discovery [10 – 15] approaching two decades ago have attracted much attention. FDU-12 is a mesoporous silica synthesised using the non-ionic block copolymer F127 as a structure directing agent. The structure of FDU-12 has been shown, by a combination of HRTEM, XRD and N₂ adsorption, to be based on a face centred cubic arrangement (figure 4.1.1) of large pores (10 nm in diameter) [16] separated by amorphous silica walls and connected, one to another, through windows some 4 nm in diameter [17]. The space group symmetry is assigned as Fm-3 m, on the basis of the diffraction data.

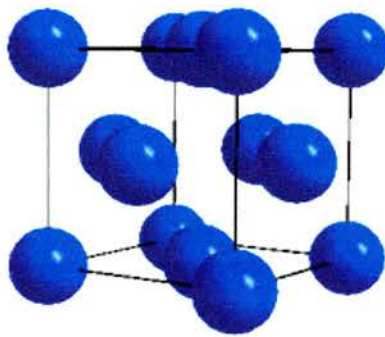


Figure 4.1.1. Face centred cubic arrangement of FDU-12.

The supercage structure of FDU-12 is similar to that reported previously for the cubic regions observed in SBA-2 but on a larger scale [18]. The high connectivity of the cages, the larger window sizes and high surface area suggest applications as templates for new materials [19], catalysis [17] and separations [20].

The block copolymer, F127 (EO₁₀₆PO₇₀EO₁₀₆) that directs the synthesis of FDU-12 is more hydrophilic than the P123 counterpart (EO₂₀PO₇₀EO₂₀) and although P123 can arrange to form both the hexagonal and bicontinuous cubic phases in a simple solution as a function of surfactant concentration and temperature the phase diagram of F127 forms only a cubic mesophase (figure 4.1.2) [21].

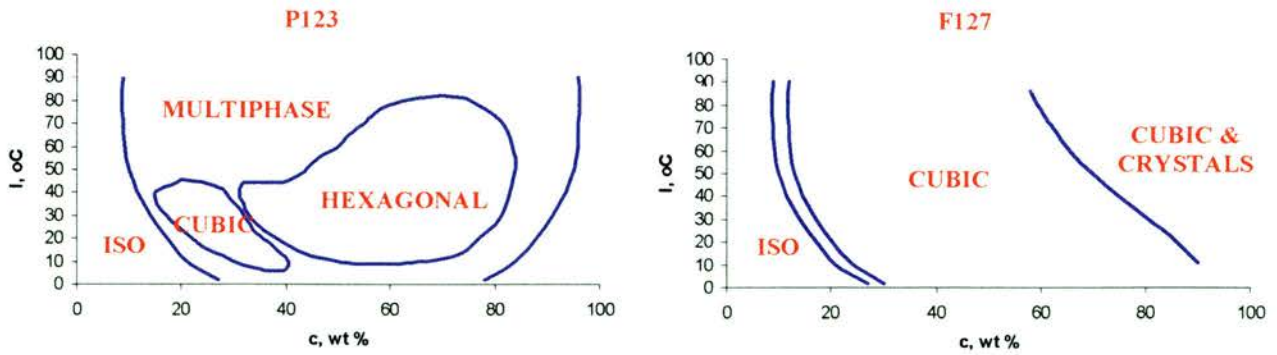


Figure 4.1.2. Illustration of the phase behaviour of concentration solutions of the non-ionic triblock Pluronic surfactants P123 (left) and F127 (right) observing relative structures obtained [21]

In a discussion of the structure of the ‘mesocaged’ silica SBA-1 (Pm3n), Anderson simulates the structure by suggesting that silica wraps around high surface curvature globular micelles giving rise to the cubic phase. The smaller windows connecting the cavities arise as the silica condenses around water coated micelles. The silica is excluded from a region between the micelles by the water coating (figure 4.1.3) [22]. Sizes of cavities and connecting windows depend on the size, shape and contact angle between micelles.

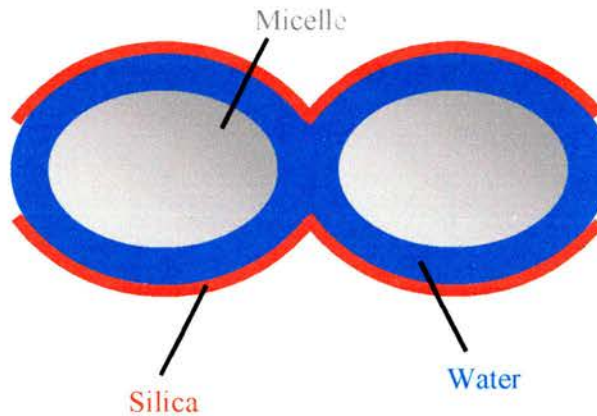


Figure 4.1.3. Water coated globular micelle excludes polymerisation of silica between micelles giving rise to smaller windows connecting cavities

It has been found that varying synthetic conditions for FDU-12 results in variation of pore entrance sizes in the final product. A significant increase in the pore size can be observed while the cavity increases by a much smaller relative amount. The ‘pore engineering’ of mesoporous materials is of importance for applications where various molecular sizes are employed and is a key factor if mesoporous solids are used for the immobilisation of enzymes and for applications in which mass transportation and

diffusion of larger molecules are necessary [17]. Enzyme immobilisation on solid supports facilitates highly selective catalysis using robust materials that are both readily separated from the reaction mixture and can also be recycled [23,24]. 3D pore systems exhibit advantages in mass diffusion compared with 1D channel systems.

In the synthesis of FDU-12, the silicate precursor is added to a strongly acidic solution of F127, together with additives such as inorganic salts (KCl) or organics such as trimethylbenzene (TMB). The role of these additives in the syntheses are incompletely understood, TMB is expected to concentrate within the micelle and enlarge the mesopore size, as in SBA-15, and the window size, in caged mesostructures like FDU-12 [17]. (Decane can also swell the micelles leading to larger pores. It also acts to modify the morphologies: in the case of SBA-15 synthesis it can give SBA-15 with channels running parallel to the short axis [25]).

Highly hydrophilic block copolymers like F127 readily give rise to less ordered mesostructured silica as the interaction of the silica species with the non-ionic block copolymers is weak. This can be overcome by the addition of inorganic additives in the form of salts such as for example KCl, NaCl to the synthesis. This leads to a process called 'salting-out' which lowers the CMC value of the copolymers and gives rise to highly ordered mesoporous silica at lower block copolymer concentrations [26]. Inorganic salts are also thought to improve the ordering as the 'salting-out' process dehydrates the PEO units and renders them more hydrophobic, increasing the silica-block copolymer interactions [17,27].

The small mesopore system SBA-2, is, like FDU-12, thought to be based on the close packing of surfactant micelles. Detailed electron microscopic investigation of SBA-2 has shown the presence of stacking faults that result in different regions possessing different structures, including the end-member hexagonal (ABAB) and cubic (ABCABC) close packed sequences (figure 4.1.4). SBA-2 was first reported [28,29] to contain the 3D hexagonal structure – ($P6_3/mmc$) with a hexagonal close packed, *hcp*, array of pores. After extensive HRTEM studies it was reported [30] that SBA-2 contains a mixture of the hexagonal phase as well as a cubic phase. SBA-12 synthesised with $C_{18}EO_{10}$ (Brij 76) was again first reported to have the 3D hexagonal geometry $P6_3/mmc$ [31] but was later revealed by HRTEM studies to consist mostly

of the cubic close packed phase with relatively small amounts of the 3D hexagonal phase [32].

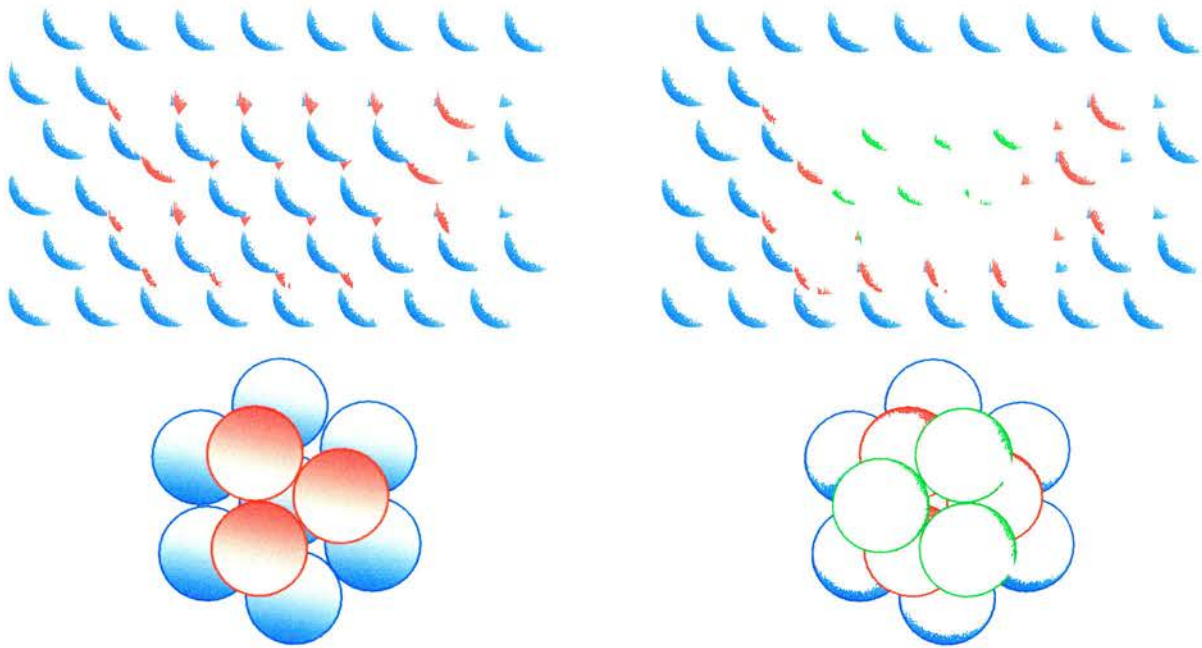


Figure 4.1.4. Close packed structures with the stacking sequence: ABABAB for the hexagonal close packed (*hcp*) array (above left); ABCABCABC for the cubic close packed (*ccp*) array (above right) with a closer look (below)

The well ordered mesoporous solid based on a hexagonal close packed arrangement of micelles/pores, symmetry $P6_3/mmc$, has been reported by Che *et al.* [33] for a small pore silicate prepared under acidic conditions using cetyltriethylammonium bromide (CTAEBR) as surfactant. The material has a distinctive morphology shown in figure 4.1.5 displaying hexagonal tapered prisms [34].

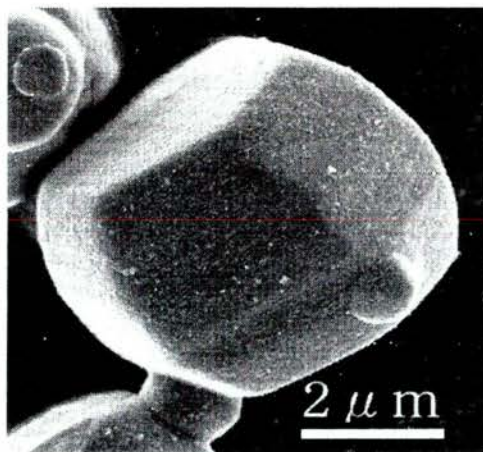


Figure 4.1.5. SEM micrograph of typical morphology of 2D-hexagonal $P6_3/mmc$ [29]

In this chapter, the effects of *in situ* functionalisation of the FDU-12 silica with MPTES are described in detail. As observed for syntheses involving P123, important structural changes are observed as a function of the added thiol groups. In addition, the accessible thiol content of extracted samples is measured via the Ellman's reagent method described in Chapter 3 and compared with the values for the SBA-15/STA-11 system [35].

4.2 Experimental

Synthesis of propylthiol-functionalised silicas using Pluronic F127

FDU-12 was prepared starting from the reported synthesis by Zhao *et al.* [17] for the pure siliceous mesoporous solid. Thiol-functionalised siloxanes were incorporated at levels between 0 – 10% based on total silica. The non-ionic triblock copolymer Pluronic F127 (Prill form; EO₁₀₆PO₇₀EO₁₀₆ Mr_{av.} 12,600; BASF) acts as the surfactant template and TEOS (98% Aldrich) makes up the majority of the silica source for the formation of FDU-12 in the presence of an acidic media and KCl and 1,3,5-trimethylbenzene (TMB) as additives. MPTES (95%, Avocado) added at required concentrations gave sol-gel compositions: (1-x) Si(OEt)₄ : x (EtO)₃Si(CH₂)₃SH : 0.004 F127 : 6.08 HCl : 141 H₂O : 1.70 KCl : 0.42 TMB, 0 ≤ x ≤ 0.10. The surfactant and additives at a temperature of 313 K were dissolved in acidic media and stirred for 24 h before the simultaneous addition of TEOS and MPTES. The sol-gel was stirred continuously at 313 K for a further 24 h followed by hydrothermal treatment in a Teflon bottle under static conditions at 373 K for 72 h. The resulting solid was filtered and air-dried and the template was removed either by calcination or solvent extraction as for the samples with Pluronic P123 (described in chapter 3). The quantification of the accessible thiol groups available to Ellman's reagent was determined as described in Chapter 3. Characterisation of the solids by TEM, XRD, N₂ adsorption along with TGA and CHN analysis is as described previously.

4.3 Results & Discussion

In the first place, solids were prepared and characterised with loadings of 2, 5, 7 and 10% MPTES. The structural and morphological changes observed at 5% and 7% loadings prompted further variation in the synthetic procedure to investigate the effects of temperature, siloxane concentration and the order of addition of the organic functionality and TEOS on the product mesostructure.

4.3.1 Elemental analysis and Ellman's quantification

Elemental analysis on extracted silicas templated by F127 surfactant functionalised with different levels of the MPTES organo-siloxane have been analysed confirming that the trialkoxysilane groups are incorporated into the final silica product in ratios close to those in the sol-gel synthesis apart from the 10% MPTES containing solid where the efficiency of incorporation is slightly lower (table 4.3.1.1).

Non-ionic surfactant	SH loading (based on SiO ₂)	C content	H content	S content	S _{expected}
F127	2%	19.93%	3.78%	0.68%	0.90%
F127	5%	20.11%	3.98%	1.52%	2.20%
F127	7%	12.00%	2.16%	2.67%	2.85%
F127	10%	20.38%	4.04%	3.03%	4.25%

Table 4.3.1.1. Elemental analysis of extracted propyl-thiol functionalised mesoporous silica templated by P123

Ellman's analyses indicate (table 4.3.1.2) that at least 50 – 60 % of the total incorporated thiol groups are accessible to Ellman's reagent, suggesting that at least this fraction is attached to the internal surface of the materials. The Fm-3m/P6₃/mmc

materials show a slightly lower degree of thiol accessibility to the Ellman's reagent compared to the p6mm/1a-3d solids where the accessibility of the thiol groups are in the region of 54 – 76%.

Sample*	% SH accessibility
2% MPTES	50
5% MPTES	56
7% MPTES	60

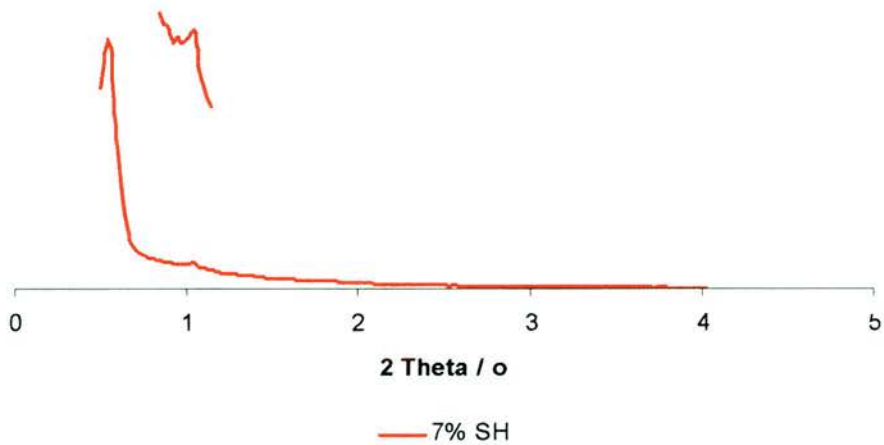
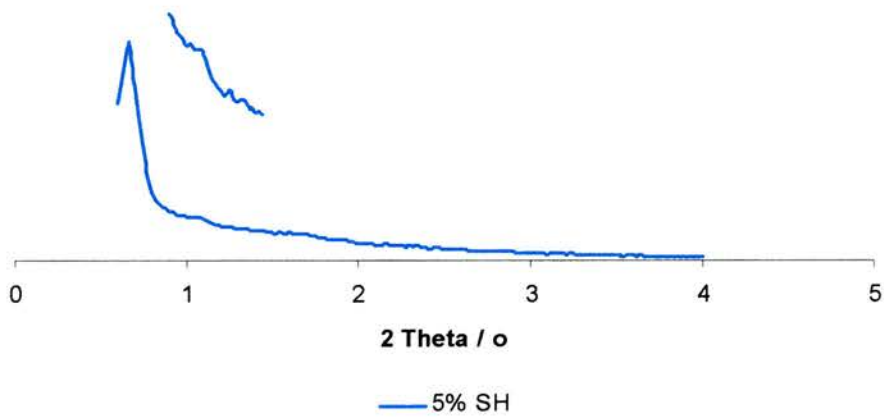
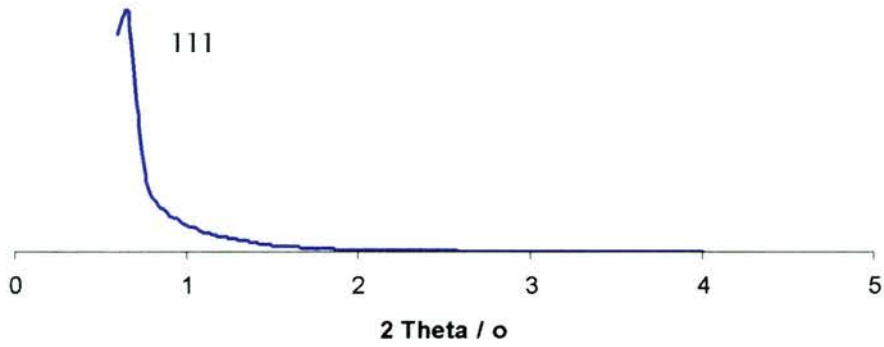
*All samples extracted

Table 4.3.1.2. Quantification of thiol groups via Ellman's reagent for extracted MPTES-functionalised materials templated by P123

4.3.2 XRD characterisation of Thiol-functionalised mesoporous silica templated by F127.

XRD patterns (figure 4.3.2.1) of thiol-functionalised 'FDU-12' samples give poor long-range order throughout the SH loading series. The first and major peak, the (111) reflection, is the only peak present in the scan range for all thiol-functionalised solids and reflects the poor long-range order. The low two theta peak positioning of the (111) reflection for the 2% and 5% solids in the region of $0.65^\circ/2\theta$ suggest similar unit cell size whereas the (111) reflection for the sample containing 7% MPTES is at a lower two theta angle of $0.54^\circ/2\theta$ suggesting a larger unit cell (see figure 4.3.5.1 also – N_2 adsorption measurements with capillary condensation at higher relative pressures). The intensity of the only reflection in the 10% MPTES solid is relatively low compared to the rest reflecting the increased degree of disorder present (the isotherm of this sample also reflects this degree of disorder). The disorder becomes apparent later through TEM (section 4.3.4) upon observation of a significant amount

of disruptions to the stacking sequence which include stacking faults and twin planes. Overall the XRD patterns reflect the local disruptions.



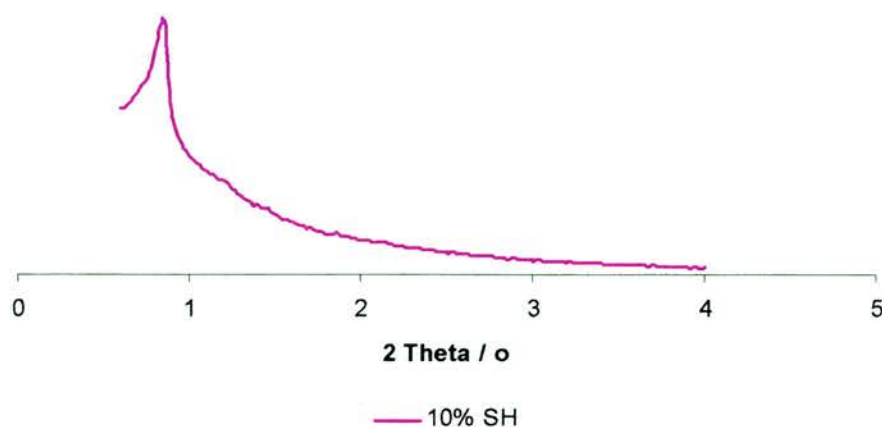


Figure 4.3.2.1. XRD diffractograms of thiol functionalised FDU-12 samples templated by Pluronic F127. Both *ccp* and *hcp* packing are present along with stacking disruptions leading to poor long-range order. XRD patterns are separated for clarity.

4.3.3 SEM characterisation of Thiol-functionalised mesoporous silica templated by F127.

The pure siliceous sample is reported [17] to possess spherical morphology. In the pure silica material prepared in this work there is a suggestion of some faceting and a distinct change in morphology is clearly seen with solids containing MPTES. Scanning electron microscopy reveals in that in the pure silica materials (figure 4.3.3.1A) the shapes are not very well defined, with both rounded and faceted particles present. Increasing the thiol content to 2% (figure 4.3.3.1B) results in a more clearly defined hexagonal prismatic morphology, and by 5% thiol (figure 4.3.3.1C – D) the particles have a clearly defined hexagonal prismatic geometry, tapering towards the basal faces. The 7% thiol-containing sample (figure 4.3.3.1J – K) consists of hexagonal plates, with a much reduced (length/cross sectional area) ratio. At 10% MPTES (figure 4.3.3.1L) no clear particle morphology is observed.

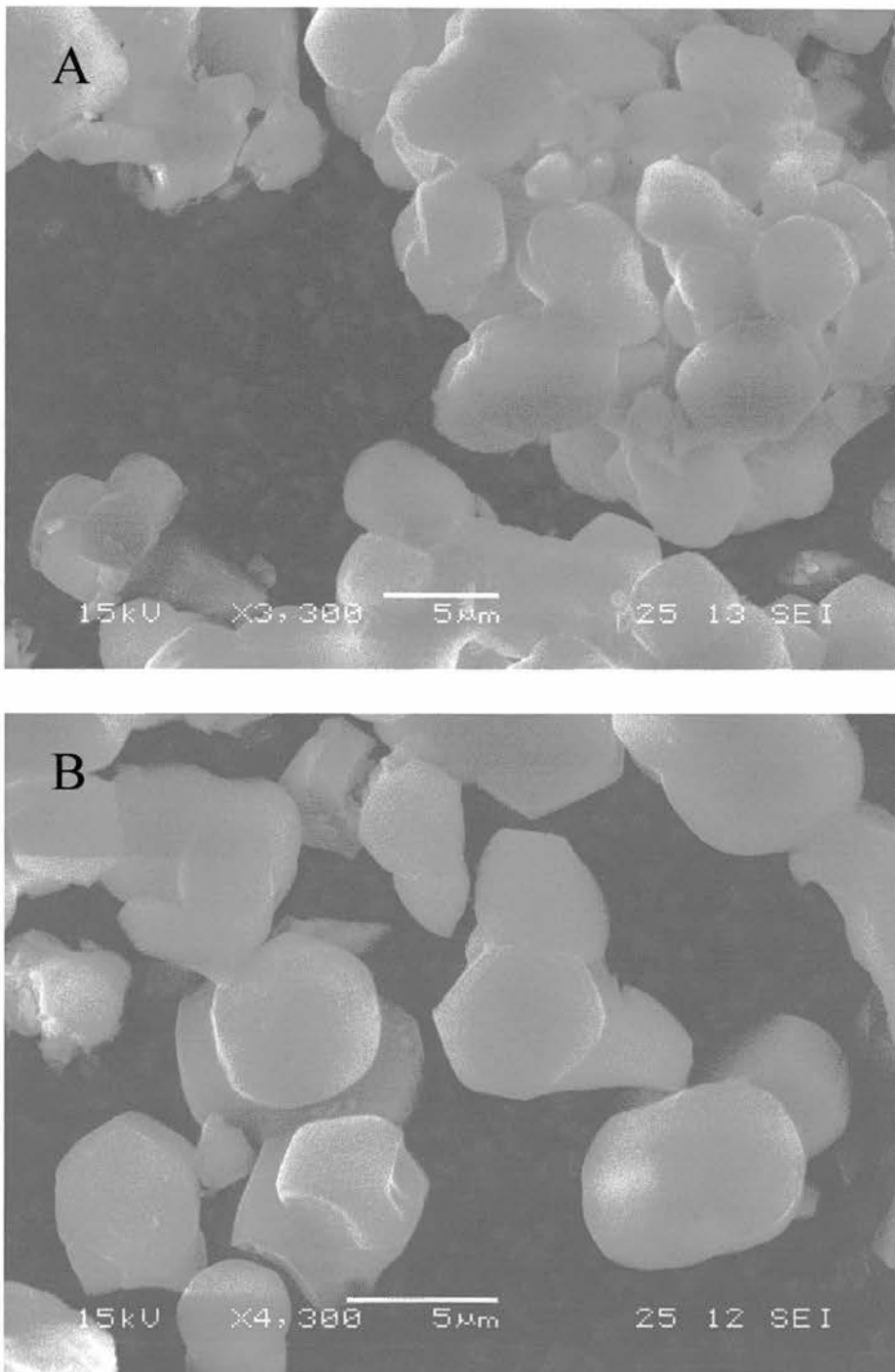


Figure 4.3.3.1. SEM micrographs of (A) pure siliceous FDU-12 showing poorly defined morphology; (B) 2% MP TES loading tending towards a hexagonal prismatic morphology

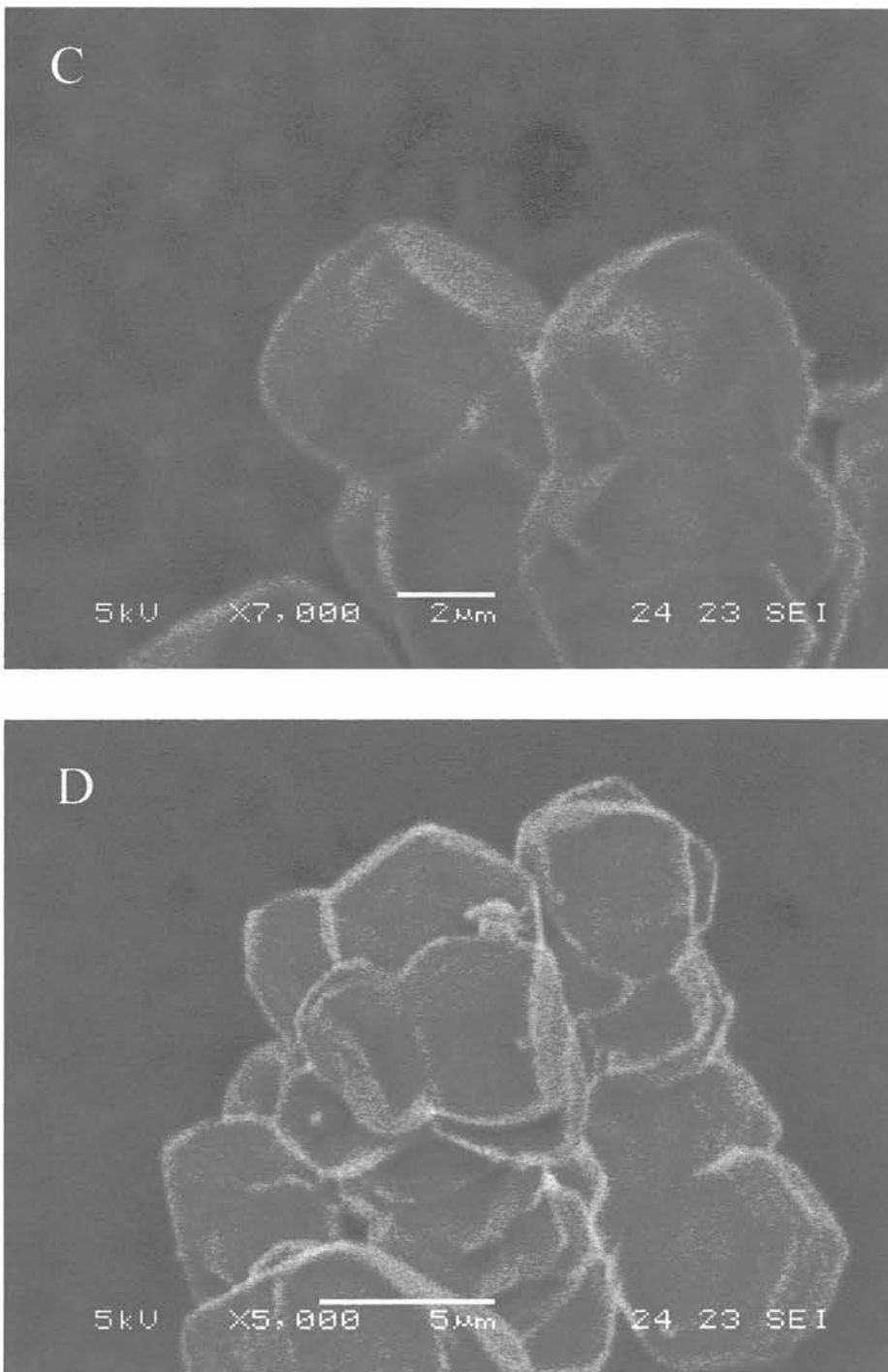


Figure 4.3.3.1. SEM micrographs (C – D) of FDU-12 loaded with 5% MP TES showing hexagonal prisms with clear sharp edges

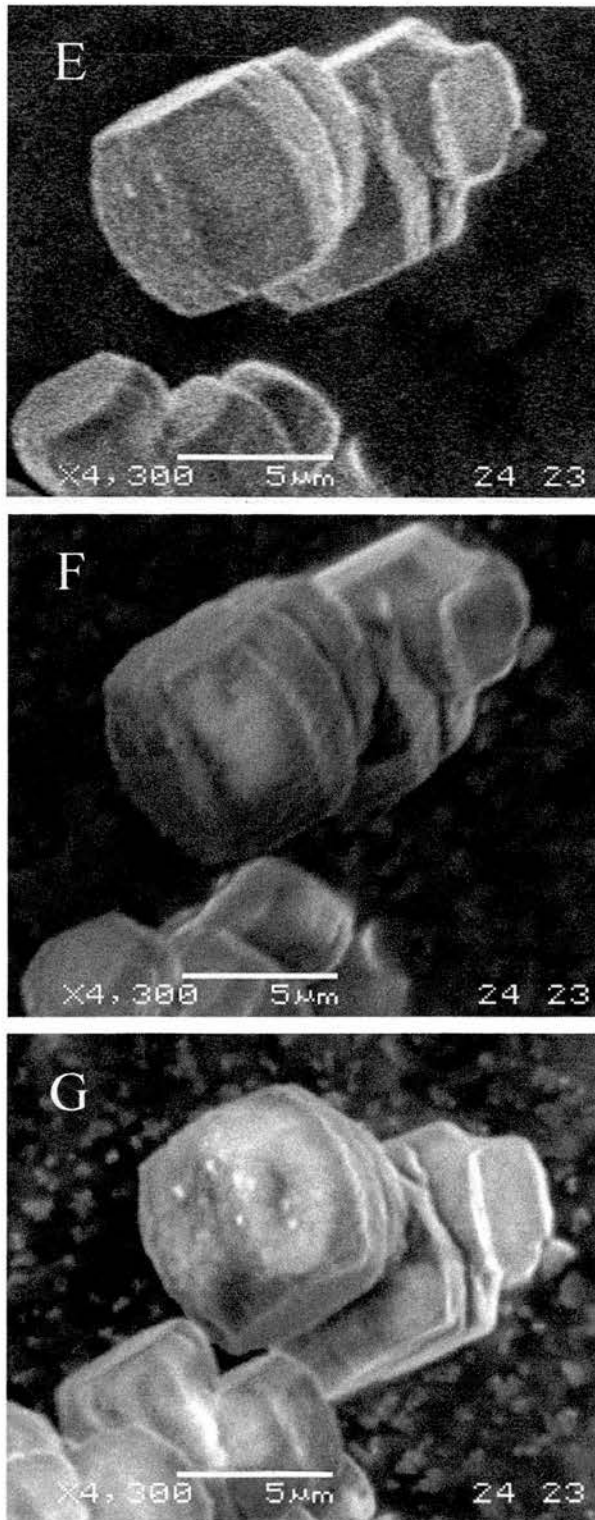


Figure 4.3.3.1. SEM micrographs (E – G) of FDU-12 loaded with 5% MPTES. Rotation of particle displaying hexagonal prism with morphology of reported $P6_3/mmc$ morphology

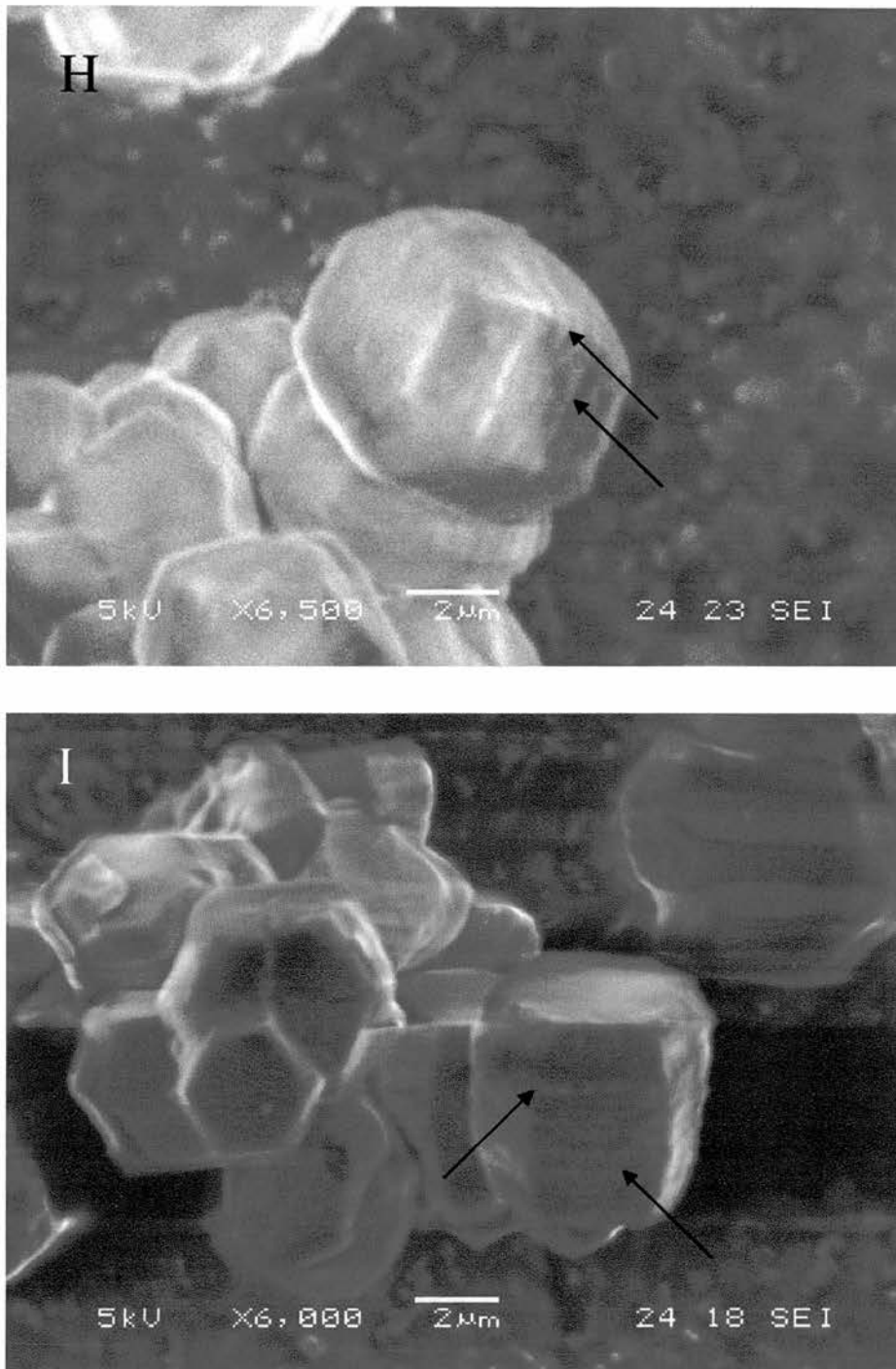


Figure 4.3.3.1. SEM micrographs (H – I) of FDU-12 functionalised with 5% MPTES. The hexagonal prismatic particles show streaking parallel to the growth (indicated by arrows) thought to be related to the local disruptions

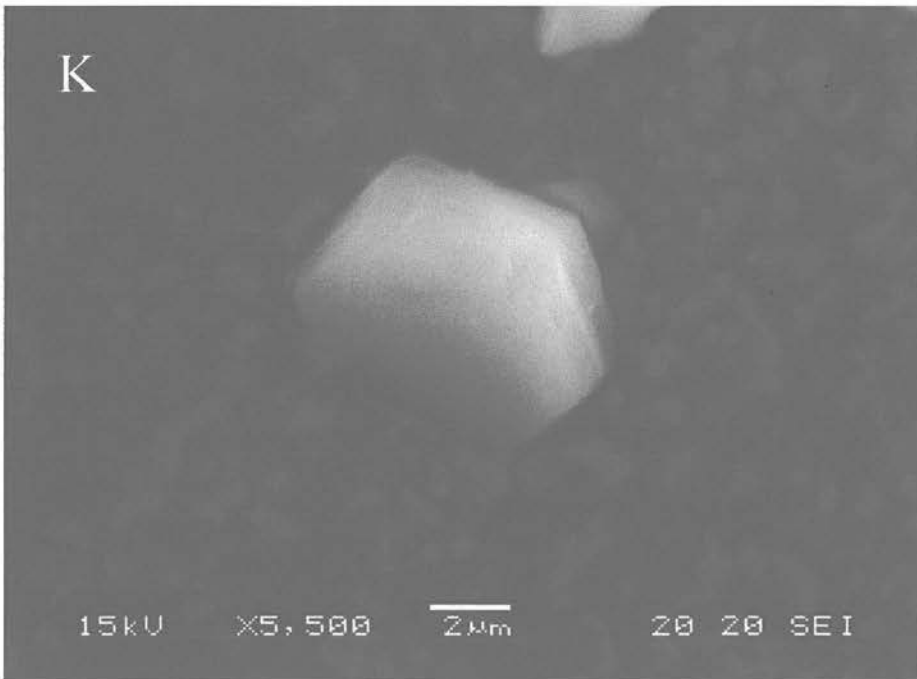
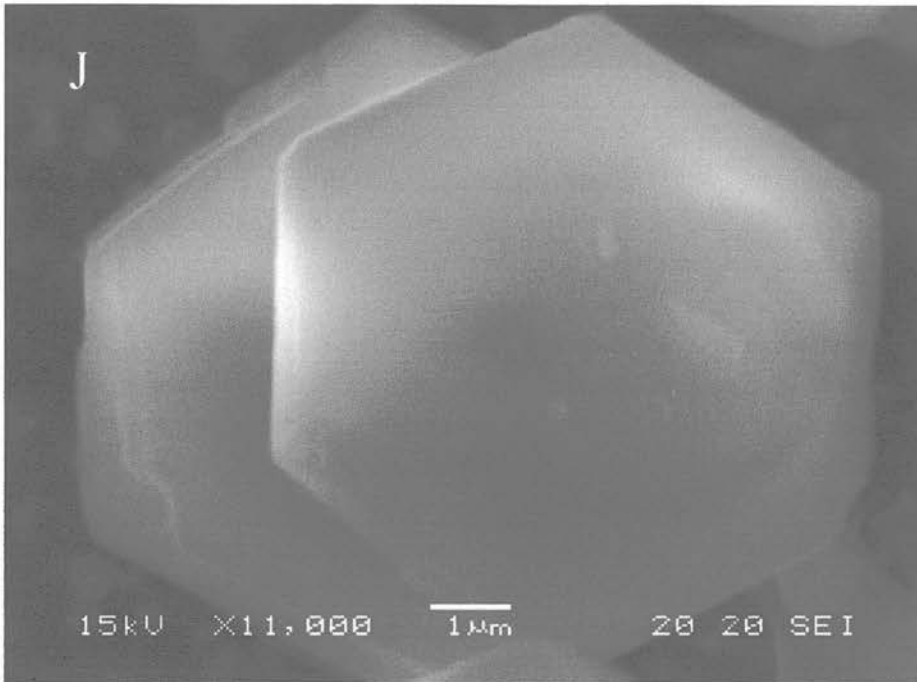


Figure 4.3.3.1. SEM micrographs of FDU-12 with 7% MP TES loading (J – K) showing hexagonal plates with reduced length to cross section area ratio

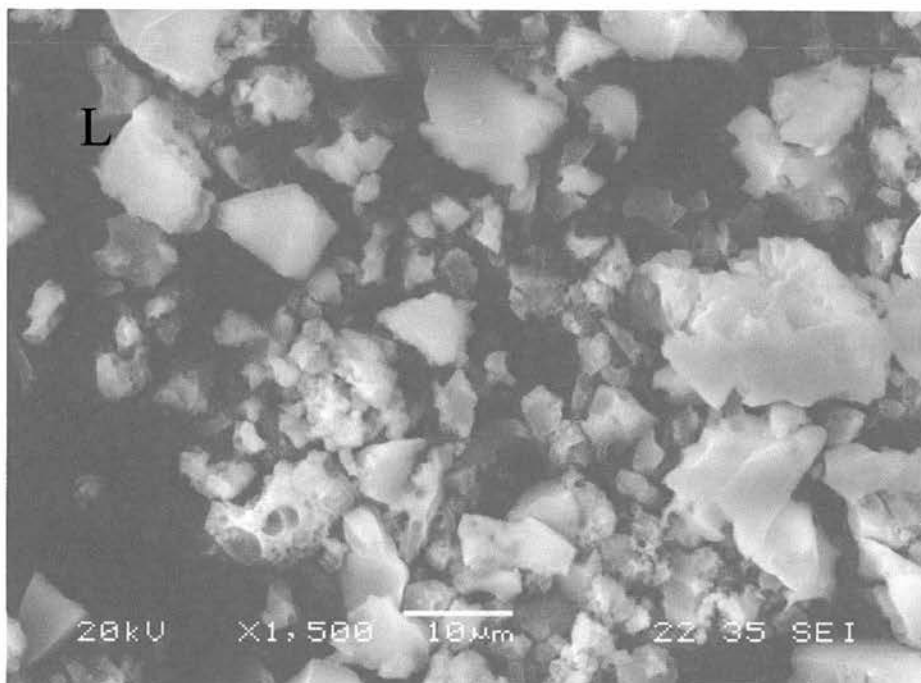


Figure 4.3.3.1. SEM micrographs of FDU-12 with 10% MPTES loading (L) showing no defined particle morphology

4.3.4 TEM characterisation of Thiol-functionalised mesoporous silica templated by F127.

Some materials produced do exhibit more than one phase present which makes it difficult to unambiguously determine space groups by XRD and HRTEM has been required to elucidate such systems. For example, FDU-1 was first reported to possess a body centred cubic $\text{Im}\bar{3}\text{m}$ structure [36] but recent observations using HRTEM has suggested the face centred cubic $\text{Fm}\bar{3}\text{m}$ structure with 3D hexagonal intergrowths [37]. For FDU-12 in this work the reason for the change in morphology becomes apparent upon observation of the electron micrographs. For the pure siliceous samples the *ccp* array of the reported $\text{Fm}\bar{3}\text{m}$ symmetry is noticed with no disruptions to the stacking sequence. Figure 4.3.4.1a and 4.3.4.1b show the micrographs with the incident electrons parallel to the [001] and [110] axes of the $\text{Fm}\bar{3}\text{m}$ unit cell

respectively where the a cell dimension is *ca.* 27 nm and 21 nm for the extracted and calcined solids respectively. Distances were measured directly from the micrograph using the DigitalMicrograph program as the distance between the minima of the electron density and the unit cell parameter calculated appropriately. Here the observed packing of spheres correlates to the ideal ABCABCABC stacking sequence.

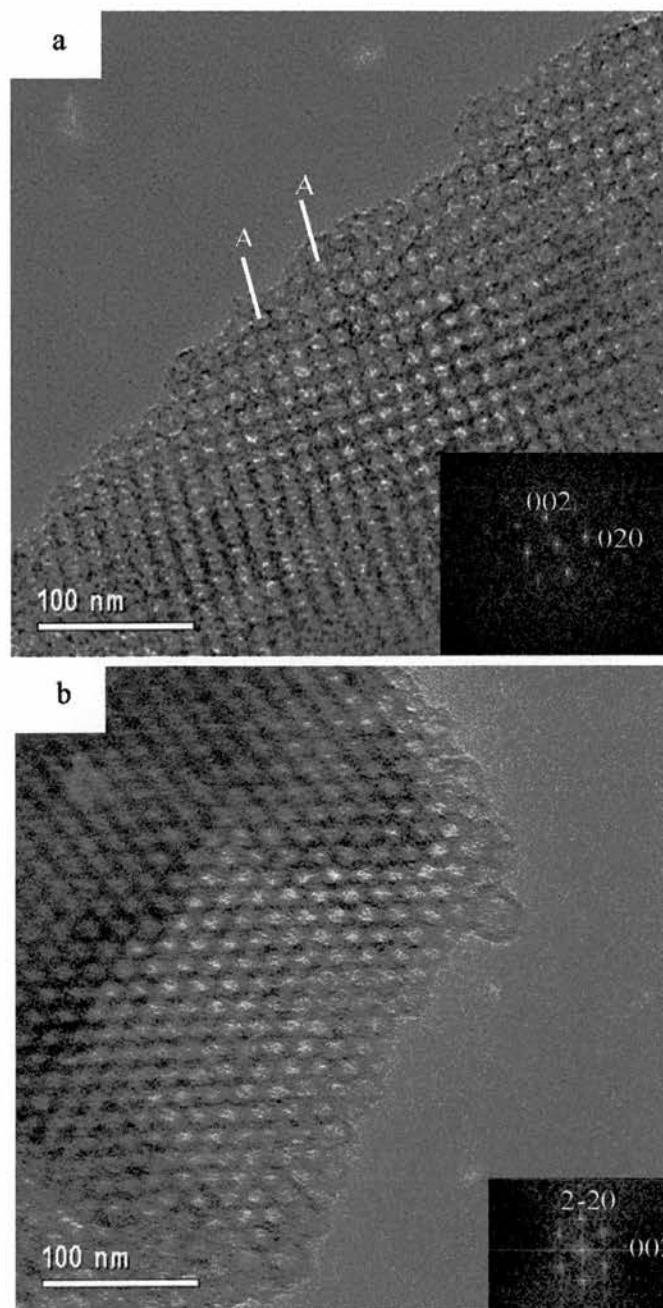


Figure 4.3.4.1. HRTEM micrographs for pure siliceous FDU-12 templated by F127 showing the cubic $Fm\bar{3}m$ geometry with no defects with (a) incident electrons parallel to the $[001]$ zone axis and (b) viewing the $[110]$ plane

The sample containing 2% MP TES shows similar micrographs to the pure siliceous sample although a higher degree of long-range appears to be present.

The SEM micrographs for the 5% MP TES-containing solid was already shown to display a change in shape to hexagonal prismatic. Initially it was thought that this might indicate a hexagonally closed packed structure, since the morphology approaches that reported [33] for the fully ordered smaller pore $P6_3/mmc$ material prepared with cetyltriethylammonium cations. Such an ordered arrangement (ABABAB) has also been reported in small nanodomains of SBA-12 [32]. Analysis of the micrographs viewed parallel to the close packing plane show however, that this is not the case. Instead, the hexagonal prismatic particles arise from predominantly cubic close packing with some disruptions to the stacking sequence. These disruptions comprise of stacking faults, twin planes and nanodomains of both the cubic (ABCABCABC) and hexagonal (ABABAB) stacking sequences. For some smaller particles the ordered cubic structure is retained but the majority of the larger particles, contain stacking faults. As with the P123 templated solids the introduction of MP TES to the sol-gel synthesis has an important effect on the mesoproducts structure and morphology. Figure 4.3.4.2 displays some of the structural defects that occur upon MP TES addition as well as the cubic stacking sequence that is in some examples demonstrated.

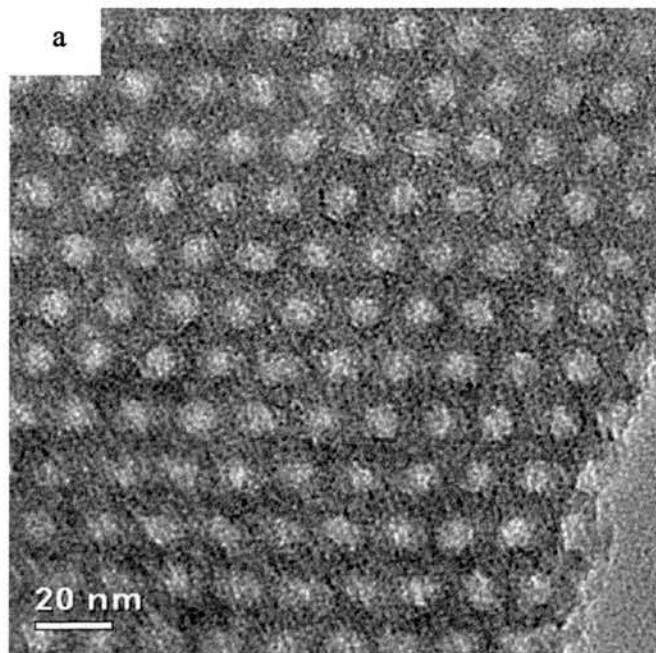


Figure 4.3.4.2. (A) HRTEM micrograph of FDU-12 loaded with 5% MP TES with particle retaining the cubic close packed (ABC) array without any local disruption to the stacking sequence

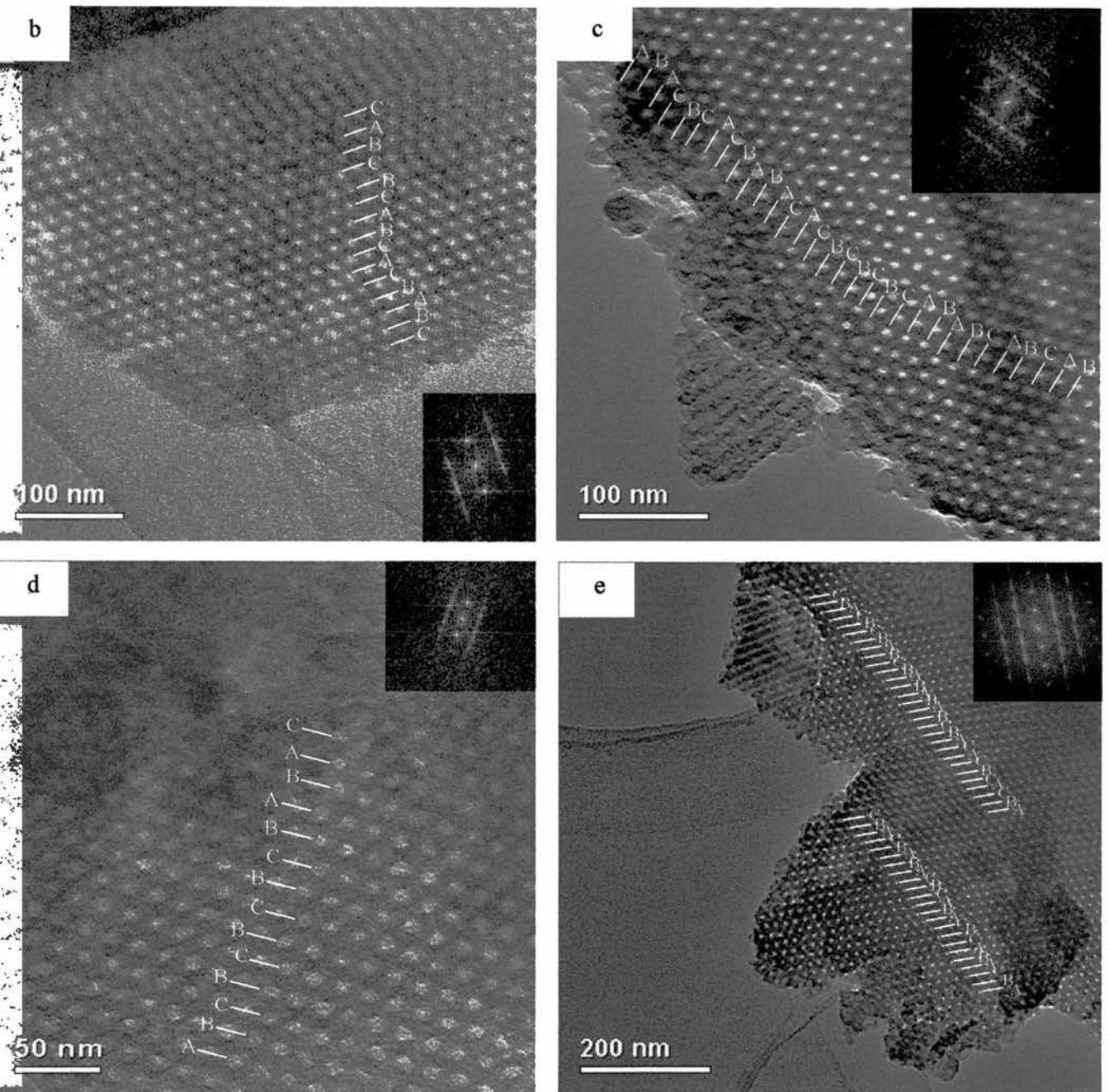
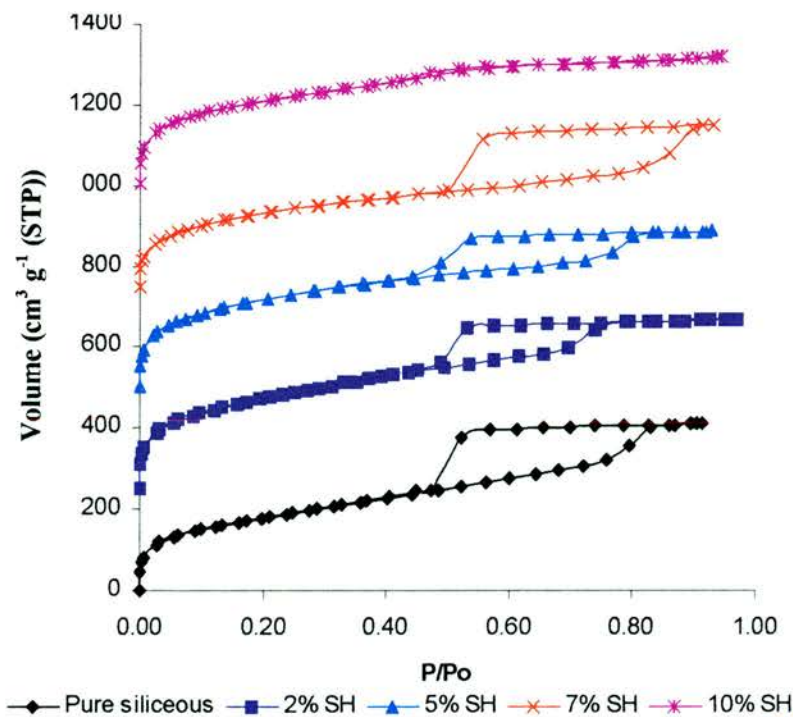


Figure 4.3.4.2 (B – E). HRTEM micrographs of 5% MP TES mesoporous solids templated by F127. The particles have significant stacking disruptions including nanodomains of the hexagonal close packed array giving rise to the hexagonal prismatic morphology. (B): displaying a twin plane and a stacking fault with the sequence CABCBCABCACBABC. (C): shows a nanodomain of the cubic packing and the hexagonal packing separated by a stacking fault followed by a series of stacking faults with the sequence BACBACBABACBCBCBCACABABCACBCABA. (D): a region of the hexagonal packing array together with a stacking fault; sequence – ABCBCBCBCBABAC. (E): a large particle displaying many structural defects in the form of stacking faults across the entire particle with discrete small cubic and hexagonal domains.

4.3.5 N_2 adsorption characterisation of Thiol-functionalised mesoporous silica templated by F127.

The nitrogen adsorption isotherms obtained on extracted and calcined samples of the close packed ‘supercage’ silicas were measured to define more accurately the dimensions of the pore system. The results are shown in figure 4.3.5.1. Most of the samples display well defined hysteresis loops of type H₂, that is to say the hysteresis loops are typical of large pore structures made up of large cages connected by windows. The 10% MPTES solids, both extracted and calcined, show poorly defined hysteresis loops, which result from their poorly defined structure.

In addition, in all cases calcination increases the uptake (for the 7%SH sample: extracted 13% mass uptake; calcined 24% mass uptake) at low partial pressures (< 0.05 P/P₀). In this low pressure region there is typically an increase in N₂ uptake on average of 60%. This behaviour is similar to that observed for the SBA-15/STA-11 system although in this case a greater average increase (133%) is observed. The increase is attributed to the production of the free microporosity as residual template or organic functional groups are removed from the walls by calcination.



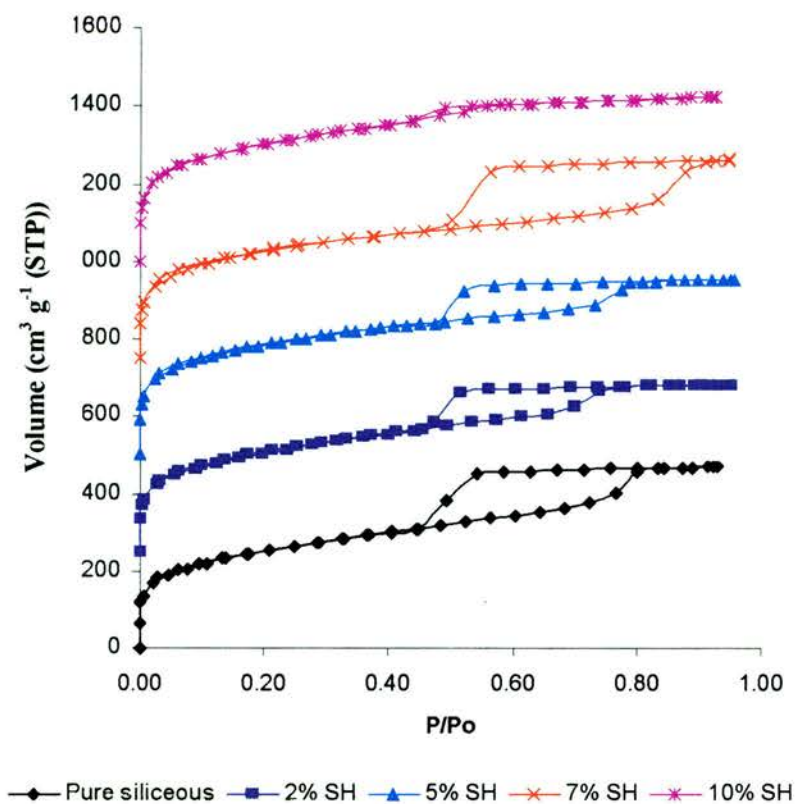


Figure 4.3.5.1. N_2 adsorption and desorption isotherms of 'FDU-12' solids templated by F127 with various loadings of MPTES measured at 77 K. Top – extracted samples; bottom – calcined samples. Isotherms are offset by $250 \text{ cm}^3 \text{ (STP)/g}$ for clarity.

It can be seen from the P/P_0 values of the capillary condensation steps on the adsorption branches that the addition of MPTES to the synthesis has an effect on the cavity size – this is also in line with the morphological and structural changes observed by microscopy. As with the P123-templated materials the 10% MPTES containing F127 templated material shows a smaller capillary condensation step with a reduced hysteresis loop. This reflects the poor quality of the material and suggests the micellar ordering is not optimal during product formation. Inflection points on the adsorption branches are between P/P_0 of 0.75 – 0.86 for both extracted and calcined samples.

The desorption of N_2 is governed by the size of the entrance window and the smaller this pore size the lower relative pressure is required for desorption to occur. N_2 adsorption on 'FDU-12' samples containing 2 – 7% MPTES show (figure 4.3.5.1) that the increasing loading of the thiol constituent does not alter the entrance size

significantly – the inflection points of the desorption branches occur at similar P/P_0 values (in the region of 0.5) for both extracted and calcined samples. With all samples having the same hydrothermal treatment of 373 K this is in line with the data reported by Zhao on pure silica FDU-12, indicating that the pore size of the entrance window is approximately 4 nm. The pore size distribution curves (figure 4.3.5.2) for the entrance windows are consistently sharp at constant values as suggested by the desorption branches of all isotherms. The pore sizes of the F127 templated FDU-12 mesocaged materials can not be compared to the P123 templated SBA-15/STA-11 cylindrical materials due to the differences in pore shapes.

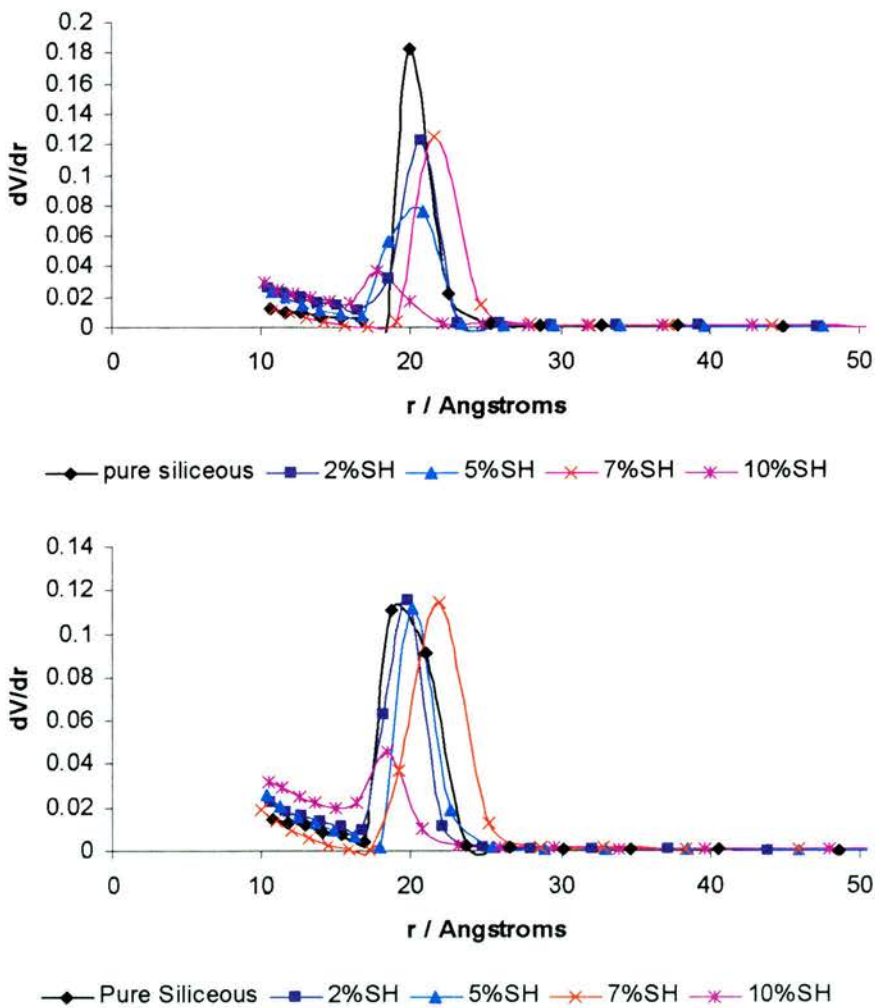


Figure 4.3.5.2. Pore size distribution curves measured from the desorption branch of the (top) extracted and (bottom) calcined isotherms for MPTES F127 templated solids. It can be seen that the window entrance size for all is in the region of 4 nm.

The pore size of the cavities – taken from the adsorption branches of the isotherms (figure 4.3.5.3) are much larger in diameter than that for the respective entrance sizes with the exception of the 10% MPTES solid. It can be seen that the 7% MPTES containing solid compared to the other solids has a larger pore size. With the volume of the cavity being greater than the volume of the entrance window the majority of the mass uptake of N_2 will be within the cavity and therefore is represented in the adsorption branch of the isotherm. Table 4.3.5.1 summarises the porosity measurements.

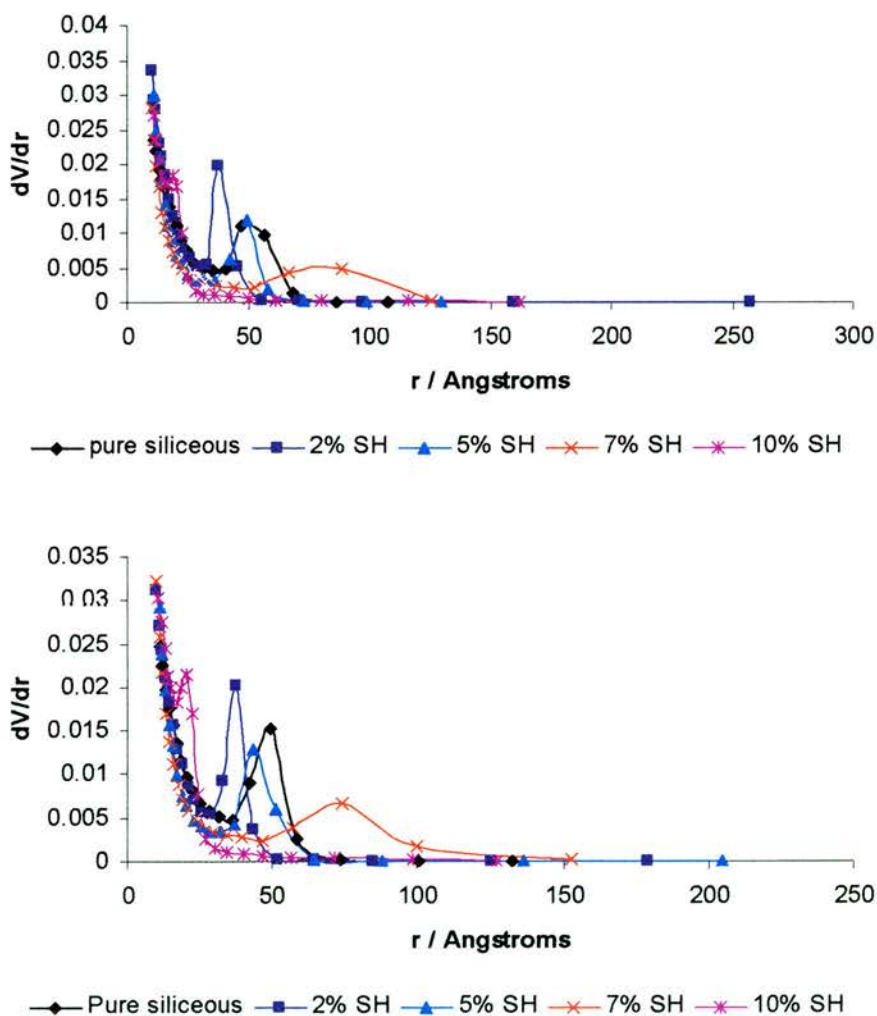


Figure 4.3.5.3. Pore size distribution curves measured using the De-Boer model on the adsorption branches of the isotherms for (top) extracted and (bottom) calcined MPTES containing 'FDU-12' solids.

Material	*Specific surface area BET m ² /g		†Pore size mode Å				Total N ₂ uptake cm ³ (STP) g ⁻¹	
	extracted	calcined	extracted		calcined		extracted	calcined
			a	b	a	b		
SiO ₂ pure siliceous	637	809	104	40	99	37	410 (51 wt%)	472 (59 wt%)
SiO ₂ 2% SH	774	825	75	41	75	39	417 (52 wt%)	432 (54 wt%)
SiO ₂ 5% SH	741	897	99	41	87	40	385 (48 wt%)	456 (57 wt%)
SiO ₂ 7% SH	604	877	-	43	148	44	400 (50 wt%)	520 (65 wt%)
SiO ₂ 10% SH	702	955	-	35	-	36	320 (40 wt%)	432 (54 wt%)

*BET surface area calculated within 0.05 – 0.4 P/P₀.

†Pore size distribution using the de Boer model measured on a) the adsorption branch for cavity size and b) desorption branch for entrance size. Taken as the maximum in the pore size distribution curve.

Table 4.3.5.1. Porosity measurements of MPTES solids templated by F127. Here both the entrance and cavity pore sizes are given as the silica solids are cage-type molecular sieves

The hysteresis curve exhibited for SBA-15/STA-11 solids are of type H₁ and are typical for mesoporous silicas possessing uniform cylindrical pores of narrow distribution [37 – 39]. Complex structures made up of interconnected networks of cages, with narrower windows (such as the F127 templated FDU-12 materials) display large H₂ hysteresis loops. Zhao reported the effect of the hysteresis upon varying hydrothermal treatment which upon increasing from 373 K to 413 K gave a shift in the hysteresis on the desorption branch to higher relative pressures and also resulted in a change from H₂ to H₁ with a smaller hysteresis loop. Solids such as SBA-1 and SBA-2 possessing smaller cavities and entrances display no hysteresis and therefore upon increasing the condensation temperature for FDU-12 materials which gives rise to smaller hysteresis it would be thought that the cavity decreases in size. In fact, the cavity does however slightly increase (by 23%) but the entrance increases

significantly (by 123%) and hence the ratio of the entrance : cavity increases which in turn is similar to the cavity decreasing in size as a function of entrance size [17].

4.3.6 Variation of synthesis of Thiol-functionalised mesoporous silica templated by F127.

The observation that the addition of thiol-functionalised siloxane changed the packing and morphology of the silicate mesophase suggested that it might be possible to prepare for the first time the fully ordered extra large pore $P6_3/mmc$ solid by optimising this synthesis procedure. Such a solid would be of intrinsic interest as it would possess three dimensional and yet anisotropic connectivity. It would also be possible to solve the structure of the fully ordered phase more fully. To this end, the effect of small changes in the temperature of synthesis, amount of MP TES added to the sol-gel, as well as the order of addition of the organic functionality and TEOS were explored.

- The order of MP TES and TEOS addition

The addition of MP TES to the surfactant solution before the addition of TEOS – the major silica source – at 313 K shows similar particle morphology to the initial FDU-12 (5%SH) solid with a high concentration of stacking defects. Figure 4.3.6.1 shows well-defined changes to the morphological growth that being in the form of hexagonal prisms also consistent to the 5% thiol sample as previously described. Complementary HRTEM micrographs (figure 4.3.6.2) also confirm the changes in morphology as changes to the close packed array.

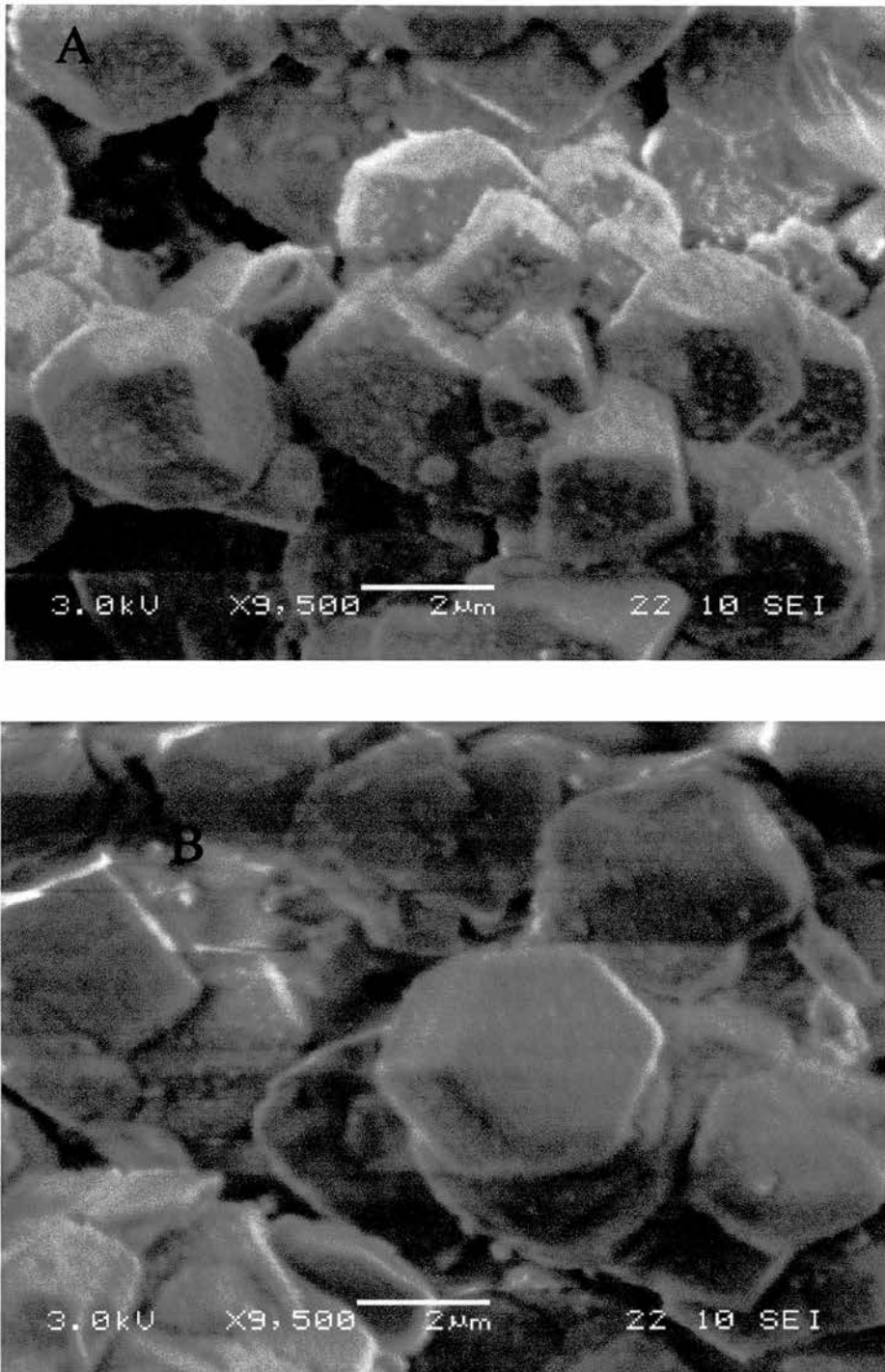


Figure 4.3.6.1. SEM micrographs of 'FDU-12' functionalised *in situ* with 5% MPTES. Here the addition of the organo-siloxane is added to the synthesis mixture before TEOS. Clear changes in morphology can be observed due to the cubic close pack array possessing defects in the structure.

- The MPTES sol-gel concentration

As with the P123 templated materials very subtle differences in MPTES stoichiometry led to immediate noticeable structural changes to F127 templated solids. (e.g. 3% MPTES addition gives hexagonal prismatic particle morphology observing whereas 2% MPTES gives poorly defined particles (figure 4.3.6.3)). The HRTEM micrographs of the 3% MPTES sample (figure 4.3.6.4) are almost purely cubic with few defects so that the presence of only a few defects is required to change the particle morphology very noticeably.

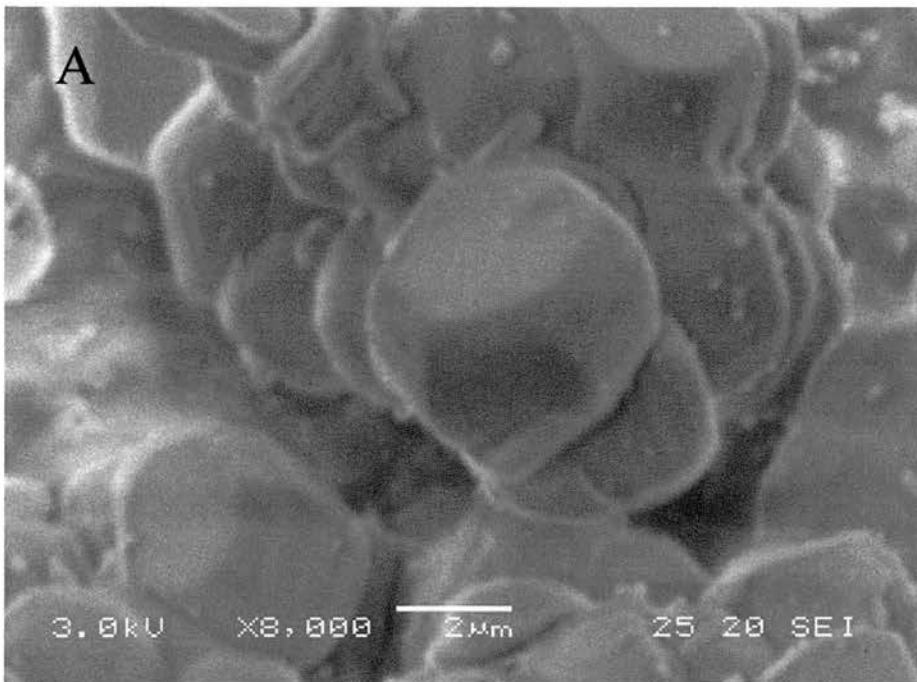


Figure 4.3.6.3. SEM micrographs of 3% MPTES addition to F127 templated materials. Significant morphological changes are observed to those seen with 2% MPTES solids.

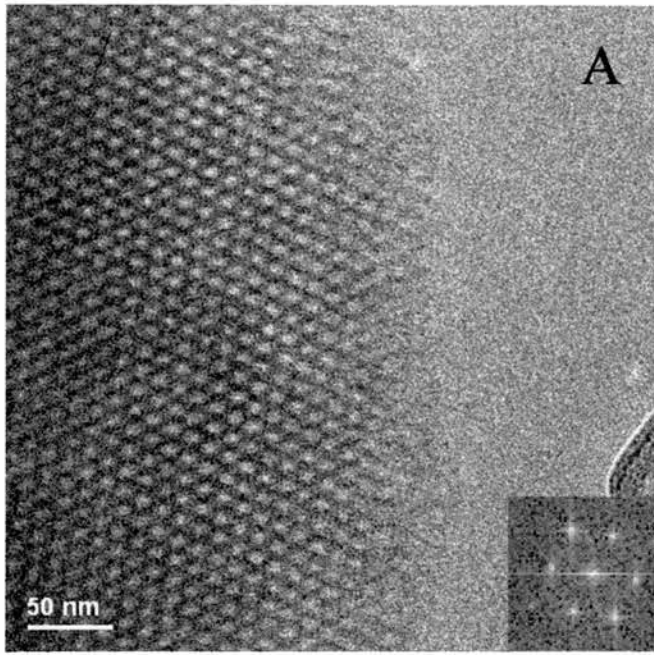


Figure 4.3.6.4. HRTEM images of 3% MPTES containing F127 templated solids. Few structural defects are present in the cubic array.

- Room temperature synthesis

Performing the hydrolysis step at room temperature results in a solid with a less defined morphology than the corresponding synthesis at 313 K. HRTEM micrographs (figure 4.3.6.5) confirm the presence of the well-defined cubic mesophase present without defects.

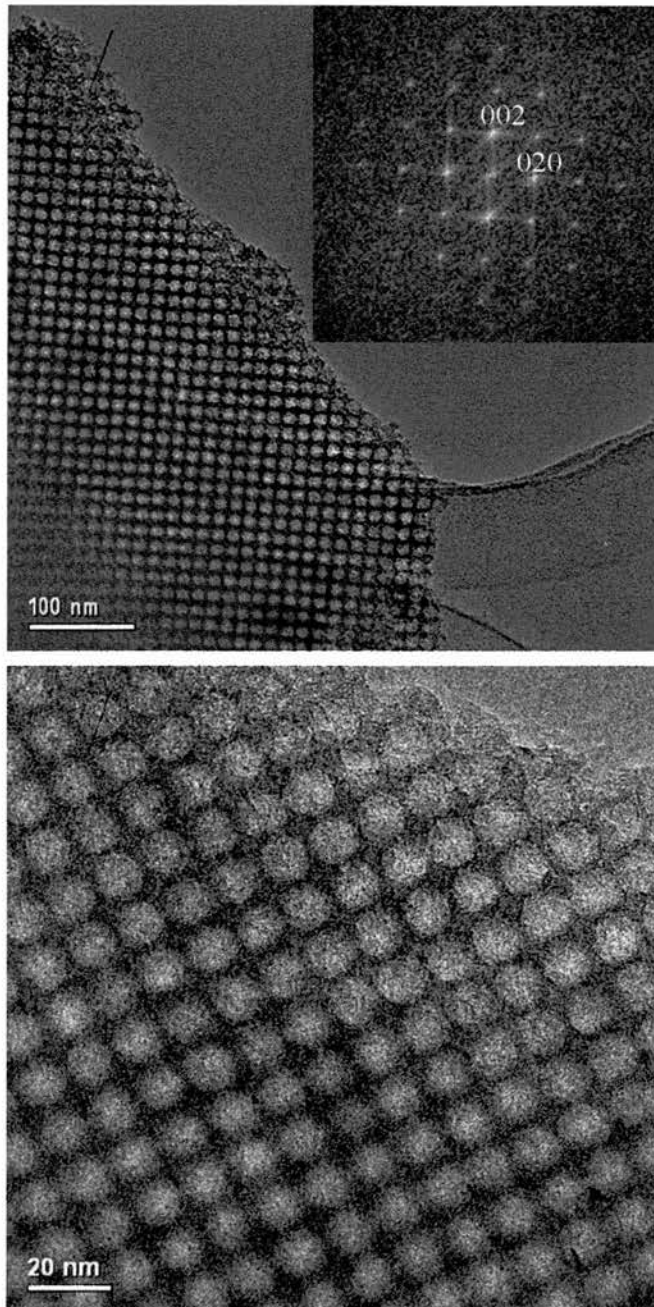


Figure 4.3.6.5. HRTEM micrographs of the Fm-3m cubic mesophase viewing the [001] zone axis with no observable defects present

4.4 Conclusions

The addition of MPTES to the sol-gel syntheses of Pluronic F127 templated mesoporous solids causes structural and morphological changes. Without organo-siloxane addition, the reported Fm3m cubic phase is observed without defects. Adding thiol to the preparation results in the introduction of twin planes and stacking faults within the stacking sequence. Domains of the 3D P6₃/mmc hexagonal phase are also present. Unlike the p6mm to Ia3d phase transition with P123 solids, there is no obvious change in micellar curvature in the Fm3m to P6₃/mmc transition, if the structure corresponds to ideal close packing, because the difference in structure lies in the relative stacking sequence rather than the local structure. Associated with the changes to the sequence of close packing, the particle morphology is observed to change to well-defined hexagonal prismatic geometry tapering at the basal faces or to hexagonal plates, depending on the thiol concentration.

N₂ porosity measurements suggest that the entrance sizes are not affected by the addition of MPTES as the pore size distribution curves for all solids remain close to 4 nm. Having consistent window sizes may be beneficial for applications where molecular sieving is crucial. Thiol accessibility to Ellman's reagent is slightly lower than for P123 solids although sufficiently high for the solids to be viable for applications such as heavy metal extraction from solution or conversion to sulphonic acids to act as acid catalysts.

Attempts to obtain the hexagonal perfectly ordered close packed structure have not been successful. Further work towards this goal would manipulate the sol-gel synthesis with other organo-siloxanes and further variation of the stoichiometric ratios of the other reagents.

4.5 References

- [1] A. Corma, *Chem. Rev.*, 1997, **97**, 2373
- [2] U. Ciesla, F. Schüth, *Micro. Meso. Mater.*, 1999, **27**, 131
- [3] M. Lindén, S. Schacht, F. Schüth, A. Steel, K. Unger, *J. Porous. Mater.*, 1998, **5**, 177
- [4] Y. Liu, T.J. Pinnavaia, *J. Mater. Chem.*, 2002, **12**, 3179
- [5] R. Anwender, *Chem. Mater.*, 2001, **13**, 4419
- [6] J.Y. Ying, C.P. Mehnert, M.S. Wong, *Angew. Chem. Int. Ed.*, 1999, **38**, 56
- [7] A.P. Wright, M.E. Davis, *Chem. Rev.*, 2002, **102**, 3589
- [8] D.E. de Vos, M. Dams, B.F. Sels, P.A. Jacobs, *Chem. Rev.*, 2002, **102**, 3615
- [9] F. Schüth, *Chem. Mater.*, 2001, **13**, 3148
- [10] V. Chiola, J.E. Ritsko, C.D. Vanderpool, US Patent No. 3556725 (1971)
- [11] F. DiRenzo, H. Cambon, R. Dutartre, *Micro. Meso. Mater.*, 1997, **10**, 283
- [12] J.S. Beck, N.Y. Princeton, US Patent No. 5 057 296, 1991
- [13] C.T. Kresge, M.E. Leonowicz, W.J. Roth, J.C. Vartuli, J.S. Beck, *Nature*, 1992, **359**, 710
- [14] J.S. Beck, J.C. Vartuli, W.J. Roth, M.E. Leonowicz, C.T. Kresge, K.D. Schmitt, C.T.W. Chu, D.H. Olson, E.W. Sheppard, S.B. McCullen, J.B. Higgins, J.L. Schlenker, *J. Am. Chem. Soc.*, 1992, **114**, 10834
- [15] T. Yanagisawa, T. Shimizu, K. Kuroda, C. Kato, *Bull. Chem. Soc. Jpn.*, 1990, **63**, 988
- [16] F. Kleitz, D. Liu, G.M. Anilkumar, I.S. Park, L.A. Solovyov, A.N. Shmakov, R. Ryoo, *J. Phys. Chem. B.*, 2003, **107**, 14296
- [17] J. Fan, C. Yu, F. Gao, J. Lei, B. Tian, L. Wang, Q. Luo, B. Tu, W. Zhou, D. Zhao, *Angew. Chem. Int. Ed.*, 2003, **42**, 3146
- [18] H.M.A. Hunter, A.E. Garcia-Bennett, I.J. Shannon, W. Zhou, P.A. Wright, *J. Mater. Chem.*, 2002, **12**, 20
- [19] S. Jun, S.H. Joo, R. Ryoo, M. Kruk, M. Jaroniec, Z. Liu, T. Ohsuna, O. Terasaki, *J. Am. Chem. Soc.*, 2000, **122**, 10712
- [20] M.E. Davis, *Nature*, 2002, **417**, 813
- [21] I.M. Hamley, *Developments in block copolymer science & technology*, John Wiley & sons, 2004

- [22] M.W. Anderson, C.C. Egger, G.J.T. Tiddy, J.L. Casci, *Stud. Surf. Sci. Catal.*, 2002, **142**, 1149
- [23] H.H.P. Yiu, P.A. Wright, N.P. Botting, *J. Mol. Catal. B: Enzymol.*, 2001, **15**, 81
- [24] H.H.P. Yiu, C.H. Botting, N.P. Botting, P.A. Wright, *Phys. Chem. Chem. Phys.*, 2001, **3**, 2983
- [25] H. Zhang, J. Sun, D. Ma, X. Bao, A. Klein-Hoffmann, G. Weinberg, D. Su, R. Schlögl, *J. Am. Chem. Soc.*, 2004, **126**, 7440
- [26] C.Z. Yu, B.Z. Tian, J. Fan, G.D. Stucky, D.Y. Zhao, *J. Am. Chem. Soc.*, 2002, **124**, 4556
- [27] Y.Q. Wang, C.M. Yang, B. Zibrowius, B. Spliethoff, M. Lindén, F. Schüth, *Chem. Mater.*, 2003, **15**, 5029
- [28] Q. Huo, R. Leon, P.M. Petroff, G.D. Stucky, *Science*, 1995, **268**, 1324
- [29] Q.S. Huo, D.L. Margolese, G.D. Stucky, *Chem. Mater.*, 1996, **8**, 1147
- [30] W. Zhou, H.M.A. Hunter, P.A. Wright, Q. Ge, J.M. Thomas, *J. Phys. Chem. B.*, 1998, **102**, 6933
- [31] D. Zhao, Q. Huo, J. Feng, B.F. Chmelka, G.D. Stucky, *J. Am. Chem. Soc.*, 1998, **120**, 6024
- [32] Y. Sakamoto, I. Díaz, O. Terasaki, D. Zhao, J. Pérez-Pariente, J.M. Kim, G.D. Stucky, *J. Phys. Chem. B.*, 2002, **106**, 3118
- [33] S. Che, S. Lim, M. Kaneda, H. Yoshitake, O. Terasaki, T. Tatsumi, *J. Am. Chem. Soc.*, 2002, **124**, 13962
- [34] O. Terasaki, T. Ohsuna, Z. Liu, Y. Sakamoto, A.E. Garcia-Bennett, *Stud. Surf. Sci. Catal.*, 2004, **148**, 261
- [35] R.P. Hodgkins, A.E. Garcia-Bennett, P.A. Wright, *Micro. Meso. Mater.*, 2005, **79**, 241
- [36] C. Yu, Y. Yu, D. Zhao, *Chem. Commun.*, 2000, **7**, 575
- [37] J.R. Matos, M. Kruk, L.P. Mercuri, M. Jaroniec, L. Zhao, T. Kamiyama, O. Terasaki, T.J. Pinnavaia, Y. Liu, *J. Am. Chem. Soc.*, 2003, **125**, 821
- [38] X. Liu, B. Tian, C. Fu, F. Gao, S. Xie, B. Tu, R. Che, L. Peng, D. Zhao, *Angew. Chem. Int. Ed.*, 2002, **41**, 3876; *Angew. Chem.*, 2002, **114**, 4032
- [39] S. Che, A.E. Garcia-Bennett, X. Liu, R.P. Hodgkins, P.A. Wright, D. Zhao, O. Terasaki, T. Tatsumi, *Angew. Chem. Int. Ed.*, 2003, **42**, 3930; *Angew. Chem.*, 2003, **115**, 4060

Chapter 5

Metallated Azamacrocycles supported on SBA-15

Synopsis

This chapter details the further functionalisation of propylchloride-SBA-15 with the azamacrocycles cyclam (1,4,8,11-tetraazacyclotetradecane) and TACN (1,4,7-triazacyclononane) and the formation of metallated azamacrocycles. A multi-frequency ESR study on Cu(II) cyclam helps to improve the synthesis and complements thermal and elemental analyses. TACN complexes, supported on SBA-15 and complexing transition metals, are studied as potential catalysts for epoxidation under mild conditions.

5.1 Introduction

The functionalisation of mesoporous materials, either by an *in situ* approach or by direct synthesis, offers many potential modifications to the surface chemistry. As expressed in chapter 3, functionalising mesoporous solids with organo-siloxanes can allow further modification if the functional groups are reactive. Such groups as propyl chloride tethered from the silica surface can be further modified by reaction with amines. In this thesis, the aim was to covalently tether azamacrocycles (containing secondary amine groups) to the surface of propyl-functionalised SBA-15 before metal complexation – a different approach to using charged zeolite frameworks. The work formed an extension of attempts in our laboratory to incorporate azamacrocycles within microporous solids and has the potential to prepare a series of functional solids. Wright and co-workers have utilised nitrogen containing macrocycles (figure 5.1.1), such as the azamacrocycles, cyclam (1,4,8,11-tetraazacyclotetradecane), TMTACT (1,4,8,11-tetramethyl-1,4,8,11-tetraazacyclotetradecane) and TMTACN (1,4,7-trimethyl-1,4,7-triazacyclononane) amongst others for the syntheses of novel metalloaluminophosphates. The metal cations play an important role in conjunction with the azamacrocycle SDA in the phase that crystallises as Mg^{2+} cations with TMTACT forms STA-6 [6] as too do Mn^{2+} and Fe^{2+} whereas Co^{2+} and Zn^{2+} cations form STA-7 [7] along with Mg^{2+} and Co^{2+} cations with HMHACO (1,4,7,10,13,16-hexamethyl-1,4,7,10,13,16-hexaazacyclooctadecane) as the SDA

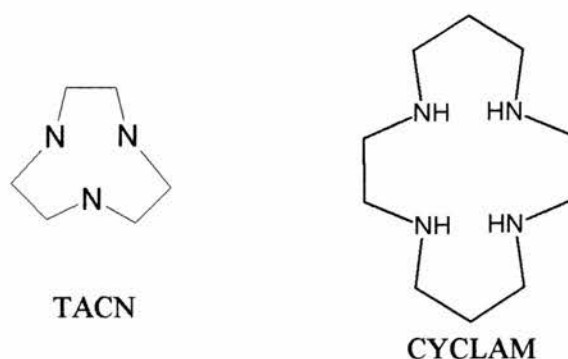


Figure 5.1.1. Some common azamacrocycles of varying structure and cavity size for use as SDA's in the syntheses of novel microporous metalloaluminophosphates

Since their discovery [1], macrocyclic compounds have been found to form stable complexes with a wide range of metals and to exhibit a very wide range of host-guest chemistry [2]. ‘Crown’ compounds (macrocycles) were named due to their chemical structure and shape and can generally be described as: ‘compounds having electron donor heteroatoms such as O, N or S in the ring structure with the ability of incorporating cations into the ring’ [3]. Macrocyclic compounds with oxygen as the electron donor were the first to be synthesised; nitrogen- and sulphur-containing macrocycles were soon prepared [4].

Metal complexation with amine ligands are important in co-ordination chemistry, complexes with polydentate chelating ligands are more stable than complexes with monodentate ligands, described as the chelate effect, where stability increases as more donors are incorporated into the polydentate ligands. A typical sequence of stabilities for Cu (II) complexes can be seen in figure 5.1.2.

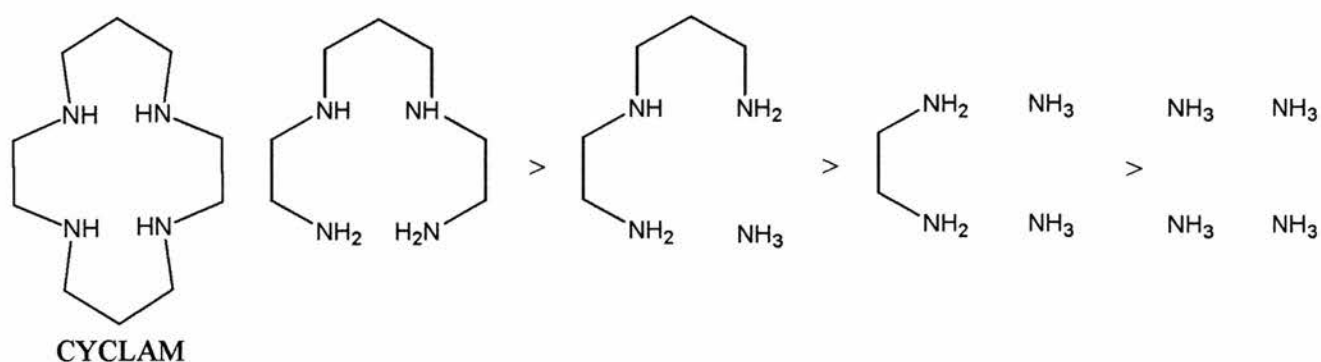


Figure 5.1.2. The stability of copper(II) complexes containing four nitrogen donors increases with the ligand denticity

Complexes with multidentate ligands are more stable over those containing the same number of equivalent monodentate ligands which gives rise to the macrocyclic effect as cyclic ligands give more stable complexes than corresponding open-chain ligands. The macrocyclic effect was first quantified for Cu (II) complex 5.1 (below) which was found to be 10^4 times more stable than the open chain complex 5.2 (figure 5.1.3). Cyclic compounds are therefore ideal complexing agents with transition metals [5].

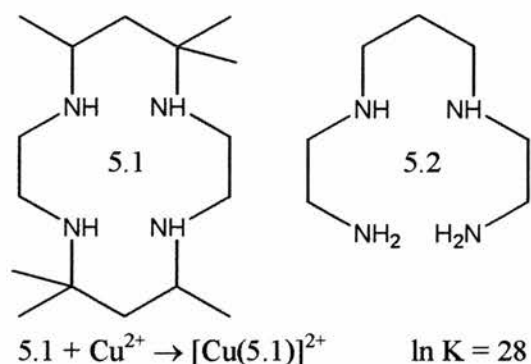


Figure 5.1.3. The macrocyclic effect gives rise to more stable complexes over the equivalent open-chain analogues. Higher $\ln K$ values indicates stronger complexing constant

The host-guest chemistry exhibited by macrocyclic compounds plays a pivotal role in their applications as the ability of a particular macrocycle differs depending on the diameters of both the macrocycle cavity and guest cation as well as the interactions the donor atoms present and hence fine tuning of the compounds characteristics can be tailored for particular applications. Their size and shape play an important role in the synthesis of open framework solids: varying the heteroatoms and ring size changes the affinity to coordinate to different metal cations.

Metallated nitrogen containing complexes are widely used to mimic the catalytic properties of monooxygenases, which selectively hydroxylate organic substrates [8]. Monooxygenases are enzymes that reduce molecular oxygen by incorporating one oxygen atom into its substrate and the other one in water. Dioxygen can be incorporated directly into organic compounds in reactions catalyzed by enzymes termed oxygenases. Oxygenases that catalyze the incorporation of both atoms of dioxygen into substrates are known as dioxygenases; those that catalyze the incorporation of only one atom of dioxygen are termed monooxygenases. The second atom of dioxygen is reduced to water either by the substrates themselves or by a co-substrate reductant. Iron and copper complexes are especially active catalysts for the mimicking of monooxygenases [9] whose typical active sites, for example, can be Fe (III) / Cu (II), surrounded by biological or synthetic cyclic ligands. Close structural analogues of enzymatic active sites possessed by some metal complexes down to simple metal salts, which are catalytically active are often termed “biomimetic” [10] sometimes use molecular oxygen but frequently require more reactive oxidants, such as peroxides, iodosylbenzene, etc., operating at room temperature.

Conversion of readily available, low-cost alkanes to more valuable oxidised products using oxygen or air as an oxidant are of great significance to the chemical industry [8,11]. The oxidation of cyclohexane under mild conditions is of great interest with research for the preferred oxidant still ongoing. The products formed are the intermediates for Nylon-6 manufacture [12] as is cyclohexene oxide produced from epoxidation of cyclohexene using Mn TACN based compounds as catalysts [13]. H_2O_2 is an alternative oxidant as it only produces water as a by-product in an environmentally friendly reaction; tert-Butyl hydroperoxide is a more reactive oxidant but is expensive while molecular oxygen is cheap and selective at temperatures not higher than 343 K [12] although finding active catalysts for these conditions is the challenge. Unfortunately, cyclohexane oxidation with H_2O_2 catalysed by biomimetic systems still gives low conversions and turnovers and the metal containing molecular sieves which are possible catalysts do show signs of metal leaching [14] especially with H_2O_2 and tert-Butyl hydroperoxide as oxidants. Molecular oxygen can decrease the leaching in comparison.

Biomimetic oxygenations of organic substrates using metal co-ordinated complexes as catalysts ideally should use dioxygen as the oxidant since O_2 is the source directly used by oxygenase enzymes they are trying to mimic [15]. However, metalloporphyrins and related azamacrocycles developed for such reactions require alternative oxidants to dioxygen since dioxygen itself gives either no reaction itself or undesired side products. An apparent exception is if an aldehyde is added to the reaction mixture, for example olefins can be epoxidised by dioxygen, in the presence of aldehydes and transition metal-containing catalysts to give the epoxide [16] figure 5.1.4.

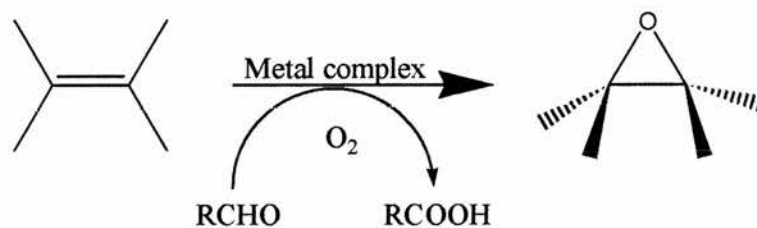


Figure 5.1.4. Epoxidation of olefins with oxygen in the presence of aldehydes

This chapter reports attempts to immobilise metallated macrocycles onto functionalised SBA-15. Complexes included in this way would be expected to be readily accessible to incoming reactants and oxygen sources. Reaction conditions reported in the literature for the oxidation of cyclohexane [17] and cyclohexene [16] were adopted for a series of metallated macrocyclic species. Examples where amines have been used in this way include the work of Páez-Mozo [18] towards supported basic catalysts. Here an iron complex is ion-exchanged with Na zeolite Y before azamacrocycle complexation. Electrostatic forces are responsible for retention of the complex within the pores. These species were included using a method developed initially for a copper (II) cyclam bearing system, the preparation of which was followed carefully by a detailed ESR study. ESR is a powerful tool for the study of the local environment of paramagnetic species, as described in Chapter 2. In particular, it was used here to study the environment of Cu^{2+} (d^9) in (and out) of cyclam. Copper (Cu^{2+}) is particularly amenable to ESR studies of this type and is the metal of choice to investigate in this way [19] however, the ESR of other transition metal ions, for example, Fe^{3+} in mesoporous solids the interpretation of the spectra is less informative where assignments of signals can be ambiguous [20,21]. ESR is a useful tool in a wide range of sciences from biological and organic free radical studies to catalysis and transition metal complexes and helps to give information on the paramagnetic species. Metallated azamacrocycle environments has been studied by ESR and in particular Cu(II) complexes [19,22] and also the study of Cu (II) silicas containing nitrogen compounds [23] and Cu (II) exchanged silicas [24]. Trivalent Fe containing mesoporous silica has also been reported [25] although the assignments of the resonance signals are somewhat ambiguous [26]. ESR within this chapter has helped to improve the synthesis conditions of the azamacrocycle addition to the silica support and also compliments elemental analysis from TGA and CHN results.

5.2 Experimental

SBA-15 functionalised *in situ* by the co-condensation of propylchloride-triethoxysilane with TEOS was used as the support for the incorporation of azamacrocycles. The organo-siloxane loading was incorporated at 5% (based on total

SiO₂) as this loading gives the highest amount of functionality without compromising the mesostructure of the final silica product as documented in Chapter 3.

Synthesis of azamacrocycle-functionalised SBA-15 materials

The *in situ* functionalised propylchloride SBA-15 was used to tether the nitrogen containing compounds cyclam (1,4,8,11-tetraazacyclotetradecane) (Alfa Aesar, 98+%) and TACN (1,4,7-triazacyclononane) (Aldrich, 95%). The corresponding azamacrocycle was dissolved in toluene to which a stoichiometric equivalent – based on the moles of propylchloride – of the mesoporous support was added, together with NaI as a catalyst. The chloride group in the mesoporous solid is replaced by the iodide group, which is a better leaving group in nucleophilic substitution and therefore reacts more easily with the nitrogen on the azamacrocycle. Similar nucleophilic substitution to incorporate cyclam into propylchloride functionalised SBA-15 has been reported [27]. For example, for 1 g of SBA-15-Cl-5% used 0.1667 g of cyclam or 0.1075 g TACN and gives the stoichiometric equivalent dissolved in toluene in the presence of 0.25 g NaI. The suspension is then refluxed for 8 hours and the solid filtered and washed with water. The solid is then suspended in water and stirred overnight before being recovered by filtration and air-dried [28]. An excess of physisorbed azamacrocycle remains (as discovered by ESR and TGA/CHN analysis) and must be removed by washing the functionalised silica in warm ethanol.

Incorporation of metal complexes to azamacrocycle-functionalised SBA-15 materials

Metal cations, were incorporated into the azamacrocycle ring by complexation from alcoholic or aqueous solutions (depending on the solubility of the metal salts in the different solvents). The metal ions were added at molar ratios to the included macrocycles of values between 0.4 – 0.9 : 1.0. (The amounts of macrocycle were determined via elemental CHN analysis). Iron(III) citrate (Lancaster, 24-26% Fe content) was complexed to the azamacrocycle from an aqueous solution (55 – 200 ml) involving between 0.3 – 4.0 g of SBA-15 functionalised with the azamacrocycle with stirring of the suspension at *ca.* 50 °C overnight. Typically for a 90% azamacrocycle filling 1 g of functionalised SBA-15 would be added to a solution containing 0.043 g

or 0.018 g iron(III) citrate for TACN and cyclam containing SBA-15 respectively. The solid was then filtered off and dried. Complexation with stoichiometric equivalents of Cu (II) (cupric acetate, Fisons, 99%) and Mn (II) (manganese (II) acetate tetrahydrate, Aldric, 99+%) were from alcoholic (ethanol) solutions under the same conditions.

ESR analyses on these samples are described in Chapter 2 and for CHN using a CE Instruments ES 1110 analyser.

Catalytic measurements

Preliminary results are presented for the oxidation of cyclohexane with metallated cyclam and also for the epoxidation of cyclohexene with metallated TACN.

Cyclohexane oxidation reactions were carried out according to experimental conditions reported in the literature [17]. The oxygen source for this reaction was hydrogen peroxide, and the reported products of the reaction included cyclohexanol and cyclohexanone. For each oxidation experiment, the total volume of solutions was 19 ml, with 17ml acetone as solvent, 2 ml cyclohexane substrate (18.5 mmol) and 2 ml H₂O₂ (30%) (58.8 mmol). 76 mg (0.06 mmol) of the M(cyclam)-SBA-15 solid was added and heated to 373 K for 12 hrs with stirring. After the reaction period the mixture was cooled to room temperature and the solid removed by filtration. The products were analysed by gas chromatography. Control experiments (without added solid, without metallating the azamacrocycle) were also performed.

Initially the reactions were carried out in a Teflon-lined and magnetically stirred autoclave (Parr 4842), but some loss of volatile organics were observed so further reactions were performed in a sealed glass vessel designed and built 'in house' (figure 5.1.5).



Figure 5.1.5. 'In house' glass vessel for cyclohexane oxidation reactions

Cyclohexene epoxidation was chosen as a reaction that was expected to be catalysed under mild conditions than alkane oxidation. The reaction conditions reported by Valentine [16] were adopted. The solvent – acetonitrile (5 ml); substrate – cyclohexene (0.2464 g; 3 mmol); an aldehyde – isobutyraldehyde (1 ml) and an inert internal standard – chlorobenzene (0.1 ml) was added to the Schlenk tube along with 24 mg (0.02 mmol) of the metallated TACN supported catalyst with O_2 bubbled through under stirring at room temperature for 4 hrs. After the reaction, the solid was filtered and the filtrate containing the product, cyclohexene oxide (the epoxide of cyclohexene), analysed by GC. A blank without any catalyst in the mixture was also run and also a non-metallated SBA-15-TACN complex.

The data obtained for the catalysis on the above sample was from a Philips, PYE Unicam PU4500 gas chromatograph equipped with a Supercowax 10 polar capillary BP20 column (30 m \times 0.53 mm internal diameter) with a 0.5 μ m film thickness (Supelcowax 10) and a flame ionisation detector. The starting temperature of 323 K was held for 2 mins before a ramp rate of 16 $^{\circ}$ C/min up to 423 K and finally held for 5 mins. Before the GC analysis could be quantified, retention times and response factors for different compounds (reactants and products) were measured.

5.3 Results & Discussion

The results within this chapter are divided into two sections. The first discusses the metallation of cyclam within SBA-15, with particular emphasis on the use of ESR to monitor the local environment of Cu^{2+} in cyclam-functionalised SBA-15 during preparation and after use of the solid in oxidation reactions. The second section describes the results of the epoxidation of cyclohexene over SBA-15 functionalised with TACN and with a range of transition metals incorporated in the solid.

ESR was performed on three different samples of $\text{Cu}[\text{cyclam}]^{2+}$ -SBA-15. The first sample to be examined was the solid prepared by initial reaction of the propylchloride SBA-15 with cyclam, followed by water washing and copper ion complexation ($\text{Cu}[\text{cyclam}]$ -SBA-15 A). A combination of the ESR spectroscopy and chemical and thermal analysis indicated that a physisorbed cyclam species was present, so exhaustive washing and extraction in ethanol was performed before Cu^{2+} complexation ($\text{Cu}[\text{cyclam}]$ -SBA-15 B): this was then shown to remove most of the physisorbed species, and a full ESR characterisation of copper complexed within the strongly bound cyclam was possible. Finally, a sample that had been used in oxidation reactions was examined ($\text{Cu}[\text{cyclam}]$ -SBA-15 C)

5.3.1 Multi frequency ESR studies of Cu^{2+} [cyclam] SBA-15

A powder ESR spectrum of an anisotropic solid will be the sum of the signal from the complex in all possible orientations. The expected four Cu^{2+} ($S = 1$; $I = 3/2$) transitions will not appear as a single, average g value (g_{iso} ($g_{\text{xx}} = g_{\text{yy}} = g_{\text{zz}}$)) but in general as separate g tensors. In this particular case the Cu^{2+} environment possesses axial symmetry, with different g values parallel and perpendicular to the field ($g_{\text{xx}} = g_{\text{yy}}$ (g_{\perp}) \neq g_{zz} (g_{\parallel})). The powder ESR spectrum of $\text{Cu}[\text{cyclam}]$ -SBA-15 A measured at a frequency of 9.5 GHz (X-band) is given in figure 5.3.1.1.

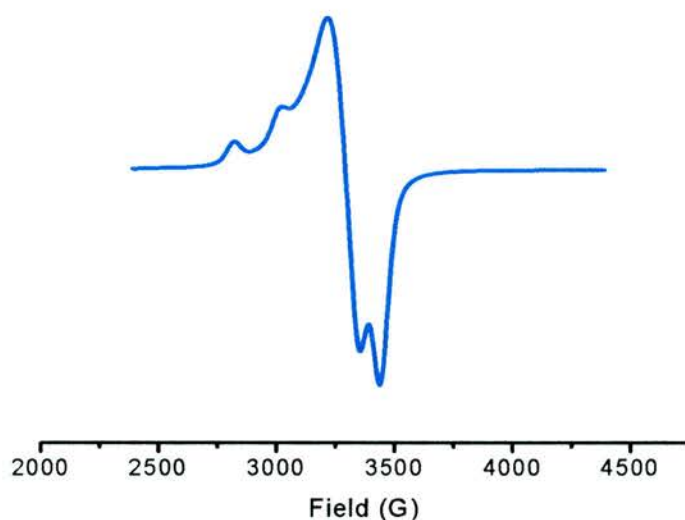


Figure 5.3.1.1. Powder ESR spectrum measured at X-band (9.5 GHz) of Cu^{2+} [cyclam]-SBA-15 A

In order to determine accurately the spin Hamiltonians, simulation* of the spectrum obtained was determined to help characterise the Cu^{2+} species. It was found after many attempts that it was difficult to obtain a high quality fit due to the broad hyperfine features observed on the parallel side (low-field) and also the increasing base-line in this region. Obtaining an acceptable simulated pattern could only be achieved by assuming the presence of two Cu^{2+} species being present (figure 5.3.1.2).

* Simulation at the national high-field ESR facility, St. Andrews University using XSophe package.

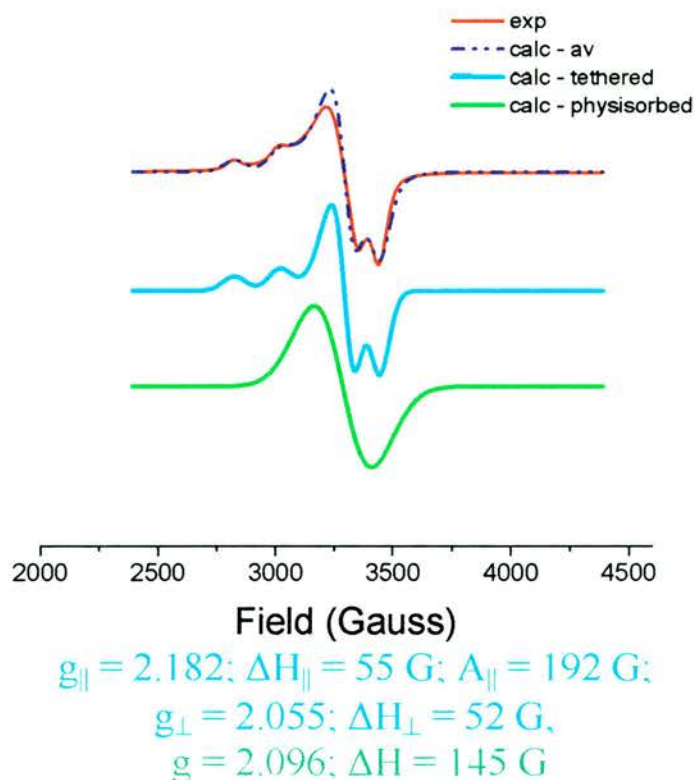


Figure 5.3.1.2. Simulated X-band spectra of Cu[cyclam]-SBA-15 A with the presence of two Cu^{2+} species present (cyan and green lines) to give an averaged (blue dotted line) which shows an acceptable fit to the experimental spectrum (red line).

Examination of thermogravimetric analysis and elemental analysis supports the hypothesis of two different copper environments for this sample. The N content is found to be 5.5 wt%. Taking into account the weight loss on heating of the as-prepared sample, it can be calculated that a 1 : 1 reaction of the chloropropyl groups would give a N content of around 2.5 wt% (figure 5.3.1.3). Based on this, there must be considerable physisorbed cyclam on the SBA-15 surface. The rapid loss of mass (at around 220 °C) can be attributed to this physisorbed cyclam being removed. The process seems to be slightly exothermic through cyclam decomposition with a slight reduction in temperature after the rapid loss of organics.

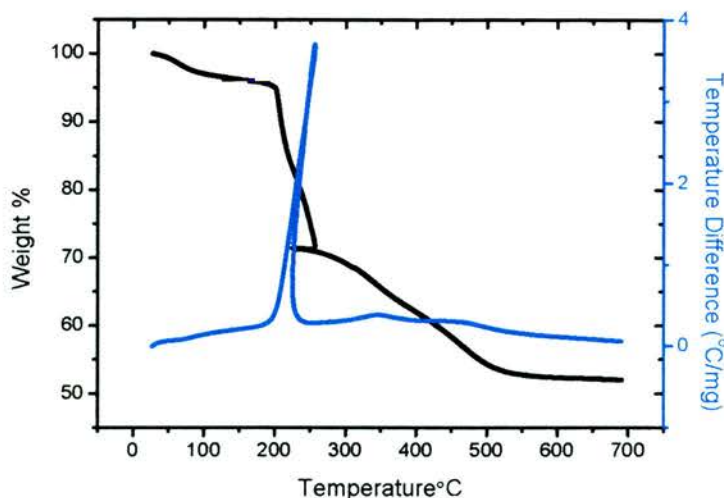


Figure 5.3.1.3. Thermogravimetric analysis of the non-metallated SBA-15-cyclam solid revealing the presence of 52% SiO₂

This explains the need for two separate environments when simulating the ESR spectra (figure 5.3.1.2). Strongly bound, tethered Cu[cyclam]²⁺ species could be far enough apart not to interact with each other – bearing in mind that the degree of propylchloride functionalisation, onto which the cyclam binds, is only 5% maximum of the total solid – and so the electron-nuclear interactions dominate giving rise to the hyperfine structure as seen in the ‘tethered’ spectrum. It is possible that physisorbed Cu[cyclam]²⁺ aggregates so that the Cu²⁺ co-ordinated complexes are close enough that individual Cu²⁺ cations experience electron-electron type interactions, which dominate over electron-nuclear type interactions, and suppress hyperfine structure in the spectrum (green line). This would explain why the parallel hyperfine features are particularly broad and stray away from the base-line. Certainly simulation without the physisorbed component (green line) results in a poor fit.

Only 2 clear parallel hyperfine coupling constants are observed at X-band frequency and not the expected 4 due to an overlap of the parallel and perpendicular regions, making difficult the determination of the spin Hamiltonians. Since the hyperfine coupling constants are field independent and g values are field dependent, measuring the spectrum at a higher field results in separation of the parallel region from that of the perpendicular region. K-band measurement at 24 GHz (figure 5.3.1.4) shows this effect: here there are 3 clear hyperfine features present. Here ‘clear’ is with respect to the parallel side separating from the perpendicular side.

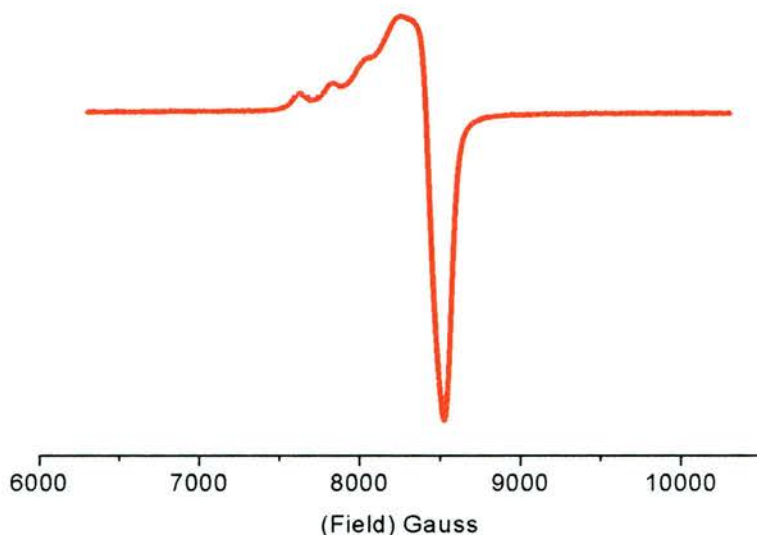
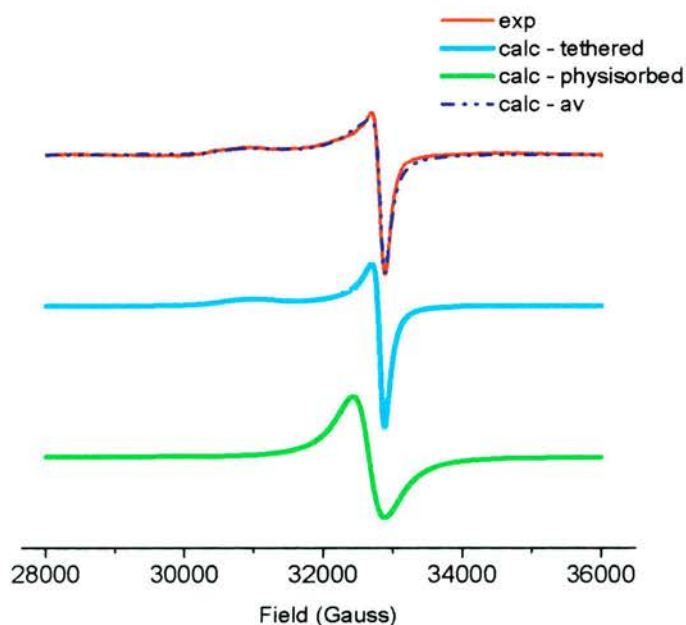


Figure 5.3.1.4. Powder ESR spectrum measured at 24 GHz (K-band) of Cu[cyclam]-SBA-15 A showing the separation of the parallel and perpendicular sides

High-field measurements at W-band (94 GHz) (figure 5.3.1.5) show complete separation of the parallel and perpendicular regions.



$$\begin{aligned}
 g_{\parallel} &= 2.185; \Delta H_{\parallel} = 180 \text{ G}; A_{\parallel} = 200 \text{ G}; \\
 g_{\perp} &= 2.055; \Delta H_{\perp} = 120 \text{ G}, \\
 g &= 2.096; \Delta H = 400 \text{ G}
 \end{aligned}$$

Figure 5.3.15. Powder ESR spectra of experimental (red line) and simulated (blue dotted line) calculated from chemisorbed (cyan line) and physisorbed (green line) from the 2 Cu species within Cu[cyclam]-SBA-15 A measured at 94 GHz (W-band)

However the resolution of the parallel (low field) side is low due to an increase in line broadening (ΔH_{\parallel}) compared to the X-band measurements. This is a sign of ‘g-strain’ effect [29]. If it was possible to take a single crystal of Cu[cyclam]-SBA-15 and place it in the cavity and orientate the crystal parallel to the field resonance signals would appear at low-field. Upon rotating the crystal towards the perpendicular region there would be a shift of resonance to higher field. Although the sample here is powder and all orientations are observed, within selected orientations of the Cu[cyclam], for example the extreme parallel side, the orientation of the paramagnetic Cu^{2+} cations within the diamagnetic host can slightly vary (figure 5.3.1.6). Here the ‘g-strain’ can be thought of as being this variation of orientation of the paramagnetic species within a specifically orientated diamagnetic host.

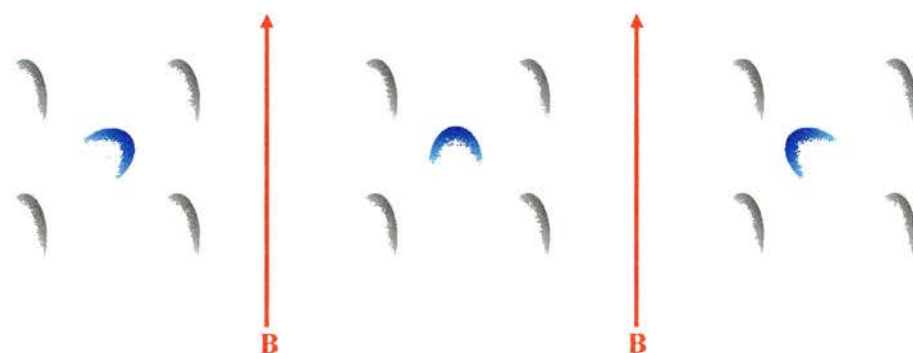


Figure 5.3.1.6. g-strain within Cu[cyclam]-SBA-15: the varying orientation of the diamagnetic Cu^{2+} cations within a specifically orientated diamagnetic host

Therefore individual hyperfine features may arise from multiple components from varying field positions contributing to the overall observed feature, although at X-band there is insufficient resolution to see this (figure 5.3.1.7).

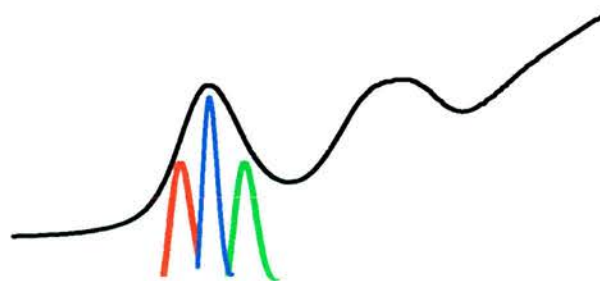


Figure 5.3.1.7. g-strain giving rise to varying components contributing to overall observed hyperfine feature

The apparent broadening in the parallel region at W-band is due to an increase in resolution. The increase in resolution comes about through the separation of the \parallel region from the \perp region as g is field dependent. The problem lies in that this increase in resolution is also observed in the varying features from the g -strain components and so at higher fields g -strain becomes more prominent [30] and the overall net resolution is decreased (figure 5.3.1.8).



Figure 5.3.1.8. Increased resolution between resonance signals as a function of field position at higher frequencies *ca.* W-band contributes to an increase of g -strain resolution which lowers overall net resolution in the parallel region

In light of the previous results, it was clear that to arrive at a sample containing only strongly bound cyclam, the reacted cyclam-SBA-15 composite should be exhaustively extracted before the Cu^{2+} was introduced. To perform this, the functionalised mesoporous solid was washed exhaustively with ethanol and extracted with hot ethanol. This reduced the total organic content so that the theoretical N content for 1 : 1 reaction of cyclam with chloride was 3.5 wt%, whereas there was now only 3.3 wt% N in the extracted sample. The TGA reveals only a minor sharp weight loss at *ca.* 220 °C, where physisorbed cyclam is lost from the sample (figure 5.3.1.9).

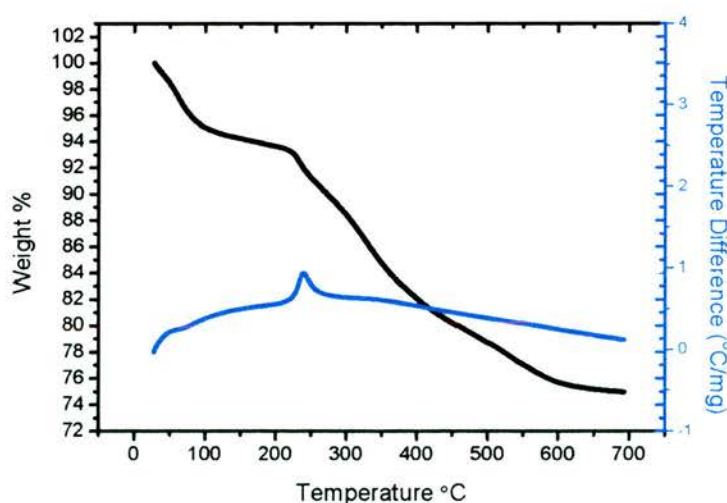


Figure 5.3.1.9. Thermogravimetric analysis of the non-metallated SBA-15-cyclam solid revealing the presence of

Upon complexing Cu^{2+} into the cyclam from copper (II) acetate solution, the powder ESR spectra measured at X-band are clearly now sharper with A_{\parallel} features narrower with a greater tendency to approach the base-line (figure 5.3.1.10), presumably due to a significant removal of the physisorbed species. There is also less interference of the physisorbed species broadening out the perpendicular region (figure 5.3.1.2, bottom of green line), also indicating the increase in the proportion of the dilute, more strongly bound species.

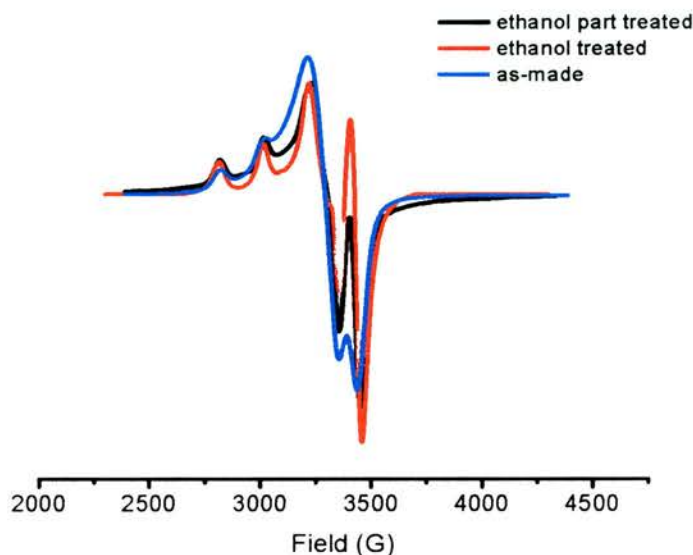


Figure 5.3.1.10. X-band powder ESR spectra of the initial Cu[cyclam]-SBA-15 A (figure 5.3.1.1) (blue); initial support washed with cold ethanol before Cu[cyclam] incorporation (black) and initial support stirred in hot ethanol before Cu[cyclam] B incorporation (red)

The levels of incorporation of cupric acetate into this cyclam-functionalised SBA-15 support was varied. Figure 5.3.1.11 shows powder ESR spectra measured at a frequency of 9.5 GHz (X-band) of various Cu^{2+} loadings into SBA-15-cyclam (for 10 – 80% equivalents). This gives increase in resonance intensity upon increasing Cu(II) loading but the spectra remain the same shape. It is therefore reasonable to suggest that the Cu^{2+} ions are located within the same type of sites upon increased loading.

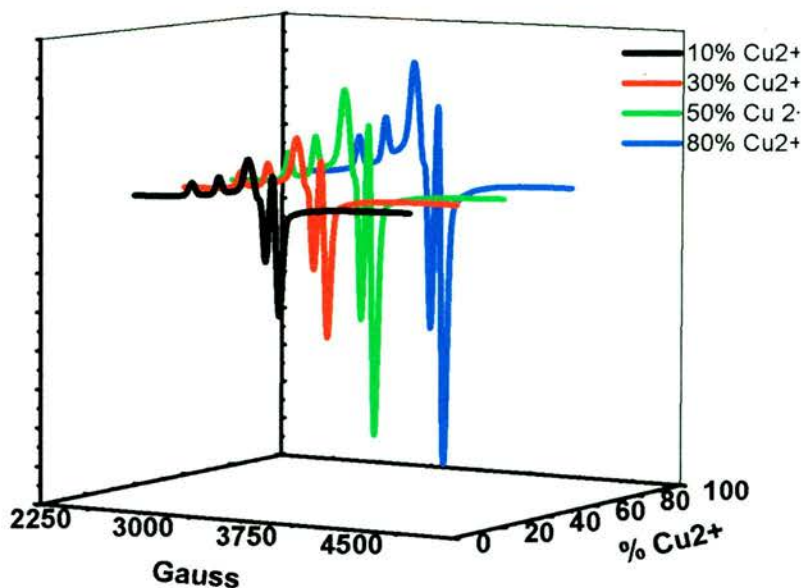
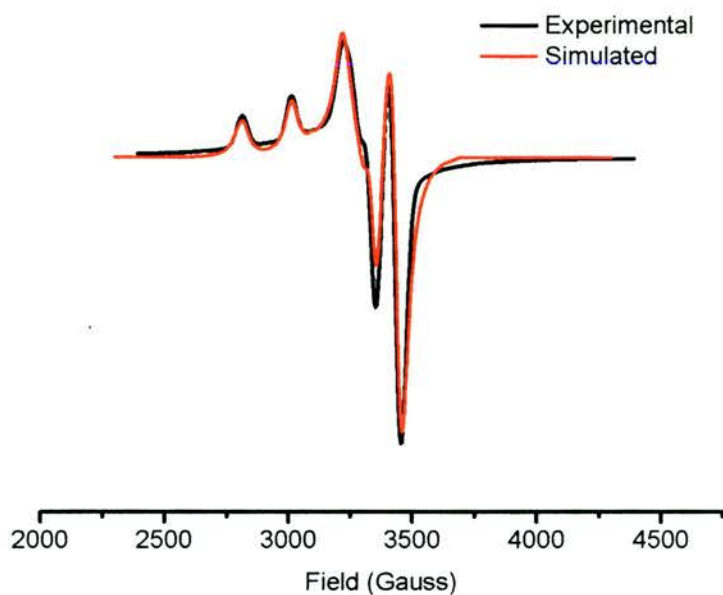


Figure 5.3.1.11. Powder ESR spectra measured at X-band (9.5 GHz) of Cu^{2+} [cyclam]-SBA-15 B with varying loadings of Cu^{2+} . Increasing Cu^{2+} loading increases resonance intensity

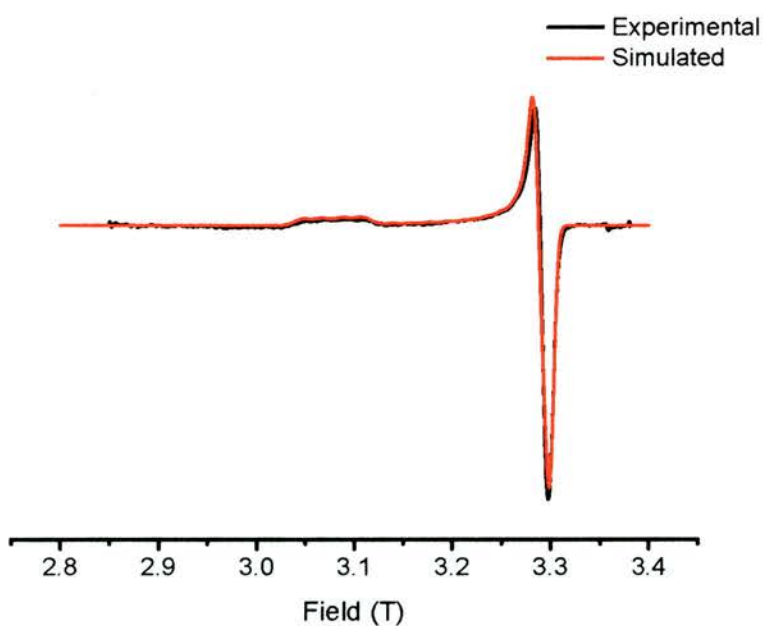
The ESR spectra therefore complement the TGA and CHN analysis for the ethanol treated SBA-15-cyclam solid. It is now possible that there is no physisorbed cyclam present.

Simulation of the ethanol treated Cu [cyclam]-SBA-15 B is much more consistent within the different frequencies compared to the simulation of the untreated analogue (figure 5.3.1.12). It should be also noticed that no values are given for A_{\perp} as there is no resolution between the perpendicular hyperfine splittings. It is often acceptable not to publish Cu^{2+} A_{\perp} values although an upper-limit of the value used in simulating the spectrum is normally admissible [31] and in this case the value of 30 G is the upper-limit.



$$g_{\parallel} = 2.182; A_{\parallel} = 198 \text{ G}; \Delta H_{\parallel} = 30 \text{ G};$$

$$g_{\perp} = 2.04; \Delta H_{\perp} = 45 \text{ G}$$



$$g_{\parallel} = 2.182; A_{\parallel} = 198 \text{ G}; \Delta H_{\parallel} = 50 \text{ G};$$

$$g_{\perp} = 2.04; \Delta H_{\perp} = 100 \text{ G}$$

Figure 5.3.1.12. Powder ESR spectra of experimental (black) and simulated (red) ethanol-treated Cu[cyclam]SBA-15 B measured at X-band (above) and W-band (below) showing much sharper spectra, especially for X-band, and more consistent spin Hamiltonions

An aside on the ESR of Cu[cyclam]-SBA-15

There is another feature of the X-band spectrum that is typical of some Cu^{2+} complexes. This is a low-field phenomenon which diminishes upon increasing the frequency. The highest-field resonance transition (figure 5.3.1.12 – X-band) is not a peak that correlates to the perpendicular region but is in fact an ‘off-axis’ overshoot peak [32] which does not correspond to the three principle axes of the field (figure 5.3.1.13) (illustrated in black).

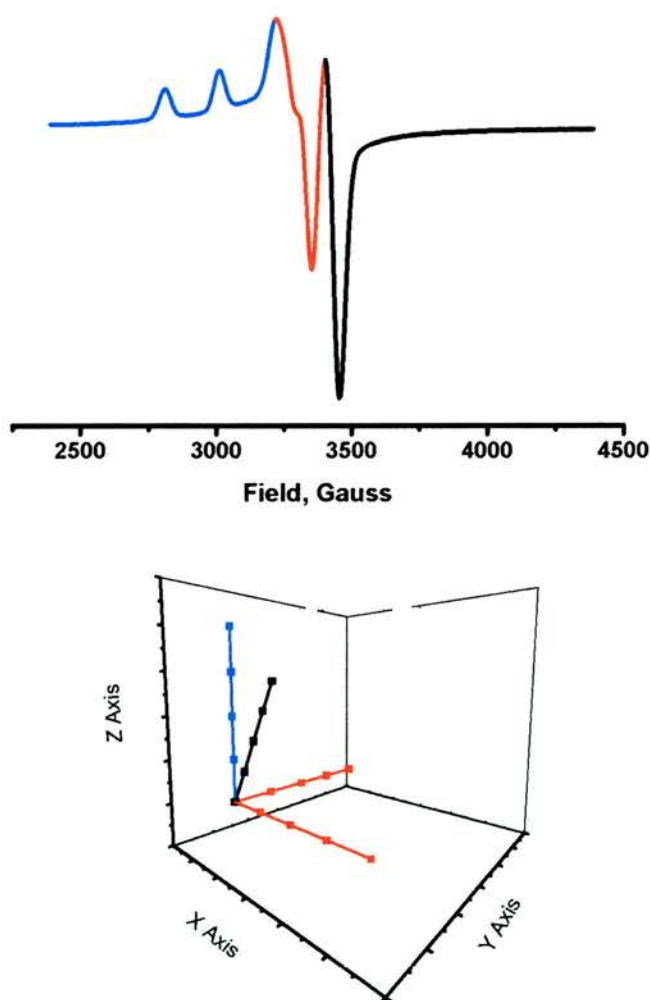


Figure 5.3.1.13. The appearance of an ‘overshoot’ peak – a low frequency phenomenon – off-axis to the principle axes should not be interpreted as perpendicular peak

The reason for the appearance of the ‘overshoot’ peak comes about through an extra off-axis turning point being created [33]. If one takes a single crystal and orientates the crystal \parallel to the field ($\theta = 90^\circ$) and rotates the crystal carefully using a goniometer towards the \perp region ($\theta = 0^\circ$) the field positions of the resonance peaks can be determined as a function of theta [34]. Plotting the angle dependency of field position as a function of theta enables one to see the hyperfine coupling constants decrease from the \parallel region to the \perp region (figure 5.3.1.14).* Cu(II) complexes should not have g values below 2 which could be the case if the overshoot peak is mistakenly taken as being part of the perpendicular region.

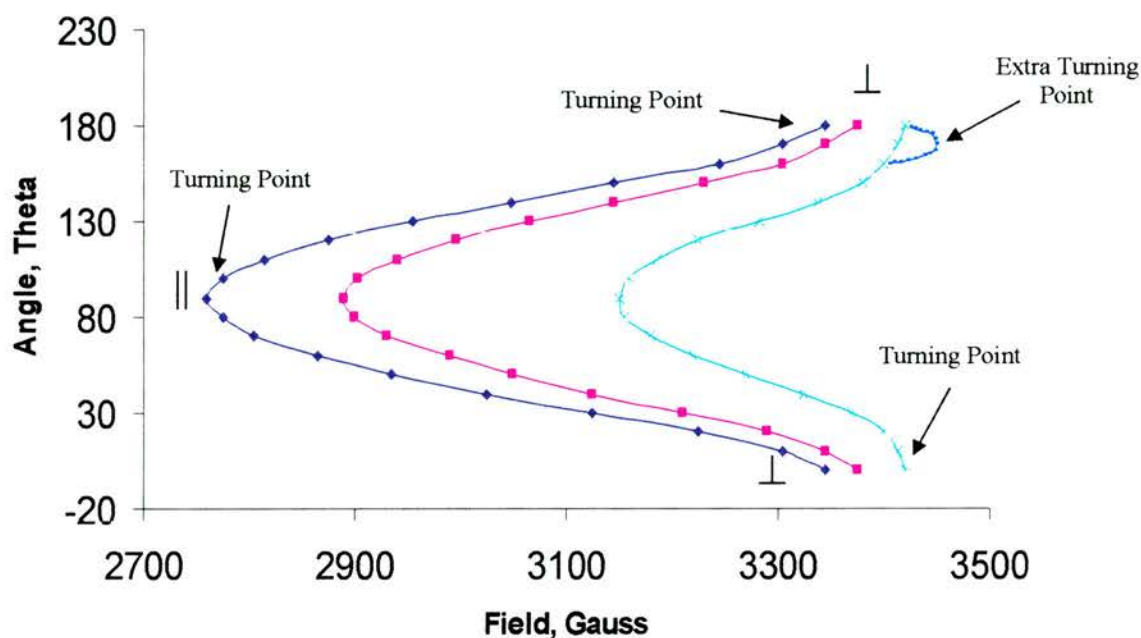


Figure 5.3.1.14. An angle dependency plot of a Cu^{2+} complex to show how the angle dependency lines vary with field position as a function of theta

* Figure 5.3.1.14 is graph that shows how the angle dependency lines of $\text{Cu}^{2+}(\text{acac})_2$ varies in field positions as a function of θ . This does not correspond to the angle dependency lines of $\text{Cu}(\text{II})[\text{cyclam}]\text{-SBA-15 B}$ and also for the relative hyperfine splittings. As neither a single crystal or a large crystal (containing individual crystals with the same orientation) of $\text{Cu}(\text{II})[\text{cyclam}]\text{-SBA-15 B}$ can be isolated therefore a field dependency plot can not be obtained. The field dependency plot in figure 5.3.1.14 was obtained [34] using a prepared crystal of a different Cu^{2+} complex. The reason for showing this plot is to give the reader a pictorial view of how the ‘overshoot’ peak arises due to the creation of an extra off-axis turning point, albeit exaggerated for clarity.

The features obtained on powder ESR spectra come from the turning points of resonance fields plotted as a function of angle [34] and it is these features where one can obtain the Spin Hamiltonian parameters and thus retrieve information on the geometry and environment of the paramagnetic species. Here the paramagnetic d^9 Cu(II) species bearing axial symmetry has Jahn-Teller elongated axial ligands.

If the system was a Jahn-Teller compressed Cu(II) ion then the crystal field predicts d_z^2 as the ground state (figure 5.3.1.15) and if B is \parallel to z then the d_z^2 couples with no other d-orbital and so there is no shift of g hence $g_{zz} = g_e$. However if B is \parallel to $x(y)$ then the d_z^2 orbital couples with $d_{xz,yz}$:

$$\Delta g_{xx} (= \Delta g_{yy}) \propto - \frac{n\lambda}{E_{z^2} - E_{xz,yz}} \quad \text{Equation 5.3.1.1}$$

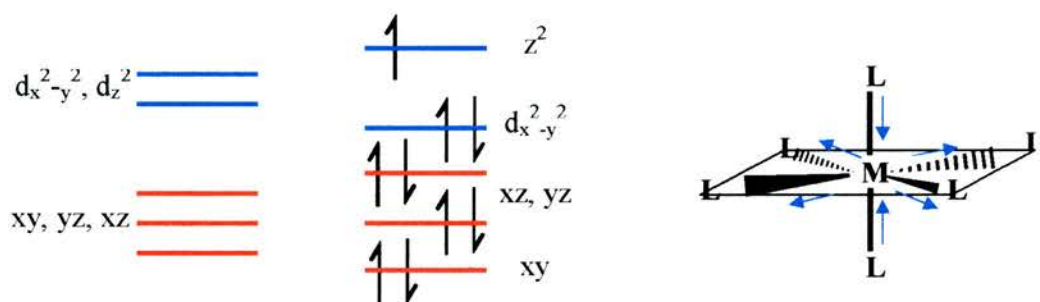


Figure 5.3.1.15. Crystal field prediction for a Jahn-Teller compressed system with the d_z^2 orbital as the ground state

and a shift from g_e arises and therefore the axial spectrum would look as shown in figure 5.3.1.16. $g_{xx} = g_{yy} > g_{zz} \approx g_e$. Since the experimental spectra obtained did not look like figure 5.3.1.16 then the experimental spectra with that for the theory of the Jahn-Teller elongated axial ligands was compared.

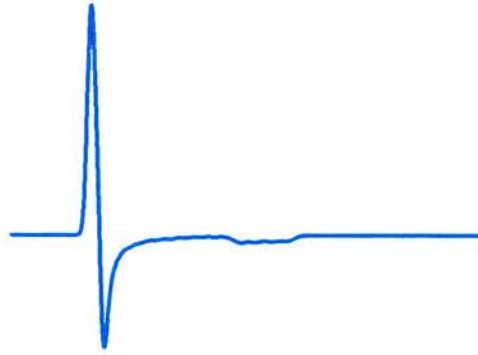


Figure 5.3.1.16. Powder ESR spectrum of a Cu(II) ion displaying a Jahn-Teller compressed with $g_{xx,yy}(\perp) > g_{zz}(\parallel)$

If the field, B, is parallel to the z direction the $d_{x^2-y^2}$ orbital can mix with the d_{xy} orbital. Hence;

$$\Delta g_{zz} \propto -\frac{n\lambda}{E_{x^2-y^2} - E_{xy}} \quad \text{Equation 5.3.1.2}$$

there is a small number as the denominator and hence a bigger shift of g_e compared to if the field is parallel along x(y) with mixing of the $d_{x^2-y^2}$ orbital with the $d_{xz,yz}$ orbital and;

$$\Delta g_{xx} (= \Delta g_{yy}) \propto -\frac{n\lambda}{E_{x^2-y^2} - E_{xz,yz}} \quad \text{Equation 5.3.1.3}$$

giving a bigger number on the bottom and hence a smaller shift in g_e (figure 5.3.1.17). $g_{zz} > g_{xx} = g_{yy} > g_e$. As this fits the experimental spectra it is reasonable to assume that the elongated form of distortion is present in the system.

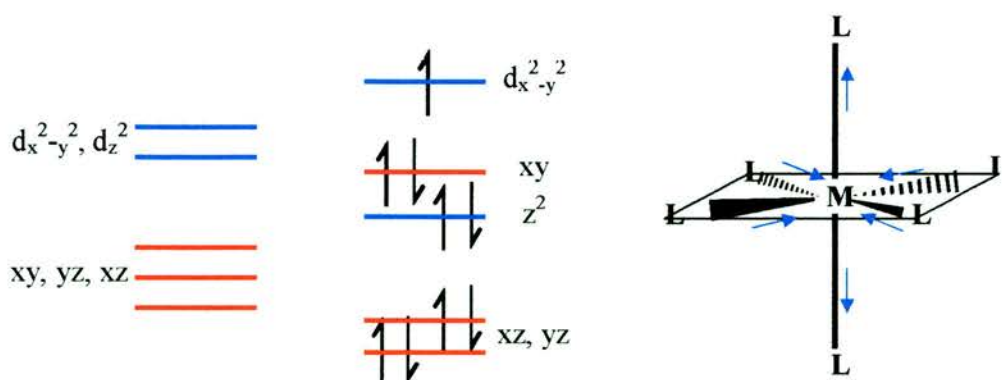


Figure 5.3.1.17. Jahn-Teller elongated Cu(II) ion whereby if B is parallel to (i) z the $d_{x^2-y^2}$ orbital can mix with the d_{xy} orbital or (ii) x(y) the $d_{x^2-y^2}$ orbital can mix with the $d_{xz,yz}$ orbital. The larger the energy difference the smaller the shift in g and therefore for the elongated system g_{zz} has a greater shift away from g_e than $g_{xx,yy}$.

The resonance features observed by the Cu[cyclam]-SBA-15 sample therefore displays a Jahn-Teller elongated Cu(II) ion with the unpaired electron in the $d_{x^2-y^2}$ orbital. The time that the lone electron spends in this orbital can be calculated via [35]:

$$A_z - A_{x,y} = P_d \left[-\frac{6}{7} a^2 + \Delta g_z - \frac{5}{14} \Delta g_{x,y} \right] \quad \text{Equation 5.3.1.4}$$

where the a^2 term is the probability of the electron in the aforementioned orbital, P_d the electron-nuclear dipolar coupling parameter and is $+400 \cdot 10^{-4} \text{ cm}^{-1}$, and A converted to cm^{-1} units.* The correct signs of A can be obtained from equation 5.3.1.5 whereby obtaining a positive value for the a^2 term.

$$A_z - A_{x,y} = -\frac{6}{7} a^2 P_d \quad \text{Equation 5.3.1.5}$$

It turns out that the unpaired electron from the Cu(II) ion is present in the $d_{x^2-y^2}$ orbital 70% of the time, i.e., the a^2 term is equal to 0.7 ± 0.03 (dependent on A_{\perp} value). (Much more information can be retrieved from the powder spectrum than in the

* $A_{\text{cm}^{-1}} = A_{\text{gauss}} \cdot 0.46686 \cdot 10^{-4} \cdot g$

isotropic case. The g and A tensors however have not completely averaged out into single tensors due to slow orientations of the molecules bulky nature and thus the spectrum (figure 5.3.1.18) displays only g_{iso} and A_{iso} values as the dipole-dipole interaction averages to zero in solution).

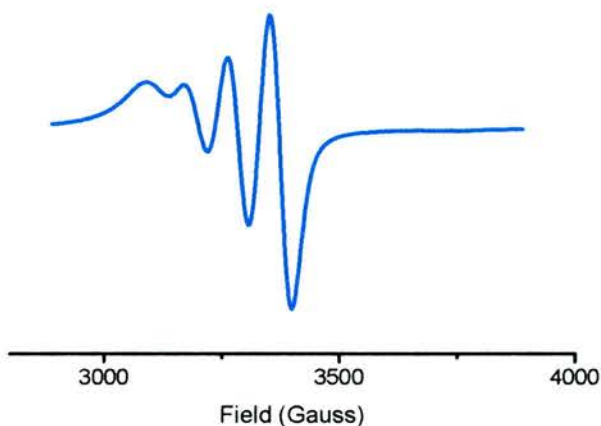


Figure 5.3.1.18. Isotropic spectrum of Cu[cyclam] in ethanol

ESR spectra of Cu(II) complexes possessing square planar co-ordination geometry are characterised by the sequence $g_{\parallel} > g_{\perp} > 2.00$ and A_{\parallel} values in the region of $(150 - 210) \cdot 10^{-4} \text{ cm}^{-1}$ [22]. The Cu[cyclam]-SBA-15 B complex exhibits a g_{\parallel} value $> g_{\perp}$ (g_{\parallel} 2.182 and g_{\perp} 2.04) with A_{\parallel} being 198 G ($202 \cdot 10^{-4} \text{ cm}^{-1}$). The hyperfine coupling constants A_{\parallel} and A_{\perp} arise from the parallel and perpendicular regions, respectively, between the nuclear magnetic moment of Cu(II) and that of the electron spin. g_{\parallel} and A_{\parallel} are sensitive to the change in the ligands around the environment of Cu(II) and can give an insight into the type of co-ordination involved [36]. Hyperfine coupling constants are a better indication of distortion away from square planar, values ranging from 217 G for $[\text{Cu}(\text{cyclam})]^{2+}$ to around 60 G for blue copper proteins such as azurin where the geometry is close to tetrahedral [19]. The A_{\parallel} value of 198 G for Cu[cyclam]-SBA-15 B shows a slight deviation away from 217 G hence a distorted square planar and also true square planar is disfavoured upon increasing N-alkylation [19]. It has been suggested that the ratios of $g_{\parallel}/A_{\parallel}$ (in cm^{-1}) can be viewed as the empirical amount of the tetrahedral distortion in Cu(II) complexes. If this ratio is in the range of 105 – 135 cm , a square planar geometry is suggested [37]. The calculated ratio for the Cu[cyclam]-SBA-15 B complex is 108 cm at the extreme

lower range also indicating a distortion away from square planar. No superhyperfine coupling to the N within the azamacrocycle is observed although ENDOR spectroscopy does show strong N coupling (not shown). The Cu^{2+} environment is found to be in a slightly distorted square planar symmetry with respect to the nitrogens of the cyclam ring with elongated Jahn-Teller axial ligands.

ESR after catalysis

The environment of the copper salt after catalysis at 373 K (conditions described in [17]) is visibly seen to change after the oxidation of cyclohexane at 373 K with 16 % conversion of cyclohexane (with selectivity for cyclohexanone (33%) and cyclohexanol (18%) products). $\text{Cu}[\text{cyclam}]\text{-SBA-15 B}$, as-made, is a purple colour and after reaction the solid turns green (figure 5.3.1.19).

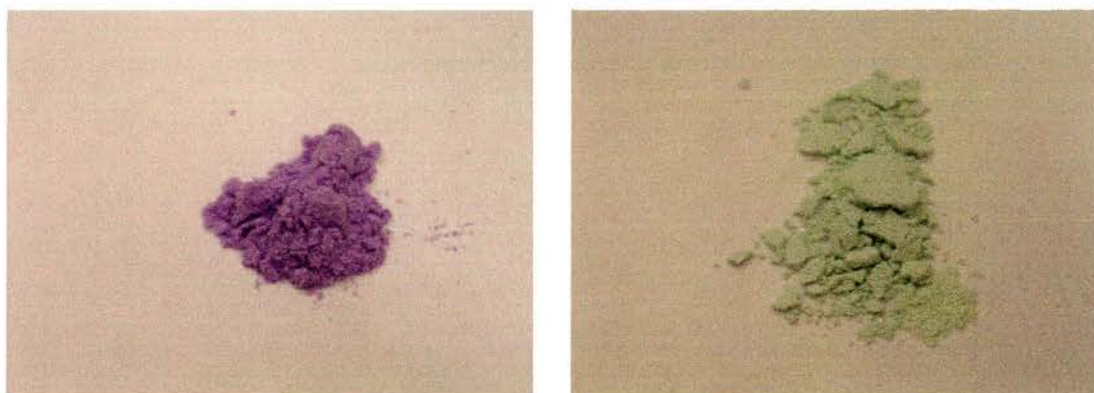


Figure 5.3.1.19. $\text{Cu}[\text{cyclam}]\text{-SBA-15}$ before (left) and after (right) oxidation of cyclohexane catalysis

The ESR spectrum of $\text{Cu}[\text{cyclam}]\text{-SBA-15 C}$ also, as expected, displays a different resonance pattern to the solid before its use in the reaction (figure 5.3.1.20 – left). The powder spectrum of the solid after catalysis is very similar to that observed for a green solid prepared by calcining a $\text{Cu}[\text{cyclam}]^{2+}$ templated magnesioaluminophosphate (figure 5.3.1.20 – right) [38]. STA-6, a microporous MgAlPO

solid templated by $\text{Cu}[\text{cyclam}]^{2+}$ is calcined at 550 °C to render the solid porous leaving Cu(II) as an extra-framework species coordinated to the oxygen from the framework. It is feasible to assume that breakdown and loss of the azamacrocycle occurs during the catalysis and the Cu(II) species remains as an extra-framework species. CHN analysis reveals there to be 2.39% of N in the solid before catalysis and only 0.50% N present after reaction. Therefore leaching of the azamacrocycle does seem to have occurred and the remaining cyclam in the solid may have decomposed to a linear form.

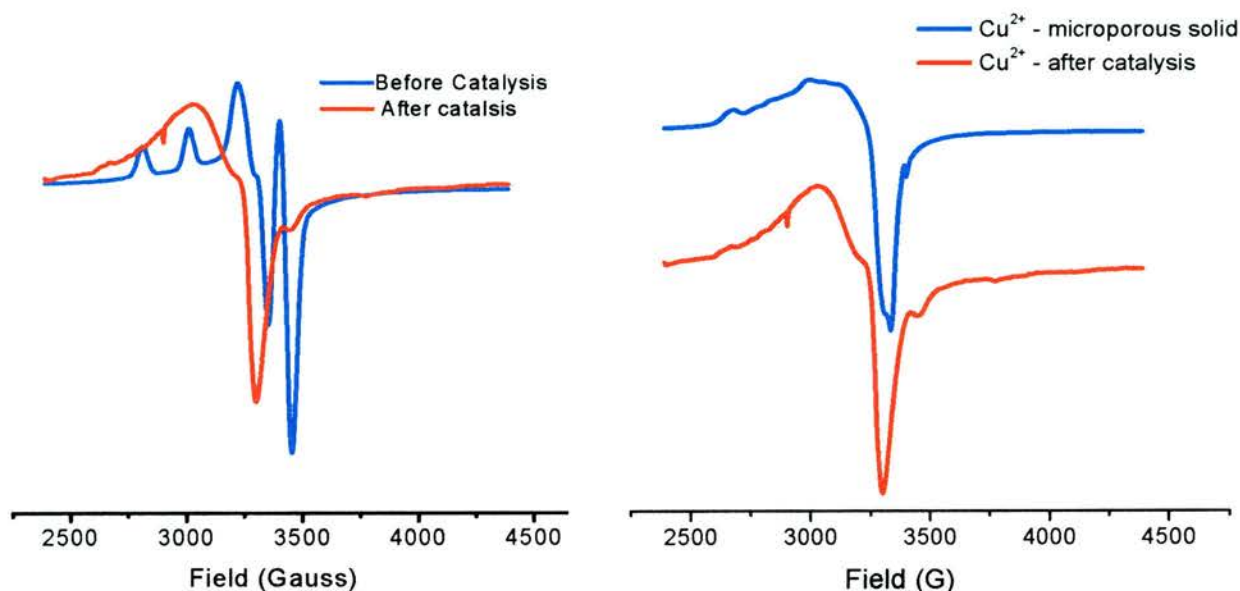


Figure 5.3.1.20. ESR powder spectra of a $[\text{Cu}(\text{cyclam})]^{2+}$ -SBA-15 solid as made (blue) and after the oxidation catalysis of cyclohexane (red) (left); the same spectrum after catalysis (red) is comparable with a Cu^{2+} sample in a calcined microporous solid where cyclam is burnt out (blue) (right)

Attempted reaction at 313 K does not seem to affect the geometry of the metallated cyclam as the ESR spectrum after catalysis has the same features present as the ‘before catalysis’ spectrum. However there is no reaction under these conditions.

5.3.2 Metallated [TACN] supported SBA-15: Epoxidation of cyclohexene

Unsuccessful catalysis for the oxidation of cyclohexane with the resultant degradation and leaching of $\text{Cu}[\text{cyclam}]^{2+}$ at temperatures of 373 K led our efforts towards oxidation of cyclohexene under milder conditions using metallated TACN complexes (TACN is well known for activity in epoxidations). With metal complexes (especially Fe and Cu) of ligands containing nitrogen molecules widely mimicking the catalytic properties of monooxygenases it was thought that such reactions would proceed under mild conditions (since enzymes work under mild conditions) which may suppress the metal leaching found in the high temperature oxidation reactions. SBA-15-TACN complexed with Mn^{2+} , Fe^{3+} and Cu^{2+} were prepared for a series of epoxidation reactions at room temperature and at 313 K.

Elemental analyses on nitrogen on potential supported catalysts in the form of Fe^{3+} , Mn^{2+} and Cu^{2+} incorporated TACN supported SBA-15 are given in table 5.3.2.1 before catalysis, after catalysis and after re-using the catalyst further.

	Room Temperature								
	Unused			Used			Re-used		
	C	H	N	C	H	N	C	H	N
Fe[TACN]	7.83%	1.42%	1.55%	9.41%	1.44%	1.16%	9.59%	1.51%	0.89%
							9.42%	1.40%	0.91%
Cu[TACN]	9.21%	1.65%	1.61%	11.20%	1.74%	1.46%	9.91%	1.67%	0.87%
							10.58%	1.44%	0.93%
Mn[TACN]	9.45%	1.73%	1.66%	13.75%	2.03%	0.91%	17.74%	2.22%	0.77%
							15.99%	1.66%	0.74%
313 K									
	Unused			Used			Re-used		
	C	H	N	C	H	N	C	H	N
Fe[TACN]	7.83%	1.42%	1.55%	9.80%	1.27%	0.93%	10.06%	1.95%	0.83%
							10.54%	1.39%	0.82%

Cu[TACN]	9.21%	1.65%	1.61%	9.68%	1.31%	0.81%	13.10%	1.69%	0.71%
							13.02%	1.79%	0.69%
Mn[TACN]	9.45%	1.73%	1.66%	11.79%	1.53%	0.84%	14.84%	1.82%	0.74%
							13.70%	2.04%	0.69%

Table 5.3.2.1. CHN elemental analyses of metallated TACN supported SBA-15 before, after and re-use in epoxidation catalysis

The supported catalysts are brightly coloured indicating that the transition metals have been included into the support (figure 5.3.2.1).



Figure 5.3.2.1. Metal[TACN] supported SBA-15 with (left) Fe^{3+} , (middle) Cu^{2+} and (right) Mn^{2+} .

After using the respective catalysts in the epoxidation of cyclohexene at room temperature it can be seen that both the Fe^{3+} and Cu^{2+} samples retain their colour after catalysis while the Mn sample loses its colour. Upon filtering the catalysts, leaving the products in solution the filtrates are clear for the Fe^{3+} and Cu^{2+} samples and the Mn^{2+} samples has a coloured filtrate indicating leaching has occurred (figure 5.3.2.2).

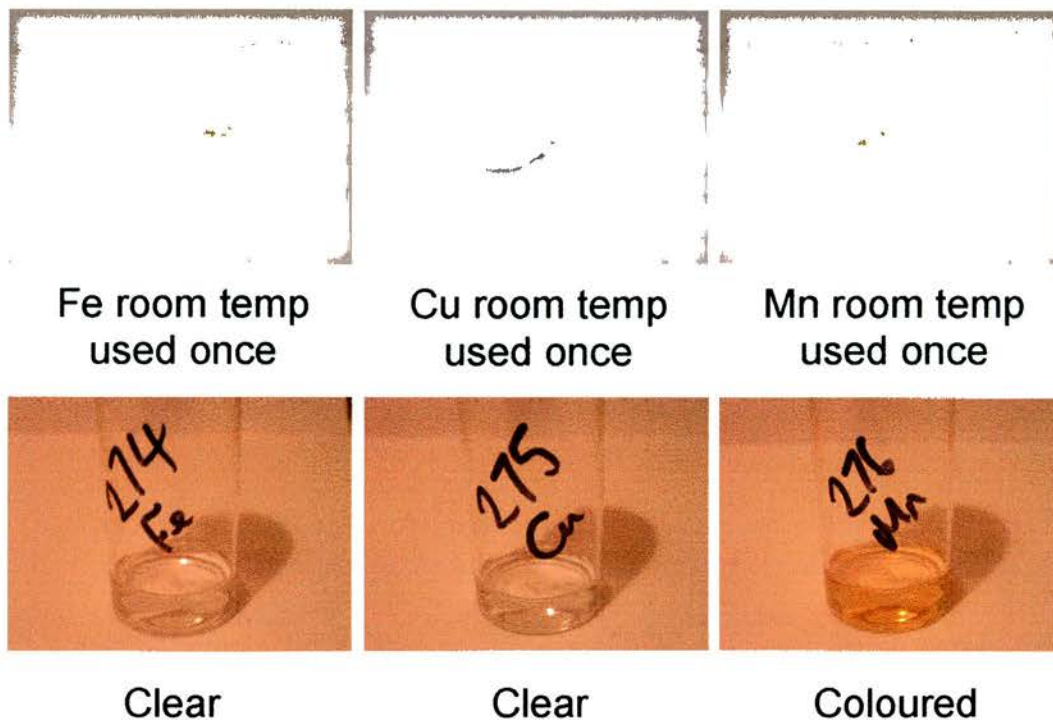


Figure 5.3.2.2. Recovered catalyst and collected filtrates of metallated [TACN] epoxidation reactions at room temperature. Mn shows signs of leaching (as seen in table 5.3.2.1).

Re-using the catalyst in a second epoxidation reaction at room temperature results in the loss of colour of all three recovered catalysts indicating that leaching has taken place. The filtrates are coloured although the Mn filtrate is only slightly coloured as a significant amount of leaching occurred in the initial epoxidation reaction (figure 5.3.2.3).

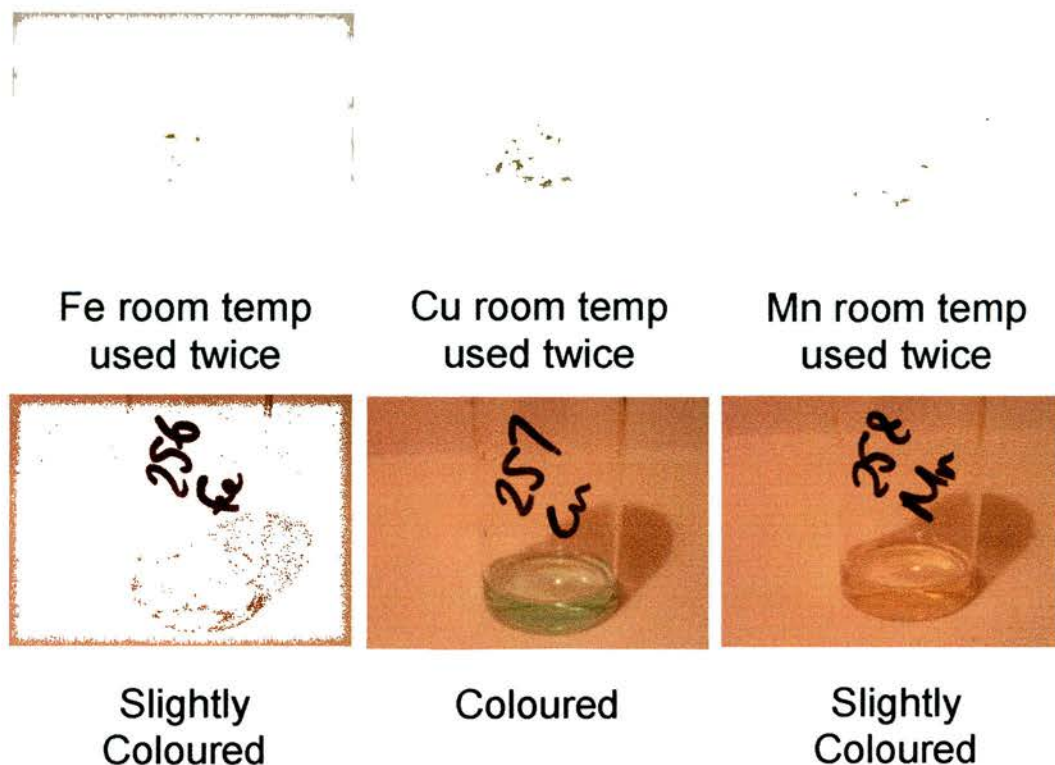


Figure 5.3.2.3. Recovered catalyst and collected filtrates of re-used metallated [TACN] epoxidation reactions at room temperature. All three solids show sign of leaching shows signs of leaching (as seen in table 5.3.2.1).

Performing the epoxidation reaction at 313 K results in leaching of all three metals into their respective filtrates as seen by the loss of some of the colour of the recovered solids. Here the N contents of the solids are similar to those observed on the re-used catalysts at room temperature (table 5.3.2.1). Therefore no further catalysis was performed as major leaching renders the solids ineffective as catalysts.

The respective catalytic performance of the supported catalysts with regards to conversion of the cyclohexene substrate and also the selectivity can be seen in table 5.3.2.2. It can be seen that the epoxidation results in cyclohexene oxide as the major oxidation product with cyclohexenone as the minor product (less than 10% of cyclohexene oxide). High conversions > 85% are observed with the exception of the Cu sample at room temperature which seems to suppress the reaction. The non-metallated blank also show signs of reactivity with conversions in the region of 30% and similar selectivities.

Room temperature				
Selectivity				
	Conversion	Cyclohexene oxide	cyclohexenone	Turnover
Fe	87%	40%	2%	367
Fe re-used	86%	55%	1%	363
Cu	46%	8%	0.5%	194
Cu re-used	87%	51%	1%	368
Mn	94%	50%	3%	397
Mn re-used	98%	48%	2%	414
Blank	31%	53%	2%	-

Table 5.3.2.2. Catalytic performance of metallated TACN supported on SBA-15 for epoxidation of cyclohexene under mild conditions

Although some catalysis was possible in single stage reactions, at room temperature, it was clear that metallated azamacrocycles supported on SBA-15 in this way do not give robust, re-usable catalysts and as such no further characterisation was carried out.

5.4 Conclusions

Successful incorporation of cyclam into SBA-15 has been achieved. Elemental analyses/thermo gravimetric analyses complemented by ESR spectroscopy has helped to improve the conditions of syntheses whereby removal of physisorbed species to leave the required tethered species can be clearly seen. It is important to remove the physisorbed species as any catalytic behaviour should ideally come from metals within the tethered azamacrocycles. Incorporation of transition metals into the ring of the azamacrocycles gives brightly coloured solids and the environment of Cu^{2+} cyclam has been investigated by ESR.

It was found through powder spectra that the co-ordination of Cu(II) in cyclam had axial symmetry with Jahn-Teller elongated axial ligands with the lone electron lying *ca.* 70% of the time in the $d_{x^2-y^2}$ orbital. The Cu(II) complex lies in a distorted square planar geometry with respect to the nitrogens in the cyclam ring. The importance of multi-frequency ESR measured at three frequencies (9 – 94 GHz) permits unambiguous determinations of the spin Hamiltonians and circumvents complications at low field, namely overlapping parallel and perpendicular regions and the low-field phenomenon off-axis overshoot peak at X-band.

Cyclohexane oxidation at 373 K results in some catalytic activity although the catalyst itself once recovered differs to the un-used catalyst. The geometry of Cu(II) has changed, seen visually by the colour change from purple to green and also by ESR, however, under milder conditions the catalyst remains structurally fine although the catalytic performance diminishes as no oxidation products are observed.

Attempts to prepare active, reusable catalysts by tethering and metallating azamacrocycles to chloropropyl SBA-15 were not successful. Using cyclam-based species for cyclohexane oxidation at 373 K resulted in some conversion, but also in degradation of the catalyst and leaching of the metal. Similarly, initial attempts to prepare tethered triazacyclononane catalysts gave materials that suffered strongly from leaching, even under the milder conditions required for cyclohexene oxidation. These results were not considered sufficiently promising for further characterisation studies on these materials.

5.5 References

- [1] V. Patinec, P.A. Wright, P. Lightfoot, R.A. Aitken, P.A. Cox, *J. Chem. Soc. Dalton Trans.*, 1999, **22**, 3909
- [2] P.A. Wright, M.J. Maple, A.M.Z. Slawin, V. Patinec, R.A. Aitken, S. Welsh, P.A. Cox, *J. Chem. Soc. Dalton Trans.*, 2000, **8**, 1243
- [3] C.J. Pedersen, *J. Am. Chem. Soc.*, 1967, **89**, 2495

- [4] C.J. Pedersen, *J. Am. Chem. Soc.*, 1967, **89**, 7017
- [5] M. Hiraoka, *Crown Compounds; their characteristics and applications*, Elsevier, Amsterdam, 1982
- [6] E.C. Constable, *Coordination Chemistry of Macrocyclic Compounds*, Oxford University Press, 1999
- [7] F. Delprato, L. Delmotte, J.L. Guth, L. Huve, *Zeolites*, 1990, **10**, 546
- [8] R.A. Sheldon, J.K. Kochi, *Metal-Catalysed Oxidations of Organic Compounds*, Academic Press, New York, 1981
- [9] J.B. Vincent, G.L. Olivier-Lilley, B.A. Averill, *Chem. Rev.*, 1990, **90**, 1447
- [10] J.A. Labinger, *J. Mol. Catal. A*, 2004, **220**, 27
- [11] K.A. Suresh, M.M. Sharma, T. Sercheli, *Ind. Eng. Chem. Res.*, 2000, **39**, 3958
- [12] U. Schuchardt, D. Cardoso, R. Sercheli, R. Pereira, R.S. da Cruz, M.C. Guerreiro, D. Mandelli, E.V. Spinacé, E.L. Pires, *Appl. Catal. A*, 2001 **211**, 1
- [13] D.E. De Vos, J. Meinershagen, T. Bein, *Angew. Chem. Int. Ed. Engl.*, 1996, **35**, 2211
- [14] P. Tian, Z. Liu, Z. Wu, L. Xu, Y. He, *Catal. Today*, 2004, **93-95**, 735
- [15] B. Meunier, *Chem. Rev.*, 1992, **92**, 1411
- [16] W. Nam, H.J. Kim, S.H. Kim, R.Y.N. Ho, J.S. Valentine, *Inorg. Chem.*, 1996, **35**, 1045
- [17] W.A. Carvalho, M. Wallau, U. Schuchardt, *J. Mol. Catal. A*, 1999, **144**, 91
- [18] J. C. Madina, N. Gabriunas, E Páez-Mozo, *J. Mol. Catal. A*, 1997, **115**, 233
- [19] A.E. Goeta, J.A.K. Howard, D. Maffeo, H. Puschmann, J.A.G. Williams, D.S. Yufit, *J. Chem. Soc., Dalton Trans.*, 2000, **12**, 1873
- [20] F. Martinez, Y.J. Han, G. Stucky, J.L. Sotelo, G. Ovejero, J.A. Melero, *Stud. Surf. Sci. Catal.*, 2002, **142**, 1109
- [21] P. Selvam, S.E. Dapurkar, S.K. Badamali, M. Murugasan, H. Kuwano, *Catal. Today*, 2001, **68**, 69
- [22] M. Lachkar, R. Guilard, A. Atmani, A. de Cian, J. Fischer, R. Weiss, *Inorg. Chem.*, 1998, **37**, 1575
- [23] P.J. Carl, S.L. Baccam, S.C. Larsen, *J. Phys. Chem. B*, 2000, **104**, 8848
- [24] P.J. Carl, S.C. Larsen, *J. Phys. Chem. B*, 2000, **104**, 6568
- [25] A.B. Bourlinos, M.A. Karakasides, D. Petridis, *J. Phys. Chem. B*, 2000, **104**, 4375
- [26] S.K. Badamali, A. Sakthivel, P. Selvam, *Catal. Lett.*, 2000, **65**, 153

- [27] R.J.P. Corriu, A. Mehdi, C. Reyé, C. Thieuleux, A. Frenkel, A. Gibaud, *New. J. Chem.*, 2004, **28**, 156
- [28] Personal communication, Dr. T.D. Coombs, formerly of St. Andrews University
- [29] P.J. Carl, S.L. Baccam, S.C. Larsen, *J. Phys. Chem. B*, 2000, **104**, 8848
- [30] Personal communication, Dr. G.M. Smith, National high-field ESR facility, University of St. Andrews
- [31] Personal communication, Dr.s E.J. McInnes, D. Collison, National multi-frequency ESR facility, University of Manchester
- [32] F.E. Mabbs, D. Collison, *Studies in inorganic chemistry 16, Electron paramagnetic resonance of d transition metal compounds*, Elsevier, 1992
- [33] 1st workshop on the theory and practice of EPR and ENDOR spectroscopy, Organised by the national EPSRC service for EPR spectroscopy, Cardiff University, 2002
- [34] 2nd workshop on the theory and practice of EPR spectroscopy, Organised by the national EPSRC service for EPR spectroscopy, University of Manchester, 2003
- [35] J.R. Morton, K.F. Preston, *J. Magn. Reson.*, 1978, **30**, 577
- [36] X.H. Zong, P. Zhou, Z.Z. Shao, S.M. Chen, X. Chen, B.W. Hu, F. Deng, W.H. Yao, *Biochemistry*, 2004, **43**, 11932
- [37] H.R. Gersmann, J.D. Swalen, *J. Chem. Phys.*, 1962, **36**, 3221
- [38] Personal communication, Dr. Paul A. Wright, University of St. Andrews

Chapter 6

Functionalised mesoporous silicas as hosts for gold nanoparticles

Synopsis

This chapter details the inclusion and dispersion of precious metals, mainly gold, into functionalised silicas. The precious metal uptake is found to be facilitated by the organic functionalities. Various uptake and reduction methods of metallic complexes are described and their efficiency is evaluated in terms of the size and homogeneity of the metal nanoparticles formed. HRTEM is a key characterisation technique in this study.

6.1 Introduction

The practical advantages of mesoporous silica as catalyst supports are the large surface areas (typically $> 850 \text{ m}^2\text{g}^{-1}$) such solids possess, offering a high concentration of active sites per mass of material, and their well defined surface structure and composition. Thomas was among the first to realise their potential for supporting organometallic complexes [1,2] and identified three key requirements for ideal catalysts of this sort: ready molecular diffusion to and from the active site; ability to operate under mild, environmentally-friendly conditions and well defined single-site active centres. In many cases, catalytic complexes supported on mesoporous solids achieve these requirements. Using large pore supports such as mesoporous solids offers uninhibited diffusion to reactants and products of a size that would be discriminated against by smaller pore hosts. The robust nature of the inorganic silanol groups present on the internal surfaces offer potential tethering sites for organometallic complexes. Examples of the preparation and use of such supported catalysts are give by Schüth [3] and represented schematically in figure 6.1.1.

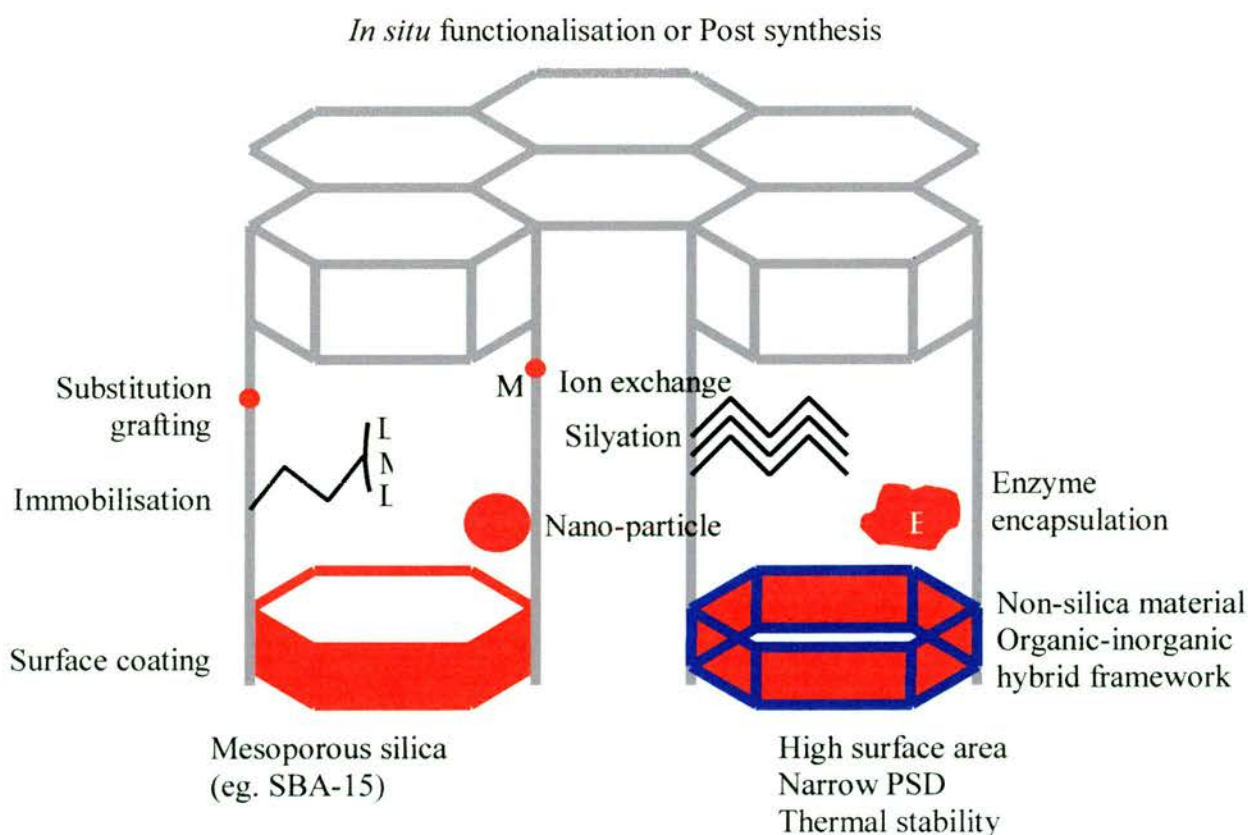


Figure 6.1.1. Schematic sketch for various methods of functionalisation of mesoporous silica to incorporate novel properties into such materials [3].

A wide range of functionality can be introduced within mesoporous silicas, so that catalytic complexes can be immobilised on the internal (or external) surfaces through different immobilisation strategies. With a high surface coverage of silanol groups present ranging from 1 – 3 OH/nm² [4 – 8] the surfaces are readily functionalised with organic constituents, for example with vinyl groups [9,10] or with thiols [11]. The latter can be further oxidised to sulphonic acids [12] to give solid acid catalysts. Another advantage of such inorganic molecular sieves is that a number of catalytically active atoms can be incorporated in place of silicon within the framework [13]. Ti^{IV} ions embedded within the walls of mesoporous silica for selective oxidation [14 – 16] were studied extensively after the first reported syntheses of ordered mesoporous silica [17,18] with further advances achieved upon grafting Ti^{IV} active centres onto the internal walls using organometallic precursors [19] for epoxidation of fatty acid methyl esters [20] and terpenes [21].

Mesoporous solids have also been studied as supports for nanoparticles of transition metals [22,23] and precious metals [24] within the pores. If finely dispersed, such metal nanoparticles would be expected to possess important catalytic properties. As well as the more obvious catalytic functions it may be possible to coat their surfaces by chemisorption of chiral ligands to promote chiral catalysis, in a similar to that developed by, for example, Thomas [25] and Baddeley [26]. The ever-increasing demand for enantiomerically pure products, especially in the pharmaceutical and agrochemical industries is of importance both practically and legislatively. Chirality, widely known in organic molecules, notably in biological molecules as in DNA, is rare in inorganic materials [27]. Recent advances has brought about mesoporous materials possessing ordered, chiral mesopores [28] that could potentially lead to mesoporous silicas being used in catalysis or separation where shape selectivity and enantio-selectivity are desired in the synthesis of single enantiomers. Until now, asymmetric catalysis has largely been performed homogeneously* by well-defined, organo-metallic complexes. The cost of the sophisticated ligand and noble metal means that catalyst recovery is of great importance, so that heterogeneous, regenerable, asymmetric catalysts could be superior to their homogeneous counterparts. The main problem, however, has been that, the majority of attempts to

heterogenise homogeneous chiral catalysts has led to below par performances as many different active sites are generated by the methods of heterogenisation [30]. Thomas recognised that mesoporous silica with large pores and functionable protruding silanol groups offer (as described above) opportunities for the design of heterogeneous chiral catalysts owing to the spatial restrictions (for prochiral reactants) after the grafting of asymmetric (homogeneous) catalysts within the internal pores. Hence the use of such supports will avoid a spectrum of active sites, and only single sites would exist – as for their homogeneous analogues [25,31]. The spatial restrictions mentioned can indeed improve enantioselectivity as grafting chiral catalysts onto the inner walls of such mesoporous solids – a concave surface – compared to the same chiral catalyst anchored to a convex silica surface (Cabosil) shows enhancement of enantioselectivity [32,33].

Immobilisation of chiral homogeneous transition metal complexes on high area non-catalytically active mesoporous solids is not the only approach to heterogeneous chiral catalysis; others are to graft an ‘ordinary’ active site onto a chiral solid support or to graft a chiral ligand exhibiting stereoselectivity to a catalytically active non-stereoselective solid. The work of Baddeley has looked at such efforts and in particular the latter. Studying the modified reactive Cu metallic surfaces with chiral modifiers/ligands such as (R,R)-tartaric acid for enantioselective hydrogenation of methyl acetoacetate to the R-enantiomer of the product molecule methyl 3-hydroxybutyrate [34] has led to an understanding of the enantiomeric process. The modifiers generate crystal surface faces, some of which lose symmetry elements of the underlying metal and present chirality to the modified surface. Hence chiral channels are produced exposing the bare metal catalyst and thus limit the reactant molecules to orientate and approach the metal active-sites on the enantiomeric side of the modifier [26] with the OH groups on the tartaric acid also having an importance on chirality [35]. Fundamental investigations of enantiomeric heterogeneous catalysis have been reviewed by Baddeley [36].

Hydrogenation of the β -ketoester – methylacetoacetate on a Ni surface will occur producing a racemic mixture from the unmodified catalyst, however chiral ligand

* The importance of such catalytic asymmetric synthesis was recognised by The Royal Swedish

(R,R-tartaric acid) modification of the Ni surface produces enantiomeric products. If complete surface coverage of the chiral modifier does not exist (i.e. existence of bare Ni sites) both enantiomeric products can form. To circumvent the problem layers of Au are alloyed with Ni as a function of annealing temperature [37]. R,R-tartaric acid physisorbs on the Au-rich surface and chemisorption to Ni only occurs once Ni has reached a threshold level on the surface (at a higher annealing temperature) – with a reduction of the bare Ni sites, quenching of the reactivity of Ni can be controlled and hence leading to the reduction of a racemic mixture and thus obtaining the desired enantiomeric product [38].

At the time of starting this thesis, relatively little work had been performed on the inclusion of precious metal within surface-functionalised mesoporous silicas, and it was envisaged that the range of functional groups that could be included (such as thiol, carboxylic acid and cationic groups) would permit the ready inclusion and dispersion of precious metal species that could be reduced and thereby act as catalytic species. In particular, *in situ* functionalisation offers a ready route to the inclusion of organic groups that would facilitate this process.

During the course of this work, studies have appeared in the literature that also deal with the issue of including precious metal species into functionalised silicas and reducing them to nanoparticles. Without exception, these have concerned mesoporous silicas that have been functionalised post-synthesis [39 – 44], or indeed using pure siliceous materials [45,46] and the studies detailed in this thesis differ by dealing specifically with mesoporous silica supports that have been functionalised *in situ*. Examples where mesoporous solids have been functionalised post-synthesis and used to take up precious metals include that to control the morphology of metal nanoparticles, including gold, within mesoporous silica.

In this work the aim was to include organic functionalities within the silica that interact strongly with the metallic complexes and so to establish routes to the inclusion of precious metals such as gold and palladium. Most of the research involved the inclusion of gold. Gold nanoparticles have attracted a great deal of

Academy of Sciences with an award of the Nobel Prize in chemistry in 2001 [29].

recent interest for their surprisingly high catalytic activity in reactions such as CO oxidation which in turn has attracted the catalytic market [47,48]. Furthermore, it was expected that the types of functional groups that could be included during synthesis of the mesoporous solids (in particular thiol, but also alkylammonium groups) would be expected to interact strongly with gold complexes in aqueous solution and the idea to *in situ* functionalise the mesoporous solids with such groups would facilitate a route to uniformly dispersed tethered groups on the silica surface. The problem with trying to incorporate colloidal particles onto mesoporous silica is the fact that ideally incorporation should occur within the intramesochannels, which in having restricted voids provides confined space for nanoparticles and hence restrict colloidal growth to that beyond the pore diameter.

To include gold nanoparticles into the mesoporous solids, advantage was taken of the ease of reduction of gold chloride. This is readily observed in the presence of citrate ions to give stable sols [49]. The initial aim was to explore routes to use this to achieve well dispersed distributions. The approaches were

- (i) to reduce gold chloride in solution (citrate method) in the presence of mesoporous solids (and later compared with macroporous titania);
- (ii) to develop a 2-stage process, by which gold complexes were first included (through interaction with functional groups) and then reduced.

It was found that gold chloride taken up on thiol-functionalised solids readily auto-reduced, and so this process was followed in detail. The results were comparable with results published during the course of this thesis by Ghosh *et al.* [50] on thiol-functionalised MCM-41. In order to improve the dispersion, other routes were explored. These included a reverse Au micelle method, a route adapted from that described by Lin *et al.* [51] for reaction in colloidal dispersion. In this method reverse micelles are arranged of an inner aqueous gold chloride/butanol solution surrounded by the cationic surfactant, CTAB, importantly in a hydrocarbon solvent. A second reverse micelle whereby the gold complex is replaced by sodium borohydride which acts as the reducing agent (figure 6.1.2) is prepared and upon mixing the gold is reduced to its metallic state, as confirmed by a change in the suspension colour and the evolution of H₂. Here the thiol groups act as anchoring agents to suppress

agglomeration of Au nanoparticles. This method followed the literature procedure [51] whereby the reduction of the reverse Au micelles is done in suspension, without any solid present. From this the method was adapted to incorporate the reverse Au micelle within an extracted MPTES-functionalised material, followed by reduction. Finally, an *in situ* approach was taken in which the two different micelles (both containing the cationic CTAB surfactant) were incorporated directly into the sol-gel synthesis of thiol-functionalised SBA-15. This synthesis had to be carefully controlled due to the presence of the two different surfactants. It was found that adding reverse micelles to the sol-gel after an initial period of hydrolysis still gives high-quality SBA-15.

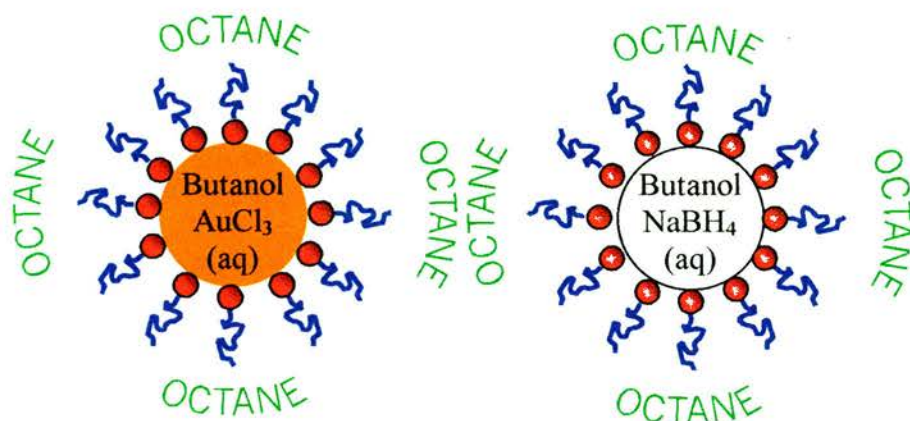


Figure 6.1.2. Schematic representation of reverse micelle system: two separate micelles of (left) Au and (right) NaBH_4 with organic surfactant and co-surfactants which upon mixing reduce the chloroaurate complex to colloidal Au with the formation of H_2 .

Another route to the formation of Au nanoparticles supported by functionalised mesoporous silicas is via *in situ* functionalisation of the silica solids with charged cationic groups, ion exchange with anionic metal complexes, and subsequent reduction in H_2 [52]. Here strong interactions of the guest metal precursor with the organically-functionalised host enable a quick and efficient exchange that leads to highly dispersed Au nanoparticles.

A more restricted set of experiments were performed on inclusion of palladium complexes. PdCl_4^{2-} was included by ion-exchange on alkylammonium modified materials and allylpalladium chloride was incorporated using thiol-modified solids and subsequent reduction under mild conditions in the presence of amines.

6.2 Experimental

6.2.1 Sodium Citrate Reduction of Gold Chloride within Mesoporous Silica

Pre-extracted mesoporous solid (SBA-15 or STA-11) functionalised with thiol groups by co-condensation of MPTES is used as a support for the attempted incorporation of gold colloids. The composition of the molecular sieve is as previously described in Chapter 3. The method was adapted from [49]. 16 g of 0.6% w/v AuCl₃ (Alfa Aesar, Au 65% assay) solution was added to 200 ml of boiling distilled H₂O under stirring and brought back to boiling. Addition of 10 ml 1% w/v tri-sodium citrate dehydrate (Fluka 99.5%) to the solution under stirring causes the reduction of the gold after ~ 5 mins giving a sol with a ruby red colour. The citrate ions act as stabilising ligands to suppress agglomeration. 0.5 g of mesoporous solid STA-11 (i.e. stoichiometric ratio of SH : Au of 1 : 0.5) is added to the suspension and stirred for 1 hr before filtering and air-drying.

This approach was also adopted with macroporous titania as the host as the solid offers alternative surface properties to silica – under the pH values used it bears a positive charge. This should allow the electrostatic incorporation of negatively charged gold sols without the need for organic-functionality. (Silica is negative at most pHs (isoelectric point pH 1.2) so that organic groups are required to attract such metal sols). Macroporous titania is templated from latex free polystyrene spheres [53]. A pre-prepared suspension of spheres were used (courtesy of P.G. Bruce's group) synthesised with 210 ml styrene washed with NaOH (210 ml; 0.1 M) then 200 ml H₂O. The washed styrene was added to 1700 ml H₂O at 343 K in a 5-necked r.b. flask and stirred using an electric motor. Potassium persulfate (0.663 g in 100 ml H₂O) was heated to 343 K and added to the styrene/H₂O mixture with stirring for 28 hrs before being filtered through glass wool. Finally centrifugation of the suspension at 3000 rpm for 20 hrs, decanting of the H₂O and drying of the spheres leads to the template. Millimeter sized portions of the spheres are added to a Büchner funnel under vacuum and wetted with ethanol. Titanium ethoxide in ethanol is pipetted over the spheres before drying in a desiccator overnight and calcining at 848 K for 8 hrs

leads to the final macroporous titania. The ethanol dilution permits control of hydrolysis ($43_{\text{ethoxide}} : 57_{\text{ethanol}}$ by volume).

6.2.2' Auto-Reduction' of Gold Chloride within Mesoporous Silica

Extracted thiol-functionalised SBA-15(2%SH) or STA-11(7%SH) solids were used as catalysts for the 'auto-reduction' of AuCl_3 to colloidal Au in a straightforward process [50]. In the procedure a suspension of the solid in water (plus slight excess of HCl) adsorbs the $\text{H}^+\text{AuCl}_4^-$ complex. The molar ratio of Au : SH (total) was varied between 0.4 – 0.7 : 1. For example, 1 g of STA-11 (7% SH loading) added to 0.25 g AuCl_3 dissolved in an aqueous solution ~ 150 ml with a slight excess of acid would give a Au : SH ratio of 0.7 : 1. According to Ghosh [50], the gold chloride auto-reduces after 4 days of stirring the suspension. In this work, it was observed that after 10 hrs of stirring the initial yellow suspension turns to a translucent light grey before a pink suspension is observed after 3 days of stirring. As the interaction of gold with SH groups is strong the affinity for gold to absorb onto thiol-functionalised porous solids is high and it was found that stirring of the suspension for 30 mins is sufficient for all of the gold species to be taken up by the thiol-functionalised solid. If the yellow solid prepared after only 30 mins is filtered and dried it was observed to turn red/pink at 353 K after 10 mins.

6.2.3 Metallic Gold within Mesoporous Silica from Reduction of Reverse Gold Micelle by Sodium Borohydride

The method for the generation of gold nanoparticles by mixing reverse micelles outlined in the introduction [51] was adapted in an attempt to generate colloidal gold particles within the pores. Three different approaches were taken. In the first the gold nanoparticles were pre-prepared, with the hope that the presence of dodecanethiol in the preparation would cap the gold particle growth to a size small enough to enter the pores, where they could be exchanged by thiols tethered to the solid. In the second, the micelles were added to a thiol-containing solid in an attempt to prepare the gold nanoparticles within the pores, where the surface thiol groups would bind and cap the growing particles, in a similar way to the dodecanethiol used in the literature preparation. In the third, *in situ* approach, the reverse micelle suspensions are added

during the synthesis of the thiol functionalised SBA-15. It was thought that the surfactant (CTAB) present in the reverse micelles might affect the order of the SBA-15 product, so the hydrolysis and structure formation was allowed to take place (3 hrs) before adding the reverse micelles. It was hoped that these micelles could diffuse through the PPO core of the P123 surfactant to give rise to gold throughout the pores. The reverse micelles were formed from mixtures with the following molar composition: 1 CTAB (Aldrich) : 10.64 octane (Aldrich 98%): 4.10 Butanol (Aldrich 99%). Two such colloidal suspensions were made, one containing gold chloride and the second the reductive sodium borohydride and these were vigorously stirred for 10 mins – these are named as reverse micelle (A) and (B) respectively. To prepare these reverse micelles 1.48 ml (0.056 M) AuCl_3 and 1.48 ml (0.32 M) NaBH_4 (Aldrich 99%) is added to reverse micelle (A) and (B) respectively whilst under ultrasonication. Reverse micelle (A) turns an orange/red colour whilst (B) becomes clear.

For the first method the addition of (B) to (A) results in a very dark ruby red colour with the presence of effervescence – hydrogen gas as a decomposition product – indicating the reduction of gold. 0.5 ml of dodecanethiol (Aldrich 98%) is added to 1 ml aliquots of the mixture to act as a capping agent before the addition of 13.5 ml toluene and further ultrasonication for 40 mins. The final stage was to allow the mixture to settle (as white precipitate from surfactant remains) and to transfer the gold-sol containing toluene solution to the thiol-containing solid slowly by syringe pump in aliquots over 7 days (stirring in between aliquot additions). It was hoped that thiol-capped Au nanoparticles would ‘swap’ dodecane thiol groups with thiol groups on the solid.

The idea of the second method was to use the thiol groups within the solid directly as the capping agents in place of dodecanethiol. So with the same composition as above, reverse micelle (A) and (B) were stirred vigorously for 10 mins before the relative additions of AuCl_3 and NaBH_4 respectively. Reverse micelle (A) was added to a desired amount of extracted SBA-15(2%SH) solid and sonicated. The red colour turns clear after 5 mins. Addition of reverse micelle (B) to the solid results in the dark ruby red colour and effervescence under continuous sonication. The solid is further sonicated for 30 mins before filtering.

In the third *in situ* approach the reverse micelle suspensions were added during the synthesis of SBA-15-SH-X% (prepared as described in Chapter 3). As mentioned the problem here is that the use of two surfactants – Pluronic P123 and CTAB – are present during the synthesis. Therefore the two silica sources (the majority TEOS and the co-condenser MPTES) were added to the dissolved Pluronic mixture and stirred under normal conditions for 3 hrs to allow phase separation before the addition of the reverse micelles (composition as above). Also there was some variation in that: 1) reverse micelle A was added after 3 hrs followed by reverse micelle B then the hydrolysis and condensation steps followed as normal; 2) reverse micelle A added after 3 hrs and the hydrolysis step carried out (24 hrs total) before the addition of reverse micelle B and the condensation step and 3) reverse micelle A added after 3 hrs and the hydrolysis and condensation steps finished with filtering, washing and drying of the solid before reverse micelle B was added. After condensation the as-made samples remain white in colour (or slightly purplish on an increased Au loading) and white upon extraction. If however the solid is calcined in flowing N₂ then O₂ the samples turn to pink/orange.

6.2.4 N-trimethoxysilylpropyl-N,N,N-trimethylammonium Chloride functionalised Mesoporous Silica for noble metal complex ion exchange and reduction by Hydrogen

The basis of this approach is to use trimethylammonium groups attached to the surface to generate a monolayer of charged groups on the pore surface to facilitate uniformly distributed ion-exchanged metal complexes as previously reported for post-synthesis functionalised SBA-15 [52]. *In situ* functionalisation using organo-siloxanes is again used to modify the internal surface of the mesoporous silica. TEOS is the main silica source along with N-trimethoxysilylpropyl-N,N,N-trimethylammonium chloride (TMPTMAC) (50% in methanol, Gelest) as a co-condenser templated by the non-ionic triblock copolymer Pluronic P123 in acidic media. The composition of the sol-gel is: 1 TEOS : 1-x TMPTMAC : 0.018 P123 : 195 H₂O : 3.1 HCl. The final product contains a loading of 3.75% TMPTMAC based on total silica. The hydrolysis step at 313 K for 24 hrs with stirring precedes hydrothermal treatment at 373 K for 48 hrs before the solid is filtered and dried. Solvent extraction is as previously described in chapter 3.

For the exchange of the complex, the required metal complex is dissolved, (e.g. AuCl_3 as $\text{H}^+\text{AuCl}_4^-$ or $\text{NH}_4^+\text{PtCl}_4^-$, ammonium tetrachloroplatinate (II) (Strem Chemicals 99%)) before addition of the functionalised silica support. Here it is expected that the anionic metal complex will exchange with the counter balancing chloride ions from the TMPTMAC source. Because the electrostatic interaction with the cationic TMPTMAC group and the anionic metal complex is strong, stirring for 15 mins is sufficient for ion-exchange to occur. The solid is filtered, dried, then heated at 423 K in a flow of H_2 (5% in Ar) for 2 hrs for reduction to take place.

6.2.5 Allyl Palladium Chloride dimer reaction with MPTES-functionalised silica

Here a pre-extracted thiol functionalised solid is the inorganic silica support for the incorporation of the palladium complex. The thiol groups are expected [54] to reduce the complex to Pd^0 under mild conditions in the presence of an amine group. Dry THF (*ca.* 150 ml) is syringed onto the allylpalladium chloride (available as the dimer, Acros 98%) under nitrogen. The relative stoichiometric ratio of Pd : SH is 1 : 1. Under flowing nitrogen, *ca.* 0.5 ml dipropylamine (Aldrich 99%) is added to the solution along with the required amount of mesoporous solid. The suspension is refluxed under nitrogen for *ca.* 5 hrs until a change in colour to dark green is observed. The solid is filtered and dried.

6.2.6 Analysis Methods

UV/Visible absorption spectra were recorded on a PerkinElmer Lambda 35 UV/Vis spectrometer using a matching pair of quartz cuvettes (pathlength 1 cm). The spectra have a starting wavelength of 500 nm and a finishing wavelength of 250 nm with a scan speed of 60 nm/min. ICP-MS were recorded using a Agilent 7500 spectrometer coupled to a laser ablation (Merchantech New-wave UP213) using argon as the carrier gas. Each sample mixed with Teflon in pellet form were ablated 6 times and the average elemental values taken. HRTEM is that described in Chapter 2 and EDX (Energy Dispersive X-ray Spectroscopy) was recorded using a Oxford Instruments Links ISIS coupled to the JEOL 2011. The emitted x-ray spectrum normally from 0 keV to 20 keV was analysed using the associated software, Microanalysis Suite.

6.3 Results & Discussion

The results within this chapter give an overview of the effectiveness of different preparation routes in producing supported nanoparticles from the noble metal precursors. The uptake is studied by UV-visible spectroscopy and, in the final solids, by ICP-MS coupled with laser ablation. The composition, size and distribution of metal within the solids is studied by HRTEM and EDX.

6.3.1 Chemical Analysis

Table 6.3.1.1 gives the metal contents of the various preparations, showing the ratio of metal : silica (or titania) and the calculated 'efficiency of uptake' for the accessible functional groups. The gold contents were calculated using the samples prepared by auto-reduction as a standard. The chosen samples were observed (by UV-visible spectroscopy) to take up all of the added gold chloride, so their gold contents were known. Palladium and platinum contents were calibrated assuming the same efficiency of ion-exchange as Au (on the alkylammonium-functionalised solids) but taking into account the divalency of the anionic metal precursors.

	Target loading	Experimental Ratio: (Metal/Oxide) _{signal}		Molar Metal/Oxide _{calibrated}	wt% _{metal}	Efficiency of uptake
Reverse Au Micelle	SBA-15 (2%SH) 50% Au loading Post synthesis	0.011		0.004	1.4	40%
	<i>In situ</i> extracted	0.027		0.011	3.5	40%
	<i>In situ</i> calcined	0.004		0.002	0.5	50%
Auto-Reduction	SBA-15 (2%SH) 50% Au loading	0.028		0.011	3.6	100%
	STA-11(7%) 100% Au loading	0.094		0.037	12.0	100%
	SBA-15 (2%SH) 30% Au + 30% Pd loading	Au	0.030	0.012	3.9	100%
		Pd	0.021	0.009	1.7	47%
	STA-11 (7%SH) 40% Pd loading	0.088		0.040	6.9	57%
	SBA-15 (2%SH) 40% Pt loading	0.017		0.008	2.5	38%
Ammonium chloride (3.45%NMe ₃)	100% Au loading before H ₂	0.054		0.021	6.9	60%
	100% Au loading after H ₂	0.039		0.015	5.0	43%
	50% Au + 50% Pd loading before H ₂	Au	0.031	0.012	4.0	35%
		Pd	0.010	0.005	0.8	13%
	50% Au + 50% Pd loading after H ₂	Au	0.025	0.010	3.2	28%
		Pd	0.010	0.005	0.8	13%
	100% Pt loading before H ₂	0.035		0.016	5.1	46%
100% Pt loading after H ₂	0.022		0.010	3.2	29%	
Na Citrate	STA-11(7%SH) 50% Au loading	0.218		0.085	27.9 [†]	100%
	Titania 10% Au loading (based on TiO ₂)	0.057		0.022	5.5	-
AllylPd Chloride dimer	STA-11 (7%SH) 100% Pd loading	0.149		0.067	11.7	96%

[†]Likely that laser ablated an aggregation of gold nanoparticles unevenly distributed within the sample to give high wt% value

Table 6.3.1.1. Efficiency of uptake of selected metal complexes through different preparations along with the final wt% of metal in the support calibrated through the uptake of gold chloride in the auto reduction procedure were all gold is known to be adsorbed

The reverse micelle (post synthesis) method shows a reduced efficiency for gold uptake. This is likely to be due to pore blocking from the reverse micelles themselves as high levels of Br (from CTAB) are observed. Also the N₂ adsorption isotherms of such samples show a reduced capacity uptake. The *in situ* method too has only an adequate efficiency of uptake as maybe the CTAB does not all diffuse into the P123 surfactant. The auto-reduction approach for the uptake of gold is strong, quick and efficient as the Au – SH interaction is strong, although for Pd and Pt the interaction seems to be less in this case. The efficiency of uptake for all cases using the alkyammonium groups show that after reductive treatment a drop in efficiency occurs probably due to sintering of the metal at high temperatures. However, gold shows the highest efficiency over Pt and also predominantly adsorbs onto the support over that of Pd. Both the sodium citrate and allylPd Cl methods for uptake of gold and Pd respectively show high efficiencies at the chosen levels of loadings.

6.3.2 Sodium citrate reduction of AuCl₃ within STA-11.

It can immediately be seen (figure 6.3.2.1) by TEM that reduction of AuCl₃ by sodium citrate and the uptake onto STA-11 does give colloidal nanoparticles, but that they are too large to be incorporated into the pores (~80 Å) as colloids in the region of 50 – 100 nm are observed.

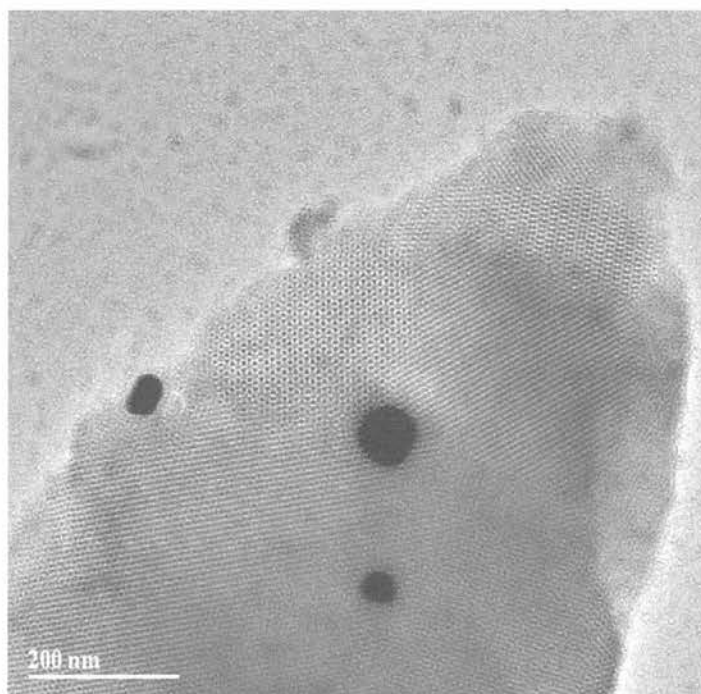




Figure 6.3.2.1. Sodium citrate reduction of AuCl_3 into STA-11 (7% MPTES). HRTEM micrographs of large Au nanoparticles on external surface of mesoporous support (above) and distribution of 50 – 100 nm Au colloids indicating their location on the external surface due to their size (below).

The colloids do not fully coagulate either in solution or once on the solid, (the ruby red/pink colour of the suspension indicates that the citrate ions are in fact acting as stabilising ligands – thoroughly coagulated Au colloids in solution give the suspension a deep navy blue colour [49]) (figure 6.3.2.2).

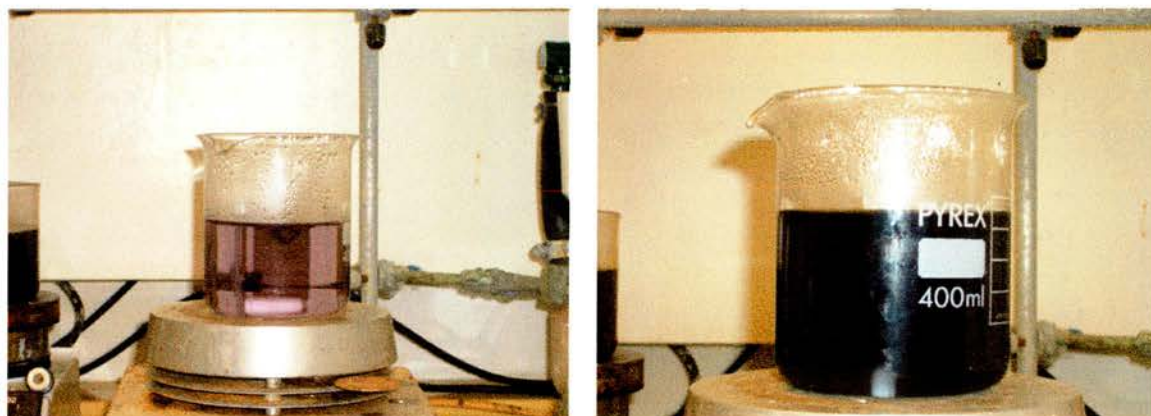


Figure 6.3.2.2. Reduction of AuCl_3 by sodium citrate in aqueous solution displaying a pink colour after 5 mins stirring (left) the addition of nitric acid to suppress citrate ion efficiency to give fully agglomerated colloidal Au colloids with indicated by the navy colour (right).

Attempts to support gold nanoparticles on macroporous titania gave a material which to the naked eye possessed a purple tinge, which suggests a range of particle sizes including those observed on the red Au/STA-11 (figure 6.3.2.3).



Figure 6.3.2.3. Reduction of AuCl_3 by sodium citrate on: mesoporous STA-11 (7% MP TES) – pore size ~ 8 nm (left) and macroporous titania – pore size ~ 350 nm (right).

The spatial restrictions of the smaller pore STA-11 do not seem to suppress colloidal growth as observed through HRTEM. On the other hand the largest nanoparticles on the surface of STA-11 do not exceed 100 nm compared to those on the titania solid (figure 6.3.2.4) where colloids up to 300 nm in size are observed along with smaller comparable smaller colloids of 50 nm in diameter (figure 6.3.2.5). It may be the case that the thiol groups on the external surface, absent in the titania, control colloidal agglomeration more than the titania solid.

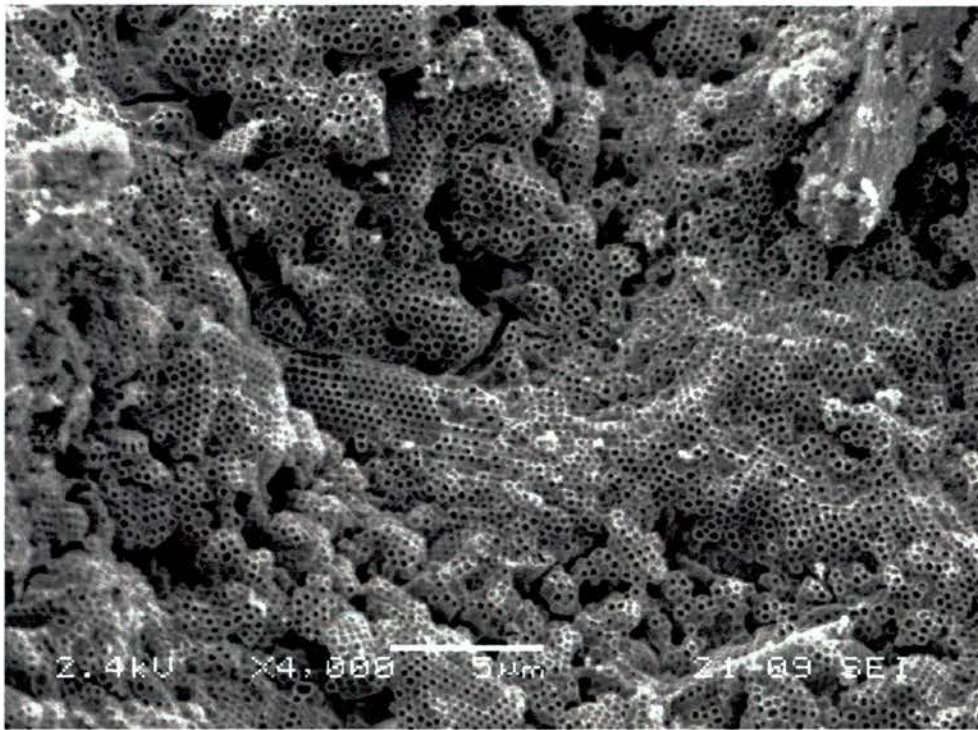
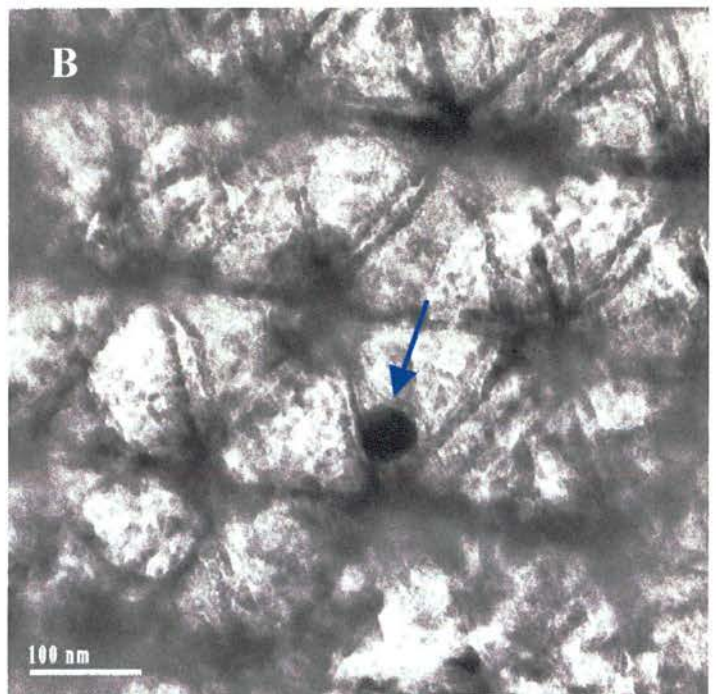
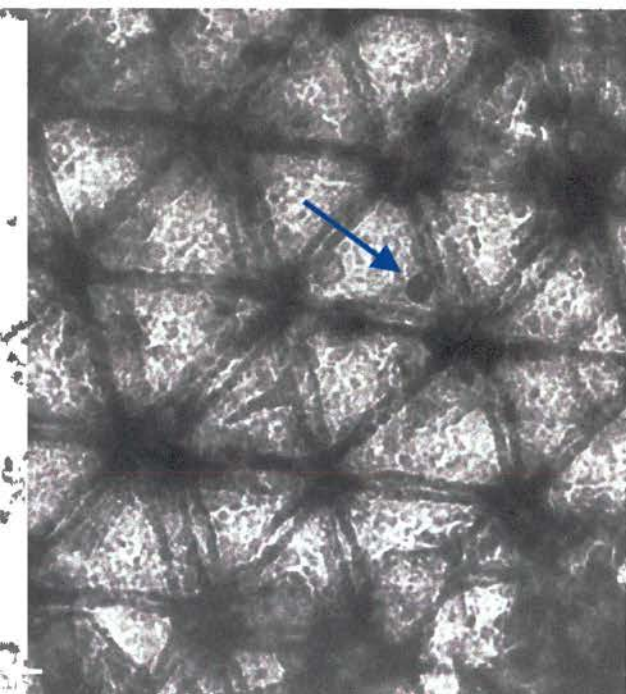


Figure 6.3.2.4. Scanning electron micrograph of calcined polystyrene (Latex) free templated macroporous titania showing the hexagonal array of large pores



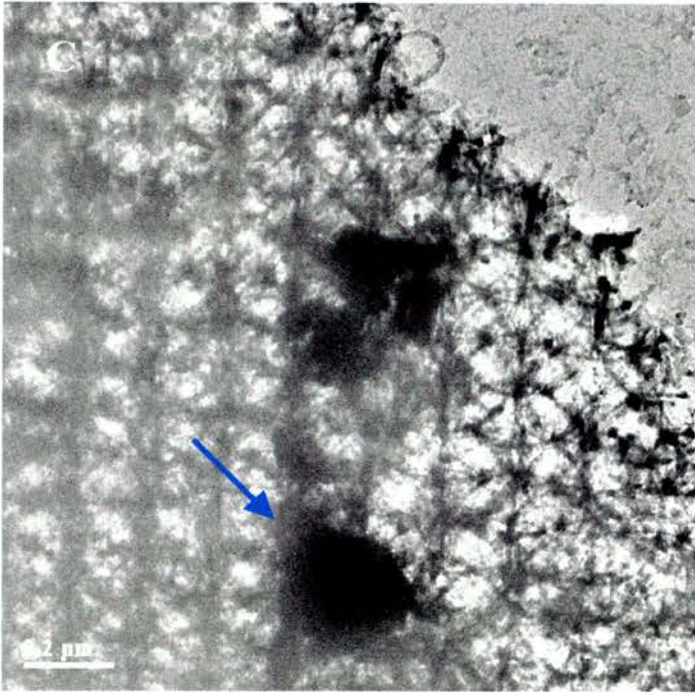


Figure 6.3.2.5. HRTEM micrographs of macroporous titania displaying varying Au colloidal sizes (reduced by sodium citrate), (A) 30 nm; (B) 50 nm and (C) 300 nm.

It should be noted that gold particles on silica can display strong colours even at low loadings (figure 6.3.2.6).



Figure 6.3.2.6. *In situ* Na citrate reduction before surfactant dissolution to STA-11 displaying a pink colour even with a low Au loading content with SH : Au ratio of:- 1: 0.0067

6.3.3 'Auto-reduction' of AuCl_3 within thiol functionalised mesoporous silica.

6.3.3.1 UV analysis of the uptake of chloroaurate complex on pure silica and thiol functionalised SBA-15

Ghosh *et al.* report [50] that surface silanol groups reduce chloroaurate ions in aqueous solution to gold nanoparticles and through anchoring to organic groups are simultaneously stabilised. Such solids can be viewed as three-layer nanocomposites where the outer sphere is the inorganic support, with the middle portion the pendant organic moiety and finally the nanoparticles capped to the polar head of the organic functionality.

The uptake of gold, in the form of the chloroaurate complex, onto thiol-functionalised SBA-15 was followed by UV-visible spectroscopy. Initially a molar gold complex / thiol group ratio of 0.4 was chosen for a 2% thiol-loaded solid, and for comparison a similar gold complex / SiO_2 ratio was examined for an unfunctionalised SBA-15. The absorbance at 314 nm of the initial yellow solution of the aqueous chloroaurate was measured by UV at $t = 0$ i.e., before the addition of the mesoporous sieve, and after the addition of the solid to form a suspension under stirring, further absorbance measurements were taken by taking an aliquot of the suspension, filtering off the solid and measuring the filtrate absorption at specified times.

The uptake of the Au complex as a function of time for an as-made pure siliceous SBA-15(2%SH) material can be seen in figure 6.3.3.1.1.

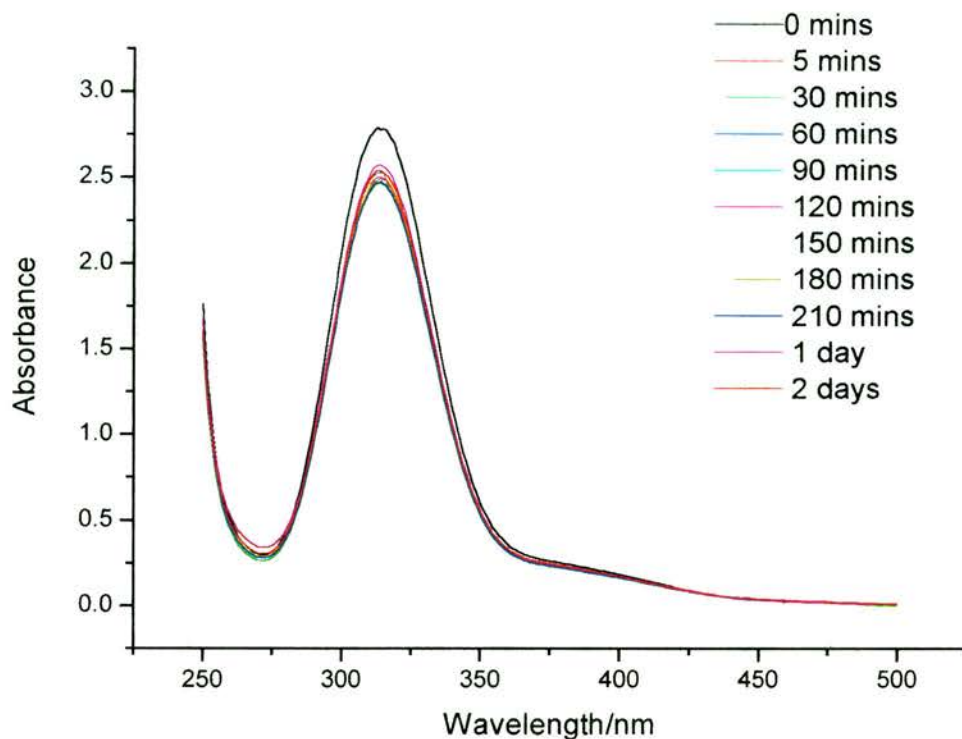


Figure 6.3.3.1.1. The uptake of aqueous $\text{H}^+\text{AuCl}_4^-$ onto an as-prepared pure siliceous SBA-15 mesoporous solid as a function of time.

The absorbance of the solution drops very little indicating that roughly 90% of the Au complex remains in solution. There will be an abundance of surface silanol groups present as the material has not been calcined and so further condensation of the silica has not taken place and so it seems that even after days of stirring the silanol groups do not play an important role in the uptake of such species. If we compare this to an as-made SBA-15 material functionalised with 2% thiol the difference in uptake is apparent even after 5 mins (figure 6.3.3.1.2). After 5 mins the absorbance value reveals that approximately 91% of the complex has been absorbed onto the solid with only 9% remaining in solution although after 30 mins and onwards (up to 210 mins) the remaining complex in solution absorbs to the silica support and remains absorbed. This shows the stronger interaction of the thiol groups with Au than that of the silanol groups as the as-made pure siliceous sample (figure 6.3.3.1.1) shows an absorbance that slightly oscillates in values suggesting that the interaction of Au with the silanol groups are weak and so dissociation away from the mesoporous solid is facile.

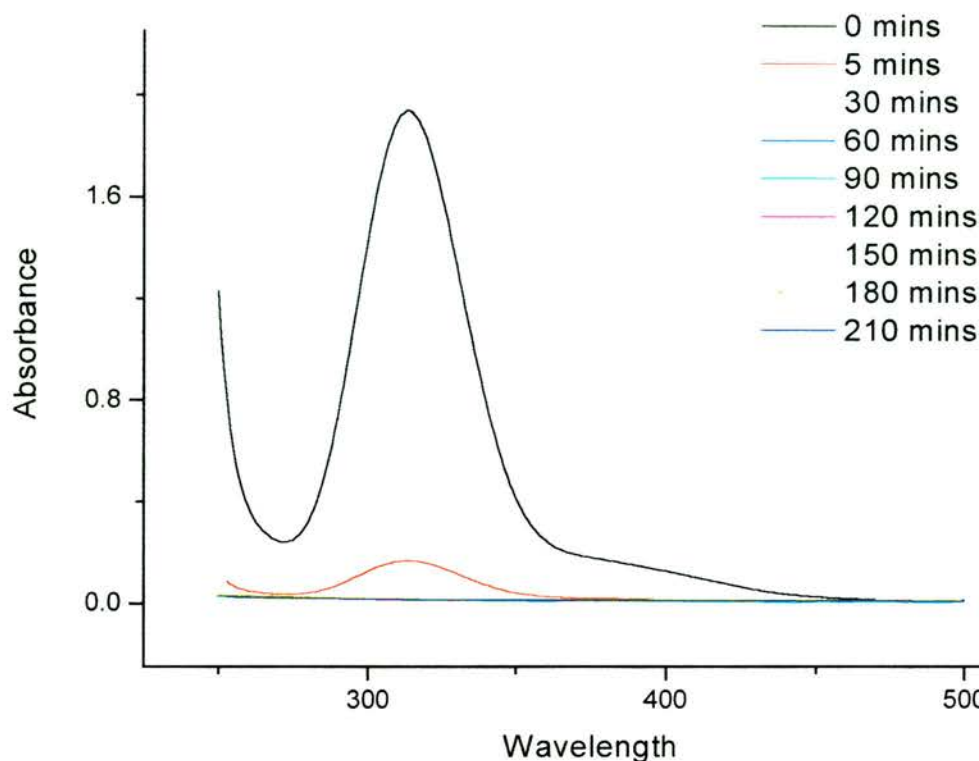


Figure 6.3.3.1.2. UV spectra of the uptake of aqueous $\text{H}^+\text{AuCl}_4^-$ onto an as-prepared SBA-15 mesoporous solid functionalised with 2% thiol as a function of time with a 40% gold loading.

The change in the colour of the filtrate is apparent even after 30 mins as the initial strong yellow colour at $t = 0$ is completely absent indicating the uptake of the Au complex (figure 6.3.3.1.3).

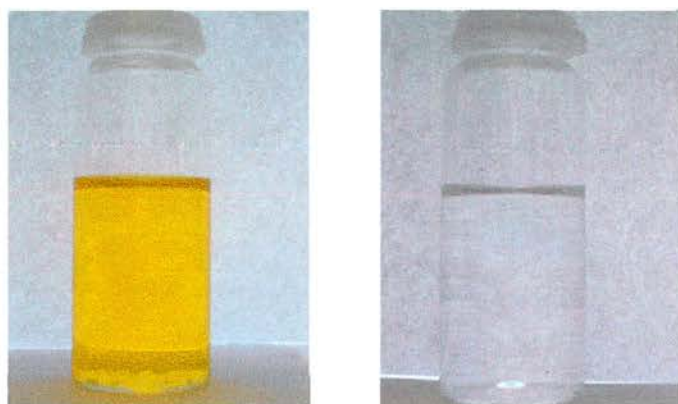


Figure 6.3.3.1.3. Chloroaurate complex at $t = 0$ before the onset of mesoporous solid displaying an intense yellow colour (left) and after the addition of an as-prepared SBA-15 solid functionalised with 2% SH for 30 mins indicating the strong affinity for the Au to absorb (right)

If a calcined solid is used in this case – where further condensation of the silica framework occurs and the condensation of silanol groups is reduced – then the uptake of the Au complex is negligible (figure 6.3.3.1.4) as roughly 98% of the aqueous chloroaurate complex (based on a 40% loading for a 7%SH loaded solid) remains in solution even after 24 hrs. Therefore it seems that a fully condensed silica framework has little effect on chloroaurate uptake. The presence of silanol groups has a small effect, but with little uptake compared to the thiol groups where the uptake is highly efficient.

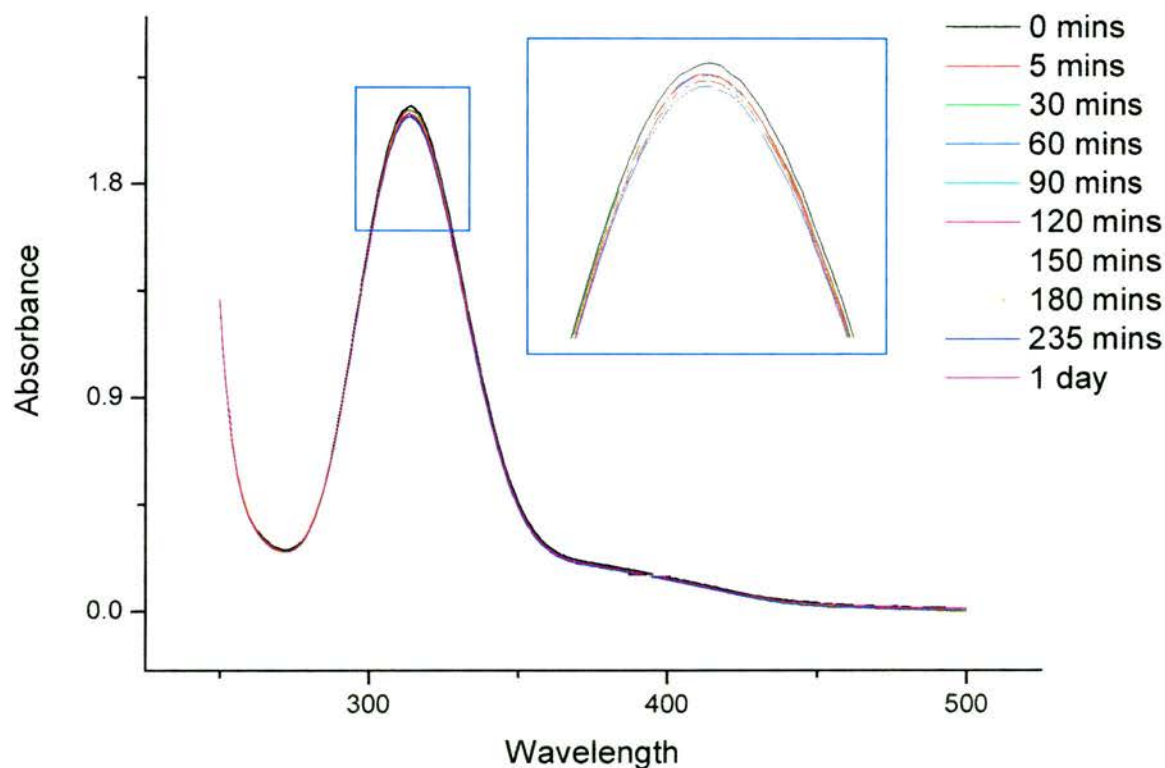


Figure 6.3.3.1.4. UV spectra of the affinity of an aqueous chloroaurate complex to absorb onto calcined STA-11 silica as a function of time. Enlarged section to show just how little is in fact taken up onto the silica – roughly 2%. Equivalent of a 40% Au loading .

The uptake of the chloroaurate complex (40% loading) onto an extracted SBA-15 silica functionalised with 2% SH is efficiently and rapid (chart 6.3.3.1.1 - left). After this first uptake, the material is able to absorb subsequent loadings. Measurements show that the gold complex can be taken up to a molar Au/-SH ratio of 1.4 in the extracted 2%SH SBA-15. Remarkably, the as-prepared 2%SH SBA-15 can take up around one half this amount. Even allowing for a certain amount of template removal

during the treatment, this suggests that much of the gold uptake and reduction takes place at the surface.

The thiol groups are clearly of great importance for the process, since very little uptake of the gold complex takes place in their absence, on either extracted or calcined pure silica SBA-15.

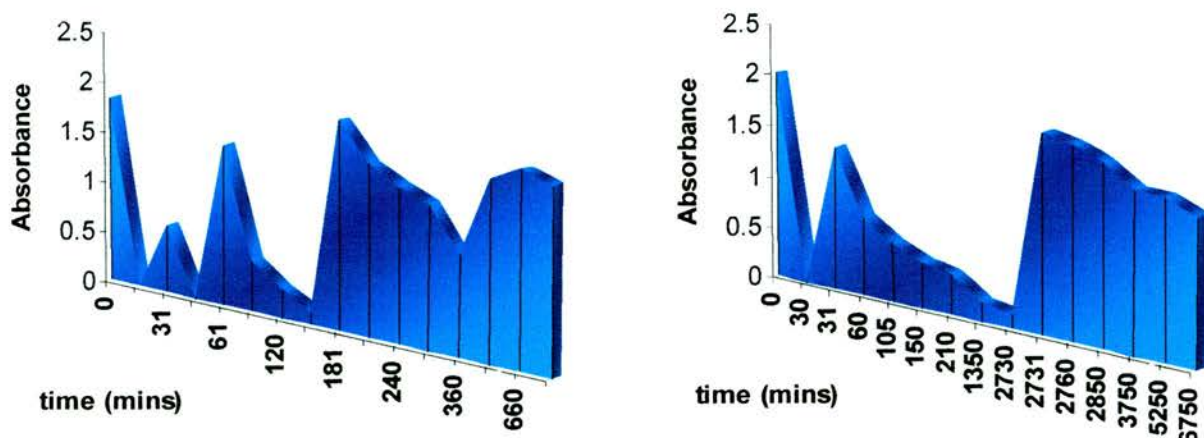


Chart 6.3.3.1.1. Relative absorbance from filtrate of multi-loading chloroaurate complex onto (left) extracted and (right) as-made SBA-15 solid functionalised with 2% SH and their trends of uptake as a function of time and loading. Chart 6.3.3.1.1 N.B. The x scale bar within each chart is not linear.

It can be seen that the uptake of the chloroaurate ions onto silica solids is much more effective in the presence of thiol groups in comparison with either pure silica containing hydroxyl groups or fully condensed silica.

6.3.3.2 TEM analysis of chloroaurate complex 'auto-reduction' on thiol-functionalised SBA-15/STA-11

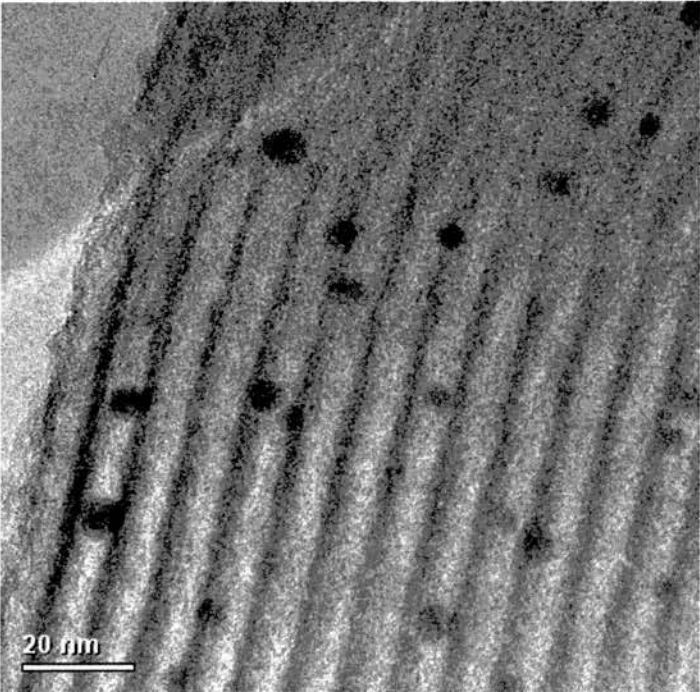
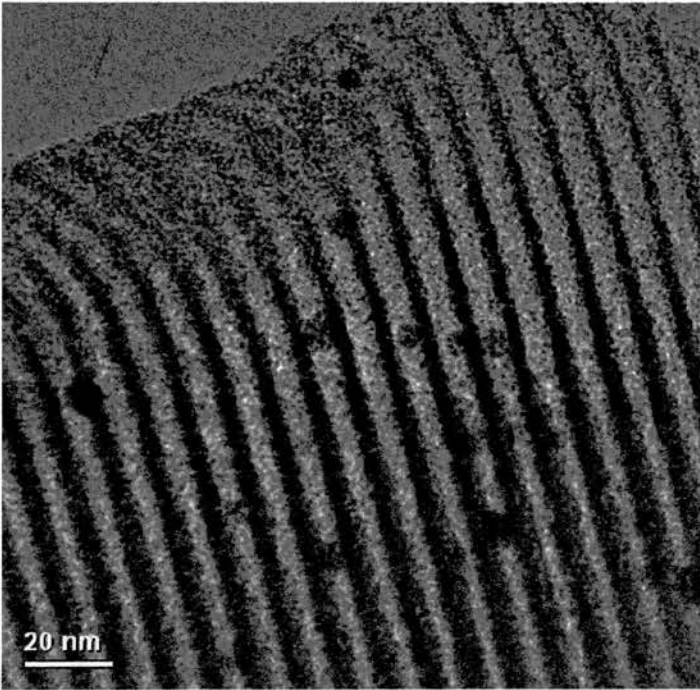
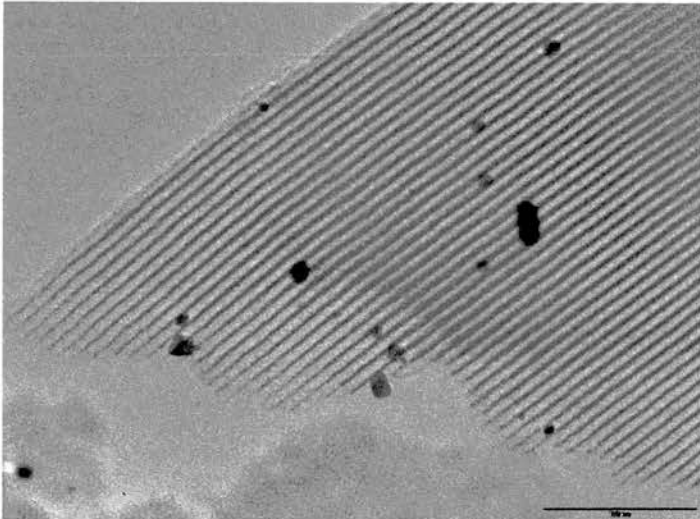
When a sample of SBA-15 functionalised with thiol is introduced to an aqueous chloroaurate solution under stirring the yellow colour observed becomes a grey colour after *ca.* 10 hrs and further continuous stirring yields a pink/red colour after a further 48 hrs. This becomes more prominent over the next 24 hrs. However if the solid is

filtered within 30 mins of stirring, (giving plenty of time for Au uptake as seen by the clear filtrate (section 6.3.3.1)), the solid quickly turns a pink colour upon drying (figure 6.3.3.2.1), the intensity of which increases as a function of time at an elevated temperature as drying at ≥ 333 K the yellow solid turns pink/red after 10 mins whereas for room temperature drying the yellow solid turns yellow/brown after 10 mins and to pink/red after 20 mins.



Figure 6.3.3.2.1. SBA-15-SH-2% in contact with an aqueous solution of chloroaurate complex for 30 mins, filtered then air-dried

The TEM micrographs (figure 6.3.3.2.2) of such samples show that Au nanoparticles are formed and furthermore they are smaller in size than those formed via the sodium citrate reduction route. Particle sizes are in the region of 5 – 7 nm in diameter and so of a size that could be included within the mesopores. There are however nanoparticles of Au slightly larger in diameter which appear to reside on the external surface of the particles with diameter sizes 20 nm at most (still significantly smaller than the particles formed via sodium citrate reduction). In addition the Au colloids are homogeneously distributed throughout the particles.



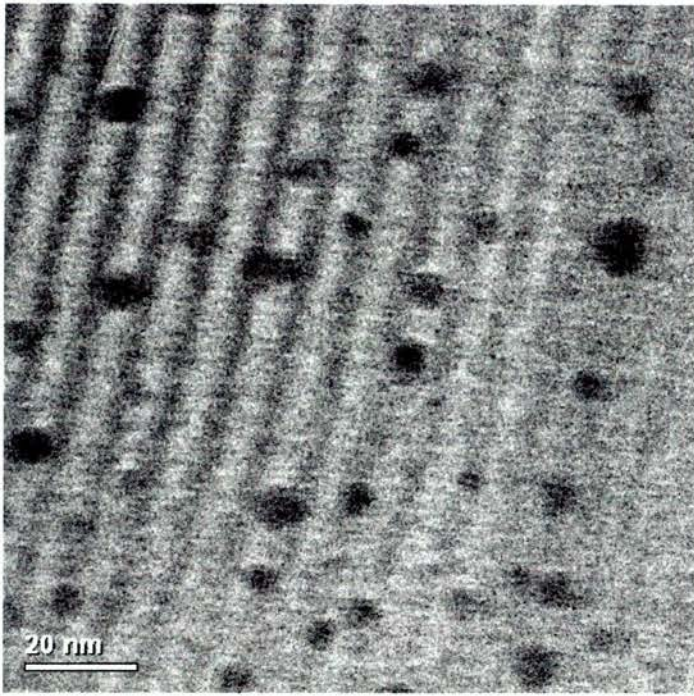


Figure 6.3.3.2.2. HRTEM micrographs viewing the [110] zone axis of auto-reduced Au onto SBA-15 functionalised with thiol showing favourable nanoparticle size homogeneously spread

In the case of the smaller pore STA-11 silica materials the auto-reduction route also gives a red solid (figure 6.3.3.2.3) but does show a clear difference in the Au nanoparticle environment. Whereas SBA-15 type solids display the significant majority of Au colloids in the diameter range applicable to position themselves within the pores the Au colloids observed by TEM (figure 6.3.3.2.4) for STA-11 are too large to be within the intramesochannels with colloidal diameters in the region of 20 – 40 nm.



Figure 6.3.3.2.3. Auto reduction of AuCl₃ into STA-11

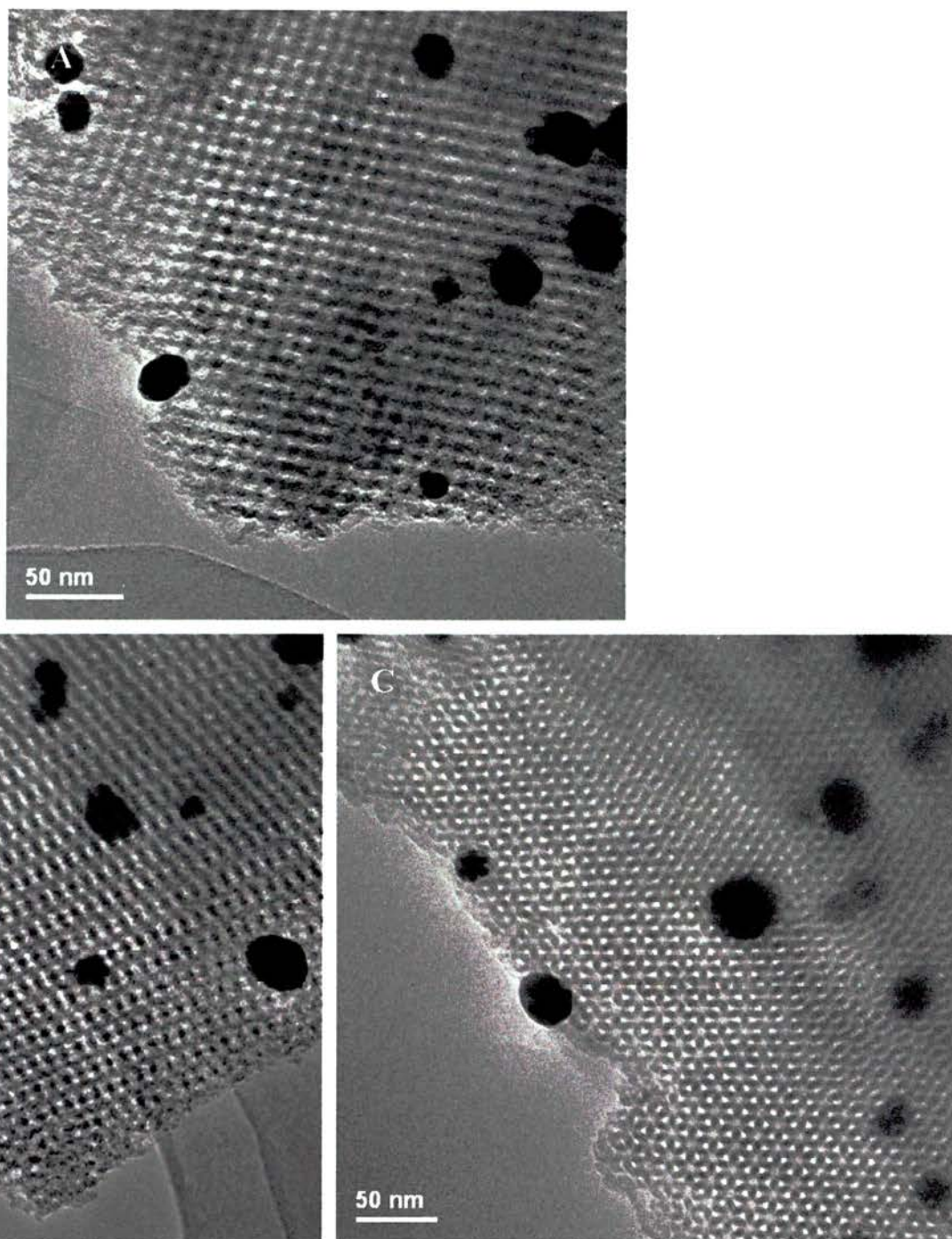


Figure 6.3.3.2.4. HRTEM micrographs of auto reduction of AuCl_3 into STA-11 viewing the (A) $[110]$; (B) $[311]$ and (C) $[111]$ zone axes displaying colloidal Au nanoparticles in the region of 20 - 40 nm positioned on the external surface

Although the method is reported by Ghosh to result in the preparation of gold nanoparticles distributed evenly throughout the mesopores, the evidence presented here suggests that the auto reduction takes place predominantly at the surface. Although the gold nanoparticles on SBA-15 are evenly distributed and of a size that could fit within the pores, the complex uptake data and the results of auto reduction

on STA-11 (7%SH) strongly suggest gold nanoparticles are prepared mainly on the particle surfaces. This is further supported by the N_2 isotherms (figure 6.3.3.2.5) as the capillary condensation step of the Au incorporated STA-11 (blue) occurs over the same pressure range as for the untreated sample (red) especially considering the desorption branch. This suggests that no modification to the pores has taken place. Capillary condensation (adsorption branch) for the Au incorporated solid occurs at a slightly lower relative pressure (results in a pore size reduction of 1 nm) due to the concept that drying of the solid after Au uptake at temperatures which could cause further silica condensation followed by unit cell contraction rather than reduction of pore size through an abundance of gold within the pores.

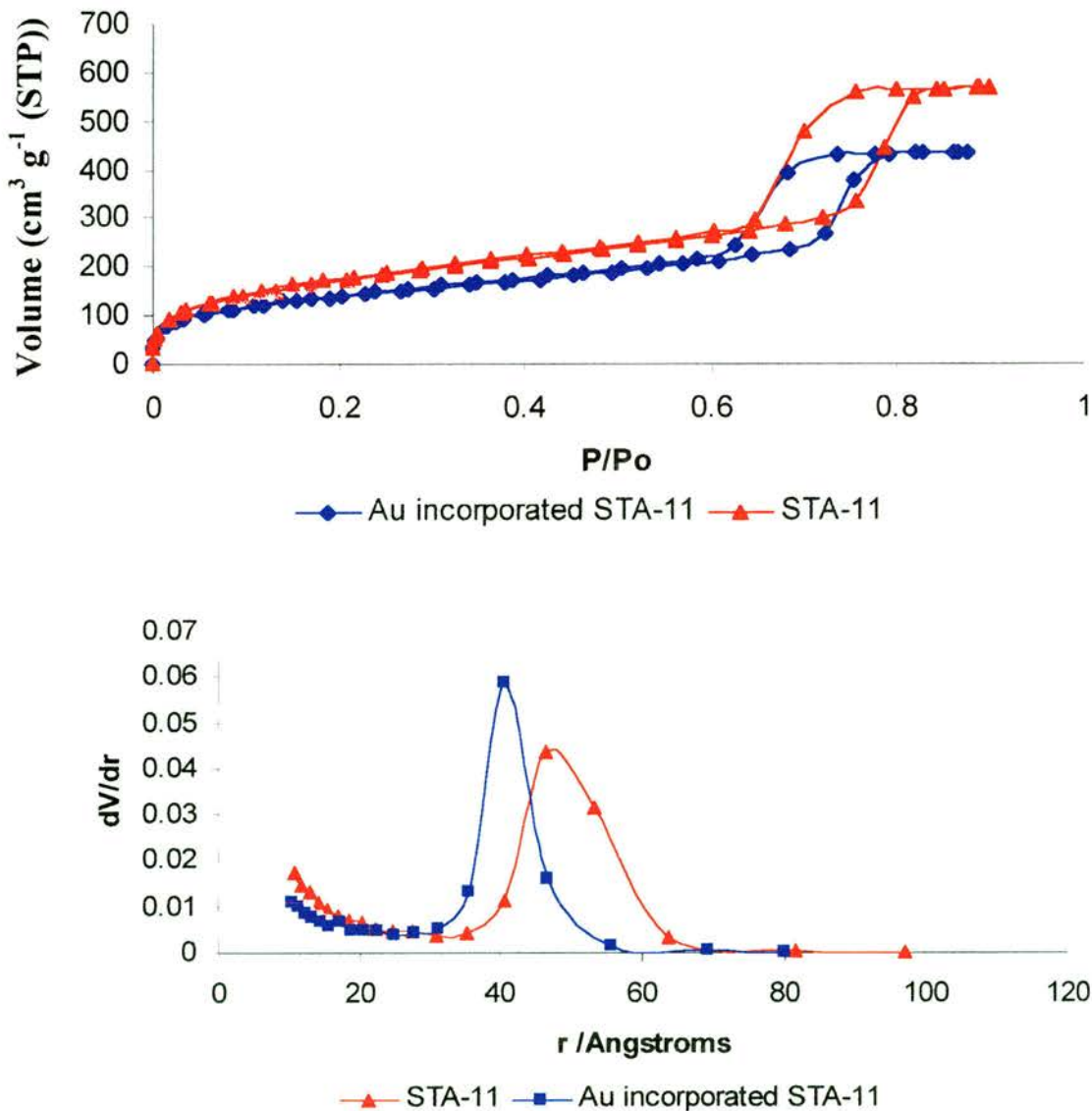


Figure 6.3.3.2.5. N_2 adsorption isotherm (above) and pore size distribution measured using the De Boer model on the adsorption branch (below) for an extracted STA-11 sample and the same sample after the uptake of Au through the auto reduction procedure

6.3.4 Sodium Borohydride reduction of Reverse Au Micelles within thiol functionalised silica

Mixing of suspensions of reverse micelles A and B (see introduction) results in the reduction of gold to form metallic nanoparticles. Dodecanethiol ($C_{12}H_{25}SH$), extracts the gold particles out of the reverse micelles and acts as a capping agent [51], forming a precipitate. The addition of toluene and sonication partly re-disperses the precipitate. After the mixture is allowed to stand, a red supernatant of Au colloids remains. The initial approach was to then decant the supernatant and add this to the thiol-functionalised silica with the idea that the thiol groups from the support would take the place of dodecanethiol and provide another route to Au-SBA-15/STA-11. However, there is insufficient exchange to incorporate a significant amount of gold as the filtrate remains the deep red colour and the solid is a light pink (figure 6.3.4.1).

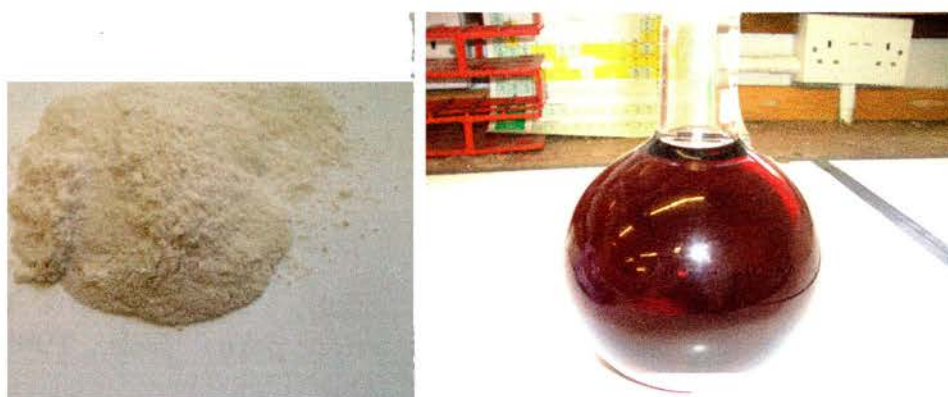


Figure 6.3.4.1. SBA-15-SH-2% silica exchanged with dodecanethiol capped Au colloids from solution (left) and filtrate that remains (right) indicating not an effective uptake

The second approach was to use the thiol groups within the mesoporous silica directly as capping agents without the need for dodecanethiol. In ‘solution’ preparation, reverse micelle A is orange/red and reverse micelle B is transparent. Upon mixing a deep purple/red results. However, the addition of reverse micelle A directly to a thiol-functionalised mesoporous solid under sonication results in the solution becoming colourless after *ca.* 5 mins while the solid remains white. The addition of reverse

micelle B to the silica support again results immediately in the dark red colour with effervescence of H_2 gas (figure 6.3.4.2).



Figure 6.3.4.2. Left to right: Reverse micelle A; reverse micelle A added to thiol loaded mesoporous solid after sonication and the addition of reverse micelle B to the mesoporous solid

Not all of the Au is incorporated into the mesoporous solid in this way (filtering of the solid leaves a dark red filtrate (figure 6.3.4.3)).



Figure 6.3.4.3. Filtrate displaying the presence of Au

Although the uptake of Au within this procedure is not as efficient as with the auto-reduction route the colloidal sizes are promising. TEM shows (figure 6.3.4.4) that although the amount of Au is not high the particles that are present are evenly distributed and are of a similar size to that of the mesopores. The presence of Au is confirmed by EDAX analysis.

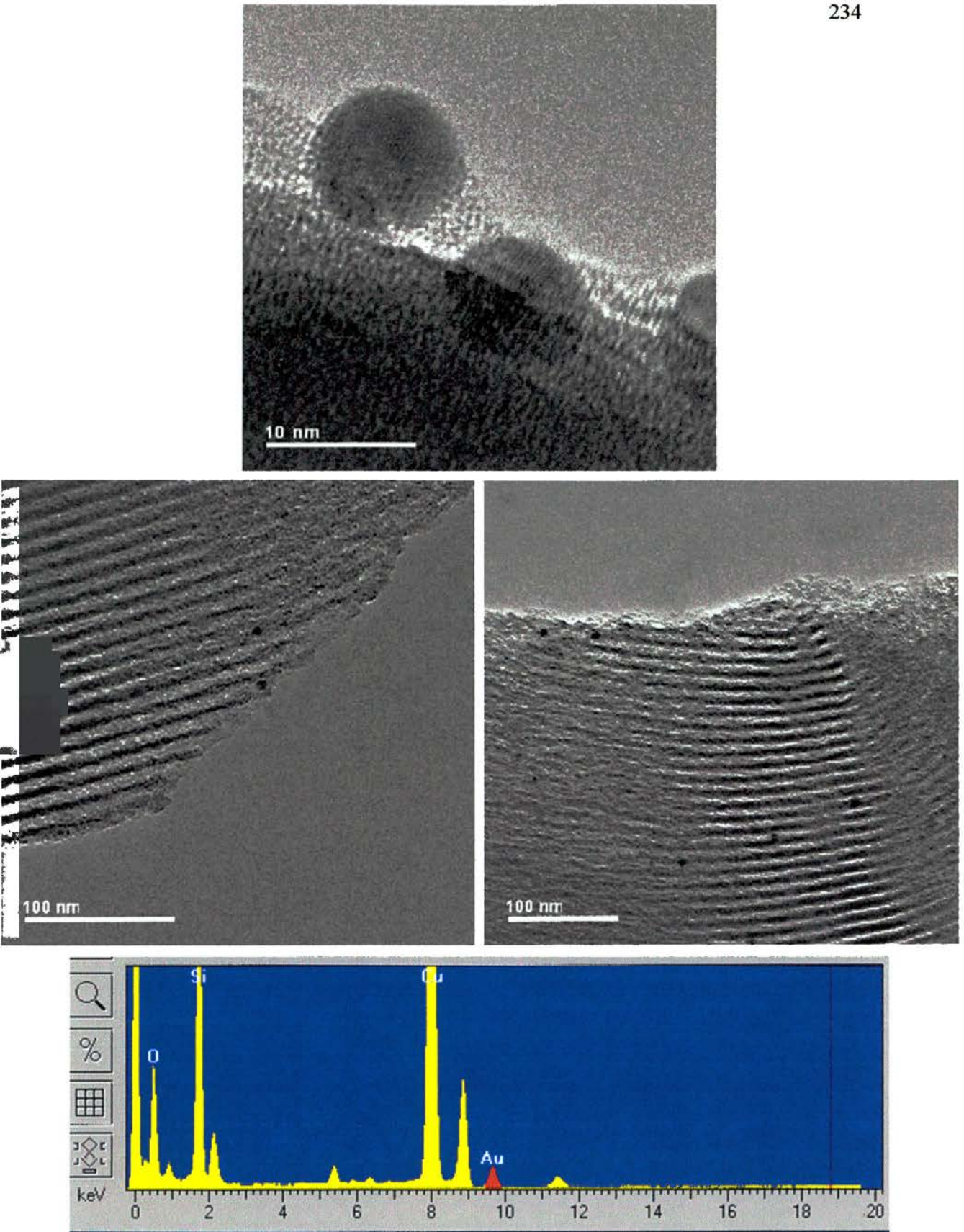


Figure 6.3.4.4. (Top) high magnification TEM micrograph of spherical Au colloids with diameter in the region of 9 nm; (middle left) lone Au nanoparticles with 6 nm diameters apparently situated within the mesopore; (middle right) homogeneously spread 6 nm Au colloids and (bottom) EDAX analysis.

In an attempt to increase the gold uptake, the procedure was adapted so that the solution containing reverse micelle A is added to the thiol-functionalised mesoporous solid, sonicated and the white solid filtered off (figure 6.3.4.5). The solution containing reverse micelles of type B was then added dropwise over the white solid, turning it pink. Notably, the original colourless filtrate also contains gold, since adding reverse micelle B to this results in an immediate red colour. Analysis of the final solid indicates a gold content of 40%.



Figure 6.3.4.5. White solid upon addition of orange/red reverse micelle A to silica support after sonication (left) along with the filtrate (right)

The idea is that when the silica support is filtered and pump-dry reverse micelle B can be added to the support drop by drop carefully over the solid to enable the sodium borohydride to pass only through the support without the filtrate. Here the solid becomes pink indicating the reduction of Au on the mesoporous solid (figure 6.3.4.6).



Figure 6.3.4.6. Addition of reverse micelle B to filtered solid that has been in contact with reverse micelle A and sonicated (from figure 6.3.4.5) (left) and to the clear filtrate (from figure 6.3.4.5) indicating that Au is not all incorporated into the solid (right).

TEM of this sample again show that colloidal sizes are favourable in that the diameters of such nanoparticles are 5 – 6 nm to be distributed throughout the mesopores (figure 6.3.4.7).

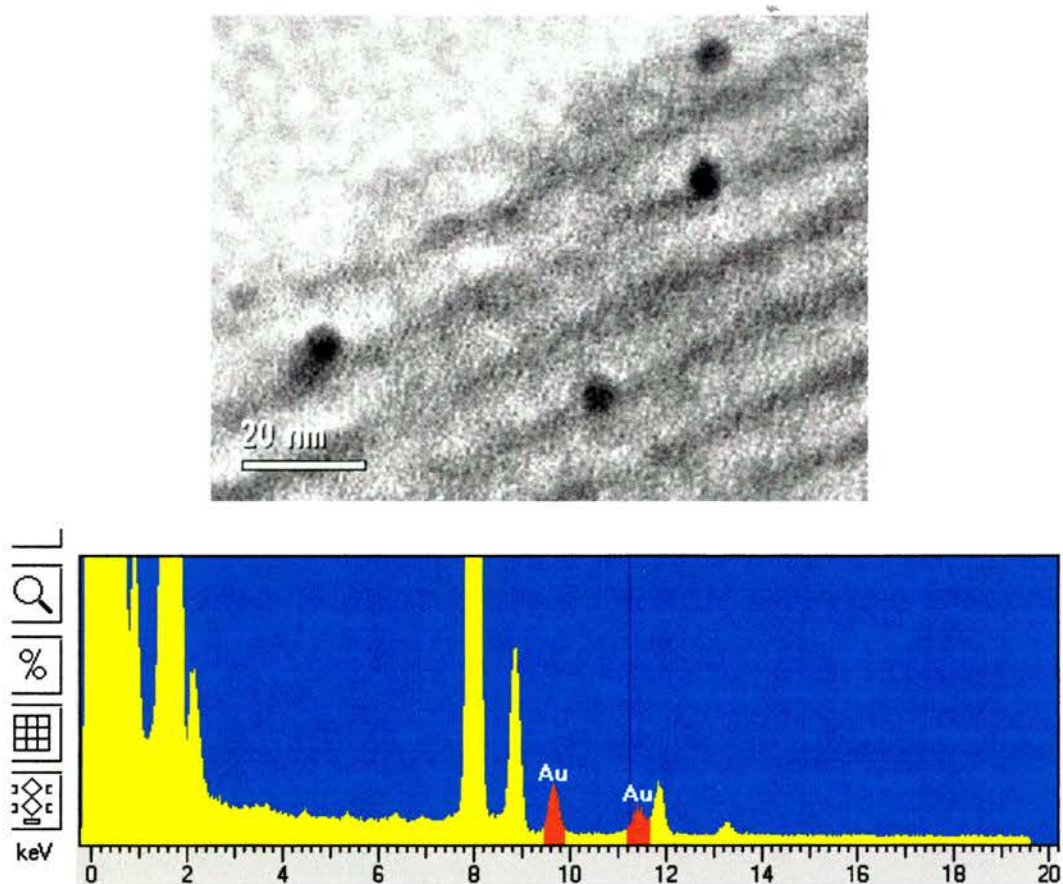


Figure 6.3.4.7. HRTEM micrographs of Au incorporated thiol functionalised mesoporous silica with colloidal sizes in the region of 5 – 6 nm viewing the [110] zone axis along with EDAX analysis

The colour change (or loss) observed as the reverse micelles containing gold (III) chloride are added to the thiol-bearing solid, are incompletely understood. One possibility is that Au (I) species are formed. Au (I) thiolates, for example, are colourless, easily reduced species [55 - 57].

N_2 adsorption measurements (figure 6.3.4.8) show that, once extracted, the gold-containing solids have a strongly reduced capacity for N_2 (14 wt% uptake, compared to 72 wt% uptake in similar extracted solids without addition of the micelles of type A and B). At the same time, chemical analysis indicates high levels of bromide, presumably due to the incorporation of cetyltrimethylammonium bromide surfactant in the pores. Upon calcination the adsorption capacity is increased to 49 wt% as the surfactant is removed. Observing pore modification in the higher pressure regions suggests that gold is within the pores of the solid and complement the TEM micrographs.

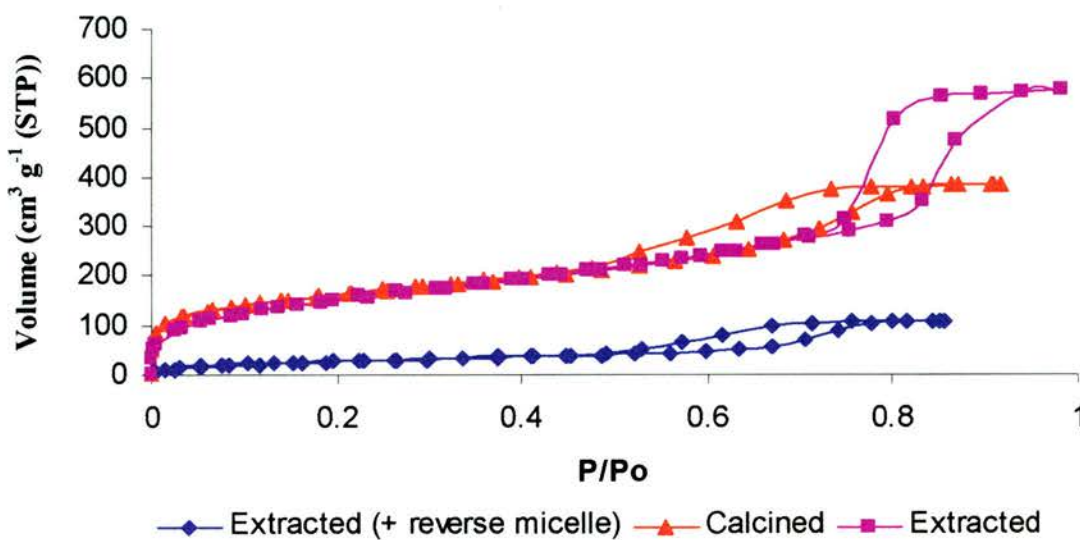


Figure 6.3.4.8. N_2 adsorption isotherms of an untreated extracted SBA-15 sample functionalised with 2% SH (purple); the sample treated with reverse gold micelles (blue) and the treated sample calcined (red)

Finally an *in situ* approach was adopted, attempting to incorporate Au during the formation of the mesoporous solid. In all cases the as-made and extracted materials gave a white solid (possibly indicating the formation of Au(I) thiolates). Upon calcination all solids turned pink indicating the possible thermal reduction of the Au(I) thiolates to form metallic Au (figure 6.3.4.9).



Figure 6.3.4.9. *In situ* incorporation of reverse Au micelles into thiol functionalised mesoporous silica – as-made (top left); extracted (top right); calcined (bottom left) and calcined with 3 stoichiometric equivalents of Au (bottom right).

TEM micrographs reveal that nanoparticles of Au are not present within the extracted samples confirming that the gold is still complexed. It is also noted that the mesostructure obtained using this *in situ* approach, is well ordered. SBA-15 type particles are observed retaining high quality mesostructure. Addition of CTAB to the synthesis after 3 hrs has no effect on the outcome. Au nanoparticles are formed after the heating under flowing N_2 , but they are in the region of 20 – 25 nm and must therefore be outside exist outside the mesochannels, although sporadically there are Au particles observed possibly within the mesopores as Au nanorods (figure 6.3.4.10).

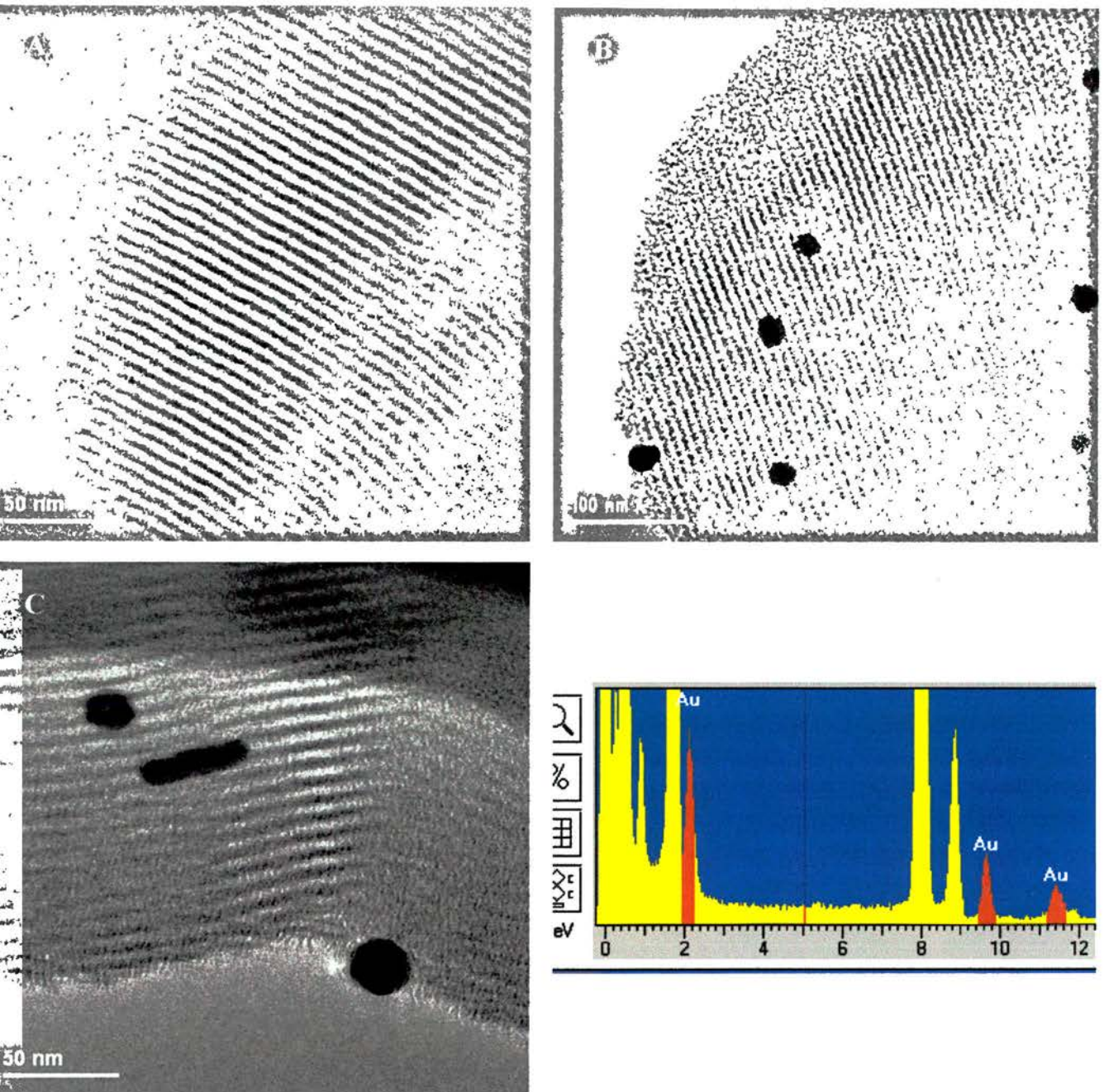


Figure 6.3.4.10. HTREM micrographs of *in situ* incorporation of reverse Au micelles into thiol-functionalised SBA-15: (A) Extracted sample showing no Au colloids; (B) calcined sample with spherical Au colloids 20 nm in diameter on the external surface of particle viewing the [110] plane; (C) calcined sample with possible Au nanorod within the mesopore along with Au nanoparticles on the external surface along with EDAX

6.3.5 Trimethylammonium Chloride functionalised SBA-15 for noble metal complex ion-exchange & reduction by H_2

In situ functionalisation of SBA-15 with the charged alkylammonium organo-siloxane at a concentration of 3.5% (based on total SiO_2) results in a high quality ordered mesostructure typical of SBA-15 as observed through HRTEM micrographs (figure 6.3.5.1).

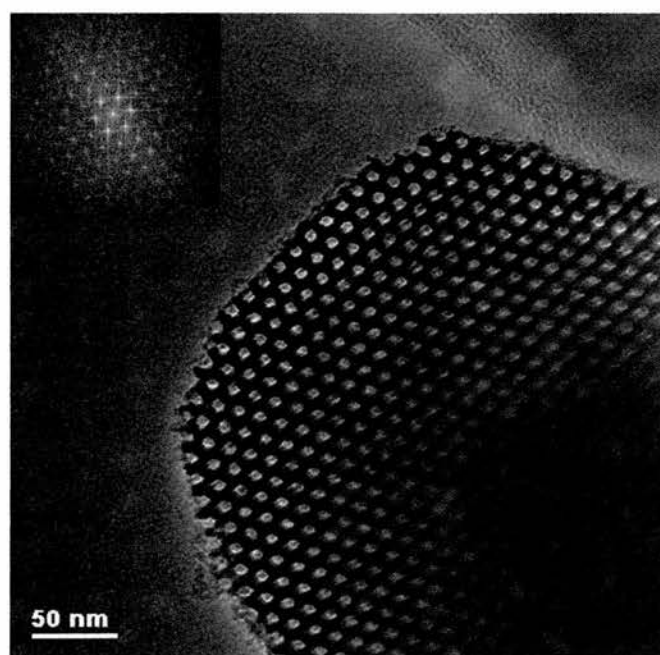


Figure 6.3.5.1. HRTEM micrograph of SBA-15 functionalised *in situ* with a charged alkylammonium organo-siloxane with the incident electron beam orientated towards the [001] zone axis along with the corresponding fourier transform showing that high quality SBA-15 mesostructure is obtained

N_2 adsorption isotherms (figure 6.3.5.2) also indicate typical type IV isotherms and show steep capillary condensation over a narrow pressure range indicating the quality of mesostructure obtained. The extracted and calcined solids exhibit substantial mass uptakes of 670 cm^{-3} (STP) (84%) and 834 cm^{-3} (STP) (104%) respectively with corresponding specific surface areas of 576 m^2 and 850 m^2 . Upon calcination an increase in microporosity is observed as unextracted surfactant is removed. Further

condensation of the silica framework slightly reduces the unit cell resulting in a reduction in pore size. The capillary condensation inflection point for the calcined sample is roughly at P/P_0 of 0.85, compared with a value for the extracted form of 0.9 (corresponding pore sizes calculated on the desorption branch using the De Boer model are 94 Å and 133 Å respectively).

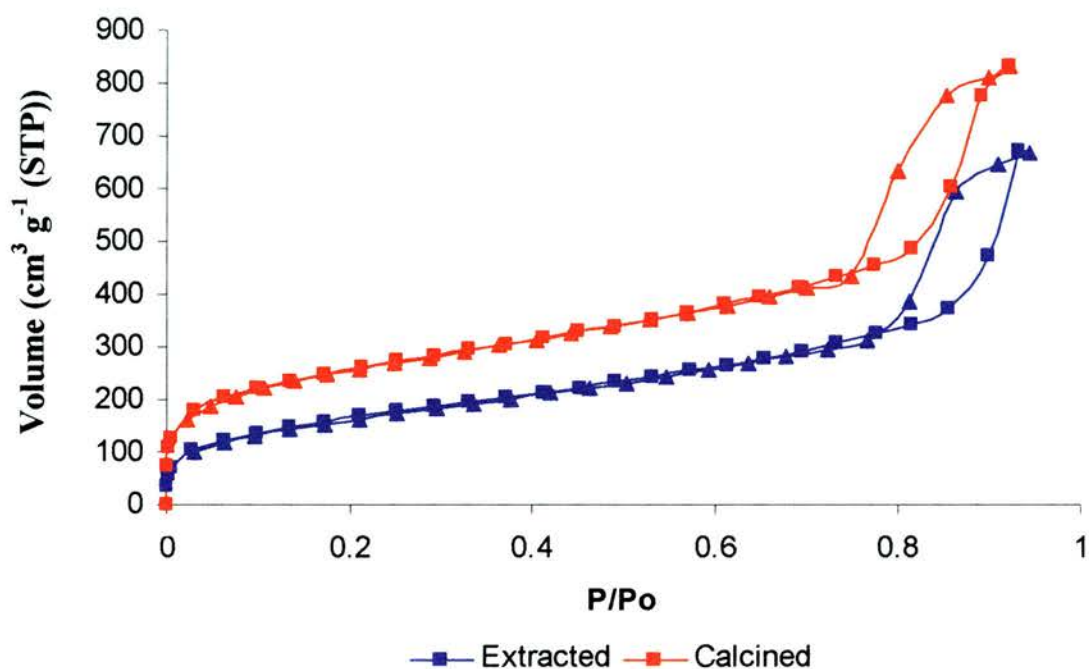


Figure 6.3.5.2. N_2 adsorption/desorption isotherms of extracted and calcined trimethylammonium chloride functionalised SBA-15

The idea of functionalising mesoporous silica with alkylammonium groups is that the mobile charge from the associated chloride ($N(CH_3)_3^+Cl^-$) is ideal to ion exchange with anionic metallic complexes such as ammonium tetrachloroplatinate. Because the electrostatic interaction between the cationic organic functionality and the anionic metal precursor is strong, stirring for 15 mins is sufficient for full ion exchange [52]. Also anionic chloroaurate ions ($AuCl_4^-$) can easily exchange with the chloride anion too.

Incorporation of Au and Pt species into the mesoporous host takes place rapidly with the resultant solids displaying intense colours. The solid hosting the Au complex before reduction under H_2 at 423 K remains a slight greenish colour, upon thermal

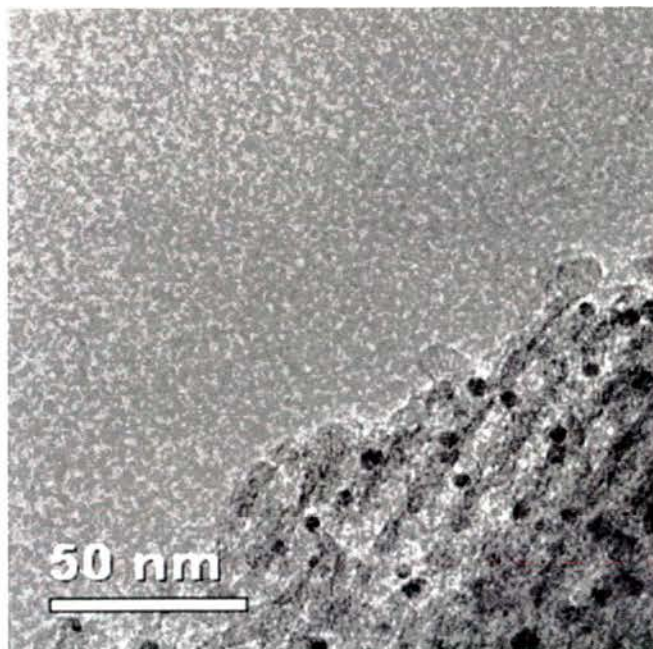
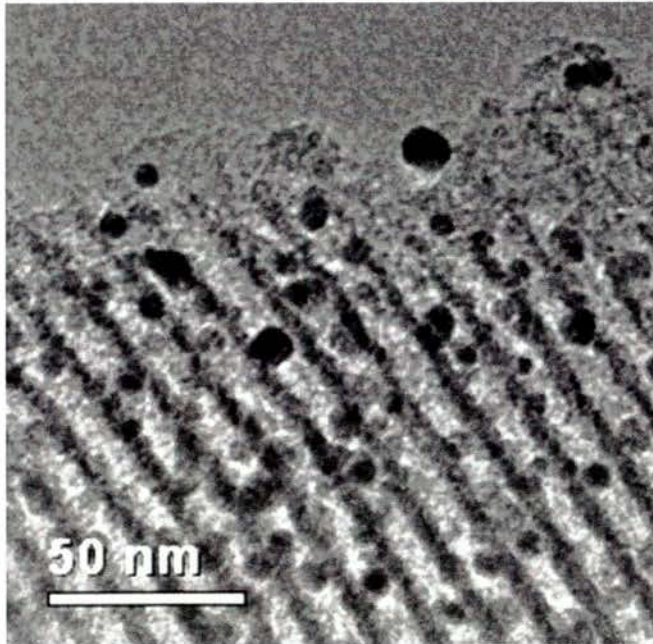
reductive treatment the solid turns a characteristic red. The solid containing complexed platinum is pink and turns grey after reduction (figure 6.3.5.3).



Figure 6.3.5.3. Thermal reductive treatment with H_2 to SBA-15 functionalised with charged trimethylammonium chloride groups with further incorporation of (top) Au; (middle) Pt and (bottom) Pt – with increased temperature on reduction

TEM investigation provides the means of direct observation to the distribution of Au nanoparticles in the Au-SBA-15 composite material. Typical TEM micrographs (figure 6.3.5.4) reveal highly dispersed Au nanoparticles with diameters ranging from 4 – 9 nm uniformly distributed within the mesopores. This reduction method yields

an abundant quantity of Au colloids of favourable dimensions with little presence of nanoparticles exhibiting diameters beyond that of the mesochannels.



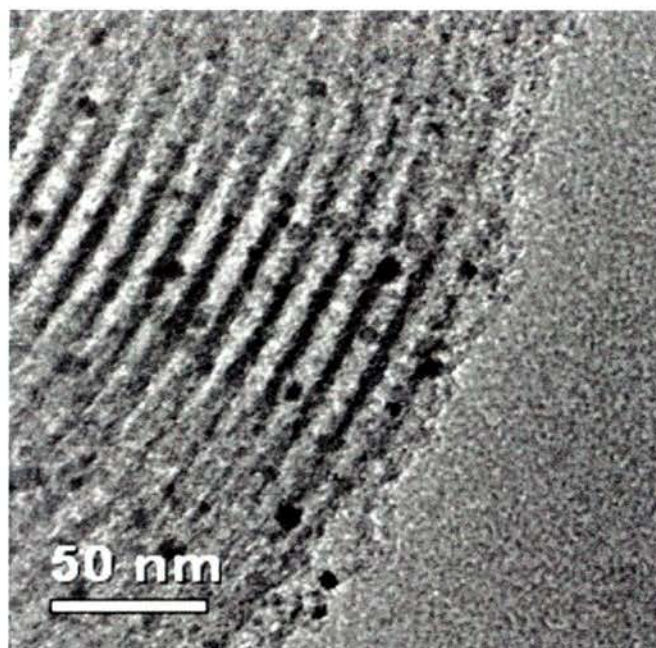


Figure 6.3.5.4. HRTEM micrographs viewing the [110] zone axis of SBA-15 functionalised with trimethylammonium groups and reductive treatment with H_2 of chloroaurate ions by ion exchange. Au colloids in the diameter range of 4 – 9 nm

Further evidence that the Au colloids are within the mesopores and are not residing on the external surface is the N_2 isotherm of the solid (figure 6.3.4.5). There is a reduction in the uptake of N_2 to 498 cm^3 (STP) (62 wt%), lower than for the non-metallated analogue. This would be expected as the density of the material has now increased and there is less uptake per mass of solid. Importantly the capillary condensation on both the adsorption and desorption branches occurs over a wider range of pressures, extending to lower relative pressures, indicating smaller pore sizes and also that the capillary condensation step occurs over a much broader pressure range indicating that the pores have been modified – in other words that Au is within the pores.

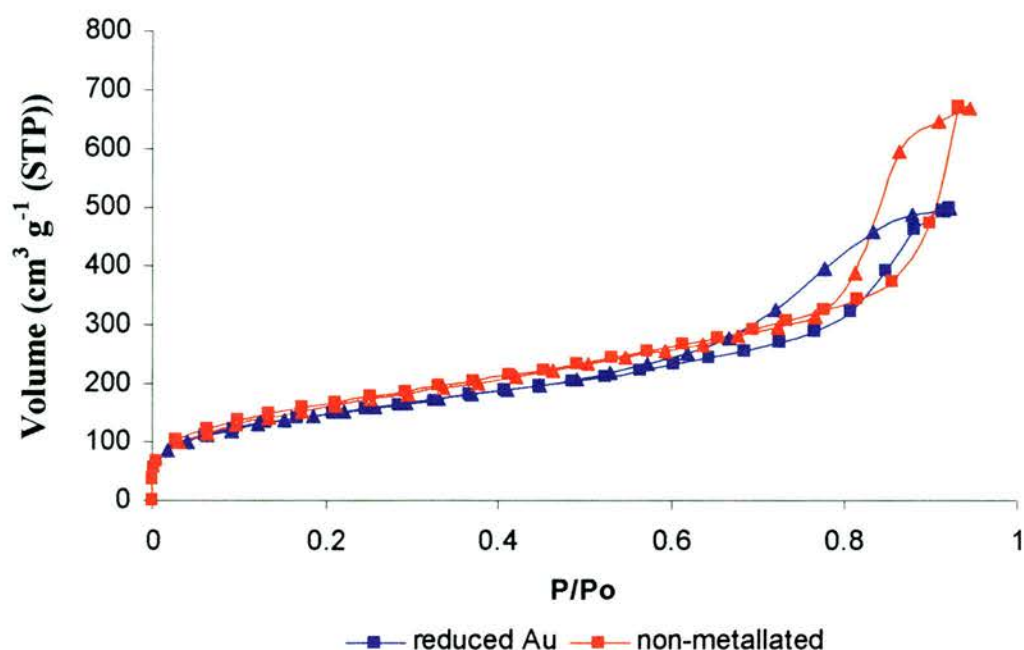


Figure 6.3.5.5. N_2 isotherms of non-metallated and Au incorporated trimethylammonium chloride SBA-15. Reduction of Au within the pores changes the capillary condensation step to lower relative pressures and which occurs over a broader pressure range

The Pt analogue shows no sign of metallic nanoparticles under thermal reductive treatment at 423 K. It may be the case that only slight partial reduction has taken place as the temperature may be insufficient to allow reduction of the Pt complex. Increasing the thermal reduction process to 573 K resulted in a change compared to the lower temperature solid in that now Pt nanoparticles are observed directly by TEM (figure 6.3.5.6). However the diameter size of the respective colloids are large, comparable with the colloids reduced via sodium citrate on the macroporous titania, with diameters in the region of 120 – 300 nm and thus, indicate the Pt nanoparticles are on the external surface. Further investigation would be required into how the temperature, ramp rate and time of the reduction method has on the formation of the Pt colloids.

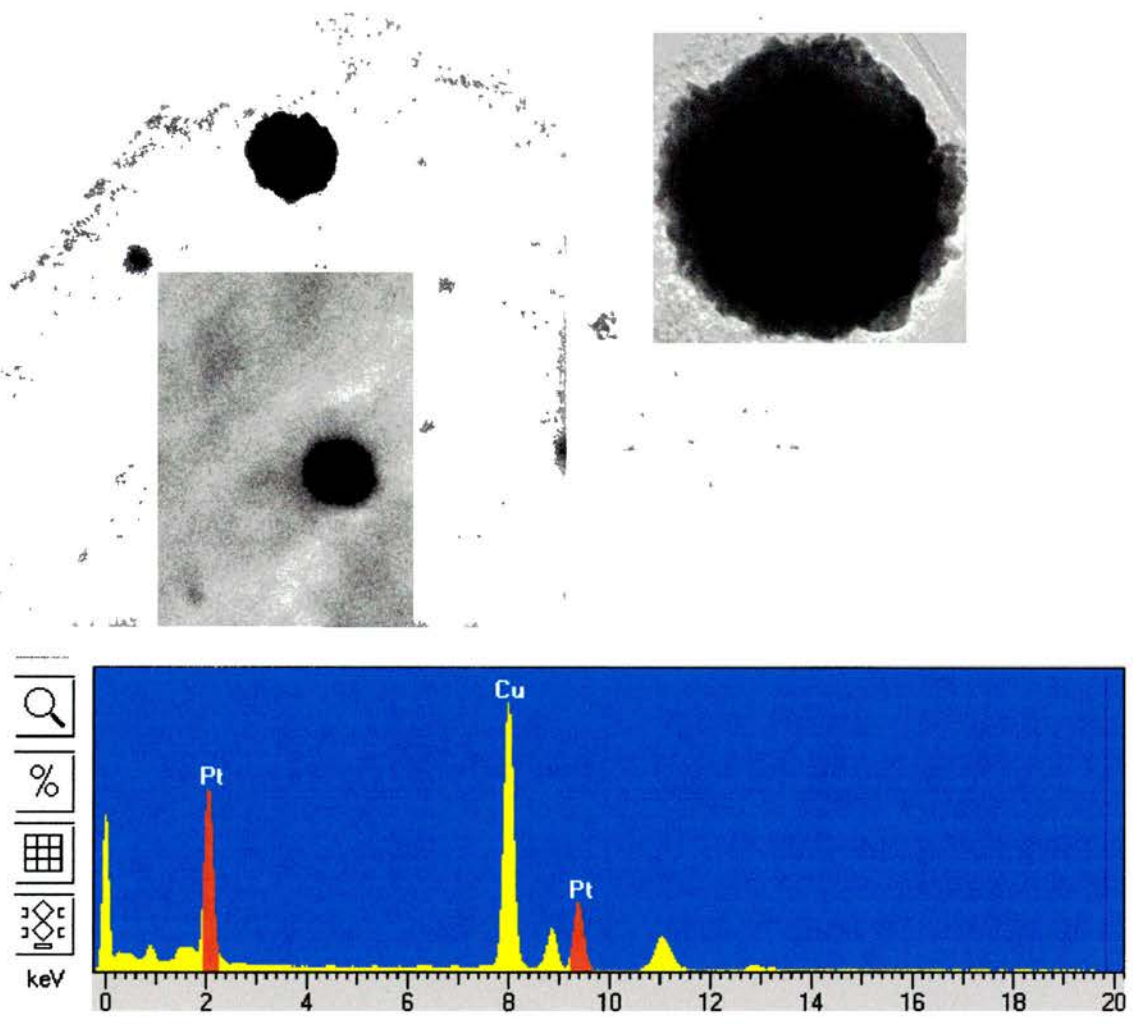


Figure 6.3.5.6. HRTEM micrographs of SBA-15 functionalised with trimethylammonium chloride organo-siloxane ion exchanged with ammonium tetrachloroplatinate and thermal treatment under H_2 applied at 523 K. Pt nanoparticles are observed indicating that the reduction has taken place although maybe the reductive conditions are responsible for the large Pt colloids which reside on the external surface and present intense Pt peaks from the EDAX analysis

6.3.6 *Thiol-functionalised silica supports for the allylpalladium chloride complex and reduction under mild conditions*

Incorporation of allylpalladium chloride into the white thiol-functionalised silica supports results in green solids (figure 6.3.6.1) after *ca.* 5 hrs of stirring under the conditions described in section 6.2.5, indicating that the uptake of the Pd complex has been achieved.



Figure 6.3.6.1. Uptake of allylpalladium chloride onto thiol-functionalised SBA-15 (2%SH) (left) and STA-11 (7%SH) (right) resulting in green solids

It is thought that thiols in the presence of amines can reduce the Pd complex under mild conditions [54] and so a mesoporous solid functionalised with organic thiol groups would potentially offer a suitable route for reduction. For the SBA-15 type materials HRTEM reveals directly that the colloidal particles have formed (figure 6.3.6.2), however, it can be clearly seen that nanoparticles accumulated to a size that surpasses the pore size with diameters typically in the region of 70 – 110 nm. Sporadically there does seem the case that Pd has indeed been incorporated into the intramesochannels as the contrast of the metal does follow the direction of the pores.

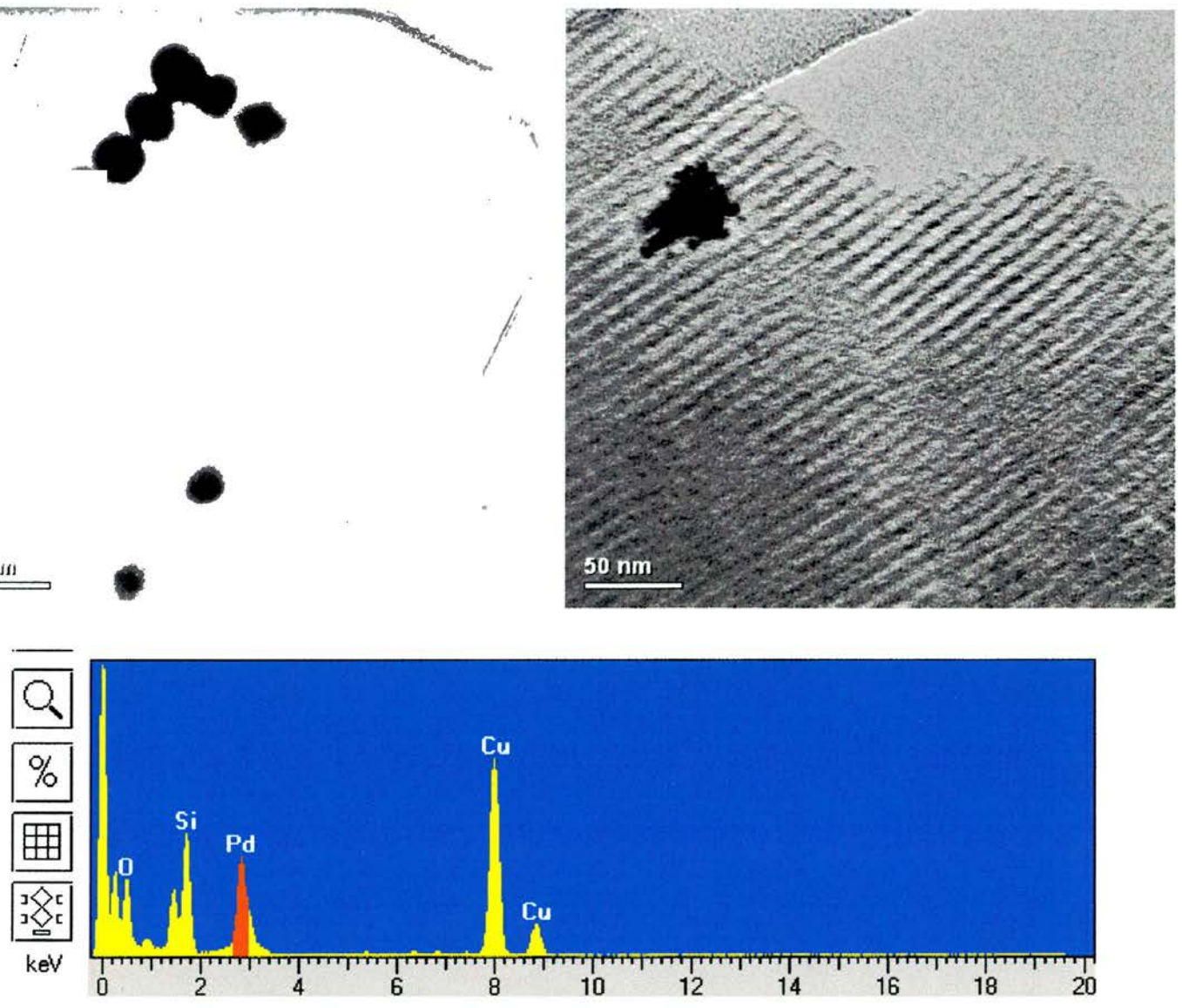


Figure 6.3.6.2. HRTEM micrographs of SBA-15 functionalised with 2% thiol with the uptake of palladium chloride showing colloidal sizes with diameters of 70 – 110 nm positioned on the external surface (above left); Pd running parallel to the mesochannels likely to be incorporated within the pores (above right) and the presence of Pd confirmed through EDAX analysis (bottom).

In the case for STA-11 type solids similar results are observed in the fact that the majority of the colloids present are sited on the external surface as the nanoparticle diameters far exceed the pore dimensions through HRTEM (figure 6.3.6.3). Although the colloids have diameters in the region of 35 – 50 nm careful observation seems to show the colloids having a non-uniform shape arising from smaller 5 – 6 nm diameter colloids agglomerating to form the bigger nanoparticles.

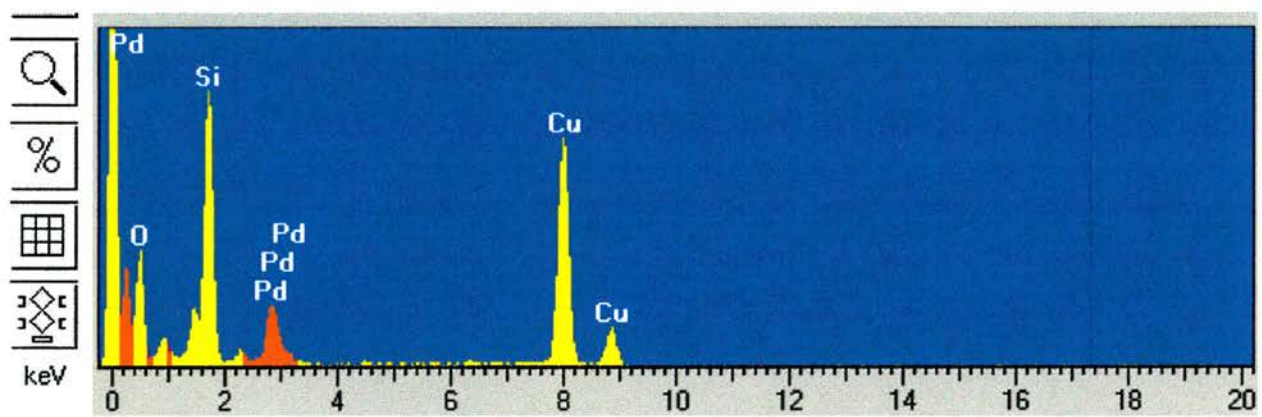
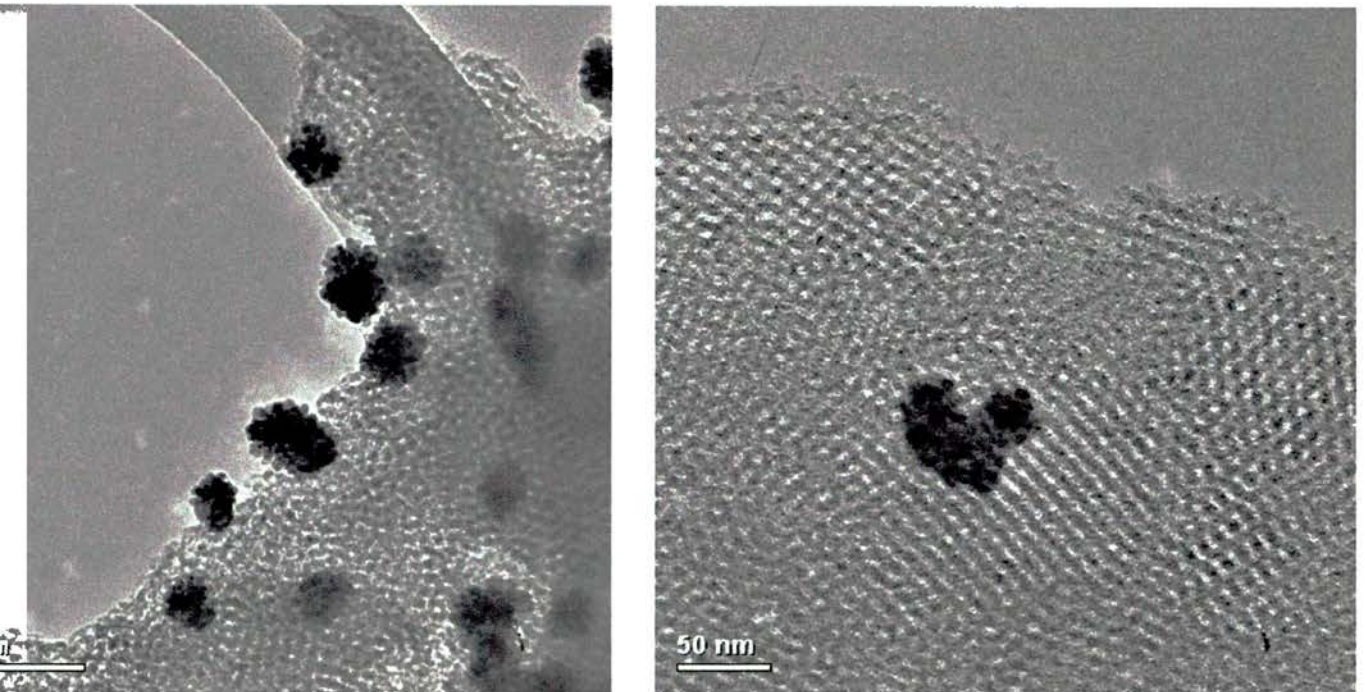


Figure 6.3.6.3. HRTEM micrographs of STA-11 type solids with the inclusion of the allylpalladium chloride complex viewing the [110] and [311] zone axes with colloidal sizes in the range of 30 nm (above); a region of Pd colloids exhibiting diameter of 35 – 50 nm from an apparent agglomeration of smaller colloids with diameters of 5 – 6 nm (middle); EDAX analysis confirming the presence of Pd on the silica support.

6.4 Conclusions

6.4.1. Individual methods

6.4.1.1 Sodium citrate reduction

HRTEM investigations reveal that the colloids formed, although randomly distributed are too large for incorporation into the pores of STA-11 as the nanoparticles exhibit non-favourable diameters in the region of 80 nm at most. It can be observed that Au has a high scattering of light as a pink solid can be obtained with loadings of Au as low as 1% (based on SH moles).

6.4.1.2 Auto-reduction

It was observed through UV that the presence of thiol groups have an important effect on the uptake of chloroaurate ions. A porous calcined silica sample shows negligible uptake of chloroaurate ions whilst a pure siliceous sample with the template still in tact (OH groups remaining) has an uptake in the region of 10%. However, an as-made thiol-functionalised sample exhibits a remarkable uptake as all chloroaurate ions are absorbed from solution within 30 mins. Extracted thiol solids exhibit rapid uptake of gold (III) chloride from solution.

HRTEM reveals that the Au particles formed on SBA-15 are of a more favourable size with diameters in the region of 5 – 7 nm with very few exhibiting diameters that exceed the pore dimensions and are spread throughout the particles and on the surface. STA-11 type solids display a quick uptake although the colloidal sizes that form are too large to be positioned within the internal pores (diameters in the range of 20 – 40 nm).

6.4.1.3 Reverse Au micelles and sodium borohydride reduction

Reducing the Au complex by mixing of reverse micelle A and B outside the thiol-functionalised silica support and using 'free' thiols in solution to act as capping agents does not allow for an efficient exchange of Au between the 'free' thiols and the tethered thiols.

Incorporating reverse micelle A directly into the thiol-functionalised supports give colloidal sizes favourable with respect to the pore dimensions of the silica solids. Here the Au nanoparticles are in the region of 5 – 7 nm and although present at low concentration seem to be positioned within the mesopores. It was observed upon filtering the solid that a Au complex was forming that gave a white solid which may give information on the route to reduction. The initial Au(III) complex may reduce to Au(I) thiolates which in the presence of hydrocarbons give white solids and are passivated by thiols [55 – 57]. Here as before favourable colloid sizes are present with diameters in the region of 5 – 6 nm that are small enough to be within the mesopores. The nitrogen isotherms of such materials (compared to the pre-treated extracted thiol-functionalised solids) display a reduced N₂ uptake capacity and with it broad capillary condensation at lower relative pressures indicating that modification to the pores have taken place – the incorporation of the micelles within the pores. Upon calcination the uptake capacity is increased so that it approaches that of the initial starting material with a slight shift of capillary condensation to lower relative pressures, again indicating that Au is within the pores.

The *in situ* approach shows that no change in the mesostructure is obtained in using the two different surfactants if SBA-15 formation is permitted before the addition of the micellar system containing the 2nd surfactant. All solids are white on formation and TEM investigation of the samples show no sign of metallic gold. Thermolysis through calcination easily reduces Au (I) further to its metallic state although the nanoparticles formed have diameters in the region of 20 – 25 nm and therefore are on the external surface.

6.4.1.4 Alkylammonium chloride functionalised solids and thermal reduction with H_2

Using the charged alkylammonium group as a co-condenser to the silica source at 4% (based on SiO_2) does not effect either the mesophase or the quality of the mesoproduct as highly ordered SBA-15 forms observed through HRTEM and indicated through N_2 measurements. The solids permit facile anion exchange, permitting the rapid uptake of $AuCl_4^-$ and $PtCl_4^{2-}$. Reduction in H_2 with the Au incorporated solids results in favourable colloidal sizes in the range of 4 – 9 nm sited within the pores of the silica support. Furthermore the nanoparticles are abundant and evenly distributed with few particles outside the pores. The N_2 isotherms of such materials reveals a reduction in mass uptake not only because of a change to a higher density solid but also because of the fact that Au is within the pores. As a result of this pore modification the capillary condensation step is spread over a broader P/P_0 range. For gold nanoparticles, this approach is therefore the most promising of those described here.

The Pt analogues show no sign of metallic colloids with reduction under mild conditions (423 K) although increasing the reduction temperature (573 K) results in particles with diameters of 120 – 300 nm far too big to be within the pores. Further investigations by studying the effect of temperature, ramp rate and time of reduction would be required to try to improve the reduction method.

6.4.1.5 Allylpalladium chloride incorporated thiol-functionalised silicas

The uptake of the Pd complex into the silica support can be observed due to the change in the solid's appearance to a green colour. However the route gives particle sizes too large to be within the pores of either SBA-15 or STA-11 type materials. It can be observed, occasionally, that within the SBA-15 type materials occasionally there seems to be Pd running parallel to the pores indicating that the metal is situated at the internal surface. The colloids on the external surface of STA-11 type materials seem to display on closer observation that smaller colloids with diameters of 5 – 6 nm have agglomerated to larger colloidal sizes in the range of 35 – 50 nm.

6.4.2. Summary

The investigation of the use of *in situ* organically-modified mesoporous solids as catalyst supports for precious metals using various routes for metal incorporation has been described. Characterisation mainly through HRTEM (and complementing porosity measurements in some cases) has helped to give information on the metal.

The auto-reduction route facilitates two different outcomes depending on the meso-product structure used. The larger pore SBA-15, there is a mix of Au particles that viewed by TEM show diameters of either 5 – 7 nm or diameters which are too large for the pore size and are on the external surface. However, for STA-11 the particle sizes are clearly only on the external surface with no sign of any pore modification. Auto-reduction as a route to include Au particles in the pores of mesoporous solids would seem to be an area where choices of silica hosts and methods of incorporation of such guest molecules need to be carefully considered to ensure optimum metal location. The reverse micelle route to reduction of the gold complex is advantageous over the auto-reduction route in terms of favourable particle size consistency although the disadvantage of the method is the lower loading that is achieved. The use of alkylammonium species tethered to the internal silica walls for gold (III) chloride uptake and subsequent reduction to metallic Au is the most promising as the particle sizes are favourable and abundant. In addition the route described underlines the potential of *in situ* functionalisation in this manner. Here high quality functionalised SBA-15 can be synthesised in a one-step process (at the mentioned loading) without the need for time consuming post-synthetic grafting of the organic species and to our knowledge is the first time SBA-15 functionalised *in situ* with alkylammonium groups gives favourable Au particles within the mesopores.

6.5 References

- [1] J.M. Thomas, R. Raja, *Stud. Surf. Sci. Catal.*, 2004, **148**, 163
- [2] J.M. Thomas, *Angew. Chem. Int. Ed.*, 1999, **38**, 3588
- [3] A. Taguchi, F. Schüth, *Micro. Meso. Mater.*, 2005, **77**, 1
- [4] M. Widenmeyer, R. Anwender, *Chem. Mater.*, 2002, **14**, 1827
- [5] X.S. Zhao, G.Q. Lu, A.K. Whittaker, G.J. Millar, H.Y. Zhu, *J. Phys. Chem. B.*, 1997, **101**, 6525
- [6] H. Landmesser, H. Kosslick, W. Storek, R. Fricke, *Solid State Ion.* 1997, **101-103**, 271
- [7] J. Jarupatrakorn, T.D. Tilley, *J. Am. Chem. Soc.*, 2002, **124**, 8380
- [8] C. Nozaki, C. G. Lugmair, A.T. Bell, T.D. Tilley, *J. Am. Chem. Soc.*, 2002, **124**, 13194
- [9] M.H. Lim, C.F. Blanford, A. Stein, *J. Am. Chem. Soc.*, 1997, **119**, 4090
- [10] M.H. Lim, A. Stein, *Chem. Mater.*, 1999, **11**, 3285
- [11] R.P. Hodgkins, A.E. Garcia-Bennett, P.A. Wright, *Micro. Meso. Mater.*, 2005, **79**, 241
- [12] I. Diaz, C. Marquez-Alvarez, F. Mohino, J. Perez-Pariente, E. Sastre, *J. Catal.*, 2000, **193**, 283
- [13] J.M. Thomas, *Nature*, 1994, **368**, 289
- [14] P.T. Tanev, M. Chibwe, T.J. Pinnavaia, *Nature* 1994, **368**, 321
- [15] A. Corma, M.T. Navarro, J.P. Pariente, *J. Chem. Soc. Chem. Commun.*, 1994, **2**, 147
- [16] G. Sankar, F. Rey, J.M. Thomas, G.N. Greaves, A. Corma, B.R. Dobson, A.J. Dent, *J. Chem. Soc. Chem. Commun.*, 1994, **19**, 2279
- [17] C.T. Kresge, M.E. Leonowicz, W.J. Roth, J.C. Vartuli, J.S. Beck, *Nature*, 1992, **359**, 710
- [18] J.S. Beck, J.C. Vartuli, W.J. Roth, M.E. Leonowicz, C.T. Kresge, K.D. Schmitt, C.T.-W. Chu, D.H. Olson, E.W. Sheppard, S.B. McCullen, J.B. Higgins, J.L. Schlenker, *J. Am. Chem. Soc.*, 1992, **114**, 10834
- [19] T. Maschmeyer, F. Rey, G. Sankar, J.M. Thomas, *Nature*, 1995, **378**, 159
- [20] M. Guidotti, N. Ravasio, P. Psaro, S. Coluccia, L. Marchese, E. Gianotti, *Green Chem.*, 2003, **5**, 421

- [21] N. Ravasio, F. Zaccheria, M. Guidotti, P. Psaro, *Top. Catal.*, 2004, **27**, 157
- [22] N.K.K. Raj, S.S. Deshpande, R.H. Ingle, T. Raja, P. Manikandan, *Catal Lett.*, 2004, **98**, 217
- [23] M.C. Chao, H.P. Lin, C.Y. Mou, B.W. Cheng, C.F. Feng, *Catal. Today*, 2004, **97**, 81
- [24] I. Yuranov, L. Kiwi-Minsker, P. Buffat, A. Renken, *Chem. Mater.*, 2004, **16**, 760
- [25] J.M. Thomas, T. Maschmeyer, B.F.G. Johnson, D.S. Shepard, *J. Mol. Catal. A*, 1999, **141**, 139
- [26] M. Ortega Lorenzo, C.J. Baddeley, C. Muryn, R. Raval, *Nature*, 2000, **404**, 376
- [27] M.E. Davis, *Acc. Chem. Res.*, 1993, **26**, 111
- [28] S. Che, Z. Liu, T. Ohsuna, K. Sakamoto, O. Terasaki, T. Tatsumi, *Nature*, 2004, **429**, 281
- [29] www.nobel.se/chemistry/laureates/2001/chemadv.pdf
- [30] H. Brunner, in B. Cornils and W.A. Hermann (eds.), *Applied Homogeneous Catalysis with Organometallic Compounds*, Vol. 1, Wiley-VCH, Weinheim, 1996
- [31] J.M. Thomas, *Angew. Chem. Int. Ed. Engl.*, 1999, **38**, 3588
- [32] M.D. Jones, R. Raja, J.M. Thomas, B.F.G. Johnson, D.W. Lewis, J. Rouzard, K.D.M. Harris, *Angew. Chem. Int. Ed. Engl.*, 2003, **42**, 4326
- [33] M.D. Jones, R. Raja, J.M. Thomas, B.F.G. Johnson, *Top. Catal.*, 2003, **25**, 71
- [34] M. Ortega Lorenzo, S. Haq, T. Bertrams, P. Murray, R. Raval, C.J. Baddeley, *J. Phys. Chem. B.*, 1999, **103**, 10661
- [35] V. Humblot, M. Ortega Lorenzo, C.J. Baddeley, S. Haq, R. Raval, *J. Am. Chem. Soc.*, 2004, **126**, 6460
- [36] C.J. Baddeley, *Top. Catal.*, 2003, **25**, 17
- [37] T.E. Jones, T.C.Q. Noakes, P. Bailey, C.J. Baddeley, *J. Phys. Chem. B.*, 2004, **108**, 4759
- [38] T.E. Jones, T.C.Q. Noakes, P. Bailey, C.J. Baddeley, *Surf. Sci.*, 2004, **569**, 63
- [39] C.M. Yang, M. Kalwei, F. Schüth, K.J. Chao, *Appl. Catal A: Gen.*, 2003, **254**, 289
- [40] P. Mukherjee, C.R. Patra, R. Kumar, M. Sastry, *PhysChemComm*, 2001, **97**, 49
- [41] C.M. Yang, P.H. Liu, Y.F. Ho, C.Y. Chiu, K.J. Chao, *Chem. Mater.*, 2003, **15**, 275
- [42] K.J. Chao, M.H. Cheng, Y.F. Ho, P.H. Liu, *Catal. Today*, 2004, **97**, 49

- [43] M.T. Bore, H.N. Pham, T. L. Ward, A.K. Datye, *Chem. Commun.*, 2004, **22**, 2620
- [44] R.I. Nooney, D. Thirunavukkarasu, A.E. Ostafin, Y. Chen, R. Josephs, *Micro. Meso. Mater.*, 2004, **75**, 183
- [45] J. Zhu, Z. Kónya, V.F. Puntes, I. Kirics, C.X. Miao, J.W. Ager, A.P. Alivisatos, G.A. Somorjai, *Langmuir*, 2003, **19**, 4396
- [46] G. Lü, R. Zhao, G. Qian, Y. Qi, X. Wang, J. Suo, *Catal. Lett.*, 2004, **97**, 115
- [47] T.M. Salama, R. Ohmishi, T. Shido, M. Ichikawa, *J. Catal.*, 1996, **162**, 169
- [48] G.C. Bond, *Catal. Today*, 2002, **72**, 5
- [49] W. Nowicki, G. Nowicka, *J. Chem. Ed.*, 1994, **71**, 624
- [50] A. Ghosh, C.R. Patra, P. Mukherjee, M. Sastry, R. Kumar, *Micro. Meso. Mater.*, 2003, **58**, 201
- [51] J. Lin, W. Zhou, C.J. O'Connor, *Mat. Lett.*, 2001, **49**, 282
- [52] C.M. Yang, P.H. Liu, Y.F. Ho, C.Y. Chiu, K.J. Chao, *Chem. Mater.*, 2003, **15**, 275
- [53] B.T. Holland, C.F. Blanford, T. Do, A. Stein, *Chem. Mater.*, 1999, **11**, 795
- [54] Personal communication, Dr. M. Clarke, University of St. Andrews
- [55] Personal communication, Johnson Matthey
- [56] M. Nakamoto, M. Yamamoto, M. Fukusumi, *Chem. Commun.*, 2002, **15**, 1622
- [57] Y.S. Shon, C. Mazzitelli, R.W. Murray, *Langmuir*, 2001, **17**, 7735

Chapter 7

General conclusions & further work

Synopsis

This chapter details the overall conclusions presented from the thesis as a whole from observations of in situ functionalisation of mesoporous silicas to their further modification with both azamacrocycles and precious metals. Details of further work including investigation of precious metal nanoparticle functionalised mesoporous solids as potential catalysts are set out.

7.1 General conclusions

Investigation of organo-siloxane inclusion directly into the sol-gel syntheses of P123-templated mesoporous materials in acidic media has shown the maximum loadings attainable for each functional group that give rise to solids with an established degree of order and defined mesoporosity. The maximum loading of the co-condensing organo-siloxane included into the final silica product (based on total SiO₂) whilst still retaining a high degree of order increase with the sequence propylchloride (5%) , phenyl (5%) < propylthiol (7%) < cyanopropyl (10%). Functionalising such silica materials *in situ* allows the effects of the organo-siloxanes on the meso-product phase and quality to be observed rather than post-synthetic grafting onto a pre-fabricated solid.

A new solid, designated **STA-11**, has successfully been prepared by co-condensing MPTES with TEOS at a loading of 7% (at a specific hydrolysis temperature, 313K).

The change in meso-product from hexagonal p6mm SBA-15 to cubic Ia $\bar{3}$ d STA-11 results in a solid with a unit cell of a 220 Å and a pore size in the region of 80 Å with a large wall thickness simulated to be 40% of the unit cell. STA-11 is a promising solid with potential advantages over both SBA-15 and MCM-48 through its bicontinuous extra large pore 3D structure having the potential for enhanced molecular diffusion of guest molecules and resistance to pore blocking. The large pore cubic solid can also be synthesised with PTES as a co-condenser at loadings of 5% although a small amount of hexagonal SBA-15 remains. The chloropropyl- and cyanopropyl-siloxanes give SBA-15 at all loading levels with cyanopropyl-siloxanes being the most readily incorporated without loss of structural regularity. The change in meso-phase is thought to come about through a difference in micellar packing, giving a lower curvature due to the functional group's hydrophobic interaction with the inner PPO core.

Thiol inclusion into F127 templated materials results in structural and morphological changes to the reported pure siliceous FDU-12 (Fm3m) cubic close packed structure (ABCABC). Loading levels of 5% result in disruptions to the stacking sequence and include stacking faults and twin planes along with domains of the hexagonal end

member (ABAB) stacking sequence. The local disruptions result in changes to the morphology, gives hexagonal prisms that taper towards the basal face. It would seem that only a few defects are required for the change in morphology. Increasing the loading to 7% results in a morphology that consist of hexagonal plates with a reduced (length/cross sectional area) ratio. The difference in mesostructure here lies in the relative stacking sequence rather than the local structure with no obvious change in the micellar curvature.

The accessibility of thiol groups within thiol-containing P123 and F127 solids has been quantified using Ellman's reagent. It was found that 54 – 72% of the thiols were accessible to Ellman's reagent for the P123-templated solids and 50 – 60% for F127-templated solids. This fraction would suggest that such samples will be useful in applications such as heavy metal extraction.

Cyclam has been successfully incorporated into SBA-15 and modified by metal ion complexation. The environment of $\text{Cu}[\text{cyclam}]^{2+}$ -SBA-15 has been investigated by ESR and with TGA and elemental analysis has helped to improve the conditions of synthesis. It was found that that the Cu (II) co-ordination was in axial symmetry and distorted square planar with respect to the nitrogens of the azamacrocyclic will Jahn-Teller elongated axial ligands. The importance of multi-frequency ESR permits unambiguous determinations of the spin Hamiltonians and circumvents complications of overlapping \parallel and \perp regions and the off-axis peak found at x-band. Attempts of selective oxidation catalysis were found to be unsuccessful as leaching of the metal complexes occurs readily so that no further work was carried out along this line.

The inclusion of precious metal complexes and metallic colloids (mainly gold (III) chloride) into organo-functionalised silicas (mainly with thiols) has been investigated by varying the routes to reduction. The range of reduction methods gave final mesoporous solids containing metal nanoparticles of various sizes. Incorporation of pre-reduced Au sols via sodium citrate onto thiol-functionalised materials show clearly that the Au nanoparticles are positioned on the external surface of the solid as the nanoparticle diameters are in the region of a factor of 10 larger than the pore diameter of the silica supports. Through the auto-reduction route it was found that the

uptake of gold (III) chloride was rapid in the presence of thiols whereas an extracted or calcined pure siliceous sample has significantly less uptake over an extended period of time. The route facilitates two varying outcomes of particle location depending on the silica support used. For SBA-15-SH (2%) the Au particles are favourable in size, viewed by TEM to be 5 – 7 nm that could be found within the mesopores although there are particles that are too large to be positioned within the mesopores. For the smaller pore STA-11 the Au particles are clearly located on the external surface with no sign of pore modification through N₂ measurements. Reduction of gold reverse micelles with sodium borohydride too results in favourable particle sizes of although there are fewer particles observed than for the auto-reduction route. Pore blocking is a possible explanation as a high loading of bromide ions associated with CTAB is found through elemental analysis and a reduction in capacity for N₂ is observed. The most promising route to include Au nanoparticles was found to be via the use of charged alkylammonium groups tethered to the walls of silica followed by efficient uptake of gold (III) chloride preceding thermal reduction in H₂. The Au nanoparticles in the region of 4 – 9 nm in diameter are abundant and evenly distributed. Pore modification through N₂ adsorption measurements is further evidence of gold within the pores.

7.2 Further work

Modification of the synthesis of P123-templated solids through incorporating more complex ligands in the form of alkoxy silanes directly into the synthesis of the sol-gel may allow ordered meso-structure/-porosity to be obtained with accessible 'ready-made' ligands on high surface area solids. Such functionalised materials would be widely applicable.

Given the structural changes from cubic Fm3m to 3D hexagonal P6₃/mmc observed with thiol-functionalised FDU-12 at a 5% loading further investigation is required to try and prepare for the first time the perfect hexagonal large pore P6₃/mmc solid. Incorporating a series of organo-siloxanes directly to the sol-gel synthesis (like that

for the P123-templated materials) at various loadings, along with variation of additive reagents could produce the pure phase.

Catalysis on the precious metal incorporated within the mesoporous solids should be performed to observe both their catalytic performance and relative stabilities with respect to how strongly the metal particles are retained. The method/conditions of reduction should be taken a step further for platinum and palladium. In addition the possibility of using stable precious metal nanoparticles within the pores to adsorb chiral ligands for subsequent chiral catalysis is a particularly attractive option.